

# Development of Real-Time Smart Data Analytic Tools for Monitoring and Optimum Operation of MGT Systems

by

Reyhaneh Banihabib

Thesis submitted in fulfilment of  
the requirements for the degree of  
PHILOSOPHIAE DOCTOR  
(PhD)



Faculty of Science and Technology  
Department of Energy and Petroleum Engineering  
2024

University of Stavanger  
NO-4036 Stavanger  
NORWAY  
[www.uis.no](http://www.uis.no)

©2024 Reyhaneh Banihabib

ISBN: 978-82-8439-240-0

ISSN: 1890-1387

PhD: Thesis UiS No. 762



# Acknowledgment

I begin by expressing my deep gratitude to Professor Mohsen Assadi, my supervisor, for providing me with the opportunity to embark on this transformative PhD study. His guidance and unwavering encouragement have been instrumental in shaping the trajectory of my research. Additionally, I extend my thanks to Mr. Øystein Arild, our head of department, for his consistent support and encouragement throughout my studies.

I am particularly thankful for the enriching multidisciplinary experience provided by the NextMGT team, offering valuable and varied resources that significantly contributed to my research journey. Dr. Peter Jansohn and Markus Josef Obrist at the Paul Scherrer Institute deserve profound thanks for their impactful contributions, warm welcome, patience, and collaborative spirit during my secondment there.

Deep gratitude is extended to the engineers at Risavika Research Center, Bjarte Ludvig Hetlelid, and Magnus Wersland for their significant contributions during the execution of tests. Their extensive knowledge and patience were indispensable to the success of this work.

A profound appreciation is reserved for my husband, Iman Hedayatnia, whose unwavering support and boundless patience have been the cornerstone of my resilience throughout this challenging journey. Finally, my deepest gratitude extends to my family in Iran—my parents and my sister—who are the pillars of any accomplishment in my life.

This PhD journey has been enriched by the collaborative spirit and unwavering support of each individual and institution mentioned here. I am profoundly grateful for the meaningful contributions that have made this experience truly fulfilling.

## Abstract

In the evolving energy landscape, a shift away from traditional centralized power models is underway. Distributed energy generation (DEG) takes the spotlight, enabling consumers to utilize a tailored mix of energy sources. Micro gas turbines (MGTs) emerge as key players, providing dispatchable power to seamlessly address renewable source intermittency. Aligned with global energy policies emphasizing renewables and efficiency, MGTs contribute significantly to sustainability goals.

This study aims to actively advance power generation technology towards higher efficiency and environmental responsibility, supporting the vision for a cleaner and more resilient energy future. The focus centers on enhancing the fuel versatility of MGTs and optimizing their integration within distributed energy systems. Aligned with the visionary goals of the NextMGT project, this endeavor focuses on advancing MGT technology for high efficiency, low emissions, and enhanced fuel flexibility.

The journey begins with an exploration into optimizing an MGT for efficient hydrogen operation — a clean fuel and potential storage solution for surplus renewable power. Despite substantial progress in the laboratory and theoretical realms, the research spotlights a critical gap: the absence of reported operational instances of MGTs running with hydrogen. This underscores the imperative to bridge the divide between theoretical prowess and real-world applications, a recurring theme in the thesis. Concurrently, the research navigates the intricate integration of MGTs into DEG, particularly those fueled by hydrogen. Addressing the challenges of integration and optimization with renewable systems, artificial intelligence (AI) based on real-world data is employed to enhance microgrid performance.

Undertaking the mission to create a functional hydrogen-fueled MGT, the research confronts challenges such as combustion stability and emissions control. Through targeted modifications in combustor design and operational adjustments, the thesis emphasizes real-world testing, highlighting the crucial need for practical implementations. Notably, the outcome is an MGT demonstrating fuel flexibility with various methane and hydrogen combinations, capable of running on pure hydrogen, all while maintaining NO<sub>x</sub> emissions below the permitted values.

A significant step in the research narrative involves adopting a dual-modeling approach—utilizing both physics-based and data-driven models. The physics-based models, also known as white-box models, rooted in physics for theoretical understanding, exhibit adaptability to diverse operational scenarios, aligning with steady state and transient responses. This model plays a crucial role during the developmental phase of the MGT for hydrogen and hydrogen-blended methane, assessing its operation in different scenarios.

In addressing the integration of MGT within a microgrid, a data-driven or black-box modeling approach is employed. These black-box models, driven by empirical data, incorporating artificial neural networks (ANNs) and recurrent neural networks (RNNs), emerge as a robust framework for MGT modeling. The versatility of the method extends beyond MGTs, laying the groundwork for advancements in various renewable energy contexts.

In a dedicated chapter, the study delves into microgrid integration and optimization. Here, a smart management system coordinates interactions among wind turbines, an MGT, and an electrolyzer. The optimizer navigates the complex terrain of economic gains and environmental sustainability. The findings emphasize the practical application of a smart management system in optimizing microgrid operations for economic efficiency, demonstrating the relevance of the research insights.

## Abstract

---

In response to Norway's imperative to curtail emissions from offshore oil and gas operations, the research broadens its focus to optimize gas turbine operations within integrated systems. The research demonstrates adaptability by transitioning from onshore microgrids with MGTs to offshore scenarios with larger gas turbines, highlighting the transformative and generalizable capacity of methodologies and insights. The optimization of offshore microgrids results in considerable cost and emission reductions. The hybrid optimization approach, efficiently utilizing genetic algorithms alongside rapid database searches, enhances efficiency without an excessive demand for computing resources. Throughout this project, the strategic adoption of an infrastructural approach has been pivotal in the development of all models and programs. This deliberate choice ensured the effectiveness of transformative insights and a seamless adaptability and expandability of the work. Integrating hydrogen-fueled MGTs with advanced AI management tools moves beyond theory; it represents a practical step toward achieving sustainable development goals. From onshore microgrids to offshore scenarios, the research illustrates a commitment to real-world applications. Its impact extends beyond theoretical contributions, actively shaping a more sustainable, resilient, and eco-friendly energy future. Additionally, by identifying areas for future research, this thesis lays the foundation for ongoing advancements in sustainable energy solutions.

# Table of Contents

Acknowledgment .....	i
Abstract .....	ii
Table of Contents .....	v
List of Figures .....	viii
List of Tables.....	xii
Nomenclature .....	xiii
List of Publications .....	xviii
1 Introduction .....	1
1.1 Background and Motivation .....	2
1.2 Microgrids: Navigating the Road to Decentralized Energy....	5
1.3 Energy Consumption Trends and Sustainable Solutions .....	6
1.4 Cogeneration of Heat and Power .....	8
1.5 MGTs as Micro CHP Units.....	9
1.6 Problem Statement .....	10
1.7 Objectives and Research Questions .....	12
1.8 Significance of the Study .....	15
2 Literature Review .....	17
2.1 Developments of MGTs Running with Hydrogen.....	17
2.2 Modeling Gas Turbines.....	21
2.3 Microgrid Operation and Optimization .....	33
2.4 Summary and Conclusion .....	36
3 Development of a Hydrogen-Powered MGT .....	38
3.1 Challenges in Hydrogen Combustion .....	38

## Table of Contents

---

3.2	Development of an MGT Running with Hydrogen Fuel.....	44
3.3	Results.....	48
3.4	Conclusion .....	50
4	Development of an MGT Model: Physics-Based Approach.	52
4.1	T100 MGT .....	52
4.2	Development of the Dynamic Model of the Fuel-Flexible MGT	55
4.3	Development of the Steady State Model of the Fuel-Flexible MGT	63
4.4	Adaptation of the Physics-Based Model to Experimental Data	68
4.5	Results.....	72
4.6	Conclusion .....	75
5	Development of an MGT Model: Data-Driven Approach....	76
5.1	The Importance of Data .....	76
5.2	Data Preprocessing.....	78
5.3	Development of a Data-Driven Model .....	87
5.4	Performance Evaluation Metrics.....	95
5.5	Conclusion .....	98
6	Optimization of MGT Operation in an Integrated System....	99
6.1	Microgrid System Description.....	99
6.2	Modeling the Microgrid.....	102
6.3	Operation of the Microgrid without Smart Management ...	105
6.4	Operation of the Microgrid with Smart Management.....	105
6.5	Results.....	109
6.6	Conclusion .....	113

## Table of Contents

---

7	Offshore Microgrid Integration and Optimization .....	114
7.1	Mitigating Offshore Oil and Gas Platform Emissions .....	114
7.2	Case Study Description: Gullfaks Platforms and Hywind Tampen.....	115
7.3	Implementing a Storage System .....	116
7.4	Managing the Microgrid Operation .....	117
7.5	Results.....	125
7.6	Conclusion .....	130
8	Concluding Remarks .....	131
8.1	Overview of the Conducted Study .....	131
8.2	Additional Studies Conducted During the PhD Program ...	133
8.3	Future Research .....	137
8.4	Conclusion .....	139
	References .....	140
	Paper I .....	162
	Paper II .....	184
	Paper III.....	204
	Paper IV .....	218
	Paper V .....	231
	Paper VI .....	243
	Paper VII.....	277

## List of Figures

Figure 1.1 EU targets for GHG reduction with renewable energy technologies penetration [2] modified with new proposed targets [3].	3
Figure 1.2 Annual capacity additions by renewable technology, main and accelerated cases, 2015-2027 [4].	3
Figure 1.3 Global CO <sub>2</sub> emissions by sector, 2019 to 2022 [8].	4
Figure 1.4 The integrated and intelligent electricity system of the future [9].	5
Figure 1.5 Final energy consumption by sector, EU-27, 2021 [16].	7
Figure 1.6 Final energy consumption of the residential sector of EU countries, 2021 [20].	8
Figure 1.7 Overview of the thesis structure, detailing chapters and their corresponding research questions.	14
Figure 2.1 Simulink scheme of the single-shaft GT from [59].	25
Figure 2.2 Schematic of an Aspen Plus model of a two-pressure CCPP from [73].	27
Figure 2.3 The developed ANN model in [87], (a) schematic of a multi-layer feed-forward network, (b) the final optimized model structure.	31
Figure 3.1 Flue gas properties in different equivalence ratios for burning methane and hydrogen, with air at 4.3 bar and 610 K. The plots are depicted using analysis conducted with Cantera [126].	42
Figure 3.2 Fuel system arrangement installed outdoors, (a) the valves, (b) fuel bottles.	44
Figure 3.3 The modified fuel system, (a) the mixing station and fuel train installed on top of the MGT enclosure, (b) the combustor.	45
Figure 3.4 The combustor of the MGT a) the original Turbec design, b) F400s ver.02.	46



## List of Figures

---

Figure 3.5 Schematic of the FLOX <sup>®</sup> combustion principle [127].	46
Figure 3.6 Expected relative combustion air over dilution hole diameter. ....	47
Figure 3.7 Structure of the MGT unit equipped with the new fuel train system, controllers, and measurement points. ....	48
Figure 3.8 Turbec T100 unit with modified combustor and fuel train for flexible fuel operation. ....	49
Figure 4.1 The T100 MGT, located at Risavika Research Center, Stavanger, Norway. ....	53
Figure 4.2 The T100 MGT, located at PSI, Villigen, Switzerland. ....	53
Figure 4.3 Schematic view of the T100 engine. ....	54
Figure 4.4 The MGT from outside (left) and its inside (right). The figure on the right side is imported from [128]. ....	55
Figure 4.5 Developed model for the T100 unit using MATLAB Simscape: (a) thermodynamic cycle, (b) user's inputs to the model, (c) a sample for reference power. ....	57
Figure 4.6 Developed model for a Turbec T100 unit using MATLAB Simulink [129]. ....	58
Figure 4.7 Controller of the T100 MGT developed in Simulink. .	60
Figure 4.8 The main components of the T100 MGT from [130]. .	61
Figure 4.9 Structure of the developed steady state model, showing the data transferred between four principal modules. ....	64
Figure 4.10 The flowchart of the steady state model. ....	66
Figure 4.11 The structure of the thermodynamic cycle module and the stream of parameters. ....	67
Figure 4.12 The process of steady state model adaptation to experimental data. ....	70
Figure 4.13 Cycle analysis of the MGT running with pure methane, producing 100 kW at ISO conditions. ....	73
Figure 4.14 Cycle analysis of the MGT running with pure hydrogen, producing 100 kW at ISO conditions. ....	73

## List of Figures

---

Figure 5.1 Visualization of experimental data, (a) engine rotational speed and (b) fuel flow rate, both plotted parallel to power output. ....	82
Figure 5.2 Monitoring points for easy reading of the visualized data. ....	82
Figure 5.3 A complete operational envelope for an MGT from start-up to shutdown. ....	84
Figure 5.4 Functionality of the steady state time recognizer module. ....	86
Figure 5.5 Structure of (a) an artificial neuron and (b) a multilayer ANN. ....	91
Figure 5.6 Schematic of a NARX model. ....	92
Figure 5.7 Visualization of the prediction accuracy for the ANN model, (a) fuel flow rate, (b) exhaust gas temperature. ....	97
Figure 5.8 Visualization of the prediction accuracy for the NARX model, (a) fuel flow rate, (b) exhaust gas temperature. ....	97
Figure 6.1 The building that represents the heat and power demands of the microgrid. ....	100
Figure 6.2 WTN250 wind turbine of the microgrid and its power curve [133]. ....	100
Figure 6.3 Schematic view of the microgrid. ....	101
Figure 6.4 The ANN models for (a) the wind turbines, and (b) the MGT of the microgrid. ....	102
Figure 6.5. The model for heat and power demand prediction in the consumer building of the microgrid. ....	104
Figure 6.6 The flowchart of the operations (a) optimization, and (b) condition-based. ....	108
Figure 6.7 Accumulated demanded power and heat, and the produced power by the wind on a daily basis. ....	109
Figure 6.8 The hourly distribution of wind power, demand power, and demand heat over the week of study. ....	110
Figure 7.1 Schematic diagram of the offshore microgrid and its smart management system. ....	117

## List of Figures

---

Figure 7.2 Condition-based operation flowchart for GFC. ....	120
Figure 7.3 Condition-based operation flowchart for GFA. ....	120
Figure 7.4 Hybrid optimization approach with outer loop for power transfer and fuel ratios and inner loop for platform operations. ....	125
Figure 7.5 Total power demand from three Gullfaks platforms in comparison to the power generated by the wind farm. ....	126
Figure 7.6 The total power produced by the seven GTs on the three Gullfaks platforms. ....	127
Figure 7.7 The total power produced by the four GTs on the GFA platform. ....	128
Figure 7.8 The total power produced by the three GTs on the GFC platform. ....	128
Figure 7.9 The power received by GFC from GFA. ....	128
Figure 7.10 The rate of hydrogen production. ....	129
Figure 7.11 The rate of hydrogen consumption. ....	129

## List of Tables

Table 1.1 Urbanization rate in percent of the total population in developing countries (DC) and industrialized countries (IC) [11].	7
Table 3.1 Comparison of the properties of hydrogen and methane in atmospheric pressure and 300K temperature [108].	39
Table 3.2 Flue gas properties comparison burning methane and hydrogen. Air composition is 21% O <sub>2</sub> and 79% N <sub>2</sub> with 4.3 bar pressure and 610 K temperature.	43
Table 4.1 AE-T100 nominal characteristics reported by the manufacturer [128].	55
Table 4.2 Model prediction error for target parameters before and after adaptation.	71
Table 4.3 Comparison of MGT operation with methane and hydrogen fuel with different power rates at ISO conditions.	74
Table 5.1 Optimized hyperparameters for the ANN and NARX model of the MGT.	94
Table 5.2 Evaluation of ANN and NARX model performance on test data.	96
Table 6.1 The error of the models' predictions on the test data set.	104
Table 6.2 Overview of island mode operation of the microgrid.	110
Table 7.1 Inputs and outputs of microgrid subsystem models.	121
Table 7.2 ANN models optimized configuration.	121
Table 7.3 Models prediction error.	122
Table 7.4 Comparison of hydrogen balance after a week of operation by different scenarios.	129
Table 7.5 Overview of grid mode operation of the microgrid.	130

## Nomenclature

a	Absolute (pressure)
C	Molecular composition tensor /Cost factor
c	Specific cost
CO	Carbon monoxide
CO <sub>2</sub>	Carbon dioxide
c <sub>p</sub>	Specific heat of gas at constant pressure
D	Dimension/ Direction
dem	Demand
E	Error
e	Total energy per unit mass
El	Electricity
el	Electrical
$\vec{F}$	Force
FHR	Fuel heating value ratio
g	Gauge (pressure)/ acceleration due to gravity
h	Heat/enthalpy
HC	Hydro carbons
HyT	Hydrogen tank
Inc	Incentive
M	Mass
$\vec{M}$	Moment
$\dot{m}$	Mass flow rate
N	Relative rotational speed/Number of gas turbines
N <sub>2</sub>	Molecular nitrogen
NO	Nitric oxide
NO <sub>2</sub>	Nitrogen dioxide
NO <sub>x</sub>	Nitrogen oxides
O <sub>2</sub>	Molecular oxygen

## Nomenclature

---

OV	Objective value
P	Power
p	Pressure
Pen	Penalty
pr	Price
pu	Per unit
Q	Heat transferred to the control volume
R	Gas constant
ReLU	Rectified linear unit
S	Speed
s	Specific entropy
T	Temperature
t	Time
u	Internal energy per unit mass
V	Valve position/Volume
$\vec{V}$	Velocity
W	Work done by the control volume
X	Measured value from a sensor
x	Weight coefficient /input parameter in ANN model
y	Output parameter in ANN model
Z	Z-score for sensor reading normalization/vertical coordinate

## Greek Symbols

$\varepsilon$	Effectiveness
$\eta$	Efficiency
$\mu$	Mean value of sensor readings
$\rho$	Density
$\sigma$	Standard deviation
$\tau$	Time constant
$\vec{\tau}$	Torque
$\varphi$	Energy flow rate

## Nomenclature

---

$\Phi$	Equivalence ratio
$\omega$	Rotational velocity

## Indices

a	Air
act	Actual
amb	Ambient
avg	Average
cmp	Compressor
cons	Consumed
cont	Content
dem	Demand
diff	Difference
ds	Desalination
eg	Exhaust gas
el	Electricity
exp	Export
f	Fuel
imp	import
maint	Maintenance
MG	Microgrid
nom	Nominal
pen	Penalty
pred	Predicted
prod	Produced
pu	Per unit
rcp	Recuperator
ref	Reference
rel	Relative
t	Total
th	Thermodynamic

## Nomenclature

---

trb	Turbine
W	wind

## Abbreviations

AC	Alternating current
AE	Ansaldo Energia/absolute error
AF	Adiabatic Flame
AI	Artificial intelligence
ANFIS	Adaptive network-based fuzzy interface system
ANN	Artificial neural network
CB	Condition-based
CCPP	Combined cycle power plant
CFD	Computational fluid dynamic
CHP	Combined heat and power
CSP	Concentrating solar power
DC	Developing countries
DEG	Distributed energy generation
DER	Distributed energy resource
DLR	Deutsches Zentrum für Luft- und Raumfahrt/The German Aerospace Center
EFMGT	Externally-fired micro-gas turbine
ELH	Electrical heater
ELZ	Electrolyzer
EPA	Environmental Protection Agency
ESS	Energy storage systems
EU	European Union
FR	Fuel ratio
GA	Genetic algorithm
GFA	Gullfaks A
GFB	Gullfaks B
GFC	Gullfaks C
GHG	Greenhouse gas



## Nomenclature

---

GM	Grid mode
GRA	Grey relational analysis
GT	Gas turbine
GTP	Gas turbines to produce power
GTQ	Gas turbines to produce heat
IC	Industrialized countries
IM	Island mode
IoT	Internet of things
LHV	Lower heating value
LSTM	Long short-term memory
MAE	Mean absolute error
MAPE	Mean absolute percentage error
MGT	Micro gas turbine
MPC	Model predictive control
NARX	Non-linear auto-regressive exogenous
NPV	Net present value
O&G	Oil and gas
OPT	Optimum
PI	Proportional-integral
RH	Relative humidity
RMSE	Root mean square error
RNN	Recurrent neural network
SCADA	Supervisory control, and data acquisition system
SGD	Stochastic gradient descent
TIT	Turbine inlet temperature
TOT	Turbine outlet temperature
WHRU	Waste heat recovery unit
WT	Wind turbine

## List of Publications

The content of this thesis relies on the papers referenced in the text with Roman numerals and appended at the end of the thesis.

- Paper I R. Banihabib and M. Assadi, “The Role of Micro Gas Turbines in Energy Transition,” *Energies*, vol. 15, no. 21, p. 8084, Oct. 2022, doi: 10.3390/EN15218084.
- Paper II R. Banihabib, T. Lingstädt, M. Wersland, P. Kutne, and M. Assadi, “Development and testing of a 100 kW fuel-flexible micro gas turbine running on 100% hydrogen,” *Int J Hydrogen Energy*, vol. 49, pp. 92–111, Jan. 2024, doi: 10.1016/j.ijhydene.2023.06.317.
- Paper III Banihabib and M. Assadi, “A Hydrogen-Fueled Micro Gas Turbine Unit for Carbon-Free Heat and Power Generation,” *Sustainability*, vol. 14, no. 20, 2022, doi: 10.3390/su142013305.
- Paper IV R. Banihabib and M. Assadi, “Dynamic Modelling and Simulation of a 100 kW Micro Gas Turbine Running With Blended Methane/Hydrogen Fuel,” in *Volume 7: Industrial and Cogeneration; Manufacturing Materials and Metallurgy; Microturbines, Turbochargers, and Small Turbomachines; Oil & Gas Applications*, American Society of Mechanical Engineers Digital Collection, Jun. 2022. doi: 10.1115/GT2022-81276.
- Paper V R. Banihabib, M. J. Obrist, M. Assadi, and P.

## List of Publications

---

- Jansohn, “Micro Gas Turbine Modelling And Adaptation For Condition Monitoring,” in *Global Power and Propulsion*, Chania, 2022.
- Paper VI R. Banihabib, F. S. Fadnes, and M. Assadi, “Techno-Economic Optimization of Microgrid Operation with Integration of Renewable Energy, Hydrogen Storage, and Micro Gas Turbine,” *Under review for Energy Conversion and Management*.
- Paper VII R. Banihabib and M. Assadi, “Towards a low-carbon future for offshore oil and gas industry: A smart integrated energy management system with floating wind turbines and gas turbines,” *J Clean Prod*, vol. 423, p. 138742, Oct. 2023, doi: 10.1016/j.jclepro.2023.138742.
- In addition to the papers included in the thesis, there are extra publications, comprising conference and journal papers, produced during this PhD but not integrated into the thesis.
- Paper VIII Banihabib, F. Skaug Fadnes, M. Assadi, and B. Bensmann, “Optimizing Micro Gas Turbine Operation in a Microgrid System With Natural Gas and Hydrogen Fuel: An Artificial Intelligence-Based Approach,” *J Eng Gas Turbine Power*, vol. 146, no. 2, Feb. 2024, doi: 10.1115/1.4063423.
- Paper IX Q. Zhang, R. Banihabib, F. S. Fadnes, T. A. S. Sazon, N. Ahmed, and M. Assadi, “Techno-economic analysis of a biogas-fueled micro gas turbine cogeneration system with seasonal thermal energy storage,” *Energy Convers Manag*, vol. 292, p. 117407, Sep. 2023, doi: 10.1016/j.enconman.2023.117407.

## List of Publications

---

- Paper X R. Banihabib, F. S. Fadnes, and M. Assadi, “Optimizing Building Heating Efficiency: A Data-driven Approach for Cost and Energy Savings,” in *2023 IEEE 11th International Conference on Smart Energy Grid Engineering (SEGE)*, IEEE, Aug. 2023, pp. 212–217. doi: 10.1109/SEGE59172.2023.10274593.
- Paper XI N. Ahmed, M. Assadi, A. A. Ahmed, and R. Banihabib, “Optimal design, operational controls, and data-driven machine learning in sustainable borehole heat exchanger coupled heat pumps: Key implementation challenges and advancement opportunities,” *Energy for Sustainable Development*, vol. 74, pp. 231–257, Jun. 2023, doi: 10.1016/j.esd.2023.04.004.
- Paper XII N. Ahmed, M. Assadi, A. A. Ahmed, R. Banihabib, and Q. Zhang, “Assessing the impact of borehole field data on AI-based deep learning models for heating and cooling prediction,” *Geothermics*, vol. 117, p. 102867, Feb. 2024, doi: 10.1016/j.geothermics.2023.102867.
- Paper XIII F. S. Fadnes, R. Banihabib, and M. Assadi, “Using Artificial Neural Networks to Gather Intelligence on a Fully Operational Heat Pump System in an Existing Building Cluster,” *Energies (Basel)*, vol. 16, no. 9, p. 3875, May 2023, doi: 10.3390/en16093875.
- Paper XIV F. S. Fadnes, R. Banihabib, and M. Assadi, “Artificial neural network model for predicting CO<sub>2</sub> heat pump behaviour in domestic hot water

## List of Publications

---

- and space heating systems,” *IOP Conf Ser Mater Sci Eng*, vol. 1294, no. 1, p. 012054, Dec. 2023, doi: 10.1088/1757-899X/1294/1/012054.
- Paper XV R. Banihabib, H. Hoenen, and M. Assadi, ‘Streamlining multi-hole probe calibration using artificial neural networks’, *Flow Measurement and Instrumentation*, vol. 97, p. 102569, Jul. 2024, doi: 10.1016/j.flowmeasinst.2024.102569.
- Paper XVI M. Assadi, R. Banihabib, and H. ten Dam, “Towards a Carbon-Neutral Future: The University of Stavanger’s Pilot-Scale Hydrogen-Based Energy System for Decarbonization of Offshore Platforms. Gulf Research Meeting,” in *Gulf Research Meeting (GRM)*, Cambridge, Jul. 2023.
- Paper XVII F. Grimm, T. Lingstädt, T. Kathrotia, R. Banihabib, M. Assadi, and P. Kutne, “Hydrogen and Hydrogen Blended Jet and Recirculation Stabilized Combustion in a Turbec T100 Micro Gas Turbine Combustor,” in *Dispatchable technology & innovations for a carbon-neutral society*, Brussels: International Gas Turbine Conference (IGTC), Oct. 2023.
- Paper XVIII M. Assadi and R. Banihabib, “A Fuel Flexible CHP-MGT Test Rig for Dispatchable Power Generation European Conference on Renewable Energy Systems,” in *European Conference on Renewable Energy Systems*, Istanbul: ECRES, May 2022.
- Paper XIX R. Banihabib, K. N. Finney, M. Assadi, P. Kutne, M. Pourkashanian, and T. Lingstädt, “Gas Turbine

## List of Publications

---

- Operation with Hydrogen Blends,” in *14th European Conference on Industrial Furnaces and Boilers (INFUB-14)*, Algarve, Apr. 2024.
- Paper XX R. Banihabib, H. Hoenen, and M. Assadi, “Efficient Calibration of Pneumatic Multi-Hole Probes Using Artificial Neural Networks: A Time and Cost-effective Approach,” in *10th International Conference on Control, Decision and Information Technologies*, Valletta: IEEE, Jul. 2024.
- Paper XXI K. Bollas, R. Banihabib, M. Assadi, and A. Kalfas, ‘Optimal operating scenario and performance comparison of biomass-fueled externally-fired microturbine’, *Energy*, vol. 296, p. 131225, Jun. 2024, doi: 10.1016/j.energy.2024.131225..
- Paper XXII K. Bollas, R. Banihabib, M. Assadi, and A. Kalfas, “On the potential of biomass-fueled externally-fired micro-gas turbines in the energy transition: off-design performance analysis,” *Under review for Journal of Engineering for Gas Turbines and Power*.

# 1 Introduction

Presently, the conventional approach to large-scale power generation, reliant on fossil fuels or nuclear technology, has fallen out of favor among climate change scientists, regulators, and an increasing majority of voters. Instead, there is a growing emphasis on distributed energy generation (DEG), which empowers customers to choose and deploy diverse energy sources in smaller increments, tailored to their specific needs. This DEG paradigm facilitates power generation at or near the point of consumption, utilizing a range of technologies including micro gas turbines (MGTs), fuel cells, diesel and gas reciprocating engines, solar panels, and wind turbines.

In response to the dynamic changes in energy technology, the NextMGT project emerged as an initiative dedicated to advancing the next generation of MGTs for high efficiency, low emissions, and fuel flexibility [1]. The current project, operating under the NextMGT framework, aims to make an impact on the progression of MGTs as a fundamental element of DEG. The primary goal is to enhance MGT technology, focusing on design, operation, and integration strategies, aligning with NextMGT objectives for a resilient European industry in distributed power generation.

Building upon this context, this chapter provides a concise overview of the evolution of electricity generation schemes. It examines the current global energy policy and associated studies to highlight the potential role of MGTs in the upcoming power generation landscape. Emphasis is placed on the significance of continued research and development in enhancing MGT performance, and the research's objectives and scope are delineated accordingly.

## 1.1 Background and Motivation

It is widely acknowledged among experts that the abnormal increase in the earth's average surface temperature is primarily attributed to the emission of greenhouse gases (GHGs). This pressing issue has become a topic of extensive discussions within national and international political spheres, as they actively seek viable solutions.

The pressing challenge of the “energy problem” has spurred the United Nations Framework Convention on Climate Change into taking resolute measures through the “COP21 Agreement.” This agreement has notably reinforced policies addressing climate change, propelling the shift towards an energy paradigm characterized by low carbon emissions.

In December 2011, the European Commission communicated on the topic “Energy Roadmap 2050”. The European Union (EU) is committed to reducing GHG emissions to 80-95% below 1990 levels, aiming to be climate-neutral (with net-zero GHG emissions) by 2050.

In October 2014 the EU adopted “Vision 2030”, outlining a clear path to increase the embracing of renewable energy technologies and improve power production efficiency. Their ambitious targets include a 40% reduction in GHG emissions by 2030 (measured against 1990 levels) [2].

The key targets of the EU for 2030 are [3]:

- At least a 40% reduction in GHG emissions (from 1990 levels), by decreasing emissions and increasing removals;
- At least a 32.5% improvement in energy efficiency;
- At least 32% share of renewable energy.

Figure 1.1 depicts the EU energy targets. These targets aim to help the EU achieve more competitive, secure, and sustainable energy systems.



## Introduction

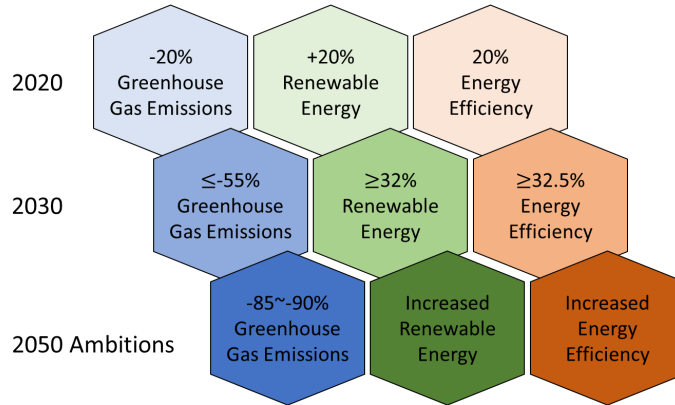


Figure 1.1 EU targets for GHG reduction with renewable energy technologies penetration [2] modified with new proposed targets [3].

The rapid rise of renewables as the leading global electricity source indicates a transformative shift to sustainable energy, with wind and solar photovoltaic expected to reach a 38% share by 2027 [4] as shown in Figure 1.2. However, this transition necessitates addressing intermittent challenges, such as fluctuations in solar and wind power impacting grid stability. Consequently, energy backup systems, including storage for oversupply periods and flexible power production for low renewable inputs, become imperative [5], [6].

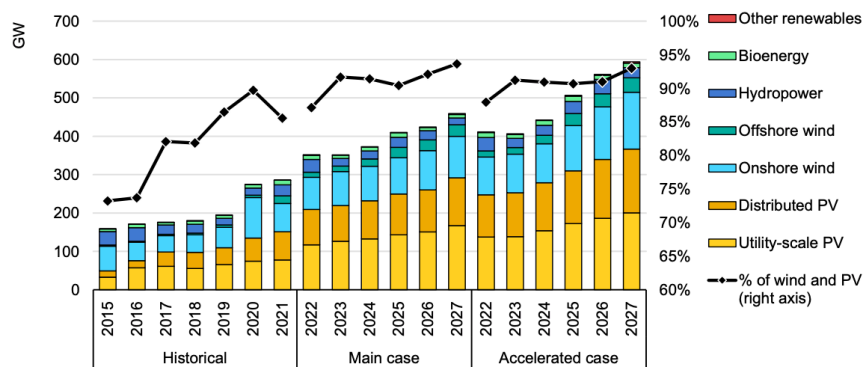


Figure 1.2 Annual capacity additions by renewable technology, main and accelerated cases, 2015-2027 [4].

A comprehensive array of energy conversion and storage technologies may involve nuclear power generation, concentrated

## Introduction

---

solar power plants, wind farms, hydrogen power plants, and innovative technologies enhancing overall energy efficiency. Additionally, the roadmap anticipates the ongoing use of fossil fuels, ultimately incorporating carbon capture and storage [7].

The power generation sector plays a crucial role among all energy sectors, given its significant contribution to GHG emissions. Despite the abundance of renewable energy sources, the power sector witnessed the most substantial absolute increase in emissions in 2022, comprising 42% of the global CO<sub>2</sub> emissions. This underscores the urgent necessity to expedite the transition towards renewable sources and diminish dependence on fossil fuels, particularly in coal-fired power generation, as an effective measure to mitigate climate change [8]. Figure 1.3 provides a visual representation of the sectoral distribution of global CO<sub>2</sub> production from 2019 to 2022.

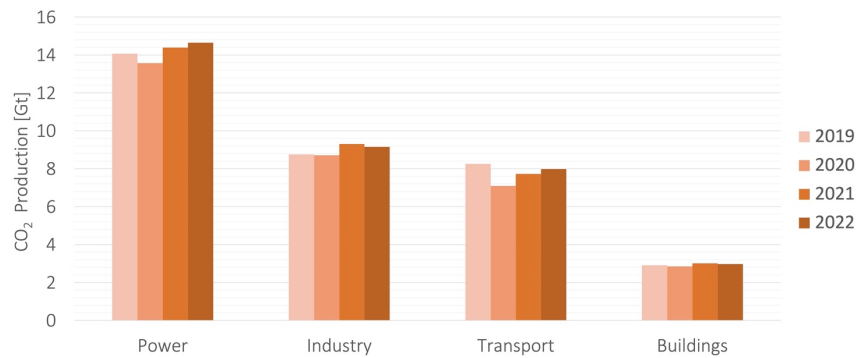


Figure 1.3 Global CO<sub>2</sub> emissions by sector, 2019 to 2022 [8].

Figure 1.4 depicts the future power generation structure, featuring a system with both large and small generators. Small generators meet local power demands, while larger stations act as backups. Thermal power plants, especially gas plants, play a crucial role in supporting low renewable energy input, though at significant costs. Despite efforts to cut GHG emissions, phasing out fossil fuels by mid-century proves challenging due to their abundance and established infrastructure.

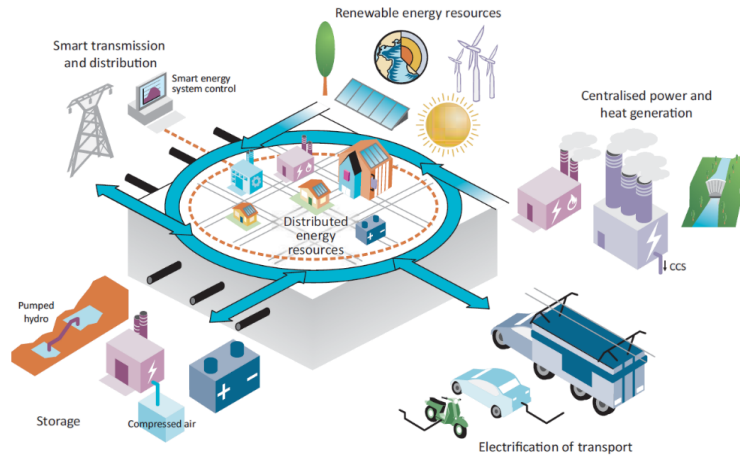


Figure 1.4 The integrated and intelligent electricity system of the future [9].

## 1.2 Microgrids: Navigating the Road to Decentralized Energy

Within the dynamic context of power generation, microgrids emerge as localized and smaller-scale power systems. These systems incorporate distributed energy resources (DERs) like solar panels, batteries, and combined heat and power (CHP) systems, and they are capable of functioning independently or in coordination with the broader grid. The significance of microgrids lies in their pivotal role in strengthening overall system resilience, enabling self-sufficiency, and facilitating the efficient management of energy resources within specific areas [10].

Microgrids represent an interconnected network of loads and DERs within specific electrical boundaries, functioning as a unified and controllable entity. They have the flexibility to connect and disconnect from the grid, operating seamlessly in both grid-connected and islanded modes [2]. The decentralized scheme offers the advantage of minimal power loss in electricity transportation due to the proximity of production units to consumers.

A microgrid is illustrated in Figure 1.4, integrating local networks with active consumers, small storage, a robust backbone network, and powerful generators. The future holds potential for synergies between power, heat, and the mobility sector by coupling electricity with chemistry [11]. The utilization of hydrogen or synthetic hydrocarbons not only enhances storage capabilities but also unlocks efficiency gains, leading to fossil energy savings and reduced CO<sub>2</sub> emissions [12].

Advanced microgrid systems are poised to enhance energy security, providing efficient, reliable, and clean power [6], [13]. Further incentivized by international energy policies aiming for reduced GHG emissions, there is a notable shift in the role of microgrids from a secondary to a primary energy supply [14], highlighting their pivotal role in managing and optimizing diverse energy resources.

The swift integration of microgrids into the electricity grid poses technical challenges, including issues related to voltage stability, distribution system operation, control, and protection [15]. While these challenges have been under scrutiny for over a decade, recent advancements have resulted in a more stable and smoother energy supply [2]. Nevertheless, there remain opportunities for enhancing the operation and maintenance of microgrid power units to further ensure reliable power generation.

### 1.3 Energy Consumption Trends and Sustainable Solutions

In 2021, the EU-27's primary final energy consumption sectors were residential (28%), transport (29%), and industry (26%) [16], as illustrated in Figure 1.5 depicting the sectoral distribution of final energy consumption in the EU-27. Global urbanization significantly influences energy demand, with over 50% of the population in developing countries living in urban areas, compared to 77.5% in industrialized regions like Europe (Table 1.1).

## Introduction

---

In developed nations, urban electrification rates surpass 95%, reaching full saturation at 100% in the EU, while rural areas achieve rates of 60 to 70%. This close relationship between urbanization and electrification trends is evident, highlighting electricity as a clean energy resource, ideal for densely populated urban areas [11]. The following sectors are anticipated to experience growing electricity demand in the future [11]:

- end-use in the private sector;
- energy-efficient buildings and smart cities;
- urban traffic;
- suburban traffic.

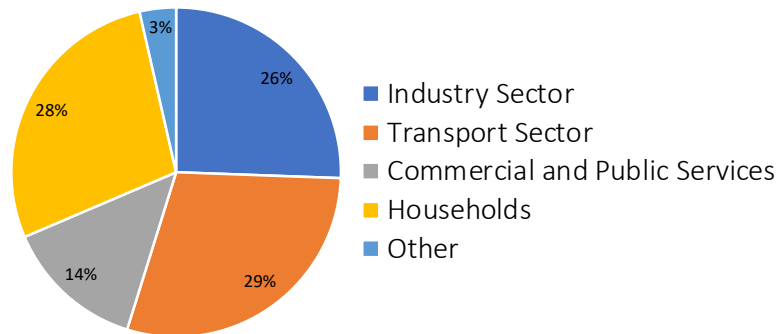


Figure 1.5 Final energy consumption by sector, EU-27, 2021 [16].

Table 1.1 Urbanization rate in percent of the total population in developing countries (DC) and industrialized countries (IC) [11].

	1950	1960	1970	1980	1990	2000	2010	2020	2030	2040
DC	18.0	21.7	25.3	29.6	35.1	40.2	45.3	50.5	56.0	61.6
IC	52.5	58.7	64.6	68.8	71.2	73.1	75.0	77.5	80.6	83.5

The EU’s energy and environmental goals hinge significantly on the building sector. Guided by the “Directive on the Energy Performance of Buildings”, the EU seeks to reduce total energy consumption in its residential sector [17]. This directive aims for low-energy buildings with exceptionally high energy performance, offering improved life quality and additional economic benefits to residents [18].

## 1.4 Cogeneration of Heat and Power

For the increasing urban population, especially in residential areas, the microgrid concept proves to be a viable solution, particularly when operating in cogeneration mode of heat and power [19]. Figure 1.6 illustrates the dominant energy consumption pattern in the residential sector of EU countries in 2021, with heating purposes taking precedence [20].

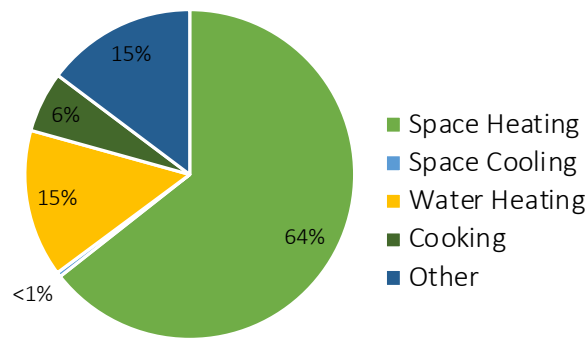


Figure 1.6 Final energy consumption of the residential sector of EU countries, 2021 [20].

Microgrids, functioning in CHP generation mode, efficiently recover residual heat for end-user utilization. This approach avoids the inefficiencies associated with traditional heat-to-power and power-to-heat conversions in centralized power generation mode. In today's predominantly centralized power generation structure, decentralized heat generation is not common due to high losses in heat distribution over long distances. The current shift toward a decentralized electricity market aligns with the distributed heat generation scheme, emphasizing the potential of decentralized cogeneration of power and heat to meet the evolving energy market structure.

While the European Union cogeneration directive sets goals for incorporating high-quality CHP into delivered electricity, these objectives are yet to be achieved [21], [22]. In the United States, many states recognize the value of DERs and CHP to mitigate emissions, fulfill environmental targets, and achieve economic

benefits [23]. Global studies, spanning U.S. states and European nations, emphasize CHP's role in reducing GHG emissions and grid dependence [24], [25], [26], [27], [28], [29].

The U.S. Environmental Protection Agency (EPA) defines CHP as an efficient and clean approach to generating electricity and thermal energy from a single fuel source [30]. Operating by generating hot water or steam and deploying recovered waste heat, CHP systems fulfill end-users' heat demand and can also provide cooling through combined cooling, heating, and power. Recognized for its economic and energy-efficient attributes, CHP, especially in industrial applications, converts a significant portion of input fuel into electricity and thermal energy onsite [31].

As climate change influences heating demands, the residential sector will experience a shift toward increased cooling needs, favoring the combined cooling, heating, and power mode of cogeneration. Various cooling technology options, including absorption chillers, are available for cogeneration of cooling, heating, and power. The U.S. EPA CHP partnership promotes the development of CHP, emphasizing small CHP technologies, or Micro CHP, as suitable options for distributed generation, defined as power generation smaller than 50 MW used either on-site or near production [32], [33].

### 1.5 MGTs as Micro CHP Units

Among various micro CHP options, MGTs stand out as a promising choice for the future. The detailed reasons behind their suitability and comparison with other micro CHP technologies are thoroughly discussed in Paper I. Moreover, a market research review provided in Paper I anticipates a notable surge in MGTs for CHP in the near future. The rising demand for low-emission energy solutions, driven by environmental concerns, is a major catalyst for the MGT market growth [34].

Favorable economic developments have also fueled market expansion. Despite challenges during the COVID-19 pandemic (January 2020 to May 2023), including a global economic slowdown, lockdown restrictions, and supply chain disruptions, government support has played a crucial role in encouraging MGT adoption, with incentives and subsidies promoting investments in the technology [34], [35].

In terms of regional dynamics, North America, led by the United States, has emerged as a dominant market for MGTs, primarily driven by demand from sectors like pharmaceuticals, construction, and mining [34]. Simultaneously, Europe is expected to witness rapid growth, attributed to strict government regulations, a rising demand for clean energy, and substantial investments in clean fuel technology [34]. While the industrial sector, encompassing mining, oil and gas, wastewater treatment, construction, and manufacturing, remains a significant end-use segment, there is notable anticipated growth in the commercial sector [34]. This trend aligns with the escalating energy demand, especially for CHP, due to the increasing urban population. Notably, MGTs, as discussed in Paper I, stand out as a promising choice to meet this growing demand.

### 1.6 Problem Statement

While gas turbine (GT) engine performance improvements have been a longstanding interest, certain characteristics set MGTs apart from larger engines in their operating and system features. These challenges are elaborated in Paper I. In summary, addressing the distinct features of MGTs involves overcoming design complexities, optimizing performance at varying speeds, managing lower pressure ratios, and ensuring efficient fuel utilization. The strategies to enhance performance, particularly component-based variables, variable bounds, and imposed constraints in MGT operation, differ from those applied to large-scale GT.



## Introduction

---

Consequently, further development is required for MGTs and MGT cycles to align with [36]:

- Higher electrical efficiency;
- Increased flexibility for integration with other systems;
- Increased flexibility towards the utilization of various sources of energy.

In the future's renewable-focused power landscape, MGTs, integrated into microgrids, frequently operate under part-load conditions. Achieving optimal efficiency involves controlling MGTs as dispatchable units, addressing off-design variations, and prioritizing efficiency improvement. MGTs play a crucial role in supporting intermittent renewables, highlighting the paramount importance of their reliability as backup power sources.

Another pivotal advance in MGTs involves enhancing fuel flexibility, particularly towards net-zero or zero-emission fuels. Biogas, derived from organic waste, offers renewable attributes and ease of integration, while hydrogen, especially green hydrogen, presents a zero-emission profile and versatile applications. Notably, hydrogen-fueled MGTs are still undergoing research and development, reflecting ongoing exploration for sustainable fuel options.

Hydrogen presents a compelling solution for energy storage [37], especially generated through electrolysis during excess renewable energy. Storing hydrogen facilitates harnessing surplus renewable energy, efficiently utilized in MGTs during demand peaks. While challenges exist for broader hydrogen adoption, MGTs, requiring less hydrogen, and allowing local production, present more manageable solutions to large-scale storage concerns and production complexities.

The integration of hydrogen-utilizing MGTs demands continuous monitoring for efficient combustion and system reliability. Online engine monitoring tracks key parameters, ensuring combustion stability and optimizing performance. Early detection of deviations

in hydrogen combustion enhances reliability and minimizes downtime. Robust online monitoring is essential for seamlessly integrating and sustaining hydrogen-based technologies in power generation.

### 1.7 Objectives and Research Questions

In pursuit of advancing the role of MGTs in the future of power generation systems, this PhD project has strategically focused on two complementary paths. The first objective aims to enhance the fuel flexibility of MGTs, specifically targeting their operation with hydrogen. The second objective addresses the intricate challenge of integrating MGTs into distributed power generation systems effectively.

To delve into these objectives, the thesis revolves around answering two fundamental questions:

1. How can the development of an MGT operating with hydrogen-blended fuel be achieved?
2. How to seamlessly integrate MGTs into distributed power systems?

Exploring these inquiries has been a focal point throughout various sections of this thesis. After an extensive review of relevant literature in Chapter 2, the investigation initiates with the first question in Chapter 3. Supported by Papers II and III, this chapter delves into the subtleties of hydrogen combustion, shedding light on challenges encountered and inventive solutions devised to overcome them. After this exploration, the section presents the experimental outcomes derived from the engine's operation on 100% hydrogen.

Chapter 4 diverges its focus by detailing the physics-based models developed to tackle challenges highlighted in Chapter 3. This chapter methodically constructs and evaluates models to simulate the operation of MGTs with varying hydrogen blends, providing a robust analysis of the engine's behavior under different conditions.

Papers IV and V delve into the exploration and discussion of these models.

In the pursuit of integrating MGTs into distributed power generation systems, advanced artificial intelligence (AI) and data-driven methods take center stage. The creation of a precise performance model for the engine proves essential in predicting operations and outputs. Chapter 5 delves into the process of developing an AI-based model, beginning from raw data and culminating in the creation of a fast and accurate data-driven model for MGTs.

Once the infrastructures are stabilized for the development of data-driven models, the groundwork for effective condition monitoring and optimized operation of MGT systems in real-time applications is established. Chapter 6 and Paper VI delves into the exploration of integration strategies, highlighting the pivotal role of AI in optimizing MGTs within the integrated energy system.

One of the core principles guiding the project is the development of an infrastructure that transcends the current scope, ensuring reusability for future endeavors. This theme resonates across all models and codes programmed throughout the project. In Chapter 7, the microgrid optimization concept is applied to an offshore microgrid, utilizing the same approach as the onshore microgrid discussed in Chapter 6 but with larger GTs to be optimized. This expanded application is supported by Paper VI.

The journey culminates in Chapter 8, where concluding remarks encapsulate the key findings and achievements of the work. The chapter also offers insights into future directions, providing suggestions for ongoing and prospective research in the field.

Figure 1.7 presents a comprehensive overview of the research questions, corresponding chapters, and the accompanying supporting papers.

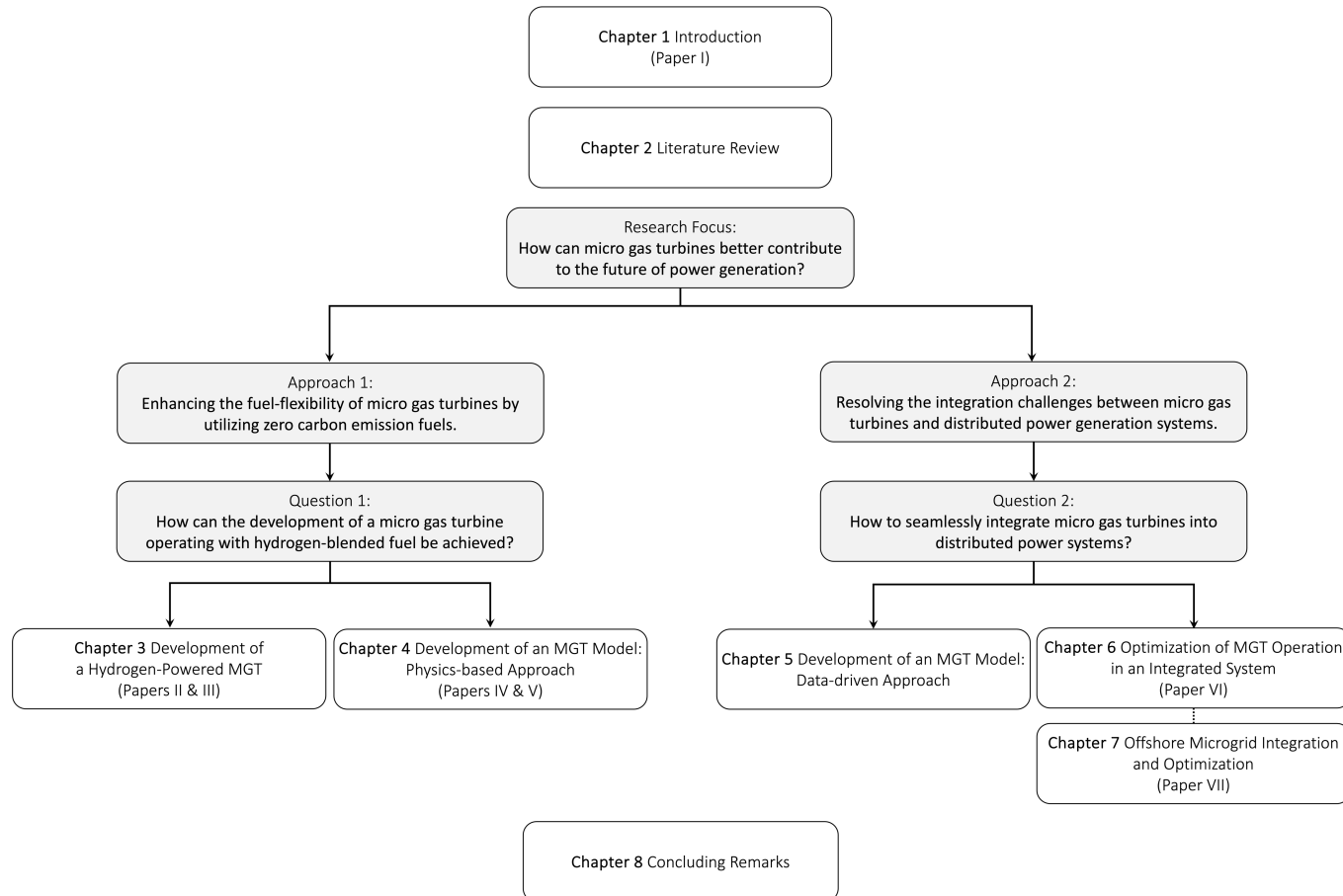


Figure 1.7 Overview of the thesis structure, detailing chapters and their corresponding research questions.

## 1.8 Significance of the Study

The research undertaken in this study represents a step forward in the field of clean energy technologies, aspiring to seamlessly integrate renewable energy sources into existing power systems. At its core, this study seeks to contribute to the development of the world's first hydrogen-fueled MGT while concurrently integrating it with renewable energy sources. The overarching goal is to make strides toward advancements in sustainable energy solutions:

1. **Advancement of Clean Energy Technologies:** This research propels the progress in clean energy technologies by introducing a hydrogen-fueled MGT. Hydrogen, a fuel with zero carbon emissions, presents a compelling opportunity to curtail carbon emissions and alleviate the environmental impact of power generation. Beyond pushing the boundaries of clean energy technologies, this study advocates for the widespread adoption of hydrogen as a viable and sustainable fuel option.
2. **Integration of Renewables into Existing Power Systems:** In the pursuit of a greener and more dependable energy landscape, it is crucial to seamlessly integrate renewable sources such as wind and solar with MGT. This study is dedicated to overcoming the challenges presented by the intermittent nature of renewables, aiming to synchronize them effectively with MGTs. The research strives to optimize the integrated system, promoting the development of a stable and reliable energy grid.
3. **Benefits of Advanced AI Management Tools:** The incorporation of AI-driven management tools yields benefits in the energy domain. Real-time condition monitoring and optimization enhance energy efficiency as the integrated system dynamically responds to changes in demand and supply. By predicting energy generation patterns and demand

forecasts, the AI tools facilitate resource allocation and energy distribution, minimizing waste and optimizing overall system performance, leading to significant cost savings in the long term.

4. Reduction of GHG Emissions: The effective integration of hydrogen-fueled MGTs and renewables plays a significant role in reducing GHG emissions. This study aligns with global initiatives to combat climate change and promote a low-carbon future by replacing traditional fossil fuel-based power generation methods with cleaner alternatives.

In summary, this research promises to advance clean energy technologies, seamlessly integrate renewables, and reduce GHG emissions. Introducing hydrogen-fueled MGT and AI-based management tools actively enhances energy efficiency, cost-effectiveness, and environmentally responsible energy solutions. The broader impact sparks innovation in the energy sector, aligning with global sustainable development goals and shaping a more sustainable, resilient, and eco-friendly energy future.

## 2 Literature Review

Embarking on this scholarly journey, the pivotal role of a robust and extensive literature review within the thesis framework is underscored. This exploration intricately weaves through three key domains, each tied to the core principles and focal points underpinning the essence of this research. Identified domains include:

- Developments of MGTs running with hydrogen;
- Modeling MGTs (physics-based and data-driven);
- Microgrid operation control and optimization.

The examination of the chosen domain serves as the foundation of this PhD project, offering the potential to deepen comprehension and provide valuable guidance for the chosen project trajectory. It holds the promise of enriching understanding and steering the direction of this doctoral research endeavor.

### 2.1 Developments of MGTs Running with Hydrogen

The growing interest in hydrogen energy is marked by increased investments, research, and policy support [38]. Researchers explore hydrogen's potential to transform heat and power generation for a sustainable, low-carbon energy system [39]. Policymakers, industries, and scientists recognize its transformative impact across various applications, including power generation with GTs [40].

Numerous research and development programs have been conducted for both large-scale as well as small-scale GT units, aiming to address complications of using pure hydrogen or hydrogen-blended fuels. In 1997 Minakawa et al. [39] developed a

prototype of a small combustor with a lean premixed swirling flame for an MGT to run with pure hydrogen. The combustor was tested at atmospheric pressure which showed high combustion efficiencies and low NO<sub>x</sub> emissions. The combustor was assembled to an MGT to assess the combustion in actual conditions [39]. During the start-up of the engine, flashbacks occurred that were not previously observed in the component test. The flashbacks were mitigated by the regulation of airflow to the combustor [39].

A year later, Morris et al. published a paper [41], presenting their observation of adding hydrogen to heavy-duty GTs originally driven with natural gas. After overcoming the challenges of mixing the hydrogen with natural gas in the plant, the effect of adding up to 10% hydrogen in volume was investigated. According to the authors, the 10% amount of hydrogen did not affect the NO<sub>x</sub> emissions, however, the carbon monoxide production decreased as hydrogen was added [41]. The authors concluded that the plants have shown to be flexible in using hydrogen content up to 10% in volume in premixed steady state modes [41].

In the same year, Waitz et. al [42] explored the development of hydrogen-powered micro combustors for MGTs, overcoming challenges associated with their compact size. The combustion approach involved upstream hydrogen introduction and air premixing, eliminating the need for a combustor dilution zone [42]. Experimental results demonstrated stable hydrogen-air combustion, showcasing the feasibility of small-scale applications [42].

Years later, York et al [43] investigated the utilization of hydrogen as a primary fuel in heavy-duty GTs, with a specific focus on addressing combustion challenges and controlling emissions. A notable contribution was the introduction of a novel premixing fuel injector featuring small-scale jet-in-crossflow mixing, representing



a departure from conventional methods [43]. Rig experiments and subsequent full-scale testing demonstrated the efficacy of the design, achieving stable, flashback-free combustion and emphasizing low-NO<sub>x</sub> emissions [43].

To assess the effect of hydrogen combustion, a computer simulation approach was chosen to simulate the combustion of hydrogen/methane blended fuels in an MGT [44]. In the paper, the authors used computational fluid dynamic (CFD) methods to investigate the characteristics of burning blended fuel with hydrogen share from 0 to 90% volumetric fraction in a can combustor that was originally designed for natural gas [44]. Evaluation of the effect of adding hydrogen on flame structure and emissions was the objective of the work [44]. The authors conducted different case scenarios to fuel the engine and concluded that although simulation results show stable combustion performance, to address the emissions, modifications to the combustor will be required and the original combustor design will not be adequate [44].

Cappelletti et al. [45] investigated the combustion of pure hydrogen in a lean premix burner with experiments and via numerical simulation. The experimental setup was built based on an existing burner from a heavy-duty GT, which was modified to enable variable premixing levels. With hydrogen combustion, high flow velocity was required to avoid the flame positioning inside the premier duct. Their findings affirmed the feasibility of advancing combustion technology using pure hydrogen fuel, while ensuring emissions remain within regulated limits.

Binesh et al. [46] performed a series of experiments to investigate the combustion behavior of hydrogen-enriched methane fuel in a swirl-stabilized type GT combustor. The amount of hydrogen in the blended fuel was increased up to 80% in volume and during the test, the upper and lower limits to provide air required to maintain stable combustion were derived [46].

Rajpara et al. [47] conducted numerical and experimental investigations to assess the effect of hydrogen injection on a GT with an upward swirl combustor, running with methane fuel. Increasing hydrogen content resulted in smaller flame dimensions with an increase in NO<sub>x</sub> emissions due to higher flame temperature, but a decrease in CO emissions [47].

Pappa et al [48] investigated the potential of air humidification to stabilize hydrogen combustion in MGTs. Large Eddy Simulations compared pure methane and hydrogen-enriched methane/air combustions with and without humidification in a Turbec T100 combustor [48]. Findings demonstrated that adding 10% water mass fraction facilitated stable hydrogen combustion, preventing flashback and enabling the use of hydrogen blends in MGTs with emission levels comparable to the reference case [48].

In the pursuit of a future hydrogen-centric society, Kawasaki Heavy Industries conducted pioneering research, collaborating with Aachen University of Applied Science and B&B AGEMA, and demonstrated the effectiveness of the Micro-Mix combustor in the hydrogen-fueled M1A-17 GT [49]. Engine tests confirmed stable ignition, a smooth starting procedure, and established fuel staging capabilities [49]. The dry low NO<sub>x</sub> combustor achieved a maximum power output of 1635 kW with consistently low NO<sub>x</sub> emissions below 55 ppm [49]. The technology's robustness was evident as all components remained issue-free post-testing [49]. November 4, 2020, witnessed successful heat and power supply to neighboring public facilities, highlighting the practicality and success of the hydrogen dry low NO<sub>x</sub> combustor for a 2MW class GT [49].

Lu et al [50] examined the influence of hydrogen-methane hybrid fuel on combustion characteristics and pollutant emissions in a counter-flow combustor of a 100 kW MGT. Numerical simulations explored varied airflow distributions, revealing that increased premixed air enlarged the recirculation region and high-

temperature zone [50]. Optimal performance, with a uniform outlet temperature of 1172 K, was observed at 30% premixed air. The study demonstrated that beyond 40% premixed air, NO<sub>x</sub> concentrations increased, peaking at 23.46 ppm (@15% O<sub>2</sub>) and decreasing to 0.717 ppm (@15% O<sub>2</sub>) at 50% premixed air [50].

Liu et al [51] employed CFD simulations to investigate the impact of air and fuel staging on combustion characteristics and emissions in an MGT combustor. Varying secondary oxygen (0–40%) and secondary fuel ratios (0–10%), the study found that increasing secondary oxygen reduced the central recirculation zone and average NO emissions [51]. Higher secondary fuel ratios led to reduced outlet velocity, improved temperature distribution, and a notable reduction in NO emissions [51]. Both air and fuel staging contributed to lower outlet temperature and NO emissions, with fuel staging exhibiting a more significant effect on NO reduction than air staging [51].

In May 2020, Kawasaki announced the successful test of an industrial GT with hydrogen fuel, through their dry low emission combustion technology [40], [52]. The combustor applied micro-mix combustion technology, which featured ultra-small hydrogen-fueled flames and achieved low NO<sub>x</sub> combustion without using water or steam, which was beneficial in terms of cycle efficiency [40], [52].

## 2.2 Modeling Gas Turbines

Modeling and simulation are integral to GT design, providing cost-efficient solutions. Reduced-order models are essential to simulate the entire GT cycle under diverse operational conditions. Researchers typically adopt distinct reduced-order modeling approaches for GTs, classifying them as white-box (physics-based) or black-box (data-driven). White-box models, rooted in physics and thermodynamics, delve into the fundamental principles governing system behavior. In contrast, black-box models rely

solely on data, while grey-box models combine physics with data-driven insights, providing a comprehensive understanding of GT dynamics [53], [54], [55]. While hybrid approaches exist, categorizing them as clear-cut grey-box models can be challenging, as these models often lean towards either a data-driven or physics-based dominance.

White-box models play a pivotal role in designing and testing control strategies, ensuring operational safety, improving response times, and facilitating predictive maintenance. While CFD methods play a crucial role in enhancing the fuel flexibility of GTs by developing innovative combustor designs [56], [57], [58], reduced-order white-box models specifically contribute to the comprehension of the dynamic behavior of a GT as a system and the intricate interactions among its components. Their low computational complexity is essential for real-time simulations and integration with control systems hardware [53], [54], [55], [59].

This section introduces diverse modeling perspectives, advancing precise and computationally efficient dynamic models for MGTs. It outlines the evolutionary path of GT models, significantly impacting MGT modeling.

### 2.2.1 White-Box Models

A white-box model, grounded in a profound understanding of the system's physics, relies on constitutive and conservation equations to realistically simulate its behavior. These equations usually include isentropic models for compression and expansion, the ideal gas law, and conservation equations (mass, momentum, and energy) applied to gas volumes and moving parts. Often referred to as "thermodynamic models," these models typically consist of 5 to 15 equations, calculating the key physical parameters such as pressure, temperature, and flow rates. The complexity of these models is associated with temporal and spatial dependencies, with a common strategy involving the simplification of system

components to their inlet and outlet boundaries. This transformation turns the models into a 0D form, making them applicable to systems with unknown geometries and offering advantages in managing computational complexity.

The evolution of simplified physics-based models began in the 1980s, initially for heavy-duty GTs in power systems studies. Pioneering this domain, Rowen [60] laid the foundation, followed by more precise models proposed by Hussain and Seifi [61] and de Mello et al. [62]. The main objective of their study was to prepare a simple model that can cover the full spectrum of GTs to be implemented in the power dispatching strategy. However, their application remained restricted in power systems simulation programs. Models tailored for processing GT operating conditions emerged later, integrating turbomachinery performance maps.

Hannett et al. [63] introduced a model for a dual-shaft GT, utilizing data acquired from a field test to support the model's parameters. The assessment of the engine governor's response to load changes and load rejections was facilitated through monitoring data obtained from conducted tests [63]. Subsequently, Ricketts [64] furthered this line of research by developing a dynamic model for a twin-shaft GT. The model was constructed using generic methods and incorporated performance data collected directly from the engine, demonstrating its capability to predict the transient performance of the turbine [64].

A dynamic model of a single-shaft heavy-duty GT in Matlab/Simulink was developed by Crosa et al. [65]. The model showed good performance in predicting key thermodynamic variables [65]. Ailer et al. [66] developed a dynamic model of a low-power single-shaft GT for control purposes in a Matlab/Simulink environment. The focus of the study was the dynamic response of the GT control system [66]. The model was simplified by several assumptions to obtain a lower-order dynamic model [66]. Comparing the model predictions with collected

experimental data, the model was verified to imitate the dynamic behavior of the engine, however, some important aspects of engine dynamics were neglected due to simplifying assumptions [66].

Abdollahi and Vahedi [67] developed a dynamic model of a single-shaft MGT in Matlab/Simulink. Their model included dynamic characteristics of main components such as the turbine and the permanent magnet generator [67]. The results of their work showed that the provided model can be utilized for dynamic simulation of MGT operation in various conditions [67].

A computer program was developed by Al-Hamdan et al. [68] in which thermodynamic equations of single-shaft GT components were implemented for dynamic modeling. The program was able to be utilized for investigating GT performance in off-design conditions and to design an efficient control system for specific applications [68]. In their paper, the analytical calculation for satisfying matching conditions between various GT components was explained, which is the basic strategy for thermodynamic models of GTs [68]. Such analytical models are capable of predicting GT performance in all off-design conditions that are covered within the components' maps [68].

Camporeale et al. [59] presented a novel approach for developing a high-fidelity real-time simulation of GTs in Matlab/Simulink. They provided nonlinear representations for the main components of the GT and solved a set of ordinary differential equations with components representing correlations to simulate the performance of the engine [59]. The proposed method provided a generic approach that was suitable for any configuration of power plants [59]. An illustration of the developed model is shown in Figure 2.1.

Garborg [69] developed a physical model of T100 in an IPSEpro environment. The model was validated by measurements collected from a partially modified engine in the Risavika Research Center, Stavanger, Norway. The modifications included an added bypass

## Literature Review

which provided a possibility to replace the combustion chamber with a fuel cell. The data was gathered from the engine with an externally installed combustion chamber through a combination of 3 measurement systems, including the T100 built-in sensors, the supervisory control and data acquisition system (SCADA), and some additionally implemented measurements. The results from the model and experimental data showed some discrepancy which was an indication of the low fidelity of the model [69].

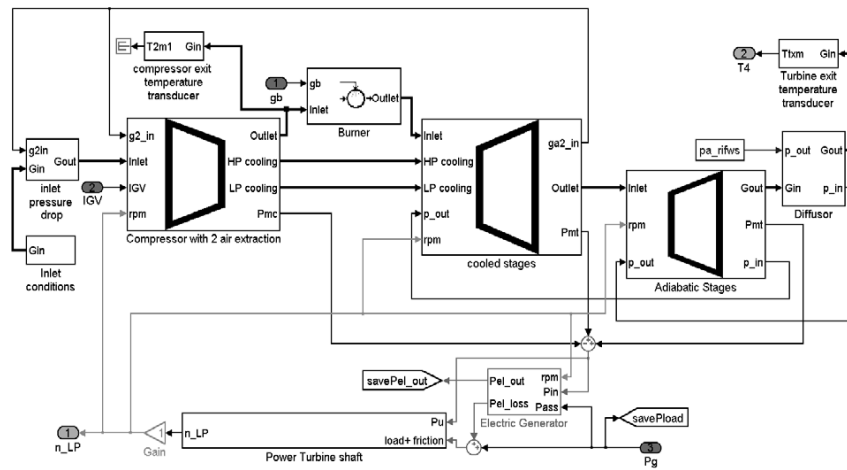


Figure 2.1 Simulink scheme of the single-shaft GT from [59].

Bang-Møller et al. [70] developed a 0D-based model of a hybrid cycle of micro CHP system, consisting of a biomass gasifier, solid oxide fuel cell, and an MGT. Optimizations based on energy and exergy calculations were performed to explore a more productive performance of the cycle [70]. The main energy and exergy loss in the cycle was recognized and modified which resulted in a configuration with an added heat exchanger and optimum operation point for the cycle with a total increased efficiency of 87.5% compared to the original 82.6% [70].

Rachtan and Malinowski [71] established an approximate mathematical correlation for the heat recovery unit in an MGT operating in CHP mode. The model underwent verification

through experimental data across various part-load performances, demonstrating its reliability for the modeling and design of micro CHP plants [71]. In a separate study, Malinowski and Lewandowska [72] developed an analytical model for the entire MGT, focusing on part-load operation. Exergy calculations were conducted for all MGT components, and the study provided formulas to address challenges arising from limited information about manufacturer-proprietary component maps [72]. The performance of the proposed model exhibited favorable agreement with the experimental data collected [72].

Shaw et al. [73] developed a model of a combined cycle power plant (CCPP) in Aspen Plus software by using data from an actual working GT. The effects of ambient temperature on the power output of the whole combined cycle as well as the simple GT cycle were investigated [73]. Results of the work indicated that the dependency of GT cycle power output on the ambient temperature is relatively high, while it is neglectable for a steam cycle [73]. From this outcome, the authors concluded that in summertime the operation of the combined cycle is more stable than a standalone simple cycle [73]. Figure 2.2 shows the presented model by Shaw et al. for CCPP [73].

Di Gaeta et al. [74] developed and validated a dynamic model for a 100 kW MGT using MATLAB/Simulink, simulating various operating conditions and considering component efficiency. Results showed accurate reproduction of electrical power and acceptable predictions for fuel consumption and turbine speed [74]. In an advanced hybrid energy grid scenario, combining MGT with a water electrolyzer proved promising, providing a 37.5% fossil fuel saving and producing 1913 kg of hydrogen in partial hybridization [74]. Full hybridization increased fossil fuel savings to 41.5%, highlighting the potential of MGT and hydrogen integration for enhancing energy system efficiency and sustainability [74].



## Literature Review

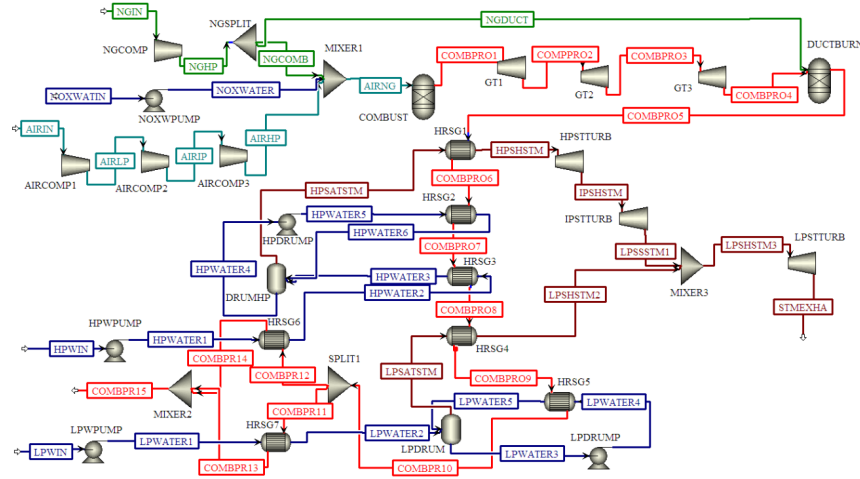


Figure 2.2 Schematic of an Aspen Plus model of a two-pressure CCPP from [73].

Nelson et al. [75] constructed a quasi-steady physics-based model for a hybrid system integrating a T100 MGT with a concentrating solar power (CSP) tower. The CSP was implemented to exploit solar energy for heating air before it goes into the combustion chamber [75]. A range of electrical loads under varying ambient conditions was investigated to study load following and operation characteristics of the hybrid cycle [75]. Moreover, sensitivity analyses were performed to investigate the performance of the hybrid cycle in various ambient conditions [75]. The performance of the hybrid cycle was investigated through an annual power demand for different cities in the U.S. [75]. The results of this work showed that the proposed hybrid cycle is capable of meeting the performance targets of an MGT working as its basic nonhybrid configuration [75]. The authors also concluded that by utilizing this hybrid configuration, fuel consumption can be reduced by 26% annually [75].

Giorgetti et al. [76] investigated the dynamic modeling and control design of a solar-hybrid system, encompassing an MGT, a tubular air receiver, and a sensible thermal energy storage system (ESS).

The study underscored the significance of an accurate model for the implementation of effective control strategies [76]. The dynamic model developed for the investigation was experimentally validated using the MATLAB/Simulink environment [76]. The influence of integrating solar energy on both system stability and fuel consumption was thoroughly examined [76]. The insights gained contributed to addressing challenges and identifying opportunities in solar-hybrid MGT systems, offering valuable guidance for control strategy development in distributed energy systems [76].

Arsalis [77] presented a detailed thermodynamic model for a small-scale natural gas/hydrogen-fueled GT system, incorporating both basic thermodynamic and exergy analyses. The model explored the impact of hydrogen addition on system performance, revealing a marginal improvement in net electrical efficiency (0.347 to 0.356) and notable gains in energetic efficiency (0.338 to 0.360) due to reduced combustor losses [77]. Off-design modeling provided insights into realistic part-load operations [77]. Additionally, hydrogen injection, even in small amounts, demonstrated a 6.1% reduction in CO<sub>2</sub> emissions compared to methane-only fueling [77]. The validated model served as a reliable basis for future decentralized power generation studies, emphasizing the positive influence of hydrogen addition on system efficiency and operational cost [77].

An organic Rankine cycle combined with a 100 kW MGT was modeled by Campos et al. [78], searching for higher electrical efficiency. The work included exploring different working fluids as well as cost evaluation for the whole system to include cost investigations for the miniature combined cycle [78]. The results showed over 4% electrical efficiency improvement (from the original 30%), however, the cost function for investing in added organic Rankine cycle was not accurate enough to decide about the economical viability of the combined configuration [78].

Reale and Sannino [79] reviewed various numerical modeling approaches applied to MGT-based energy systems. The focus was on discussing different layout solutions proposed by researchers, highlighting the modeling approaches and methods employed in the related literature [79]. The authors delved into the growing research interest in MGT-based energy systems, particularly in overcoming performance limits and integrating MGTs into hybrid energy systems for enhanced performance and source diversification [79]. The review underscored the significance of numerical modeling in investigating innovative solutions and extending the operational range of MGTs [79].

Lin et al. [80] investigated the modeling and control design of a 135 kW MGT in a power generation scenario. It established a nominal nonlinear model by integrating start-up and component characteristic map models [80]. Controllers, including nonlinear active disturbance rejection control and proportional-integral-derivative, ensured effective speed and load tracking [80]. The active disturbance rejection control outperformed, actively compensating for disturbances [80]. MATLAB/Simulink simulations demonstrated its superior performance in achieving speed and load control targets, showcasing its potential for future full-scale MGT tests [80].

### 2.2.2 Black-box Models

A black-box model is crafted when limited or no information about the physics of the system is available. In such scenarios, the model is built using data collected from the system, and its training involves replicating the system's behavior through a series of simplified mathematical calculations, not grounded in the system's physics. Commonly employed in GT modeling, especially when proprietary GT component maps are unavailable, black-box models leverage abundant data collected from the engine. This data-driven approach allows the construction of a model that

mimics the system's behavior, incorporating specific performance details of the engine that generated the data. In contrast to physics-based modeling, which applies general rules to model all engines of the same type, black-box modeling addresses engine-to-engine variations resulting from manufacturing tolerances and differing health statuses. These models are particularly useful in scenarios where empirical data is the primary source, and they often utilize methods such as artificial neural networks (ANN) [81].

In black-box models, the choice of simpler approaches is often viable. Linear models represent one such option, however, the application of these simpler models is constrained to operating points near the design, as GTs exhibit highly non-linear behaviors [82].

Chiras et al. [83] estimated a non-linear auto-regressive moving average with an exogenous input model for an aircraft engine, showcasing the application of intelligent models to GTs. Jurado [82], a few years later, proposed a non-linear auto-regressive exogenous (NARX) model specifically tailored for MGTs, with an emphasis on its application in model predictive control (MPC). These intelligent models leverage both past and present values of input and output series to construct an understanding of the system's behavior [82].

Fast et al. [84] applied the ANN technique for data-driven modeling of GTs. They implemented the operational data collected from an industrial single-shaft GT for standalone and CHP plants [85]. They concluded that performance prediction with ANN has high accuracy and can be used as an offline simulation tool or a core model for online condition-based monitoring for early detection of faults or degradation and optimizing the maintenance intervals [85].

Bartolini et al. [86] investigated the application of ANN and adaptive network-based fuzzy interface system (ANFIS) to describe the performance of an MGT. The data for training the

model was collected from the manufacturer’s testbed which did not cover the whole operation range of the MGT [86]. Therefore, ANNs and ANFIS methods were used to complete performance diagrams where there was no experimental data available [86]. The effect of ambient conditions on the power output of MGT was also investigated which showed that ambient temperature had more effect than pressure and humidity [86].

Nikpey et al. [87] provided an optimized ANN of a T100 MGT with an extended set of measurements. The most important parameters as inputs to the ANN were defined through a sensitivity analysis among measurement data gathered from built-in and added sensors to the engine [87]. The model was purely developed and verified by experimental data and proved to be accurate enough to be used for online monitoring applications [87]. The developed model is illustrated in [75] Figure 2.3.

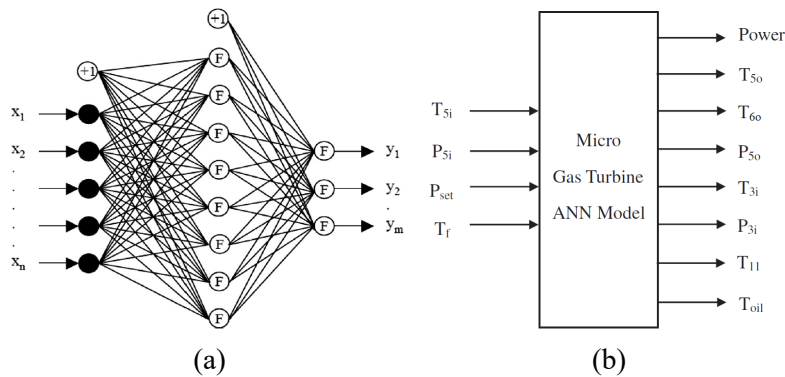


Figure 2.3 The developed ANN model in [87], (a) schematic of a multi-layer feed-forward network, (b) the final optimized model structure.

Ben Rahmoune et al [88] introduced an effective tool for ensuring the stability of GTs through dynamic modeling. Employing a dynamic NARX, the study focused on identifying the dynamic behavior of the GT system [88]. The proposed ANN-based supervision system successfully monitored vibrational dynamics, providing valuable insights into the dynamic model behavior [88]. The outcomes highlighted the tool’s capabilities in real-time

failure detection and its effectiveness in modeling complex dynamic systems, particularly in the context of GTs [88].

Aslanidou et al. [89] provided a model for fleet monitoring of MGTs with electrical power output under 100 kW. The framework included a physics-based model for predicting system behavior and an AI tool for detecting and classification of anomalies in the system [89]. The challenges for fleetwide monitoring were addressed including processing a large amount of data and the need for a predictive model for each specific engine [89].

A combined auto-associative neural network and K-nearest neighbor method were implemented for noise reduction and fault detection of a GT engine by Fentaye and Kyprianidis [90]. The performance of the proposed method was verified by the data generated from a model simulation and showed that the developed hybrid method is more effective and reliable than the conventional method for fault detection of the GT [90].

Talebi et al. [91] proposed a diagnostics scheme for MGTs in smart grids, focusing on fault detection and isolation in part-load conditions, degradation, and uncertainties. The off-design MGT model, incorporating uncertainties, formed the basis for an ANN to capture nonlinear correlations [91]. Key findings included the necessity of power and shaft speed measurements for accurate fault detection and the importance of additional parameters for fault isolation [91].

As the reviews of articles show, AI-based models of GTs using data excel in providing accurate predictions for the modeled engine. These data-driven models, rooted in simple mathematical equations, offer fast responses. The combination of speed and high accuracy makes them an excellent choice for online condition monitoring, as highlighted in [85], [87], [92]. In condition monitoring and fault diagnosis for GTs, the primary aim is to detect faults, identify problematic components, and estimate the extent of flaws within the system. Effective fault diagnosis ensures

safe performance, reduces maintenance costs, and lays the groundwork for performance improvements. Unlike traditional gas-path analysis, data-driven models surpass limitations arising from model simplifications and excel in learning from actual data. This results in superior diagnostic accuracy, particularly when dealing with the complex and non-linear characteristics of performance-related faults in GTs.

### 2.3 Microgrid Operation and Optimization

The integration of diverse generation units within distributed energy generation poses challenges due to disparate dynamics, particularly with limited control over renewable sources. In response, automated and adaptive frameworks have gained precedence over traditional centralized models for power and energy production management [93]. Microgrids exemplify this progressive approach, featuring well-defined electrical boundaries and resource management control systems, capable of autonomous operation independent of the main grid [93]. Effective modeling and optimization for microgrids' operation are crucial for enhancing reliability, efficiency, and the integration of renewable sources [94], [95]. This literature review explores studies focusing on microgrid modeling and optimization, emphasizing control strategies and applications within integrated energy systems.

A prominent approach widely adopted in the field of microgrid operation control is the “energy hub” concept, comprehensively elucidated in seminal literature [96]. This concept consolidates the intricate processes of energy generation and conversion into a unified input-output model, encapsulating within it all the intricate mathematical models specific to various units [96]. Optimization strategies grounded in this paradigm often incorporate techniques encompassing linear programming [97], dynamic particle swarm optimization, and the formation of an intricate network of energy hubs [98].

The deployment of hyper-heuristic algorithms, as demonstrated by Mallol-Poyato et al. [99], in optimizing the charging and discharging of electrical ESSs, proved instrumental in delivering significant cost savings. Additionally, Zhang et al. [100] harnessed the potential of mixed-integer linear programming to schedule renewable supply, ESSs, and CHP units, and demonstrated the advantages of MPC over day-ahead control, resulting in substantial savings for consumers. Ma et al. [101] further expanded on the optimization domain, developing an MPC-based microgrid central controller. This innovation redistributed the load, successfully alleviating peak pricing periods [101]. However, it is worth noting that their control horizon was confined to one hour, and their demand profile was impeccably predictable [101].

The growing complexity inherent in managing multi-vector energy systems underscored the necessity for simultaneous control over energy supply, demand, and storage, ensuring the provision of a stable, cost-effective, and efficient energy supply that optimally harnesses renewable resources [94], [95]. The emergence of transformative technologies, notably the Internet of Things (IoT) and AI, has revolutionized the domain of building and district energy management, offering a wealth of data to be harnessed [102].

Reynolds et al. [103] have set forth two innovative optimization strategies that harness the power of ANNs for predicting building demand and solar photovoltaic generation. In tandem, a genetic algorithm (GA) was deployed to govern CHP, heat pumps, and thermal storage outputs [103]. Their first strategy was focused on optimizing heat generation to meet building demand at minimal cost [103]. In the second strategy, they introduced control over heating set point temperatures to more effectively manage office building demand [103]. The investigation conducted within a sliding window framework, yielded compelling results, marked by increased profit margins and reduced carbon emissions when



compared to baseline scenarios [103]. The researchers recommend a future emphasis on incorporating more advanced machine-learning models and piloting these methodologies at actual sites [103].

Tooryan [104] addressed the optimization of operational costs in a hybrid residential microgrid comprising a diesel generator, wind turbine, photovoltaic array, and battery ESS. Utilizing a particle swarm optimization algorithm, the study focused on minimizing the total costs of DERs, reducing environmental emissions, and increasing the penetration level of renewable energy sources [104]. Numerical results demonstrated a 35% reduction in CO<sub>2</sub> emissions in the optimal configuration compared to scenarios relying solely on diesel generators [104]. The optimal installation of DER units in different years significantly enhanced microgrid performance, lowering fuel consumption and CO<sub>2</sub> emissions [104]. Abdalla et al. [105] introduced an optimization strategy for a microgrid, integrating combined cooling and heating power with a hybrid ESS. It outlined the operating characteristics and mathematical models of distributed micro-sources and employed an energy storage architecture for modeling [105]. The optimization focused on improving economic operation, demonstrating a 4.61% and 6.48% reduction in operation costs for winter and summer, respectively, and a 3.01% and 3.68% decrease in fuel consumption [105].

Wang et al. [106] proposed an energy management strategy utilizing a hydrogen storage system. The aim was to minimize operating costs and address load supply constraints [106]. Using MATLAB and the gray wolf optimization algorithm, the proposed model showed that implementing a hydrogen storage system and a demand-side management program reduced microgrid costs [106]. Incorporating microgrid load into the demand response program further smoothed the load curve and decreased the islanded microgrid's operating cost [106].

Mansouri et al. [107] focused on optimizing microgrid operation using the Salp swarm algorithm, a metaheuristics technique, to address uncertainties in renewable energy sources, market prices, and loads. Results demonstrated the algorithm's effectiveness in controlling operating and pollution costs, allowing compromise between the two in both grid-islanded and grid-connected modes [107]. Additionally, applying uncertainty to microgrid parameters improved the algorithm's realism, highlighting its ability to obtain optimal solutions even with indefinite values [107].

### 2.4 Summary and Conclusion

The literature review provides an overview of research efforts aimed at integrating hydrogen into MGTs. Both numerical simulations and experimental studies have explored combustion characteristics, emissions control, and design modifications for efficient hydrogen utilization. These studies offer valuable insights into the benefits and challenges of hydrogen-enriched fuels in MGTs, progressing from early experiments in the late 1990s to recent advancements. While strides have been made in addressing combustion anomalies and enhancing efficiency, transitioning theoretical advancements to real-world applications is crucial for realizing hydrogen's practical viability in MGTs. The scarcity of reported operational instances underscores the need for more practical implementations and real-world testing, essential to unlock hydrogen's full potential in MGTs and advance a cleaner, sustainable energy future.

The review of MGT models underscores the importance of choosing between white-box and black-box models based on the development stage and data availability. In the early design phases, especially when exploring hypothetical scenarios like the introduction of hydrogen, white-box models rooted in physics are essential due to the absence of empirical data. These models provide a theoretical understanding of dynamic behavior.

As MGTs progress into operational phases, black-box models come to the forefront. Leveraging empirical data, these data-driven models, such as ANNs, offer rapid and accurate predictions. They prove crucial for real-time monitoring, fault detection, and optimizing performance.

This dual-modeling approach, transitioning from white-box to black-box, ensures a comprehensive understanding of MGT systems, enabling effective decision-making across different lifecycle stages—from early design to real-time adaptability.

The literature on microgrid operation control and optimization reflects a transition to automated and adaptive frameworks, pivotal in the smart grid evolution. Studies highlight the energy hub concept's effectiveness, employing diverse optimization techniques. Integration of transformative technologies such as IoT and AI enriches building and district energy management, offering abundant data for optimization. Noteworthy strategies involve ANNs for prediction and GA for optimization, showcasing the potential of advanced modeling.

Importantly, a large portion of the literature emphasizes the necessity for accurate modeling approaches, given the disparate dynamics of microgrid components. Many papers employ simplified equations, but the complex integration of components with varying dynamics necessitates precise models for effective optimization. Additionally, for optimization purposes, speed is crucial, making data-driven models particularly intriguing for efficient real-time decision-making. Future research should focus on advanced machine-learning models, explore socio-economic impacts, and validate proposed solutions in diverse contexts.

## 3 Development of a Hydrogen-Powered MGT

The utilization of hydrogen as the primary fuel in MGTs presents significant complexities, leading to challenges in both stability and emissions. This chapter serves as an overview discussion, building upon the comprehensive insights presented in Papers II and III, exploring the complexities of employing hydrogen as the primary fuel in MGTs. It delves into challenges with a focus on achieving stable combustion and emissions control in MGT operation with hydrogen/methane blends. Progressing through the study, the chapter guides through the experimental phase, presenting results from testing with blended hydrogen/methane fuel and offering valuable insights into MGT performance under diverse conditions. It functions as a holistic guide, addressing challenges, presenting solutions, detailing modifications, and elucidating experimental outcomes in the development of an MGT optimized for a hydrogen-enriched environment.

### 3.1 Challenges in Hydrogen Combustion

Developing GT engines, including MGTs, for operation with alternative fuels presents numerous challenges. Notably, hydrogen's high reactivity necessitates combustor design modifications to accommodate it. Additionally, variations in the characteristics of combustion products can necessitate changes in other system components to ensure safe and stable operation while meeting emissions regulations. Challenges associated with running MGTs on hydrogen or hydrogen-blended fuels can be broadly categorized into two areas:

## Development of a Hydrogen-Powered MGT

---

- Component-level challenges which are combustor-related challenges arising from differences in combustion characteristics between hydrogen and fossil fuels;
- System-level challenges result from alterations in working fluid properties due to different combustion products and their impact on engine performance.

An overview of these challenges is provided in the following sections.

### 3.1.1 Component-Level Complications

The distinctive combustion characteristics of hydrogen fuel originate from the unique set of physical and chemical properties of the element. An overview of these properties is provided in Table 3.1 to compare hydrogen molecules against methane, which can be representative of natural gas as well.

Table 3.1 Comparison of the properties of hydrogen and methane in atmospheric pressure and 300K temperature [108].

Property	Methane	Hydrogen
Molecular weight	16.04 g/mol	2.02 g/mol
Density	0.65 kg/m <sup>3</sup>	0.08 kg/m <sup>3</sup>
Mass diffusivity in air	0.16 cm <sup>2</sup> /s	0.61 cm <sup>2</sup> /s
Lower heating value (per mass)	50 MJ/kg	120 MJ/kg
Lower heating value (per volume)	32.5 MJ/m <sup>3</sup>	9.6 MJ/m <sup>3</sup>
Stoichiometric air/fuel ratio	17.1 kg/kg	34.2 kg/kg
Minimum ignition energy	0.28 mJ	0.02 mJ
Flammability limits	0.5~1.67	0.1~7.1
Stoichiometric air-to-fuel ratio	17.1 kg/kg	34.1 kg/kg
Stoichiometric air-to-fuel ratio	59.7 kmol/kmol	2.4 kmol/kmol

The challenges arising from the combustion of hydrogen-blended methane due to the difference between the combustion characteristics of hydrogen and methane are detailed in Paper II. The following is a concise overview covering the main points:

- Flammability Characteristics:

## Development of a Hydrogen-Powered MGT

---

- Hydrogen exhibits a wide range of flammability (equivalence ratio: 0.1–7.1), allowing versatility in GT engines [109].
- Methane (natural gas), in contrast, has a narrower flammability range, impacting its adaptability to various air-fuel ratios [109].
- Ignition Energy:
  - Hydrogen requires approximately 10 times less ignition energy than methane, contributing to improved combustion performance and stability [38], [110], [111], [112], [113].
  - The higher ignition energy of methane poses challenges during ignitions and maintaining stable combustion, especially in low-load GT ranges [38], [110], [111], [112], [113].
- Laminar Flame Speed:
  - Increasing the hydrogen content enhances laminar burning velocity, leading to stable flames, reduced ignition delay, and improved performance in lean combustion conditions [114], [115], [116].
- Adiabatic Flame Temperature:
  - Hydrogen's acceleration of the reaction rate results in a higher adiabatic flame temperature compared to methane, particularly at stoichiometric combustion [38], [117].
- NO<sub>x</sub> Formation:
  - Elevated flame temperatures associated with hydrogen combustion contribute to increased NO<sub>x</sub> production, posing environmental concerns [118].
  - Traditional methods for mitigating NO<sub>x</sub> face challenges when applied to hydrogen-enriched fuels due to differences in flammability and reaction rates [119].

- Combustion Efficiency and Stability:
  - Hydrogen's wide flammability limits, high flame speeds, and low ignition energy offer efficiency benefits but also pose challenges such as flashback and unwanted flame propagation [120].
  - Lean premixed burners, proven for hydrocarbons, encounter challenges with hydrogen or hydrogen-enriched fuels, including combustion instabilities, flashbacks, and elevated NO<sub>x</sub> formation due to differing flammability and reaction rates. [119], [121], [122], [123].

Navigating the complexities arising from the aforementioned differences in combustion characteristics between hydrogen and methane, the development of combustor technology for hydrogen combustion becomes more intricate, especially when aiming to operate with both pure hydrogen and hydrogen-blended fuels [124].

### 3.1.2 System-Level Complications

In the context of the system-level complications associated with MGTs running on hydrogen and hydrogen-blended fuels, the unique combustion characteristics of hydrogen and methane have far-reaching consequences beyond combustion, affecting the overall MGT system behavior [123], [125]. A detailed exploration of these complications is provided in Paper II, while the following overview serves as a condensed summary.

The differences, including properties such as heating value and fuel density, influence fuel flow rates and may potentially alter the thermodynamics of the MGT cycle. A comparative analysis, simulating MGT operation at ISO conditions<sup>1</sup>, estimates the extent

---

<sup>1</sup> ISO 3977, an international standard for gas turbine design, is based on ASME 133, API 616, and API 11PGT standards. The standard specifies environmental conditions at the design point: 15 °C, 60% relative humidity, and sea level elevation.

## Development of a Hydrogen-Powered MGT

of these alterations by examining variations in adiabatic flame temperature, specific heat capacity, and flue gas density across different equivalence ratios for methane and hydrogen combustion. The observed disparities in flue gas properties become more pronounced with richer combustion, impacting fuel flow rates and necessitating considerations for cycle point alteration. This can be seen in Figure 3.1, where the flue gas properties of pure methane and pure hydrogen combustion are depicted for different equivalence ratios, using the Cantera program [126].

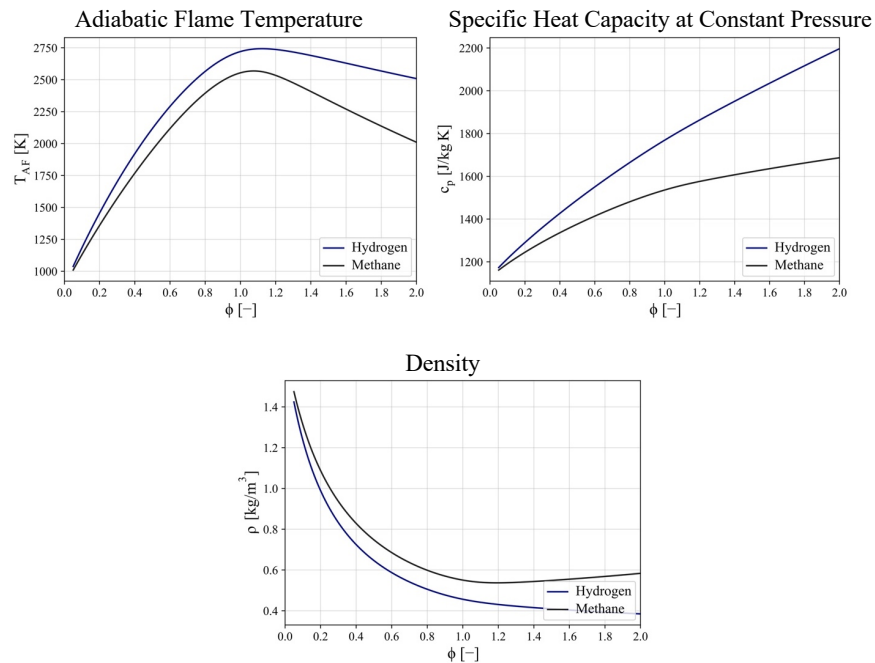


Figure 3.1 Flue gas properties in different equivalence ratios for burning methane and hydrogen, with air at 4.3 bar and 610 K. The plots are depicted using analysis conducted with Cantera [126].

The calculations reveal that the pure methane combustion in the MGT occurs in a very lean condition with an equivalence ratio of 0.14 for the MGT's baseload. This results in minor alterations in temperature, density, volumetric flow rate, and specific heat capacity during the transition from methane to hydrogen as a fuel



## Development of a Hydrogen-Powered MGT

---

source. Fortunately, this lean combustion condition mitigates the impact on the flow entering the turbine section, addressing potential challenges associated with variations in flue gas properties.

The computed values presented in Table 3.2 illustrate the changes in flue gas properties during the transition from methane to hydrogen as the fuel source. Notably, there is an approximate 6-degree temperature increase, leading to adjustments in density. Consequently, this shift results in a 1.5% increase in the volumetric flow rate at the turbine inlet, reaching 0.68 m<sup>3</sup>/s. Additionally, the specific heat capacity of the flue gas experiences a 1% increment. As it is evident, the high air-to-fuel ratio of MGT combustion has led to a small alteration of flue gas properties, and therefore, a small variation in the cycle is anticipated.

Table 3.2 Flue gas properties comparison burning methane and hydrogen. Air composition is 21% O<sub>2</sub> and 79% N<sub>2</sub> with 4.3 bar pressure and 610 K temperature.

Property	Methane	Hydrogen
Fuel flow rate for nominal power output	6.7 g/s	2.8 g/s
Air flow rate	0.8 kg/s	0.8 kg/s
Flue gas mass flow rate	0.8076 kg/s	0.8028 kg/s
Flue gas density	1.2046 kg/m <sup>3</sup>	1.1815 kg/m <sup>3</sup>
Flue gas flow rate	0.67 m <sup>3</sup> /s	0.68 m <sup>3</sup> /s
Stoichiometric air-fuel ratio	17.12	34.06
Actual air-fuel ratio	120	288
Equivalence ratio	0.14	0.12
Adiabatic flame temperature	1230.52 K	1236.51 K
Flue gas heat capacity at constant pressure	1214.8 J/kgK	1228.8 J/kgK

After outlining these challenges, a comprehensive understanding of developing an MGT for hydrogen/methane blended fuel has emerged. The following section provides an overview of the experimental setup, detailing specific modifications made to facilitate its operation with hydrogen-blended fuel, addressing each challenge systematically.

## 3.2 Development of an MGT Running with Hydrogen Fuel

The pursuit of creating an MGT capable of running on a hydrogen/methane blend entailed modifications to the existing T100 MGT situated at the Risavika Research Center in Stavanger, Norway. These modifications focused on three critical aspects: the fuel delivery system, the combustor, and the controller. A comprehensive and detailed explanation of these modifications is available in Paper II, while subsequent sections offer a concise overview, highlighting key elements for clarity.

### 3.2.1 Fuel Delivery System

The original low-pressure fuel system, relying on an external compressor for pressure augmentation, has been replaced with a new setup incorporating methane and hydrogen batteries stored in a bundle structure. Pressure reduction is achieved through relief valves, and safety measures include flashback arrestors and fuel disconnecting valves for rapid shut-off in case of a leak, as seen in Figure 3.2.

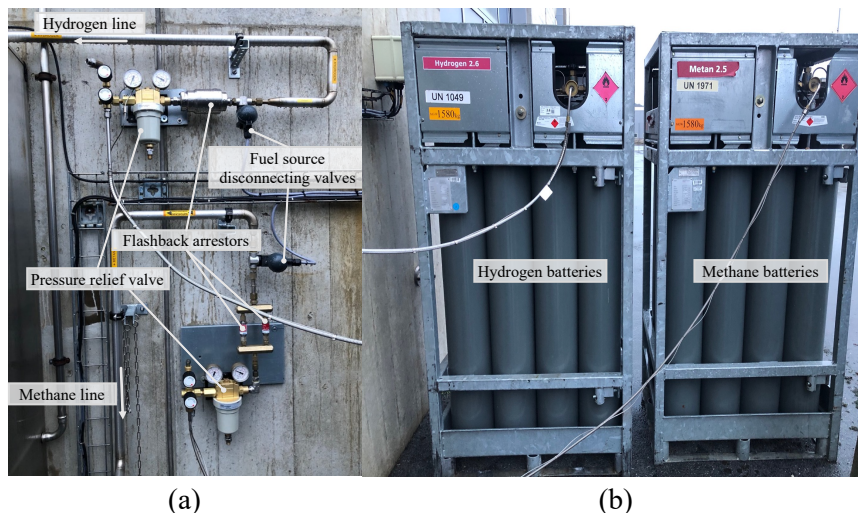


Figure 3.2 Fuel system arrangement installed outdoors, (a) the valves, (b) fuel bottles.

## Development of a Hydrogen-Powered MGT

---

The updated fuel train system, temporarily installed on the MGT (Figure 3.3), features separate lines for methane and hydrogen, mixed to control the fuel ratio. Thorough mixing is facilitated at the larger-diameter mixing station, with the mixed fuel conveyed into the combustor through two lines, utilizing one main valve and one pilot valve for proper functioning.

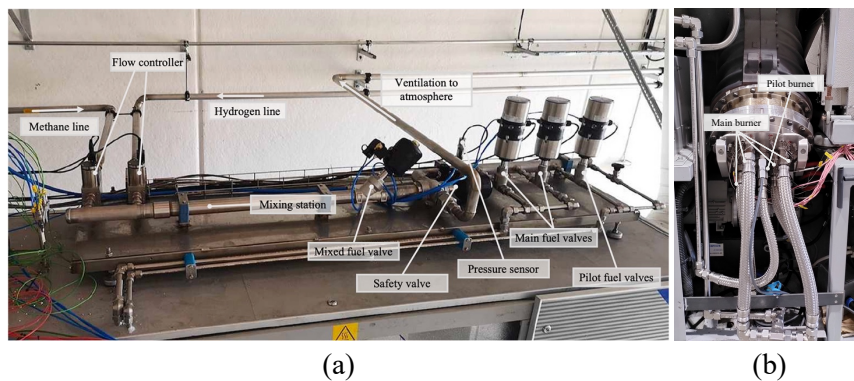


Figure 3.3 The modified fuel system, (a) the mixing station and fuel train installed on top of the MGT enclosure, (b) the combustor.

### 3.2.2 Combustor

The experimental setup employed a DLR F400s.3 combustion system to operate the MGT with hydrogen-rich fuels. This system, replaced the original Turbec swirl-type combustor in the T100 MGT, as depicted in Figure 3.4. The DLR F400's pilot stage utilized swirl stabilization, while the main stage employed the FLOX® concept, combining jet and recirculation for improved combustion stability and reduced peak temperatures compared to the original T100 combustor.

Figure 3.5 illustrates the FLOX® combustor's design, featuring ten nozzles arranged in a circular configuration for axial injection of high-momentum main-stage air. This design is engineered for versatile fuel compatibility, enhances lean equivalence ratios, lowers combustion temperatures, and minimizes the potential for NO<sub>x</sub> formation.

## Development of a Hydrogen-Powered MGT

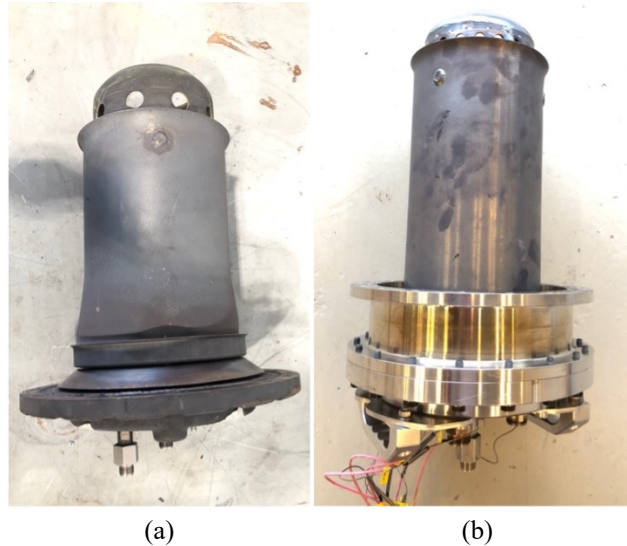


Figure 3.4 The combustor of the MGT a) the original Turbec design, b) F400s ver.02.

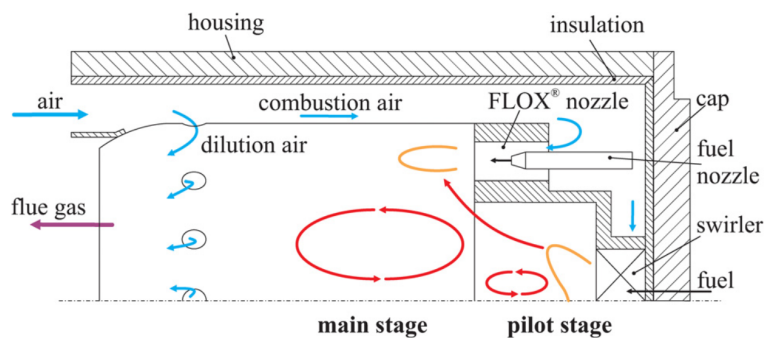


Figure 3.5 Schematic of the FLOX<sup>®</sup> combustion principle [127].

Upon integration into the MGT operating at elevated pressure levels and increased volumetric energy density, the combustor's behavior faced new parameters unaddressed in atmospheric tests. Adjustments in air allocation within the MGT combustor adapted to high hydrogen content. Four configurations (9 mm, 11 mm, 12 mm, and 13 mm) were examined, showing increased performance in leaner configurations, with a 36% air distribution increase in the 9 mm version while maintaining low NO<sub>x</sub> emissions and flame stability.

Figure 3.6 outlines the expected relative combustion air over the dilution hole diameter, providing insights into air distribution adjustments with increasing hydrogen content. The results indicate enhanced performance in leaner configurations, underscoring the combustor's adaptability to hydrogen-rich fuels.

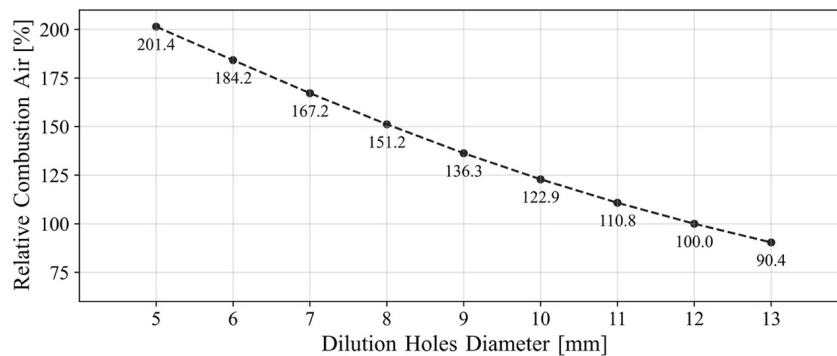


Figure 3.6 Expected relative combustion air over dilution hole diameter.

### 3.2.3 Controller System

To accommodate hydrogen-rich fuels in the MGT system, crucial modifications were implemented in the controller system. Figure 3.7 provides a view of the enhanced MGT unit, featuring a new fuel delivery system tailored for operation with fuels rich in hydrogen content. The high-pressure bottles of methane and hydrogen maintain pressures up to 250 bar with manual pressure adjustments via relief valves. The fuel train controller meticulously regulates mass flow rates to ensure a precise fuel mixture, showcasing the intricate interconnections between controllers and valves in Figure 3.7.

During the engine start-up phase, where the flammability range of hydrogen and methane poses challenges, the controller system employs a pilot mode to facilitate a controlled transition. Making adjustments to the pilot valve mapping to ensure a stable start-up, especially in conditions with high hydrogen content, led to a smoother transition during ignition and initial acceleration, addressing concerns related to hydrogen's flammability limits.

## Development of a Hydrogen-Powered MGT

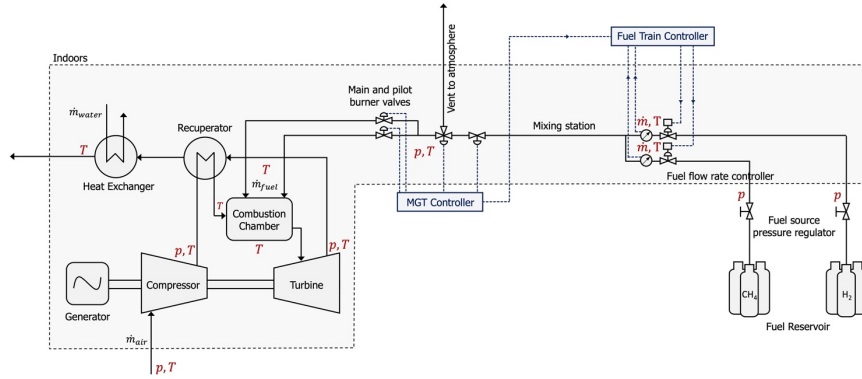


Figure 3.7 Structure of the MGT unit equipped with the new fuel train system, controllers, and measurement points.

### 3.2.4 Measurement System

The engine is outfitted with an extensive array of strategically positioned sensors which play a critical role in monitoring various parameters, ensuring precise control of the engine, and collecting abundant data for comprehensive analysis. Notably, the engine incorporates sensors to measure temperature, pressure, and mass flow rate in different stages, while also employing a gas analyzer to quantify concentrations of  $O_2$ ,  $CO$ ,  $NO$ ,  $NO_2$ ,  $CO_2$ , and  $HC$  in exhaust gases. A detailed examination of the measurement system is provided in Paper II. An elaboration on the rigorous process of data cleaning, ensuring the reliability and accuracy of the collected data is provided in Chapter 5 of the thesis.

### 3.3 Results

Figure 3.8 provides a visual representation of the final MGT engine configuration. A comprehensive examination of experiments conducted to understand the impact of enriching methane fuel with hydrogen on the performance of the MGT is provided in Papers II and III. The focus of the provided results is on investigating the influence of different hydrogen blends on emissions and the stability of combustion. In this section, a brief overview of the results is presented.



Figure 3.8 Turbec T100 unit with modified combustor and fuel train for flexible fuel operation.

In the initial experiments, the designed combustor functioned well with hydrogen content below 30% (volume basis). However, operational instabilities increased with higher hydrogen content, particularly in high-power modes. This prompted an exploration of a modified combustor design.

In the second phase, an improved version of the combustor was designed and manufactured with smaller dilution holes, enhancing airflow to the main burner and improving material cooling. Experiments involved varying hydrogen content in the fuel and operating the engine at different power outputs. Challenges emerged when the hydrogen content exceeded 55%, leading to instabilities and high NO<sub>x</sub> emissions during start-ups.

Addressing these issues necessitated iterative adjustments to the controller, guided by a trial-and-error methodology, to facilitate safe operation under high hydrogen fuel conditions while minimizing emissions. To achieve this, critical control parameters governing MGT operation during start-ups were identified, and corresponding modifications were implemented. Subsequently, the observed behavior of the MGT during start-up sequences was systematically analyzed to elucidate the influence of these



parameters on engine performance. Additionally, error codes generated during unsuccessful operations served as valuable indicators, aiding in the development of strategies to avoid such failures and ensure stable operations.

After implementing the controller adjustments, a series of experiments with an increasing share of hydrogen in the fuel, up to 100%, were conducted. In-depth analyses were performed, considering cycle parameters like rotational speed and turbine outlet temperature (TOT). The relationship between rotational speed and power output showed consistent behavior despite slight deviations from methane-fueled operation. The impact of hydrogen content on TOT and NO<sub>x</sub> production became more evident, highlighting the importance of valve adjustments in controlling emissions.

Investigation into hydrogen injection impact on electrical efficiency demonstrated steady efficiency across hydrogen contents. Overall efficiency increased with higher power outputs, mirroring behavior with conventional fuels. Increasing hydrogen content correlated with rising NO<sub>x</sub> emissions but remained within permissible levels. Anomalies arose around 55% hydrogen content, linked to initial valve settings. Higher hydrogen content led to diminished CO emissions, reaching zero for pure hydrogen. Detailed measurements, evaluations, and results are discussed in Papers II and III.

### 3.4 Conclusion

This chapter addressed challenges in developing an MGT powered by a blend of hydrogen and methane, gradually transitioning to 100% hydrogen. The focus was on achieving combustion stability, emissions control, and preventing excessive combustor temperatures to mitigate thermal NO<sub>x</sub> formation. It discussed a modified combustor design with adjusted dilution holes, enhancing airflow and material cooling efficiency, ensuring stable



## Development of a Hydrogen-Powered MGT

---

combustion with high hydrogen content. Operational results highlighted the impact of fuel valve adjustments for achieving stable operation in varying conditions while keeping NO<sub>x</sub> emissions below allowed values. For detailed findings and extensive results, Papers II and III are provided in the appendix, which offer thorough analyses of experimental procedures and scientific insights into hydrogen-enriched MGT development.

## 4 Development of an MGT Model: Physics-Based Approach

This chapter outlines the development of physics-based models for 100 kW capacity MGTs, employing two strategies: dynamic modeling with MATLAB's Simscape and steady state modeling in Python. MATLAB's Simscape provides a structured framework for dynamic modeling, offering robustness and programming flexibility. Python is chosen for steady state modeling due to its versatile programming capabilities and efficient handling of iterative processes, enabling swift derivation of steady state solutions for complex MGT systems. Despite methodological differences, both models share a common approach—systematic deconstruction of the MGT system into discrete components, each treated as an independent entity. This involves formulating correlations detailing interdependencies between components. The chapter explores dynamic model formulation, steady state model development, and their alignment with empirical data. Tailored for the Turbec T100 MGT, the models exhibit adaptability to other MGT systems, contingent upon the availability of component maps for those systems. This chapter offers an overview of the models detailed in Papers IV and V.

### 4.1 T100 MGT

The Turbec T100 MGT, initially designed by Turbec and currently produced by Ansaldo Energia (AE), is a 100 kW electrical power MGT available in CHP and electric utility configurations. Two variants were extensively studied during this research: the Turbec version located at Risavika Research Center, Stavanger, Norway (Figure 4.1), and the AE version at Paul Scherrer Institute (PSI),

## Development of an MGT Model: Physics-Based Approach

---

Villigen, Switzerland (Figure 4.2), denoted as AE-T100 for clarity. Both variants significantly contributed to understanding operational intricacies and control logic throughout the PhD program. The core components, such as the compressor, turbine, combustor, and recuperator, share the same design for both engines and the primary distinction lies in computer system advancements. Therefore a uniform approach was pursued for their thermodynamic modeling.



Figure 4.1 The T100 MGT, located at Risavika Research Center, Stavanger, Norway.



Figure 4.2 The T100 MGT, located at PSI, Villigen, Switzerland.

## Development of an MGT Model: Physics-Based Approach

The T100 MGT, equipped with a single-stage centrifugal compressor, a single-stage radial turbine, and a can-type lean pre-mix combustion chamber, operates efficiently on rich natural gas. It maintains a fuel/air equivalence ratio of 0.13 at full load, utilizing an auxiliary compressor to elevate fuel inlet pressure to 6–7 bar when natural gas is available at atmospheric pressure. If natural gas is available with sufficient fuel pressure, the need for a fuel compressor can be eliminated. The engine incorporates a bottoming air/water heat exchanger for CHP, and the power train configuration features a water-cooled high-speed permanent magnet generator, which also acts as a motor during start-up. Operating within a recuperated cycle, the engine achieves a nominal electrical efficiency of 30%. In CHP mode, it demonstrates a maximum thermal output of approximately 165 kWh, leading to a total efficiency of 80%. A pivotal factor contributing to the engine's efficiency is the incorporation of a recuperator in the cycle. This component preheats the air entering the combustor by harnessing excess heat from the flow exiting the turbine. The schematic representation of the engine's main components is provided in Figure 4.3, while Figure 4.4 offers a visual insight into the AE-T100 with identifiable parts.

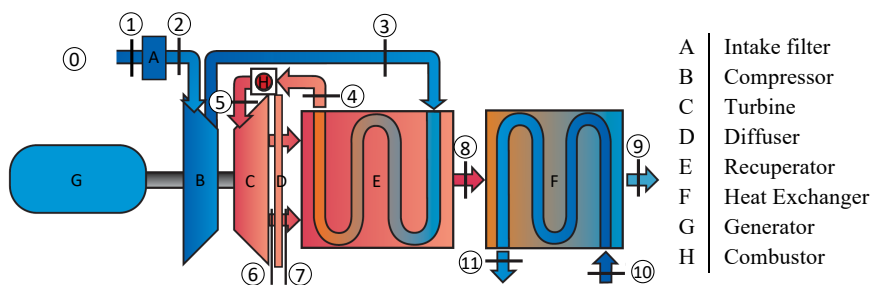


Figure 4.3 Schematic view of the T100 engine.

Operational at its design point, the engine maintains a rotational speed of 70,000 rpm. The cycle features a pressure ratio of around 4.5 and a controlled turbine inlet temperature (TIT) of 950 °C,

ensuring that the TOT remains below 645°C. A detailed summary of the engine’s specifications under baseload conditions is provided in Table 4.1.

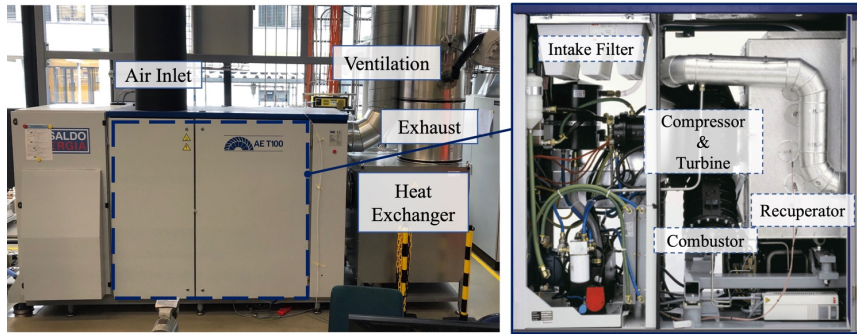


Figure 4.4 The MGT from outside (left) and its inside (right). The figure on the right side is imported from [128].

Table 4.1 AE-T100 nominal characteristics reported by the manufacturer [128].

Characteristics	Nominal Value
Pressure in the combustion chamber	4.5 bar (a)
Turbine inlet temperature	950 °C
Rotational speed	70,000 rpm
Frequency output	50 Hz (60 Hz on request)
Voltage output	400 V(AC), three phases
Required pressure for fuel	(6 ~ 8) bar(g)
Required temperature for fuel	(0 ~ 40)°C
Electrical power output	100 ± 3kW <sub>e</sub>
Electrical efficiency	30 ± 2%
Exhaust gas flow rate	≈ 0.79kg/s
Exhaust gas temperature	≈ 270°C
NO <sub>x</sub> emissions	≤ 15ppm(v) ≈ 31 mg/Nm <sub>3</sub> @15%O <sub>2</sub>
CO emissions	≤ 15ppm(v) ≈ 19 mg/Nm <sub>3</sub> @15%O <sub>2</sub>

## 4.2 Development of the Dynamic Model of the Fuel-Flexible MGT

The dynamic model of the MGT consists of an interconnected network of components, including the compressor, combustor, turbine, recuperator, and heat exchanger. Each component is

modeled using governing equations and principles based on fluid dynamics, thermodynamics, and heat transfer. This dynamic model allows for the analysis of the transient behavior of the MGT system, capturing its responses to fluctuations in operating conditions, variations in load, and the intricacies of start-up and shutdown procedures. A simplified block diagram of this dynamic model, implemented within MATLAB's Simscape, is illustrated in Figure 4.5.

Traditionally, researchers and engineers have relied on Simulink for dynamic modeling, utilizing its graphical block diagram approach for systems such as GTs and control systems. The evolution of Simscape builds upon Simulink's strengths, offering an advanced extension designed to meet the complex modeling demands of multi-domain physical systems. Simscape excels in efficiently integrating and managing interconnected domains, providing a foundational structure spanning all physical domains and a comprehensive library of physical components for detailed simulations. Unlike the conventional Simulink modeling approach, which relies on equation-based component connections, Simscape establishes authentic physical connections that accurately reflect the real-world topology of the system. While Simulink's block diagram structure facilitates modeling, it is crucial to note that the relationships between its blocks and signals do not precisely replicate the actual physical connections inherent in components, such as flow or rotor connections. Figure 4.6, extracted from [129] illustrates the T100 MGT modeled in Simulink to underscore these disparities.

## Development of an MGT Model: Physics-Based Approach

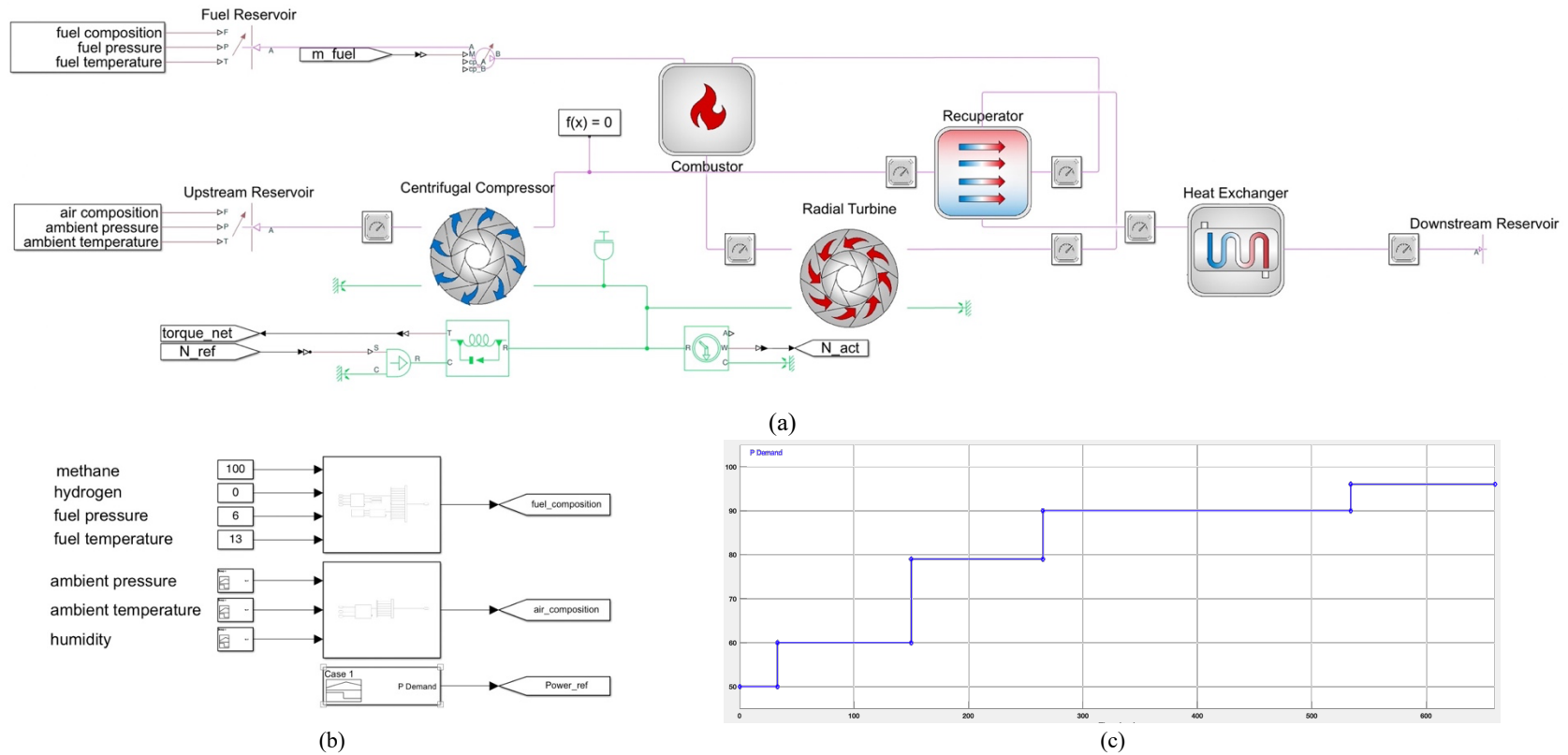


Figure 4.5 Developed model for the T100 unit using MATLAB Simscape: (a) thermodynamic cycle, (b) user's inputs to the model, (c) a sample for reference power.

## Development of an MGT Model: Physics-Based Approach

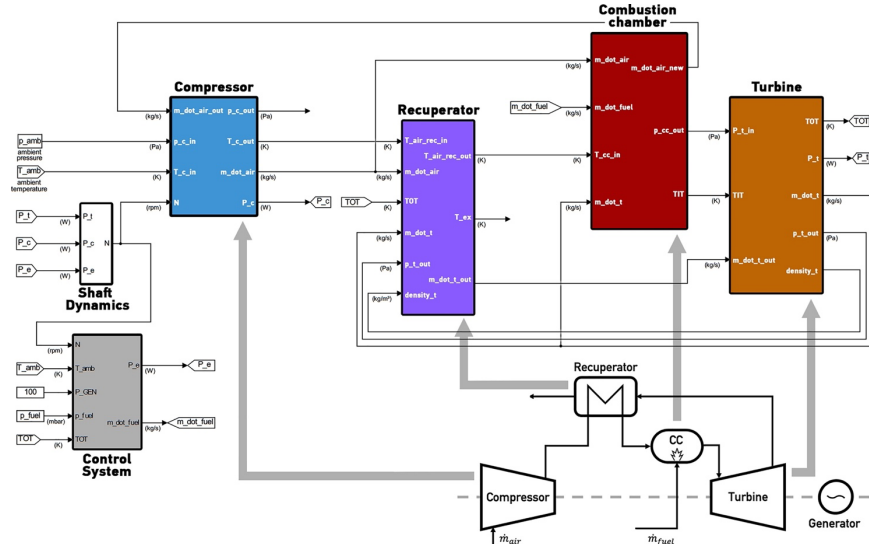


Figure 4.6 Developed model for a Turbec T100 unit using MATLAB Simulink [129].

The foundation of Simscape models rests on two crucial components: domains that signify physical fields and components that represent the elements of a system. These components are versatile and capable of spanning multiple domains, offering flexibility in constructing models.

While a detailed exploration of the dynamic model developed in Simscape is available in Paper IV, this section provides a concise overview, focusing on key aspects.

### 4.2.1 Domain Definition

Simscape domains represent physical fields like electrical or gas systems, featuring through-variables (e.g., mass flow rate) and across-variables (e.g., pressure). In the T100 engine Simscape model, gas, rotational, and thermal domains play key roles.

The gas domain is customized for MGT cycle variations, encompassing through-variables such as mass flow rate ( $\dot{m}$ ), energy flow rate ( $\dot{\varphi}$ ), and fuel flow rate ( $\dot{m}_f$ ), as well as across-variables including pressure ( $p$ ), temperature ( $T$ ), and fuel



concentration ( $x_f$ ). Equation 4.1 correlates fuel concentration and flow rate.

$$x_f = \frac{\dot{m}_f}{\dot{m}} \quad 4.1$$

The MGT model integrates the Mechanical Rotational Domain, defining torque ( $\vec{\tau}$ ) and angular velocity ( $\omega$ ) as through and across variables. The Thermal Domain simulates heat transfer, employing heat flow ( $\dot{Q}$ ) as the through variable and temperature ( $T$ ) as the across variable.

The properties of the working fluid depend on molecular composition, pressure, and temperature. User-defined molecular compositions for air ( $C_a$ ) and fuel ( $C_f$ ) determine flow properties. Pre-combustor components have zero fuel concentration, with properties determined by air composition, pressure, and temperature at the entrance. Post-combustor components have non-zero fuel concentration, and species concentrations are calculated based on  $x_f$ . The combustion chamber has varying fuel composition at its inlet and outlet, requiring distinct calculations for flow properties at each point.

Users choose fuel type, and the model calculates fluid properties, including heat capacities, gas constant, thermal conductivity, and density. Figure 4.5 (b) illustrates user input data for boundary conditions in MGT simulation, including time-dependent ambient conditions. Users configure air and fuel conditions and set the power point through the bottoming block, represented as a time-based signal in Figure 4.5 (c). This signal feeds into the engine controller, modeled by Simulink. Further details on these calculations are discussed in Paper IV.

### 4.2.2 Controller

The controller's model, depicted in Figure 4.7, is developed in Simulink, and specific parameters are fine-tuned for a balance between meeting power demands and preserving engine integrity.

## Development of an MGT Model: Physics-Based Approach

The user or grid sets the desired power output, guiding the controller's dynamic adjustments to match the power demand while prioritizing engine safety. The controller parameters play a pivotal role in the transient behavior of the MGT, encompassing start-up, shutdown, and load variation, and are meticulously fine-tuned to align with the MGT's performance in these dynamic conditions.

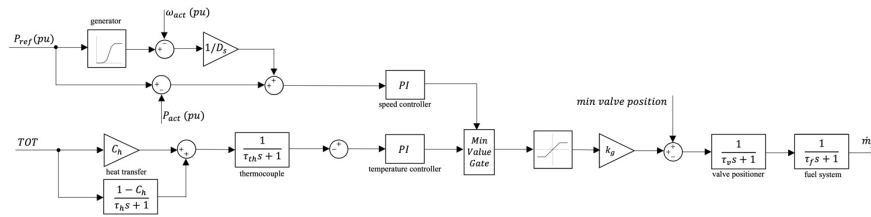


Figure 4.7 Controller of the T100 MGT developed in Simulink.

The system's controller operates automatically, responding to user inputs and real-time engine measurements, including TOT, rotor speed, and power output. Its primary goal is to meet power requirements while ensuring the TOT stays below  $645^{\circ}\text{C}$  so the turbine and recuperator are safe from high temperatures. The controller employs a dynamic strategy, adjusting fuel mass flow rate and rotational speed using proportional-integral regulators for gradual response. A correlation between reference rotational speed and desired power level is established, with safeguards to prevent rotor damage.

### 4.2.3 MGT Main Components

The main components of the MGT is presented in Figure 4.8 which provides insight into the intricate relationships among the engine components and their thermodynamic interactions. Built upon these elements, the MGT model incorporates lumped components presumed to have a finite number of inlets and outlets, with uniform flow properties at their boundaries. Typically applied between the inlet and outlet of components, signifying their zero-dimensional nature, a distinct approach is taken for the

recuperator, utilizing a one-dimensional approach within discretized cells. Time-dependent thermodynamic equations presented for all gas domain components serve as fundamental principles for mass, momentum, and energy conservation within the system. These principles are elaborated in Paper IV, and a summary of the primary governing equations is provided in this section.

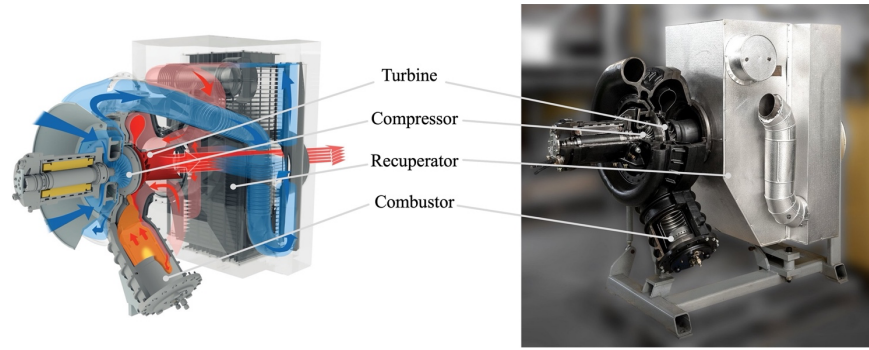


Figure 4.8 The main components of the T100 MGT from [130].

By neglecting spatial variations at inlets and outlets, the conservation of mass in each of the components is simplified to Eq. 4.2:

$$V \frac{\partial \rho}{\partial t} + \sum_i (\dot{m})_{out} - \sum_i (\dot{m})_{in} = 0 \quad 4.2$$

With the ideal gas assumption, the variation of gas density is correlated to pressure and temperature variations over time, as provided in Eq. 4.3:

$$\frac{\partial \rho}{\partial t} = \frac{1}{RT} \frac{\partial p}{\partial t} - \frac{p}{T} \frac{1}{RT} \frac{\partial T}{\partial t} \quad 4.3$$

The linear momentum and angular momentum equation is written as:

$$\sum \vec{F} = \sum (\dot{m} \vec{V})_{out} - \sum (\dot{m} \vec{V})_{in} \quad 4.4$$

$$\sum \vec{M} = \sum (\vec{r} \times \vec{V})_{out} \dot{m}_{out} - \sum (\vec{r} \times \vec{V})_{in} \dot{m}_{in} \quad 4.5$$

Similarly, the energy conservation equation for the component can be expressed as shown in Eq. 4.6:

$$\frac{dQ}{dt} - \frac{dW}{dt} = \text{Vd}(\rho e)/dt + \sum \left( h + 1/2|\vec{V}|^2 + gz \right)_{\text{out}} \dot{m}_{\text{out}} - \sum \left( h + 1/2|\vec{V}|^2 + gz \right)_{\text{in}} \dot{m}_{\text{in}} \quad 4.6$$

The sigma symbol in the above equations account for all inputs and outputs of the component. Typically, most components have a single inlet and outlet, as leakage is disregarded.

In Eq. 4.6 the parameters Q and W represent heat and work exchanges contributing to the total energy variation and the parameter e signifies total energy per unit mass, comprising internal, kinetic, and potential energy components:

$$e = \hat{u} + \frac{1}{2}|\vec{V}|^2 + gz \quad 4.7$$

Assuming negligible variations in velocity and level between inputs and outputs, and by applying the ideal gas assumption, the internal energy term takes precedence and can be related to temperature as shown in Eq. 4.8:

$$\frac{d(\rho u)}{dt} = \rho c_v \frac{\partial T}{\partial t} + \rho T \frac{\partial c_v}{\partial t} + c_v T \frac{\partial \rho}{\partial t} \quad 4.8$$

Consequently, the time derivative of the internal energy term can be calculated by rewriting the  $c_v$  terms in relation to  $c_p$  (Eq. 4.9), and the relationship between  $c_p$  and temperature, as stated in Eq. 4.10:

$$c_v = c_p - R \quad 4.9$$

$$\frac{dc_v}{dt} = \frac{dc_p}{dt} = \frac{\partial c_p}{\partial T} \frac{\partial T}{\partial t} \quad 4.10$$

As a result, all the time-dependent terms within the mass and energy conservation equations are transformed into the time derivatives of pressure and temperature.

These equations serve as fundamental principles applied universally across all key components of the MGT system, including the compressor, turbine, combustor, and recuperator.

The operational characteristics of the components in the MGT model are represented through maps and correlations detailing their flow behaviors at conditions, established through steady state test runs. These component-specific correlations are detailed in Paper IV and V. Integrated with dynamic equations for mass, momentum, and energy balance, these maps contribute to the model's robust dynamic response.

To address potential discrepancies between actual engine component behavior and representations offered by maps and correlations, a tuning process aligning the steady state operation with experimental data is conducted. A comprehensive explanation of this tuning process is provided in Section 4.4.

### 4.3 Development of the Steady State Model of the Fuel-Flexible MGT

The development of the steady state model for the fuel-flexible MGT system was undertaken using Python. To achieve steady state operating conditions, the model employs a combination of algebraic equations, iterative methods, and numerical solutions.

The architecture of the steady state model mirrors the real-world operation of the MGT, where two sets of parameters determine its performance. These include user-defined parameters such as the power set point and fuel composition, alongside environmental conditions like ambient air and fuel condition. In Figure 4.9, a comprehensive overview of the code structure is provided, featuring modules for the controller, air composition calculator, fuel composition calculator, and the thermodynamic cycle.

## Development of an MGT Model: Physics-Based Approach

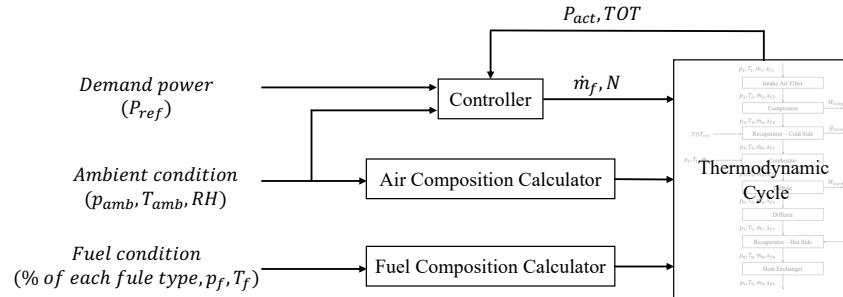


Figure 4.9 Structure of the developed steady state model, showing the data transferred between four principal modules.

The controller module plays a pivotal role in processing inputs related to power demand and ambient temperature. It calculates the fuel mass flow rate and engine rotational speed, which are then integrated into the thermodynamic cycle. This cycle encompasses the entire array of flow-based components and the generator, ensuring they operate at the specified rotational speed and fuel mass flow rate dictated by the controller. The air and fuel flow conditions are incorporated into the thermodynamic cycle through the air composition and fuel composition calculator modules.

Upon completion of the thermodynamic cycle, the controller receives data on power output and TOT. It conducts a dual comparison, first evaluating the calculated power output against the desired reference value, and second, verifying that the TOT remains below the critical limit of 645°C. The controller iteratively adjusts the rotational speed and fuel flow rate to align with reference values while maintaining the TOT within acceptable thresholds. This iterative process persists until both power output and TOT converge to the desired values, ensuring the model accurately represents the steady state behavior of the fuel-flexible MGT system.

The controller establishes the engine's rotational speed based on a correlation derived from Eq. 4.11, which takes into account the reference power and ambient temperature. This correlation has

been derived from the engine's performance under a variety of operational conditions.

$$\begin{aligned} N = & 93.035 P_{\text{ref}} + 700.698 T_{\text{amb}} + 0.564 P_{\text{ref}}^2 \\ & + 2.007 P_{\text{ref}} \times T_{\text{amb}} - 19.25 T_{\text{amb}}^2 \\ & + 43682.417 \end{aligned} \quad 4.11$$

To refine the fuel flow rate, the controller module utilizes the Secant method [131], a recognized approach known for its swift convergence. While the prescribed correlation for rotational speed typically remains stable, there are instances where iterations involving fuel flow rates may not converge within a specified number of steps. In such cases, an outer loop is activated to adjust the rotational speed. Following this adjustment, the iteration process for fuel flow rates is reiterated to ensure the convergence of both power and TOT to the desired values. The iterative procedure is visually outlined in Figure 4.10, providing a representation of the model's refining process. The parameter  $\dot{m}_1$  in Figure 4.10 represents the inlet air to the engine, as the subscript represents the location in the MGT previously defined in Figure 4.3.

The air and fuel composition modules leverage the Cantera [126] tool to determine the composition of the flow entering the thermodynamic cycle module. This cycle module is designed based on the principal components of the MGT. At the entrance of each component, the total pressure, total temperature, and composition of the flow are known. Similarly, these parameters are computed for the flow exiting each component. All calculations within the components utilize Cantera [126] to determine the properties of the flow based on its thermodynamic condition at the entrance of each component. This ensures accurate representation and calculation of the flow characteristics throughout the MGT system.

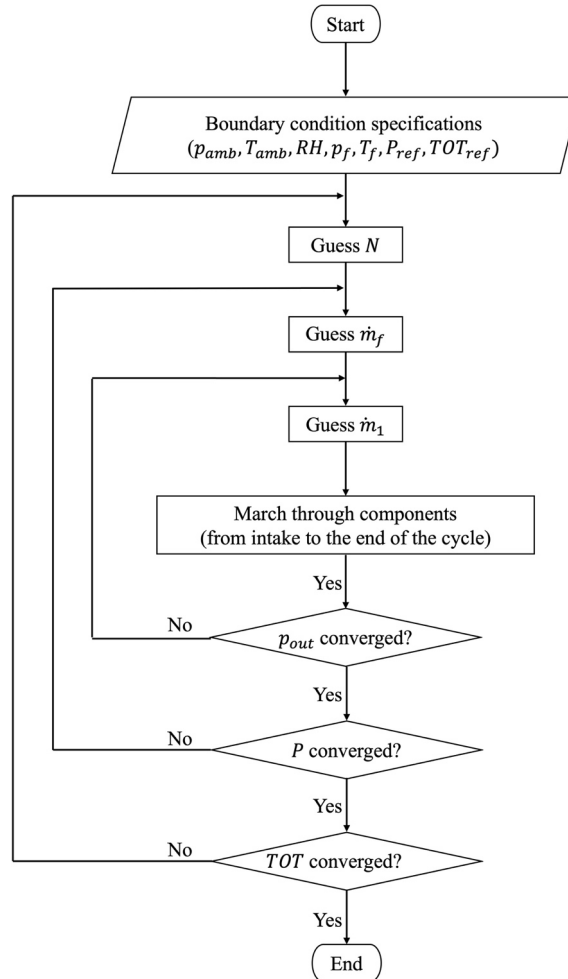


Figure 4.10 The flowchart of the steady state model.

### 4.3.1 Thermodynamic Cycle

The module's thermodynamic cycle encompasses several functions, each aligning with a specific stage of the engine's operation, as discussed in Section 4.2.3. However, in the steady state model, the time derivative terms of the equations are disregarded. Additionally, the steady state model integrates an air inlet filter and a turbine diffuser, which were absent in the dynamic model. The inclusion of these components enhances the



overall accuracy of the model. The structure of the thermodynamic model and its structure are provided in Figure 4.11.

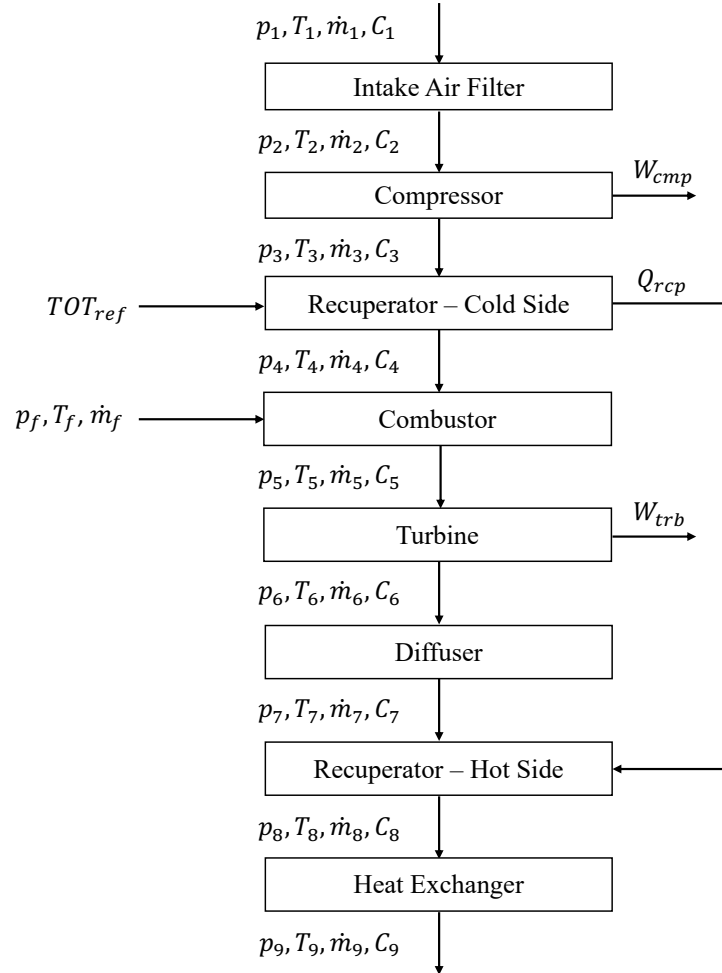


Figure 4.11 The structure of the thermodynamic cycle module and the stream of parameters.

The foundation of the model lies in equations that calculate the outlet flow conditions based on the inlets and the component's specific behavior. This modeling approach incorporates two main categories of equations: governing equations encompassing the steady state forms of mass and energy balance for a control

volume with one-dimensional open boundaries, and behavioral correlations that are component-specific and influenced by the geometry of each component. These correlations are derived from experimental data obtained from engine or individual component tests and are typically expressed as equations or organized in the form of maps.

The governing equations, particularly the mass and energy balance equations, are consistent with those utilized for the transient model, as discussed in Section 4.2.3 and Paper IV. However, in this instance, the time derivative term is omitted to represent the steady state condition. Detailed behavioral correlations for all components are presented in Paper V. This comprehensive approach ensures a robust representation of the MGT system components, incorporating both fundamental mass and energy balance principles and component-specific behavioral correlations

### 4.4 Adaptation of the Physics-Based Model to Experimental Data

While physics-based models leverage thermodynamic equations and empirical maps and correlations, it is essential to acknowledge that some deviations from the model compared to an actual engine might be observed. These deviations can stem from a variety of factors as discussed in Paper V. To adapt the model to real-world data, it is imperative to fine-tune the imperfect maps and correlations implemented in the components. This involves the incorporation of suitable coefficients within these maps and correlations, followed by optimization to minimize the disparity between the model's predictions and experimental data.

Given that imperfections in the maps and correlations are linked to the steady state behavior of the engine, the tuning process primarily focuses on the steady state model. The adaptation journey initiates with the collection of comprehensive data from the MGT operating under diverse ambient conditions and various

power rates, thereby creating an extensive database. Subsequently, a fraction of this data (comprising 2 days of operation compared to the total of 21 days) is reserved for validating the tuned model. The remaining dataset is utilized for the tuning process, involving data cleaning to remove noise and selecting the steady state portions. The determination of steady state conditions is crucial, and Section 5.2.3 details the procedure for recognizing steady state time spans.

Following these steps, a stratified sampling method is employed to choose a subset of 100 data points from the overall population of steady state data. This ensures a well-rounded representation of diverse operating scenarios by dividing the entire dataset into strata based on different power output levels and ambient conditions, and then randomly selecting data points from each stratum.

The core of the adaptation process involves an iterative procedure where tuning coefficients are adjusted to minimize the difference between the 100 experimental data points and the model's results under corresponding conditions. This intricate process utilizes a GA and is executed in two levels due to the high number of parameters. Detailed equations and adaptation procedures are available in Paper V.

Upon concluding the adaptation, the adapted model undergoes validation using the reserved 2-day dataset. If the adapted model performs well with the validation set, the process is concluded. However, if discrepancies arise, adjustments to the measures used for selecting steady state time spans are crucial. Balancing the stringency of criteria is essential to avoid including transient conditions in the adaptation or having an insufficiently representative dataset. The entire adaptation process is visually presented in Figure 4.12.

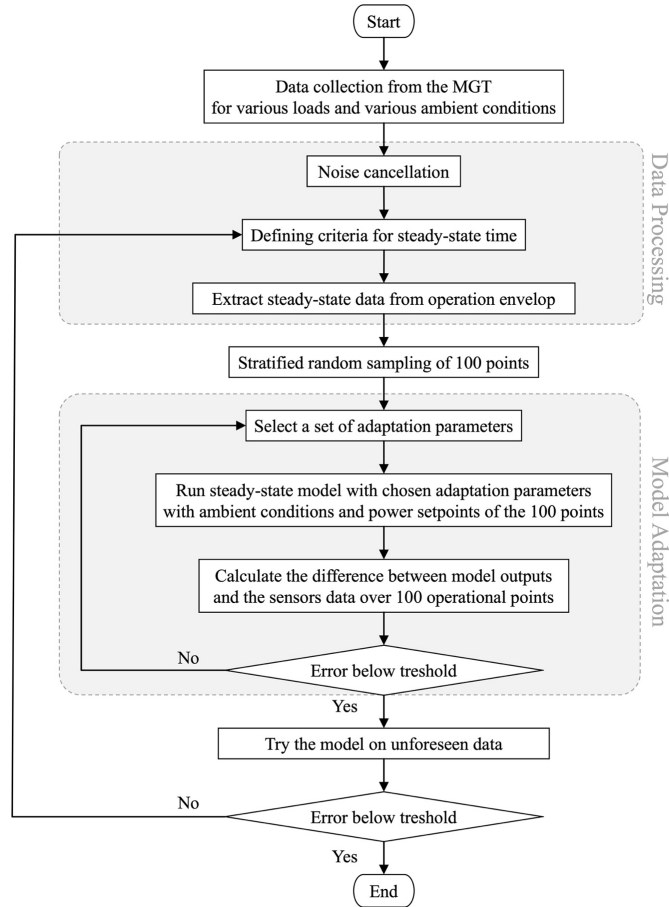


Figure 4.12 The process of steady state model adaptation to experimental data.

The impact of adaptation on error reduction is elucidated in Table 4.2, showcasing errors before and after adaptation for the dataset used in adaptation. Additionally, errors on the validation set are provided, demonstrating acceptable levels that affirm the effectiveness of the implemented methodology. The parameters are numerically subscripted, denoting the measurement location as per Figure 4.3.

As discussed earlier, the adaptation process plays a crucial role in fine-tuning the MGT model to experimental data under steady state conditions. The dynamic model, developed in

## Development of an MGT Model: Physics-Based Approach

Simscape, is inherently capable of operating under steady state conditions by excluding the time derivative term in thermodynamic equations. It is worth noting that the simulation period, even for the steady state model in Simscape, is considerably lengthier than its Python-based counterpart. Given the iterative nature of the adaptation process, the necessity for a swift model prompted the development of a fast Python-based steady state model specifically for this project.

Table 4.2 Model prediction error for target parameters before and after adaptation.

No.	Parameter	Original Model		Adapted Model		Adapted Model-validation set	
		MAE	mAE	MAE	mAE	MAE	mAE
1	$p_2$	0.0025 bar	0.0027 bar	0.0010 bar	0.0012 bar	0.0013 bar	0.0015 bar
2	$T_2$	275.99 °C	330.83°C	0.16 °C	0.64 °C	0.20 °C	0.94 °C
3	$p_3$	0.0634 bar	0.1534 bar	0.043 bar	0.069 bar	0.049 bar	0.071 bar
4	$T_3$	1.74 °C	5.20 °C	0.27 °C	0.86 °C	0.30 °C	0.89 °C
5	$T_4$	269.69°C	323.07 °C	3.54 °C	9.74 °C	3.80°C	9.98 °C
6	TOT	275.99 °C	330.83°C	1.79 °C	4.94 °C	2.00 °C	6.06 °C
7	P	30.60 kW	41.80 kW	0.66 kW	1.67 kW	0.72 kW	1.99 kW

Within the scope of this research, a dedicated steady state model and its corresponding adaptation process were devised for the AE-T100 engine, with detailed findings presented in Paper V. Subsequently, an adaptation was executed for the T100 engine, and the adaptation coefficients were incorporated into the Simscape model. This involved modifying all components utilized in the steady state model to align with the dynamic model. Notably, the air filter and the diffuser were omitted from the steady state model, and adjustments were made to the recuperator to align with the same correlation as the dynamic model. This strategic alignment ensures that the adaptation coefficients derived from the steady state model's adaptation process are directly applicable to the dynamic model. The outcomes of the adapted dynamic model, along with its comparison to experimental results, are presented in Paper IV.

## 4.5 Results

The investigation detailed in Paper IV delves into the dynamic intricacies of a fuel-flexible MGT under diverse operational scenarios, modeled by the dynamic model discussed in this chapter. The outcomes provide insights into the engine's performance, with particular emphasis on transient responses and varying fuel compositions.

The results of the development and adaptation of the steady state model are comprehensively expounded upon in Paper V. The steady state model, adeptly calibrated through adaptation to empirical data extracted from the AE-T100 MGT, yielded results that underscore its efficacy. The findings, spanning power production to temperature dynamics, demonstrate good accuracy, with a maximum power prediction error of less than 2 kW and less than 5 °C maximum error for TOT.

The physics-based model, fine-tuned with data from the T100 engine, serves as a valuable tool for investigating the engine's response to modifications, such as a switch in fuel type. Examining the MGT's operation under ISO conditions and a 100 kW load with pure methane and pure hydrogen reveals insights, as illustrated in Figure 4.13 and Figure 4.14. The model predicts a modest increase of less than 8 °C in TIT when transitioning from methane to hydrogen, accompanied by an elevation in pressure ratio and a 0.2 bar increment in combustor pressure.

## Development of an MGT Model: Physics-Based Approach

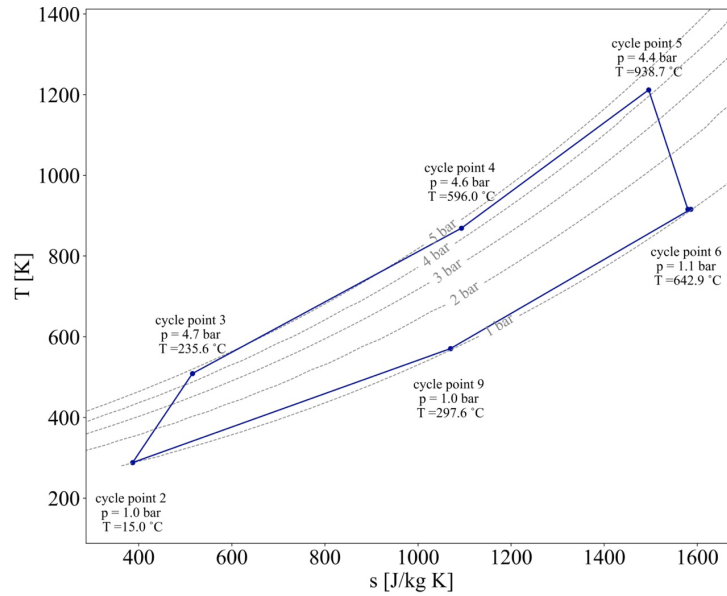


Figure 4.13 Cycle analysis of the MGT running with pure methane, producing 100 kW at ISO conditions.

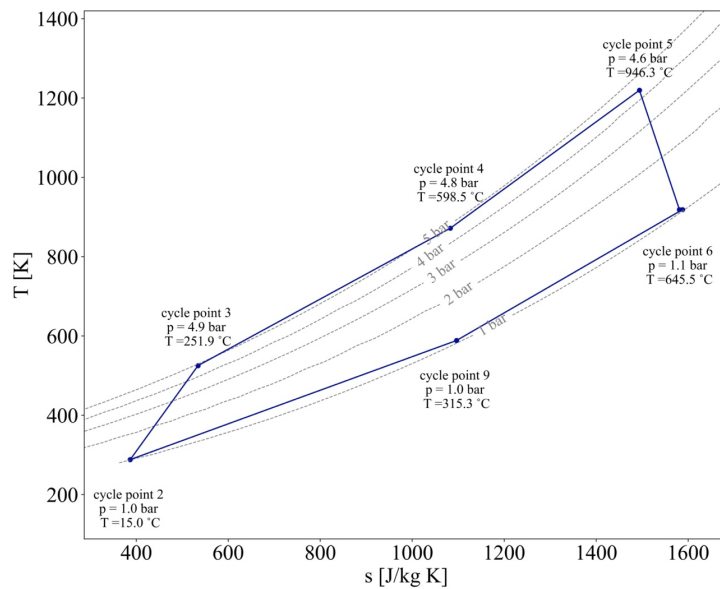


Figure 4.14 Cycle analysis of the MGT running with pure hydrogen, producing 100 kW at ISO conditions.

## Development of an MGT Model: Physics-Based Approach

This analysis is particularly pivotal during the conversion of the engine to hydrogen operation. The investigation extends to varying power rates, with a focus on the impact of replacing hydrogen with methane during part-load operation, as outlined in Table 4.3. The table encompasses key parameters, including TIT, TOT, relative rotational speed ( $N_{rel}$ ), and the thermodynamic efficiency ( $\eta_{th}$ ) of the MGT. Relative rotational speed is calculated in relation to the nominal speed of 70,000 rpm.

$$N_{rel} = N/N_{nom} \quad 4.12$$

The thermodynamic efficiency ( $\eta_{th}$ ) is evaluated based on the engine's produced power relative to the heat input:

$$\eta_{th} = \frac{P_{output}}{\dot{m}_f LHV_f} \quad 4.13$$

Table 4.3 Comparison of MGT operation with methane and hydrogen fuel with different power rates at ISO conditions.

P [kW]	Methane				Hydrogen			
	$N_{rel}$ [%]	TIT [°C]	TOT [°C]	$\eta_{th}$ [%]	$N_{rel}$ [%]	TIT [°C]	TOT [°C]	$\eta_{th}$ [%]
50	80.0	852.7	647.9	26.9	82.7	845.7	641.6	25.3
60	87.2	873.9	645.2	27.0	86.5	869.9	643.5	27.2
70	91.0	888.4	642.4	28.4	89.4	889.4	645.9	28.5
80	95.5	912.6	647.3	28.0	93.7	914.9	648.7	29.7
90	97.3	933.2	646.6	28.7	97.2	924.3	644.1	29.9
100	101.2	938.7	642.9	29.5	103.0	946.3	645.5	28.8

Notably, variations in TIT, TOT,  $N_{rel}$ , and  $\eta_{th}$  are non-uniform with changes in fuel type. While TIT is higher with hydrogen than methane at 100 kW, this trend does not persist at lower power rates. Similar non-uniform behavior is observed for engine efficiency, with instances where hydrogen outperforms methane and vice versa, depending on the power output. The same trend holds for TOT and  $N_{rel}$ .

Although these variations lack consistent patterns, the shift from methane to hydrogen induces discernible effects on engine



operation across all power rates, albeit to a minor extent. This assessment is crucial for anticipating any necessary preparations or precautions before experimental implementation. Particularly concerning is the potential impact on temperature and  $N_{rel}$ , both critical for engine safety and endurance. In the current scenario, the moderate increases in TIT and  $N_{rel}$  at 100 kW with hydrogen signify acceptable variations, ensuring operational integrity.

### 4.6 Conclusion

In this chapter, a comprehensive exploration of physics-based modeling for MGT systems was undertaken, employing MATLAB's Simscape for dynamic modeling and Python for steady state models. The dynamic model allowed a detailed examination of transient behaviors, responses to various conditions, and start-up/shutdown intricacies. Simscape's capacity for authentic physical connections was pivotal in constructing networks mirroring real-world system topology. The steady state model, integrating algebraic equations and iterative methodologies, mimicked MGT operational dynamics. The controller dynamically fine-tuned rotational speed and fuel flow for power requirements. Adaptation using a GA-enhanced model fidelity, making them potent instruments for predicting T100 MGT behavior under diverse scenarios. The dynamic model excels in capturing transient responses and adapting to varying fuel compositions, revealing load variations and fuel-specific nuances. The steady state model reproduces stable operational behavior, providing a sophisticated resource for predicting performance across power levels. Beyond T100, these models exhibit adaptability to alternative MGT systems, offering a robust platform for virtual experimentation, optimization, and analysis of performance and operational parameters.

## 5 Development of an MGT Model: Data-Driven Approach

The efficacy of physics-based models, as demonstrated in Chapter 4, has been well-established for achieving the first goal of this PhD research — designing an MGT with a hydrogen blend to enhance fuel flexibility. However, for system integration and operational optimization, the imperative of swift simulations allowing numerous iterations necessitates an exploration beyond physics-based models. In this context, data-driven methods emerge as a promising avenue, leveraging AI and sophisticated machine-learning tools with relevant physical system data to construct models that are not only rapid but also highly accurate.

In crafting models for an integrated system, precision in each constituent model is crucial for overall accuracy. This work emphasizes a delicate balance between high accuracy and computational efficiency. An intentional infrastructural approach ensures the versatility and applicability of the codes across diverse systems, aligning with the planned implementation of AI modeling. Detailed steps in creating reliable, fast data-driven models and their significant applications are explained in this chapter and upcoming Chapters 6 and 7.

### 5.1 The Importance of Data

Understanding the intricacies of data importance naturally leads to an exploration of the various modeling approaches in AI. It is imperative to delineate between AI, machine-learning, and data-driven methods. AI, the broader field, seeks to emulate human-like tasks. Machine-learning, integral to data-driven modeling, equips systems with the ability to learn and enhance performance over

time through data. Data-driven models consequently, rely on machine-learning algorithms to interpret vast datasets, extracting patterns, correlations, and insights that inform predictions and decisions. These models leverage datasets as their foundation, refining parameters autonomously through machine-learning techniques such as supervised learning, unsupervised learning, and reinforcement learning.

The accuracy of a data-driven model is intricately dependent not only on data treatment and modeling but also on the inherent quality and quantity of the data itself. The quality of data predominantly pertains to how it is collected. If sensor data becomes excessively noisy, traditional noise cancellation methods may fail to extract meaningful information, thereby reducing the quality of the resulting data and hindering the development of a functional model.

Concerning the quantity of data, dual interpretations emerge the count of sensors integrated into the system and the diversity of operational conditions from which the sensors have harvested data. The deployment of a greater number of sensors at strategic locations within the system yields richer insights into its functionality. However, pragmatic constraints such as cost limitations or logistical challenges may curtail the number and types of sensors employed. The selection of sensor types and their optimal placement becomes a pivotal facet of experimental work. While many systems host intrinsic sensors primarily designed for control and protection, additional sensors may be necessitated for a comprehensive system model.

Another pivotal dimension of data quantity revolves around the diversity of system operations captured by the sensors. The data-driven model's predictive capacity is restricted by the operational range covered during training. Therefore, for a model that adeptly forecasts system behavior across a wide operational spectrum, it is

imperative to curate a dataset that mirrors this diversity in system operation.

## 5.2 Data Preprocessing

The volume of data collected from an MGT can be substantial, depending on factors such as sensor count, data logging frequency, and test duration. The data, gathered by sensors installed on the MGT, is stored in hardware and made available in CSV format for subsequent model development. Before embarking on any modeling endeavors, the so-called “raw data” undergoes a crucial preprocessing procedure. This process, termed “preprocessing,” serves several objectives:

- Synchronizing data collected from different acquisition systems and at various frequencies;
- Creating a visual representation of the data to facilitate rapid operational assessments;
- Enhancing sensor comprehension by visually comparing data from different sensors;
- Filtering out noise from the collected data;
- Stratifying the operation data into steady state and transient time spans, serving modeling and condition monitoring purposes.

For this purpose, an “experimental data preprocessing code” has been developed using the Python language. The code is designed with a generic approach, ensuring its applicability to various testbeds, extending beyond MGTs to encompass different technologies. In this project, the code was specifically utilized to preprocess data collected from both MGTs at the Risavika Research Center and PSI.

The modules within the “experimental data preprocessing code” encompass:

- Data cleaning;
- Visualization;

- Steady state time recognition.

Subsequent sections provide detailed explanations of these modules.

## 5.2.1 Data Cleaning

### 5.2.1.1 Sensor Renaming

Enhancing readability is achievable through the adoption of concise names for sensor data that convey pertinent details about the sensor's type, installation location, and redundancy status. As the collected sensor data is inherently tagged with predefined names which does not contain such information, a step for modifying these names is required. To facilitate this process, an Excel file is supplied, delineating the old tags alongside their corresponding new names. In instances where redundant sensors occupy a specific location, a numerical identifier is appended to the sensor's name.

### 5.2.1.2 Outliers Identification

Upon renaming the sensors, the identification of redundant sensors in the same location is executed. Subsequently, an average value is computed to establish a mean measurement for that specific location, thereby mitigating localized variations that may impact the sensors' readings. The process involves the detection and exclusion of abnormal sensors among the redundant ones from the average value calculation. Abnormal sensor identification employs the computation of mean and standard deviation based on readings from all redundant sensors. Subsequently, the Z-score for each sensor reading is calculated using Eq. 5.1:

$$Z = \frac{X - \mu}{\sigma} \quad 5.1$$

In the context of sensor data processing, the Z-score calculation utilizes parameters such as  $X$  for the sensor value,  $\mu$  representing the mean of all sensor readings, and  $\sigma$  indicating the standard

deviation of all sensor readings. Z-scores falling beyond a predetermined range, often set at  $\pm 2$  or  $\pm 3$ , serve as indicators of outliers, potentially signaling a malfunctioning sensor.

Addressing identified outliers, specifically those associated with abnormal sensors, involves replacing the problematic values with the average value derived from other sensors in the same location. This corrective measure aims to enhance data consistency and mitigate the impact of malfunctioning sensors on subsequent analyses.

While the approach outlined above effectively identifies abnormalities in redundant sensors, it may not capture malfunctions in sensors lacking several redundant counterparts in a specific location. To address this, a data validation process is implemented to identify physically implausible values. For instance, in the case of temperature measurement, a predefined temperature range is established. If a sensor reports a temperature significantly outside this range, it is flagged as a potential malfunction, prompting further examination and corrective actions.

### 5.2.1.3 Resampling

In certain scenarios, data collection from a system may involve obtaining data at different frequencies or with time lags. For instance, in the MGT tests at the Risavika Research Center, two distinct data acquisition systems initiated recording at different times and concluded at varying intervals. To consolidate data from all sensors effectively, it is imperative to establish a unified data table with consistent time intervals. This necessitates a resampling process to synchronize the time steps across all datasets.

In this study, all data collected during a day of testing is organized within a folder. Subsequently, the code systematically scans through files containing data from diverse acquisition systems. It identifies time spans where all sensors have recorded data and selects the corresponding data for resampling. The resampling is

executed with a frequency equivalent to the smallest sampling rate (longest sampling time). The outcome is a comprehensive table featuring data from all sensors (columns) aligned with constant time intervals (rows), ensuring uniform temporal spacing between each data row.

### 5.2.1.4 Noise Cancellation

The sensor-collected data is susceptible to noise stemming from diverse sources, including electrical interference, sensor calibration discrepancies, and environmental conditions. This noise introduces random fluctuations and inaccuracies in the sensor measurements, potentially compromising the quality and reliability of the data. To mitigate these effects, various techniques, such as filtering, smoothing, and denoising algorithms (e.g., moving averages or median filters), have been implemented in this study to enhance the robustness of the reading data.

## 5.2.2 Visualization

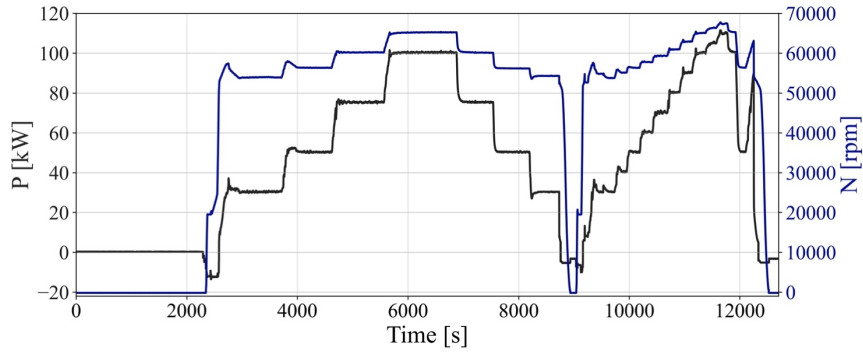
Visualization plays a crucial role in the analysis of MGT sensor data, offering insights into performance and operational characteristics. Effectively representing time-based data from sensors is essential for comprehending the dynamics of turbine operation.

Within the visualization module, an initial step involves plotting an overview of all signals against power output. Power output serves as a significant indicator of the engine's operation over time, being a primary parameter set by the operator. While power output stands as the module's default reference signal, users retain the flexibility to select any other signal as the reference for comparative plotting.

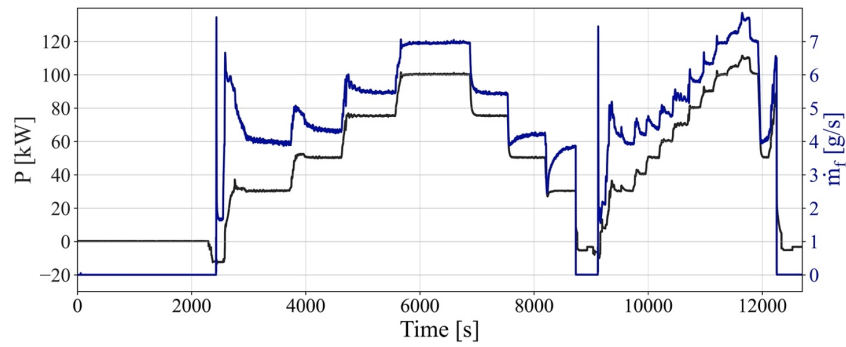
Figure 5.1 illustrates two instances of visualizations depicting rotational speed and fuel flow rate against power output. Following this comprehensive overview of the test's entire duration, the module offers diverse options for data inspection.

## Development of an MGT Model: Data-Driven Approach

Users can zoom in on specific periods, obtain spot value readings, and annotate plots based on chosen time intervals, among other features, as depicted in Figure 5.2



(a)



(b)

Figure 5.1 Visualization of experimental data, (a) engine rotational speed and (b) fuel flow rate, both plotted parallel to power output.

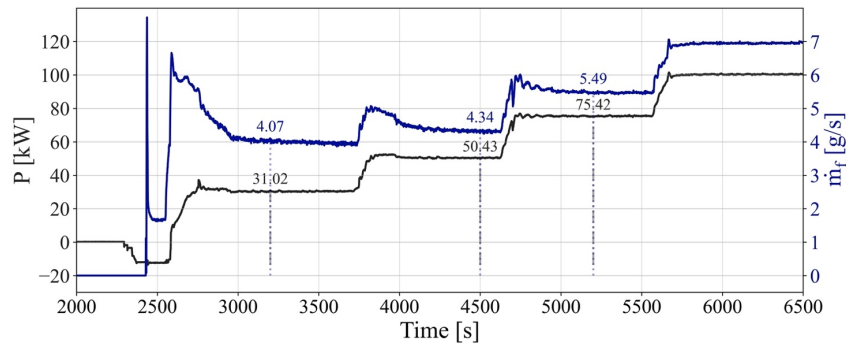


Figure 5.2 Monitoring points for easy reading of the visualized data.



### 5.2.3 Steady State Time Recognition

Throughout the MGT's operational cycle, spanning from start-up to shutdown, the engine experiences both transient and steady state conditions. The engine's transient behavior is influenced by input parameters and the engine's state at the previous time step, while the steady state is fully defined based on input parameters.

Similar to physics-based modeling, determining the type of the data-driven mode is crucial—whether it is a steady state model or dynamic. The methodology and model approach for steady state and dynamic models differ.

For a dynamic model, the time-based data, which has undergone the cleaning procedure outlined in Section 5.2.1, is sufficient. However, to develop a steady state model, the dataset used must exclusively represent steady state operations. To address this requirement, a steady state time-span recognition module is integrated into the data preprocessing program. This module can identify operational segments where the engine was in a steady state condition.

In Figure 5.3, a comprehensive representation of the engine's operational envelope is depicted. During certain periods, where the power output exhibits minimal variation, it suggests the engine is in a steady state operation. While this visualization offers a glimpse into when the engine is in a steady state and when it is not, attempting to visualize the entire dataset for recognition purposes is impractical. Furthermore, confirming if the engine is genuinely in a steady state necessitates the evaluation of all sensors to ensure consistent readings.

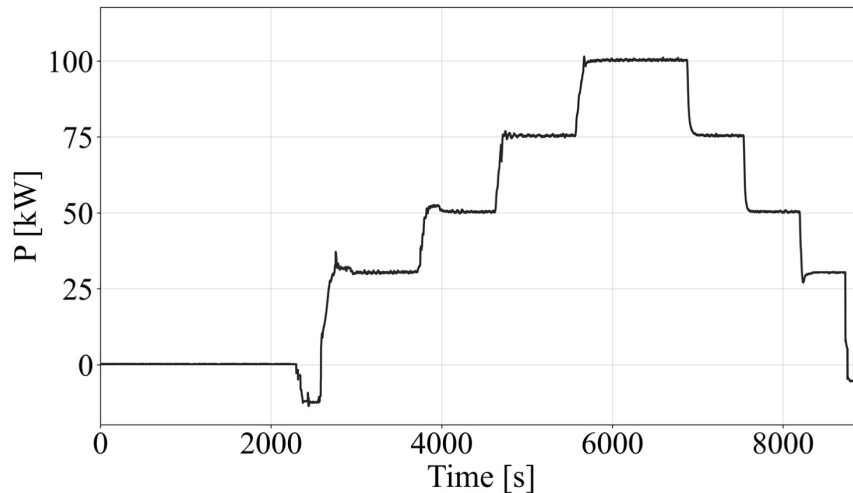


Figure 5.3 A complete operational envelope for an MGT from start-up to shutdown.

In this study, the identification of the beginning and conclusion of steady state periods is facilitated through a code that follows a procedure:

- The algorithm initiates its evaluation from the first data point in the database, proceeding sequentially toward the last entry, to determine time intervals representing steady state operation. These intervals are independently identified for each sensor by the code and subsequently consolidated to define common steady state conditions.
- The user defines an acceptable tolerance for each sensor, indicating the permissible variation during steady state conditions. Commencing from any point, the algorithm selects a window where all data points fall within the specified tolerance margin, exemplified in Figure 5.4 (a) from point A to point B.
- Subsequently, all data points within the chosen window (A to B) are monitored, and their deviation from the mean value of all points within the same interval is calculated. Points with deviations exceeding the accepted margin are discarded. In Figure 5.4 (a), points between A and A' and between B and B'

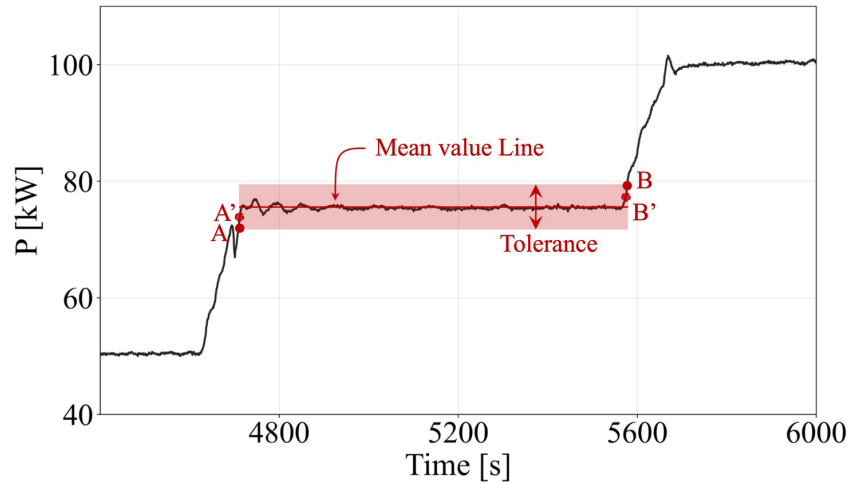
exhibit high deviations, leaving the remaining points between A' and B' representing steady state operation concerning power output.

- The algorithm then proceeds to the next evaluation window, initiating from the previous window's endpoint (B in Figure 5.4), and extending to the next point (C in Figure 5.4 (b)) within the tolerance range.
- The deviation calculation is repeated as the algorithm progresses from point B to C. During transient data, none of the points typically exhibit low deviation from the mean, except for those precisely on the mean value or in close proximity. In such cases, the length of the time span with small deviations becomes a small fraction of the entire window's length, signaling transient operation. Specifically, the duration of the small deviation period (A' to B' in Figure 5.4 (a)) must exceed 50% of the tolerance window's length (A to B in Figure 5.4 (a)) for the time interval to be categorized as steady state.

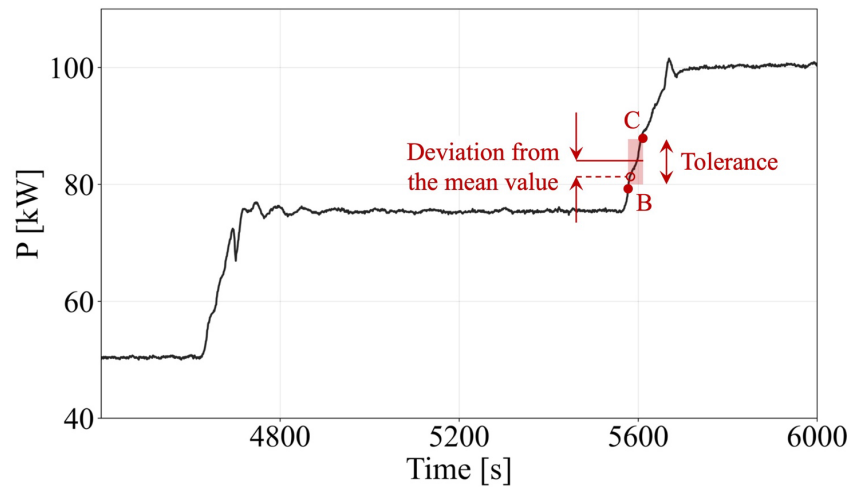
The comprehensive dataset is systematically analyzed by the implemented module, sequentially processing each signal. This procedure identifies periods characterized by steady state conditions for each specific sensor. Subsequently, common time spans shared across all signals are selected, representing the steady state operation of the MGT.

It is crucial to highlight that appropriate tolerance and deviation margin values must be defined by the user for each parameter. This determination often involves an iterative process, requiring a few trial-and-error iterations to identify the optimal combination which essentially defines the steady state criteria. Notably, these values are not universally applicable to the same parameters across different engines, as each engine may exhibit varying levels of oscillations and transient slopes. Therefore, the careful selection of

appropriate values is an essential prerequisite for executing the steady state recognition module



(a)



(b)

Figure 5.4 Functionality of the steady state time recognizer module.

The steady state time spans identified through this module serve to separate the steady state portion from the entire dataset, effectively isolating transient operations. Consequently, a new database, exclusively comprising steady state engine operation data, is

meticulously crafted and ready for utilization in modeling endeavors.

### 5.3 Development of a Data-Driven Model

After the process of data cleaning and the removal of outliers, two distinct datasets were generated. One dataset encompasses the entire sensor data, while the other specifically captures instances of steady state conditions. The subsequent steps entail feature selection, normalization, and the division of the datasets into training and testing sets.

#### 5.3.1 Feature Selection

Feature selection is a pivotal step in the modeling process, guiding the identification of variables that significantly contribute to the model's informativeness while excluding less pertinent or redundant features. This step is crucial for optimizing both model efficiency and interpretability.

For GT sensor data, a judicious selection of features not only enhances model efficiency but also unveils key insights into the turbine's performance dynamics. While various data analysis methods exist to identify crucial features for model development, this work relies on domain knowledge to pinpoint the most relevant parameters.

In essence, the inputs and outputs of the model were predefined based on the specific requirements of creating a replica of the actual system. For an MGT, operational decisions stem from the operator's choices, typically involving power output selection. In the case of the new hydrogen-fuel engine discussed in Chapter 3, user decisions also encompass the ratio of hydrogen in the hydrogen/methane mix.

Beyond operator decisions, ambient conditions significantly influence engine operation. Factors such as pressure, temperature, and relative humidity impact the properties of the air entering the

engine, necessitating their inclusion in the model's input set. Fuel conditions, including pressure and temperature upon entering the MGT, are also vital and form part of the input parameters.

The remaining parameters are outcomes of the engine's operation and are incorporated into the output list. This encompasses variables like fuel flow rate, rotational speed, and flow pressure and temperature throughout the cycle, wherever measurements are available.

### 5.3.2 Normalization

The dataset is refined to incorporate features relevant to the specified inputs and outputs. Prior to commencing model training with the data, a normalization process is applied to standardize the values of these features. Utilizing the min-max scaling technique ensures that all variables are presented on a consistent scale. This uniform scaling is pivotal for expediting convergence during training and preventing certain features from exerting disproportionate influence over others, ensuring consistent model performance.

The min-max scaling technique, as denoted by Eq. 5.2, involves utilizing  $y$  as any parameter within the database at a given time. Additionally,  $y_{\min}$  and  $y_{\max}$  represent the minimum and maximum values of the same parameter across the entire database.

$$y_{\text{scaled}} = \frac{y - y_{\min}}{y_{\max} - y_{\min}} \quad 5.2$$

This approach recalibrates the data to a range between 0 and 1. It ensured that all variables made equitable contributions to the data-driven models, effectively preventing any individual feature from exerting disproportionate influence over the analysis.

### 5.3.3 Train-Test Split

Instead of solely training on the entire dataset, 20% of the data is chosen randomly and reserved for testing. This approach assesses

the model's ability to generalize to unseen data, extending its performance beyond the training set. To further mitigate overfitting, k-fold cross-validation is employed. The training set is divided into k subsets, using k-1 for training and one for validation iteratively across k rounds. This repeated validation minimizes the risk of the model fitting noise, ensuring a reliable evaluation of its generalization performance.

### 5.3.4 Model Selection

In the context of data-driven modeling for MGTs, various methodologies are worth considering. Among the available machine-learning methods, ANNs stand out due to their ability to capture non-linear behavior—a critical feature given the intricate, non-linear relationships inherent in MGT systems. ANNs excel at accurately representing these complex interactions, making them well-suited for modeling the system's behavior.

Furthermore, ANNs demonstrate the ability to adapt seamlessly and acquire knowledge from available data with minimal intervention. Since the performance of MGTs is closely tied to their health condition, operational characteristics may evolve. This evolution introduces the potential for variance between the model's performance and the actual engine state, necessitating a re-adaptation process. This involves retraining the model to align with the changing engine behavior.

ANNs aim to emulate the intricate functions of the human brain's neural networks. In a fully connected computational system, numerous artificial neurons constitute an ANN, processing input data to generate output signals. The network's core features interconnected neurons organized into layers. In a fully connected architecture, neurons within a layer establish connections with every neuron in the preceding layer, characterized by adjustable weights and bias terms. These parameters play a crucial role in enhancing ANN performance, complementing the weighted

summation of inputs during training. The weighted inputs then undergo aggregation and processing through an activation function, whose nature varies based on the specific problem addressed.

Figure 5.5 (a) illustrates an artificial neuron, which not only receives inputs from the preceding layer's neurons but also integrates a bias term. Both weights and the bias term are adjustable during training, enhancing the adaptability and overall performance of the ANN to effectively model the relationship between input and output data.

The fundamental architecture of an ANN comprises an input layer and an output layer. However, introducing intermediary hidden layers strategically between the input and output layers can markedly enhance the model's efficacy. Figure 5.5 (b) visually represents a multi-layer perceptron with two hidden layers. In this configuration, the neural network features 4 inputs, 8 neurons in the first hidden layer, 6 neurons in the second hidden layer, and 2 outputs. The allocation of neurons to the input and output layers depends on the system's complexity, mirroring the required number of inputs and outputs [132].

While expanding layers facilitates modeling more intricate complexities, it also increases susceptibility to overfitting. Overfitting occurs when the model excessively specializes in capturing training data nuances, potentially hindering generalization to new, unobserved data. To maintain an ANN model's effective generalization, careful measures must be implemented in both the construction and training phases of the model. These measures involve applying regularization techniques to control model complexity, as well as utilizing cross-validation to evaluate performance on previously unseen data. By thoughtfully integrating these elements, ANN models achieve a harmonious balance between intricacy and generalization, ensuring reliability in real-world applications.



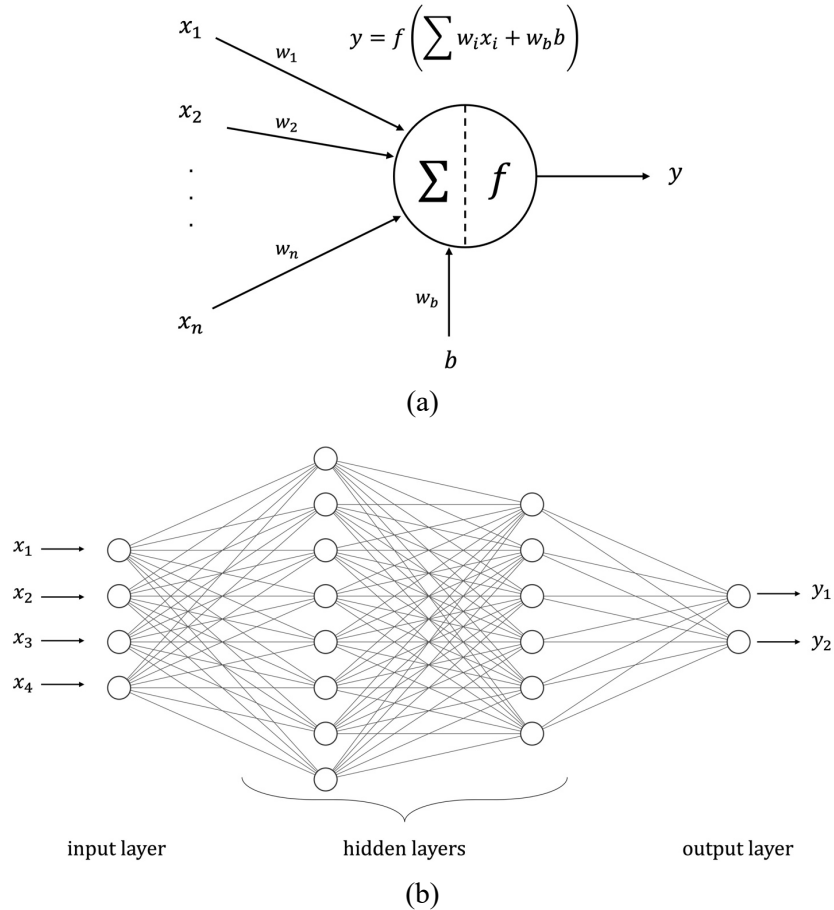


Figure 5.5 Structure of (a) an artificial neuron and (b) a multilayer ANN.

For transient-based modeling, NARX models emerge as another valuable tool. NARX models excel in capturing the dynamic responses of complex systems, crucial for modeling transient behaviors in engineering applications. Effectively handling time-dependent processes, NARX models are essential for understanding and predicting changes in MGT operation during transitions. The NARX architecture leverages both past system states and external input information to capture transient responses, enhancing accuracy and adaptability in MGT dynamic models. Figure 5.6 provides a schematic view of a NARX model.

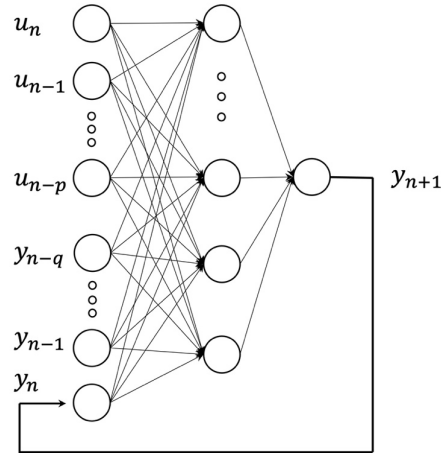


Figure 5.6 Schematic of a NARX model.

The incorporation of ANN for steady state operations and NARX models for transient behavior form a well-rounded methodology, providing a comprehensive understanding of MGT operation that covers both steady state and dynamic behaviors. Employing these modeling approaches, it becomes easier to comprehend MGT performance across various operational scenarios, ultimately enhancing the control, optimization, and decision-making effectiveness of MGTs.

### 5.3.5 Hyperparameter Optimization

The complexity of an ANN model is intricately linked to various key factors, encompassing the number of layers and neurons, and the selection of activation functions for each layer. Together, these factors define the hyperparameters of the model. However, finding the optimal combination of these hyperparameters is a time-consuming task, especially given the vast array of options and configurations. This challenge is particularly pronounced in deep learning ANNs, known for their intricate architectural designs and deep layers, intensifying the complexity of hyperparameter optimization.

Manual fine-tuning of hyperparameters becomes impractical as ANNs grow in scale and complexity. The inherent subjectivity in human-driven selection can introduce biases and hinder the search for optimal configurations. Moreover, as the number of parameters and their interactions increase, achieving peak performance becomes more challenging. Hence, adopting a systematic and automated approach becomes imperative.

Hyperparameter optimization offers a systematic, data-driven solution to these challenges. In this work, Bayesian optimization is employed as a potent strategy for navigating the complex hyperparameter landscape in the quest for superior ANNs. This approach involves constructing a probabilistic model of the target function, iteratively refined through Bayesian inference, often based on Gaussian processes.

The essence of Bayesian optimization lies in balancing exploration and exploitation. By integrating the probabilistic model with an acquisition function, it strategically selects the next set of hyperparameters for evaluation, significantly reducing the number of function evaluations required, and enhancing the selection of hyperparameters.

To ensure model convergence and mitigate overfitting, various techniques, including a learning rate schedule, early stopping, and continuous validation loss monitoring, are incorporated during training. The resulting model, with the optimized configuration and learning parameters, is presented in Table 5.1. This model, tailored for the fuel-flexible MGT, includes the operator's decision on fuel combination in the input parameter list. The outputs are the fuel flow rate and the exhaust gas temperature, providing information about the power and heat performance of the engine. Engine efficiency can be calculated from the predicted fuel flow rate, while the exhaust gas temperature offers insights into the heating potential of the hot gas leaving the engine.

## Development of an MGT Model: Data-Driven Approach

Table 5.1 Optimized hyperparameters for the ANN and NARX model of the MGT.

inputs	$P_{MGT, dem}, FR, T_{amb}, P_{amb}, RH, T_f, P_f$
outputs	$\dot{m}_f, T_{eg}$
No. of neurons hidden layers	102, 107, 48
Activation function hidden layers	Linear, ReLU, ReLU
Learning rate	1.0
Optimizer	SGD

As it is presented in Table 5.1, the activation functions for the model are linear (also known as identity function) and ReLU (rectified linear unit), which are presented in Eq. 5.3 and 5.4. The optimization function of training is stochastic gradient descent (SGD) which updates model weights by iteratively computing gradients of the loss based on randomly selected mini-batches from the training data, facilitating faster convergence and scalability to large datasets.

$$\text{Linear}(x) = x \quad 5.3$$

$$\text{ReLU}(x) = \max(0, x) \quad 5.4$$

While more output parameters are feasible, the presented model includes the principal parameters for outputs, which proved sufficient for integration purposes and microgrid optimization (Chapter 6). Numerous models were developed during this work for different purposes, accommodating trustable sensor data for diverse output predictions. The simplicity of the presented model aligns with its suitability for integration and microgrid optimization, focusing on the fundamental parameters necessary for the intended applications.

### 5.3.6 Model Training

Upon the determination of optimal configurations, the ANNs undergo training using the backpropagation algorithm. This iterative process adjusts the weights and biases based on inputs and desired outputs, gradually aligning the model's output with the expected results. As discussed, cross-validation is implemented to prevent overfitting, with approximately 80% of the data reserved

for training and 20% for testing. The selected models are trained on the training set, with the loss function being minimized by the chosen optimizer, SGD. Care is taken to avoid overfitting by implementing early stopping and regularization methods, thereby ensuring the models' ability to generalize to unseen data.

#### 5.4 Performance Evaluation Metrics

The performance of the developed ANN models has been rigorously examined. This examination is carried out on a dedicated test set, distinct from the training dataset, to ensure an objective assessment of the model's predictive capabilities. The evaluation encompasses a range of error metrics; the mean absolute error (MAE) serves as an essential metric to quantify the average magnitude of errors in the model's predictions. It is calculated as follows:

$$\text{MAE} = \frac{1}{n} \sum_{i=1}^n |y_i - \hat{y}_i| \quad 5.5$$

Where  $n$  represents the number of data points and  $y$  and  $\hat{y}$  are actual and predicted value of parameters. Similarly, root mean square error (RMSE) could be calculated:

$$\text{RMSE} = \sqrt{\frac{1}{n} \sum_{i=1}^n (y_i - \hat{y}_i)^2} \quad 5.6$$

The RSME provides a measure of the overall magnitude of errors, giving weight to larger deviations.

The mean absolute percentage error (MAPE) offers insights into the average percentage discrepancies between the model's predictions and observed data. It is expressed as:

$$\text{MAPE} = \frac{1}{n} \sum_{i=1}^n \left| \frac{y_i - \hat{y}_i}{y_i} \right| \quad 5.7$$

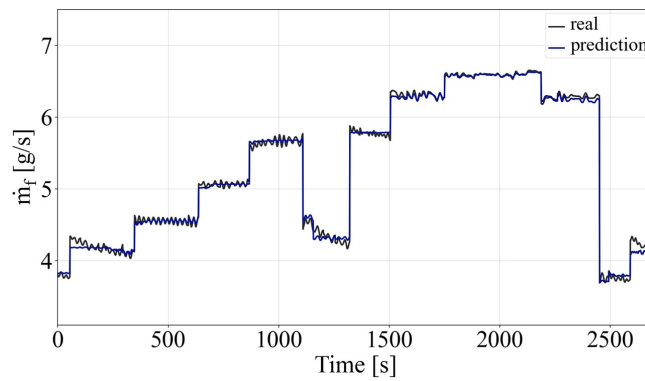
## Development of an MGT Model: Data-Driven Approach

Employing all three types of average errors—MAE, RMSE, and MAPE—is helpful as each serves a distinct purpose in evaluating the model’s performance. MAE offers insight into the average magnitude of errors, RMSE captures the overall error magnitude with emphasis on larger deviations, and MAPE measures the average percentage discrepancies. These errors together with the maximum absolute error (max AE) of the predicted parameters for both models are presented in Table 5.2. Visual illustration of the models’ accuracy is provided in Figure 5.7 and Figure 5.8.

The results demonstrate a high level of accuracy in predicting parameters, with both models achieving MAPE values of less than 2%. Notably, the steady state model outperforms the transient model, indicating the complexities associated with modeling transient behaviors.

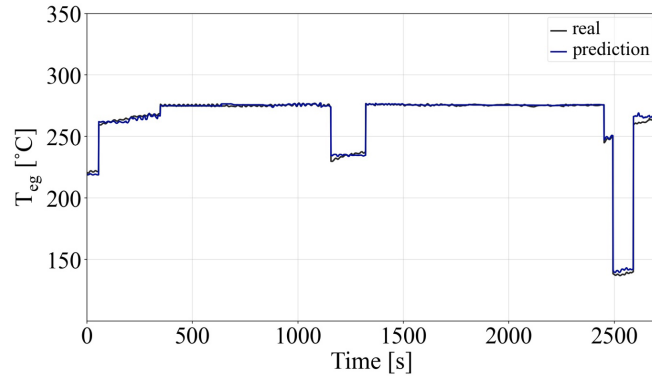
Table 5.2 Evaluation of ANN and NARX model performance on test data.

	Steady state model		Transient model	
	$\dot{m}_f$	$T_{eg}$	$\dot{m}_f$	$T_{eg}$
Max AE	0.67 g/s	19.63 K	1.73 g/s	23.2 K
MAE	0.06 g/s	2.92 K	0.14 g/s	5.2 K
RMSE	0.09 g/s	6.18 K	0.38 g/s	8.12 K
MAPE	1.17 %	0.5 %	1.78 %	0.98 %



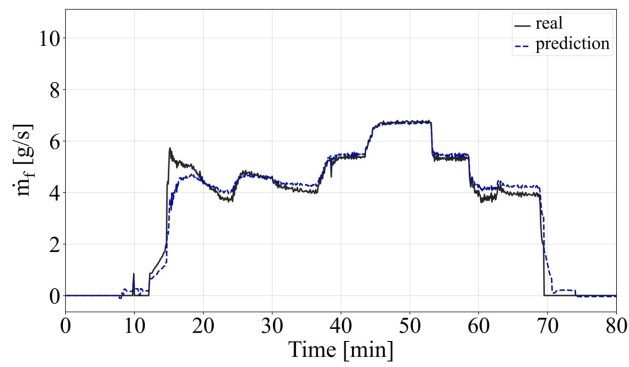
(a)

## Development of an MGT Model: Data-Driven Approach

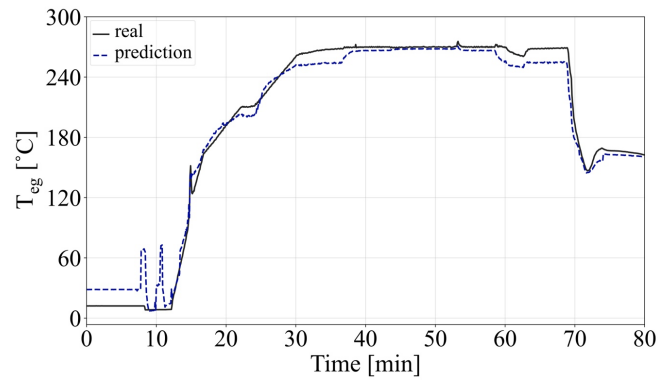


(b)

Figure 5.7 Visualization of the prediction accuracy for the ANN model, (a) fuel flow rate, (b) exhaust gas temperature.



(a)



(b)

Figure 5.8 Visualization of the prediction accuracy for the NARX model, (a) fuel flow rate, (b) exhaust gas temperature.

## 5.5 Conclusion

This chapter introduced a robust data-driven framework developed for the modeling of MGTs. It comprised key elements, including steady state time recognition, data-driven model development, and systematic hyperparameter optimization.

A distinctive feature of the framework was the inclusion of a module dedicated to recognizing steady state time spans. This facilitated the precise identification of stable operational segments within MGT performance data, ensuring data integrity—a prerequisite for accurate modeling. Leveraging ANNs for steady state modeling and NARX models for transient behavior, the framework adeptly captured intricate interactions between these operational modes.

The significance of hyperparameter optimization was underscored as an integral facet of the framework. It provided an automated mechanism for fine-tuning numerous ANN configurations, with Bayesian optimization, grounded in probabilistic modeling, navigating this intricate parameter space. The resultant optimized models consistently demonstrated high accuracy, as corroborated by robust evaluation metrics, including MAE, RMSE, and MAPE, consistently yielding MAPE values below 2%.

Moreover, the developed codes and tools exhibited infrastructural versatility, extending applicability beyond MGTs to encompass diverse systems such as heat pumps, wind turbines, and solar panels. This comprehensive approach facilitates the modeling of various components within a microgrid, contributing to the development of a unified model that spans diverse energy systems.



## 6 Optimization of MGT Operation in an Integrated System

This chapter expands on the integration of MGT within a microgrid, leveraging the AI-based model development discussed in the preceding chapter. The objective is to develop a precise model for a conceptual microgrid, incorporating renewable sources, an MGT, and a storage system. The model includes meteorological predictions, demand forecasts, and a robust governing platform. The primary focus is on optimizing the operation of the conceptual microgrid serving an office building in Stavanger, Norway. While the microgrid is conceptual, each component's model is empirically supported by over a year's operational data. The study explores various scenarios over a week, offering an authentic representation of microgrid dynamics and emphasizing the vital role of integrated management systems and optimizers. This chapter serves as a review and introduction to the broader study detailed in Paper VI.

### 6.1 Microgrid System Description

This chapter delves into the intricacies of a microgrid system designed to supply electricity and heat to a municipal office building by integrating renewable (wind turbines) with conventional energy sources (MGT) and an energy storage unit (electrolyzer and hydrogen tank). The microgrid functions autonomously in “island mode” and can connect to the grid for imports or exports in “grid mode.”

The consumer is a building in Stavanger city center, Norway, hosting the city's public pool and municipal offices, as shown in Figure 6.1. Operational data, measured at five-minute intervals,

include comprehensive records of electricity and heat consumption of the building.



Figure 6.1 The building that represents the heat and power demands of the microgrid.

The microgrid's wind turbines are WTN250, each featuring a nominal output of 250 kW, and provide reliable performance over a 25-year lifespan. They start generating power at 4 m/s (cut-in wind speed), achieve their rated output at 14 m/s, and shut down safely at 25 m/s (cut-off wind speed). Operating at 26 to 40 rpm, the fixed blade pitch angle is -20 degrees. The wind turbine and its power curve are illustrated in Figure 6.2.

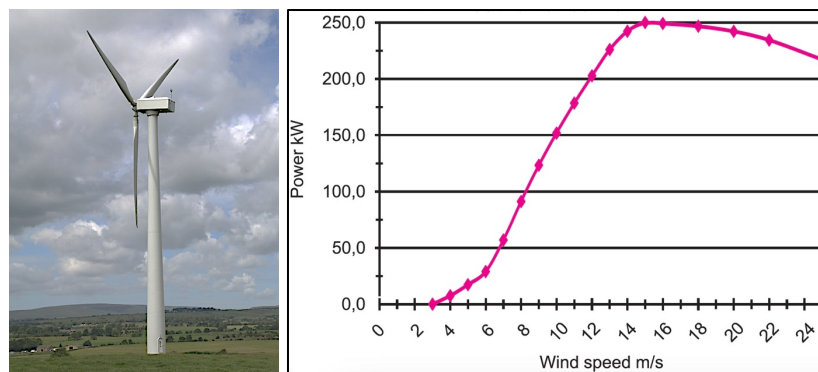


Figure 6.2 WTN250 wind turbine of the microgrid and its power curve [133].

The MGT, adaptable to part-load conditions, offers a nominal output of 100 kW and operates on a dual-fuel blend of natural gas and hydrogen, as discussed in Chapter 3.



regulations, and predictions of fuel and electricity prices to make optimal operational decisions. Advanced machine-learning techniques underpin an AI-based model, explored in subsequent sections, offering insights to optimize the microgrid’s performance across diverse scenarios. Figure 6.3 illustrates the interconnected components of the microgrid, emphasizing the importance of accurate forecasting, efficient optimization algorithms, and AI-based models for ensuring economic viability and environmental sustainability.

## 6.2 Modeling the Microgrid

A data-driven approach was employed to model individual components of the microgrid, creating an integrated data-driven model of the whole system. The architecture of the ANN models for wind turbines and the MGT is depicted in Figure 6.4, showcasing input-output relationships and the optimized model configuration.

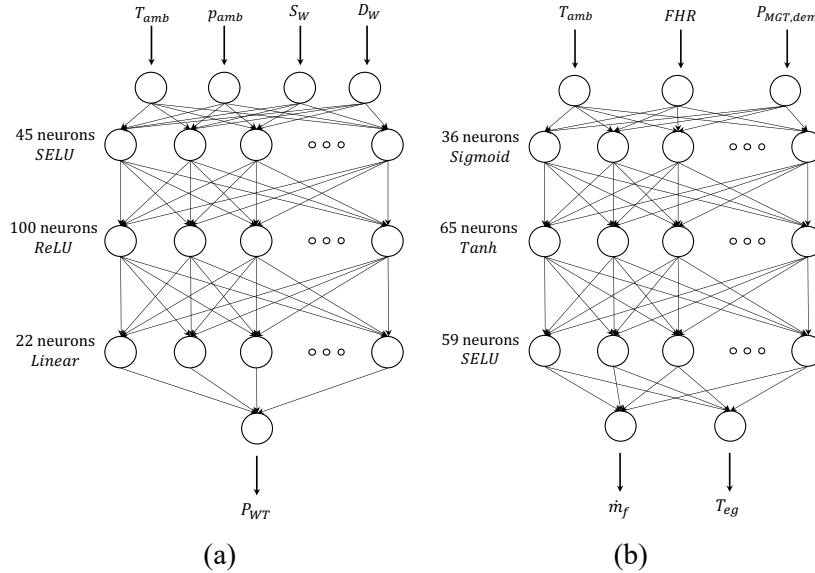


Figure 6.4 The ANN models for (a) the wind turbines, and (b) the MGT of the microgrid.

The wind turbine model utilizes inputs like ambient temperature ( $T_{amb}$ ), pressure ( $p_{amb}$ ), wind speed ( $S_W$ ), and direction ( $D_W$ ), to predict power output ( $P_{WT}$ ). The MGT model considers inputs such as ambient temperature ( $T_{amb}$ ), power set point ( $P_{MGT}$ ), and fuel heat ratio (FHR) which determines the outputs of the model that are consumed fuel flow rate ( $\dot{m}_f$ ) and exhaust gas temperature ( $T_{eg}$ ). The fuel heat ratio determines the natural gas and hydrogen blend in the fuel:

$$FHR = \frac{\dot{m}_{NG} \times LHV_{NG}}{\dot{m}_{NG} \times LHV_{NG} + \dot{m}_{H_2} \times LHV_{H_2}} \quad 6.1$$

As outlined in Chapter 5, the MGT outputs offer sufficient insights for its operation. However, the model used here features fewer inputs compared to the one presented in Chapter 5. This simplification results in a more concise version that includes only highly crucial input parameters.

Bayesian optimization guided model configuration, selecting Adadelta as the optimizer with specific learning rates. Activation functions include SELU, ReLU, Linear, Sigmoid, and hyperbolic tangent. The definition of activation functions is provided in Paper VI.

The electrolyzer's hydrogen production rate prediction considers its efficiency, influenced by operating power, as expressed in Eq. 6.2 and 6.3 [135].

$$\dot{m}_{H_2} = \frac{\eta_{ELZ} \times P_{ELZ}}{LHV_{H_2}} \quad 6.2$$

$$\eta_{ELZ} = +6 \times 10^{-7} \left( \frac{P_{ELZ}}{P_{ELZ,max}} \right)^3 - 0.0001 \left( \frac{P_{ELZ}}{P_{ELZ,max}} \right)^2 + 0.0085 \frac{P_{ELZ}}{P_{ELZ,max}} + 0.3995 \quad 6.3$$

Building energy demand prediction requires an LSTM architecture due to its effectiveness in capturing temporal transitions. The LSTM neuron addresses long-term dependency challenges in data

sequences. Training the LSTM model involves tuning weights and bias terms in various gates and memory cells.

The building's energy demand prediction model integrates historical data from the past two days and online data, forecasting hourly power and heat demand. Bayesian optimization determines the model's structure and activation function. Figure 6.5 illustrates the structure of the model developed for building demand prediction.

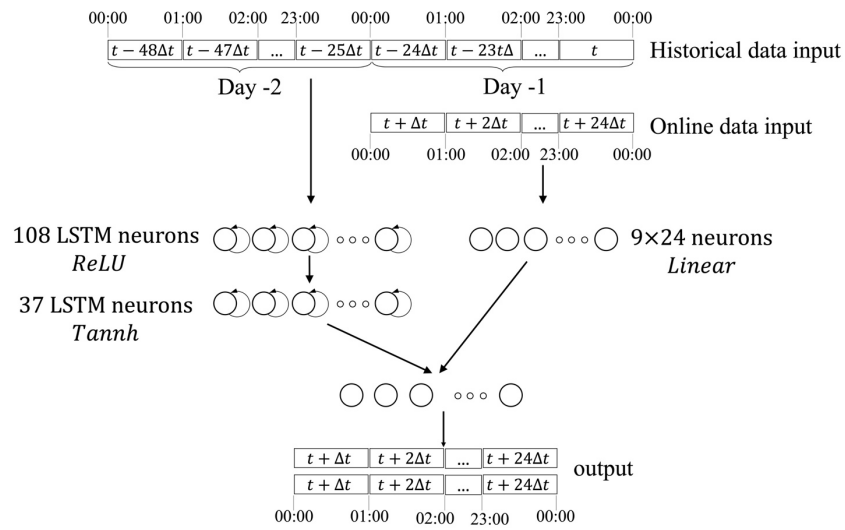


Figure 6.5. The model for heat and power demand prediction in the consumer building of the microgrid.

Table 6.1 presents an overview of errors for wind turbine, MGT, electrolyzer, and building demand models on the test dataset, demonstrating their accuracy.

Table 6.1 The error of the models' predictions on the test data set.

	Parameter	mAE	MAE	RSME	MAPE
Wind turbine	$P_{WT}$	27.2 [kW]	6.67 [kW]	11.35 [kW]	1.27 %
Micro Gas Turbine	$\dot{m}_f$	2.3 [g/s]	0.14 [g/s]	0.38 [g/s]	0.25 %
Micro Gas Turbine	$T_{eg}$	24.0 [°C]	7.4 [°C]	11.9 [°C]	0.19 %
Electrolyzer	$\eta_{ELZ}$	0.0296 [-]	0.0120 [-]	0.0179 [-]	2.61%
Consumer building	$P_{dem}$	12.01 [kW]	8.00 [kW]	9.02 [kW]	11.53%
Consumer building	$Q_{dem}$	7.03 [kW]	4.91 [kW]	5.22 [kW]	9.38%

The operational management system operates in a predefined rule mode and an intelligent mode, utilizing predictions to optimize operations. The upcoming sections delve into the investigation of both management scenarios, emphasizing the significance of accurate forecasting, efficient optimization algorithms, and AI-based models in ensuring the microgrid's economic viability and environmental sustainability.

### 6.3 Operation of the Microgrid without Smart Management

The condition-based operation managed manually without an optimizer, follows predefined rules for microgrid management. These rules consider real-time conditions, aligning power, heat demands, and renewable energy production. Key principles include minimizing MGT usage, storing excess wind power when generation exceeds demand, and maximizing hydrogen content in the fuel blend. The primary aim is to balance energy consumption, avoiding unnecessary generation from the MGT. In case of a shortfall, the MGT operates at the lowest power, with import considered only in extreme circumstances. The sequence of rules is predefined for each hour, and strategically designed for optimal economic outcomes.

### 6.4 Operation of the Microgrid with Smart Management

Microgrid optimization strives to minimize costs and emissions while ensuring adaptability across diverse operational scenarios. The optimization process spans a week, considering hourly intervals, and involves critical elements such as weather forecasts, wind turbine power calculations, and consumer power and heat demand predictions. This comprehensive approach is vital for

maintaining the microgrid's effective operation over varying conditions.

The initiation of the optimization process begins with obtaining an hourly weather forecast for the upcoming day. Leveraging this forecast, the power output of the wind turbine is calculated for the next 24 hours. Concurrently, predictions for consumer power and heat demand are derived from historical data, integrating both into a demand prediction model. To manage the microgrid effectively, the optimization process determines crucial parameters for the dispatchable units, including the MGT and electrolyzer.

For the MGT the power output and the choice of fuel combination have to be determined by the optimizer, both bound to the upper and lower limits:

$$P_{MGT} = [P_{MGT_1}, P_{MGT_2}, \dots, P_{MGT_{24}}]; \quad 6.4$$

$$20 < P_{MGT_i} < 100$$

$$FHR_{MGT} = [FHR_{MGT_1}, FHR_{MGT_2}, \dots, FHR_{MGT_{24}}]; \quad 6.5$$

$$0 < FHR_{MGT_i} < 1$$

The objective of the optimization is to minimize operational costs. The most significant cost contributor is the MGT, taking into account natural gas prices, associated CO<sub>2</sub> taxes, and maintenance costs. The maintenance costs for the MGT are determined by its operational lifetime, quantifying the cost of power produced during a time step.

$$Cost_{MGT} = Cost_{NG} + Cost_{tax,CO_2} + Cost_{MGT,maint} \quad 6.6$$

During grid mode operation, where the microgrid interacts with the external grid, both revenue and costs come into play. The cost of purchasing or selling electricity is contingent upon specific hours, with the grid tending to purchase electricity from the microgrid close to the spot price.

$$Cost_{el} = El_{imp} \times pr_{el,buy} - El_{exp} \times pr_{el,sell} \quad 6.7$$



The total cost of microgrid operation is formulated by summing up costs associated with each subsystem, including the MGT (Eq. 6.6), the operation and maintenance costs of the wind turbines, electrolyzer, and compressor, as well as the net electricity cost (Eq. 6.7):

$$\text{Cost}_{\text{total}} = \text{Cost}_{\text{MGT}} + \text{Cost}_{\text{WT}} + \text{Cost}_{\text{ELZ}} + \text{Cost}_{\text{cmp}} + \text{Cost}_{\text{el}} \quad 6.8$$

The primary focus of the objective function lies in the total cost (Eq. 6.8), but additional parameters contribute to the holistic optimization. Constraints on hydrogen consumption, dependent on availability, and incentives for preservation are pivotal factors. The latter is related to the optimizer's endeavor to recognize the future value of hydrogen by incorporating incentives to save or use it if the present value is higher. These incentives vary in island and grid modes, where hydrogen offsets natural gas costs or serves power generation and export. Eq. 4.10 shows the objective value to be minimized by the optimizer.

$$\text{OV} = \text{Cost}_{\text{total}} + \text{Pen}_{\text{HyT}} - \text{Inc}_{\text{HyT}} \quad 6.9$$

Utilizing a GA, renowned for its global minima discovery capability, the optimization process initiates with seeds from corresponding condition-based operations. Despite the potential time intensity due to numerous parameters, the optimizer's efficient initialization and the model's responsiveness ensure timely outcomes.

Visual representations in Figure 6.6 (a) highlight the complex interplay among forecasting, optimization, and real-world adjustments, emphasizing the all-encompassing nature of this approach. Additionally, a comparative diagram for condition-based operation is presented in Figure 6.6 (b).

Notably, forecasting errors inherent in demand and production predictions necessitate an iterative fine-tuning process. This involves incorporating real-time data into the optimized scenario, adjusting operations based on actual conditions, and mitigating

## Optimization of MGT Operation in an Integrated System

imbalances that may arise from inaccuracies in predictions. This interplay between forecast-driven optimization and real-world adjustments ensures the microgrid's efficient and reliable operation across dynamic conditions.

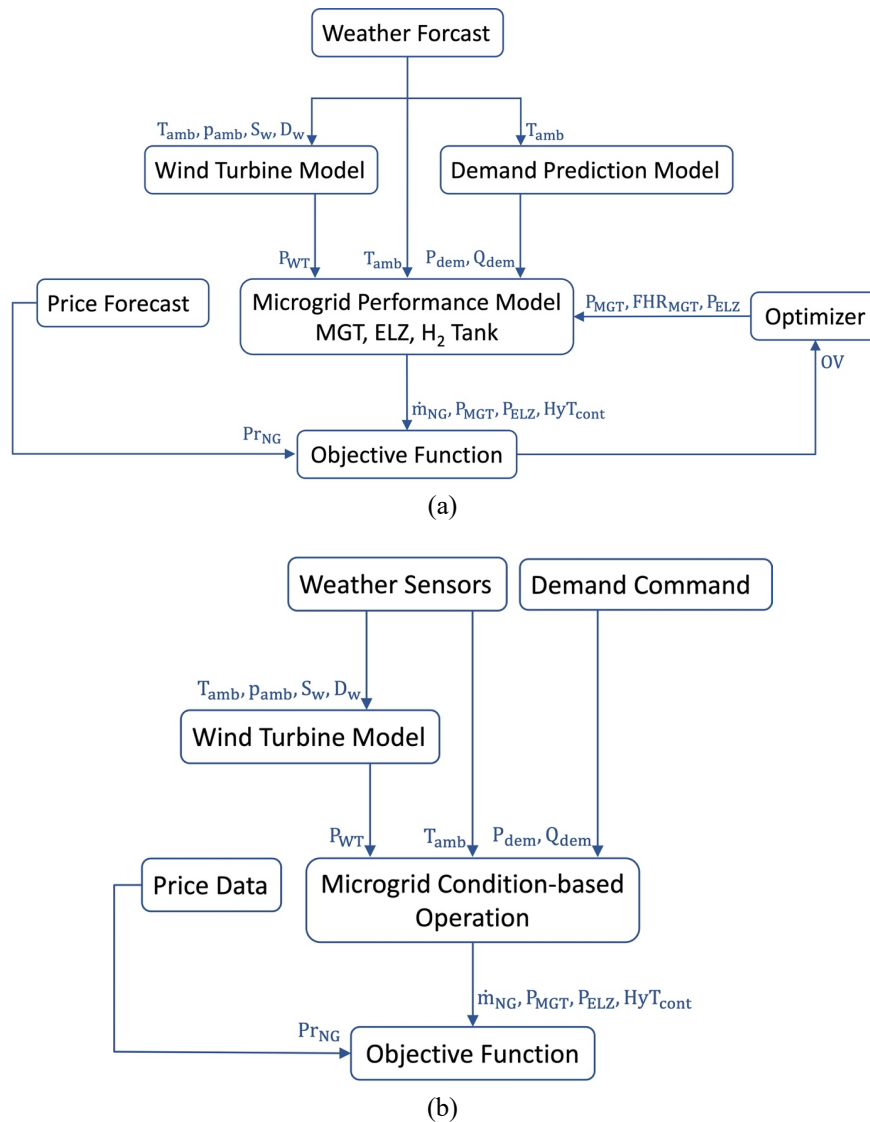


Figure 6.6 The flowchart of the operations (a) optimization, and (b) condition-based.

## 6.5 Results

The week-long microgrid analysis conducted from July 17<sup>th</sup> to 23<sup>rd</sup>, 2022, explored various scenarios, assessing operations both with and without energy storage in islanded and grid-connected modes. This investigation aimed to understand the impact of different configurations, with a benchmark provided by a condition-based operation.

Wind power was determined using the hourly distribution of weather parameters such as pressure, temperature, wind speed, and wind direction, extracted from both actual and forecasted data. This information facilitated the calculation of actual and forecasted values for wind power.

Wind power exhibited notable fluctuations, initially showing a low output for the first 2.5 days, followed by a substantial increase over three days, and a subsequent decline in the last 24 hours. A daily summary of power balance, demands, and wind power is provided in Figure 6.7.

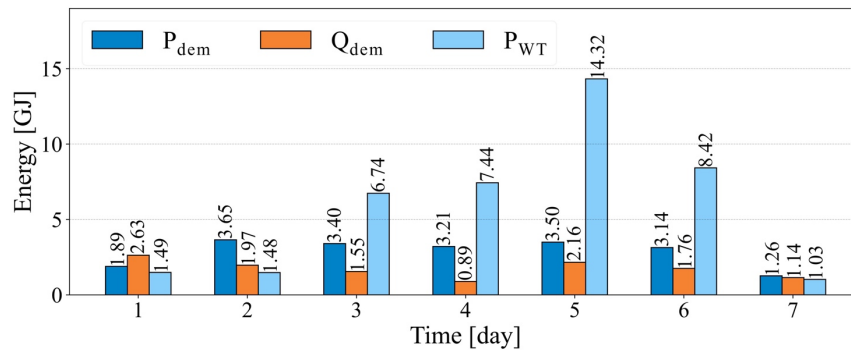


Figure 6.7 Accumulated demanded power and heat, and the produced power by the wind on a daily basis.

Cumulative power and heat demands for the week were 20.04 GJ and 12.09 GJ, respectively, with wind energy contributing 40.91 GJ. Despite this, a clear mismatch between wind power generation and demands is apparent in Figure 6.7. In Figure 6.8 the mismatch on an hourly basis is observable.

## Optimization of MGT Operation in an Integrated System

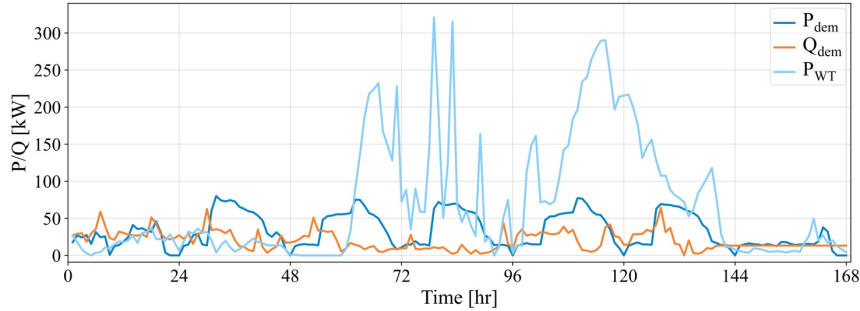


Figure 6.8 The hourly distribution of wind power, demand power, and demand heat over the week of study.

A comprehensive discussion of the results is presented in Paper VI, therefore an overview is presented here. Results of the 8 different scenarios investigated, are presented in Table 6.2. The scenarios include island and grid mode operation, both with and without storage system presence, and condition-based and optimized operation for each of those arrangements. The reported outcomes are based on operations meeting all demands for power and heat. In some instances, when the MGT operates less, lower heat production is observed, suggesting the remaining heat demand is met by the electric heater. Conversely, in scenarios where the MGT runs more frequently, it covers the entire heat demand of 12.09 GJ.

Table 6.2 Overview of island mode operation of the microgrid.

		Island Model							
		Revenue	Cost	Profit/loss	NG cons.	H <sub>2</sub> prod.	H <sub>2</sub> cons.	P <sub>MGT</sub>	Q <sub>MGT</sub>
		€	€	€	kg	kg	kg	GJ	GJ
1	w/o ELZ CB	0	542	-542	1341.7	0.0	0.0	10.26	8.27
2	w/o ELZ OPT	0	541	-541	1339.6	0.0	0.0	10.21	8.26
3	w/ELZ CB	0	441	-441	1066.6	101.8	101.4	10.26	8.27
4	w/ELZ OPT	0	441	-441	1068.1	101.8	100.8	10.26	8.27
		Grid Mode							
5	w/o ELZ CB	1525	542	984	1341.7	0.0	0.0	10.26	8.27
6	w/o ELZ OPT	4896	2219	2677	4514.4	0.0	0.0	64.07	12.09
7	w/ELZ CB	362	441	-79	1066.6	101.8	101.4	10.26	8.27
8	w/ELZ OPT	4899	2235	2664	4541.4	7.2	1.8	64.98	12.09

## Optimization of MGT Operation in an Integrated System

---

During island mode operation, the microgrid's initial functioning omitted the electrolyzer and hydrogen tank, focusing on assessing condition-based and optimized operations without storage. Notably, Table 6.2 revealed that in island mode, whether with or without storage, condition-based (CB) and optimized (OPT) scenarios displayed analogous operational results, evident when comparing rows 1 to 2 and 3 to 4. It's worth highlighting that condition-based operation yielded comparable outcomes to optimized operation but with a faster decision-making process.

Furthermore, in island mode, the introduction of hydrogen storage in both condition-based and optimized microgrid operations resulted in reduced costs, primarily due to decreased natural gas consumption. This can be observed by comparing rows 1 to 3 and 2 to 4 in Table 6.2. The storage and utilization of hydrogen revealed that excess wind power was stored and later utilized throughout the week, leading to a reduction in natural gas consumption. The introduction of the electrolyzer and hydrogen storage in the system resulted in a significant 19% cost reduction for both condition-based and optimized scenarios, accompanied by a notable 20% reduction in natural gas consumption (approximately 275 kg) and a decrease in emissions. This highlighted the environmental benefits of storing excess electricity.

Upon interconnecting the microgrid with the grid and lacking storage, the integration of the microgrid with the grid converted surplus power into a lucrative revenue source. In grid mode without storage, optimized operation (rows 6 in Table 6.2) generated higher revenue than condition-based operation (rows 5 in Table 6.2), albeit at increased costs.

Integrating hydrogen storage in the optimized operation led to a 13 € reduction in profit but conserved 5.4 kg of energy for the following weeks (row 8 compared to row 6 in Table 6.2). The potential advantage of the saved hydrogen for the upcoming week

could be assessed considering the hydrogen incentive. The adjusted profit for the optimized case with hydrogen amounted to €2678, indicating that the optimizer achieved a comparable profit in grid mode, irrespective of the presence of the storage system (rows 6 and 8 in Table 6.2).

The inclusion of storage in grid mode, particularly for condition-based operation, presented unexpected economic challenges, as evidenced by the comparison of rows 5 and 7 in Table 6.2. The results highlighted that, in the absence of optimizers in the management system, adopting a condition-based approach in grid-mode operations could result in less favorable financial outcomes when incorporating storage. This is because the condition-based operation prioritizes storage over export. Consequently, when the electrolyzer is disconnected, operators can achieve higher profits by exporting excess power to the grid.

Despite the economic challenges, incorporating storage into condition-based operation yielded a noteworthy 21% reduction in natural gas consumption (275.1 kg), as observed in the comparison between condition-based operation with and without storage (rows 5 and 7 in Table 6.2). This translated to a substantial decrease of approximately 756 kg in carbon dioxide emissions, underscoring the environmental advantages of the storage system, even when the financial outcome may be less favorable in specific operational scenarios.

Paper VI delves into the operational dynamics of the MGT and electrolyzer on an hourly basis in grid mode. The analysis uncovers that in optimized scenarios, the MGT exhibits a higher operational frequency compared to condition-based scenarios. During periods of low electricity prices, the MGT is more active, whereas it operates less frequently during high-price intervals in the optimized cases. This behavior is attributed to the optimizer's discernment of the profitability associated with MGT power generation and export to the grid. When electricity prices are low,

the optimizer opts to run the MGT less frequently, as it becomes economically unviable.

The comprehensive hourly analysis provides insight into the decision-making processes of the optimizer. This analysis highlights the optimizer's capability to adjust both MGT and electrolyzer operations according to pricing conditions, demonstrating its responsiveness to economic dynamics. Importantly, fluctuations in fuel and electricity prices exert a substantial influence on the optimizer's decisions, consequently affecting the operational outcomes of the microgrid. This economic responsiveness distinguishes optimized operation from condition-based operation, which does not consider price fluctuations when making operational decisions.

### 6.6 Conclusion

This chapter delved into the intricate dynamics of microgrid management, detailing the development of a sophisticated smart management system. It featured machine-learning-based models and offered crucial insights gleaned from diverse operational scenarios. The microgrid under consideration included two wind turbines and an MGT, incorporating an electrolyzer for green hydrogen storage.

Among the key findings compared to the condition-based operation were notable reductions in losses, natural gas consumption, and emissions during island mode with an electrolyzer. However, in grid mode, while the optimizer achieved higher profits, there was a trade-off with increased natural gas consumption and emissions. This economic-environmental balance in microgrid management underscored the complex decision-making processes involved. Comprehensive and detailed insights into the results are provided in Paper VI appended to the thesis.

## 7 Offshore Microgrid Integration and Optimization

This PhD study centers on advancing MGT operations within DEG systems, involving key phases such as developing a hydrogen-compatible MGT, modeling MGT and other energy systems, and creating integration and optimization tools. The strategic approach systematically develops infrastructural tools, ensuring adaptability to various integrated energy systems.

This chapter applies integration and optimization tools in a real-world scenario—an offshore microgrid. Integrating the offshore microgrid into the thesis expands the research’s practical applicability, highlighting adaptable solutions, refined methodologies, and crafted tools. This underscores the universal relevance of the research findings across diverse energy systems.

In Norway, offshore oil and gas (O&G) operations are the main contributors to carbon-based emissions. Optimizing offshore microgrid operations not only enhances energy efficiency but also offers an opportunity to reduce emissions in a sector that significantly impacts Norway’s carbon footprint. A detailed examination and discussion of the offshore microgrid case can be found in Paper VII, while this chapter provides an overview of the case.

### 7.1 Mitigating Offshore Oil and Gas Platform Emissions

Fossil fuel extraction in Norway, primarily by gas turbines, contributes 81% of CO<sub>2</sub> emissions on the Norwegian Continental Shelf [136], [137]. This reliance on GTs has far-reaching



environmental consequences, exacerbating global climate change and impacting local marine ecosystems. The offshore industry is adapting to regulatory changes, such as the Paris Agreement and International Maritime Organization's regulations [138], [139].

Norwegian offshore facilities are actively seeking solutions, such as integrating offshore wind turbines and hybrid energy systems with GTs. This approach offers opportunities for efficiency gains and emission reductions, further supported by government incentives and regulations [139], [140]. The expansion of offshore wind offers prospects for reducing loads on GTs and enables hydrogen production during surplus power periods. Green hydrogen, produced using renewable energy sources, emerges as a carbon-free fuel for GTs, potentially revolutionizing offshore energy systems [141].

This chapter introduces a smart energy management system designed for an O&G field in Norway connected to a floating wind farm. It introduces a smart management system aimed at reducing costs and fuel consumption, providing insights into the efficient operation of integrated energy microgrids in offshore settings.

## 7.2 Case Study Description: Gullfaks Platforms and Hywind Tampen

The Gullfaks field in the Norwegian North Sea, housing platforms Gullfaks A (GFA), Gullfaks B (GFB), and Gullfaks C (GFC), originally operated with GT from the 1980s. In response to the need for emission reduction, operator Equinor initiated a transformation by integrating renewable energy from the Hywind Tampen floating wind farm.

Situated 125 km offshore, the Hywind Tampen wind farm, featuring 11 turbines, contributes renewable energy to Gullfaks, specifically five turbines dedicated to this field. This initiative is expected to significantly cut approximately 200,000 tons of CO<sub>2</sub> and 1000 tons of NO<sub>x</sub> emissions. It aims to fulfill 30-35% of the

total energy demand across Gullfaks and neighboring Snorre platforms.

Hywind Tampen features a spar buoy foundation and Siemens SQT 8.0-154 turbines, while Gullfaks platforms are equipped with General Electric's LM2500 engines, each with a 22 MW capacity. Waste heat recovery units (WHRUs) on GFA and GFC handle most heat demands. GFA and GFC are interconnected, and a cable links Hywind to GFA for wind energy integration. GFB relies on GFA for power via cable, as it doesn't have GTs. The cables connecting platforms are limited to a maximum 20 MW power transfer.

Platform energy use includes lighting, heating, accommodations for 2-300 personnel, and management systems. O&G production is the main power consumer, using about 70% of onboard electrical power.

### 7.3 Implementing a Storage System

To achieve greater emissions reduction, expanding wind turbine installations is crucial. However, relying solely on wind power is limited by its intermittent nature. To address this, a proposed storage system mitigates power generation intermittency, as detailed in Chapter 6. Integrating wind turbines, storage systems, and GTs in a microgrid offers a promising approach to meet platform demands with minimal emissions, reducing reliance on fossil fuel gas.

Studies extensively explore the feasibility and techno-economic aspects of offshore green hydrogen production and local storage, emphasizing cost-effectiveness and economic viability [142], [143]. GFA's pivotal role suggests locating the platform near GFA for subsea hydrogen storage. The planned system includes 15 proton exchange membrane electrolyzers with a 6 MW capacity each. Pressurized hydrogen storage connected to GFA provides an alternative fuel source for GTs. This chapter delves into managing

integrated Gullfaks platforms and Hywind Tampen, detailed in Figure 7.1. While all GTs share the same model and are up to 75% hydrogen compatible, only GFA-GT1 is assumed to use hydrogen-blended fuel.

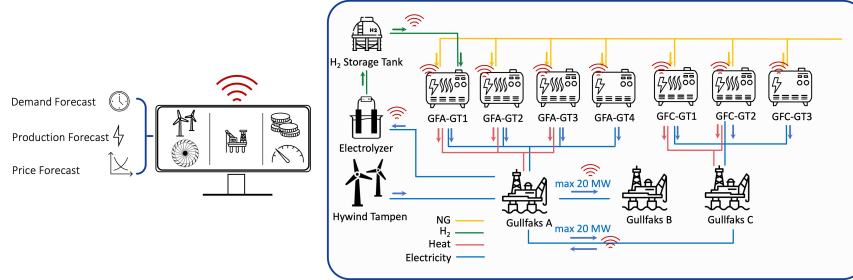


Figure 7.1 Schematic diagram of the offshore microgrid and its smart management system.

## 7.4 Managing the Microgrid Operation

The primary role of the management system is to meet the power and heat demand of each platform at each time step. The energy balance for each platform is calculated, starting with GFB due to its minimal connections and absence of an energy production unit. Equations 7.1 to 7.3 detail the energy conservation equation for GFB, considering all heat demands met by the electrical heater.

$$Q_{ELH\_GFB} - Q_{dem\_GFB} = 0 \quad 7.1$$

$$P_{ELH\_GFB} = Q_{ELH\_GFB} / \eta_{ELH\_GFB} \quad 7.2$$

$$P_{GFA\_GFB} - P_{dem\_GFB} - P_{ELH\_GFB} = 0 \quad 7.3$$

Similarly, for the GFC platform, which connects to GFA, Equations 7.4 to 7.6 describe power and heat conservation. The heat demand is met by GTs with WHRU and an additional electrical heater on GFC.

$$Q_{GFC\_GT1} + Q_{GFC\_GT2} + Q_{ELH\_GFC} - Q_{dem\_GFC} = 0 \quad 7.4$$

$$P_{ELH\_GFC} = Q_{ELH\_GFC} / \eta_{ELH\_GFC} \quad 7.5$$

$$P_{GFC\_GT1} + P_{GFC\_GT2} + P_{GFC\_GT3} + P_{GFA\_GFC} - P_{dem\_GFC} - P_{ELH\_GFC} = 0 \quad 7.6$$

Equations 7.7 to 7.9 account for the heat and power balance for GFA, considering three GTs with WHRU and an additional electrical heater. The power allocated to the electrolysis process ( $P_{GFA\_ELZ}$ ) includes water desalination, electrolysis operations, and hydrogen pressurization, as detailed in Eq. 7.10.

$$Q_{GFA\_GT1} + Q_{GFA\_GT2} + Q_{GFA\_GT3} + Q_{ELH\_GFA} - Q_{dem\_GFA} = 0 \quad 7.7$$

$$P_{ELH\_GFA} = Q_{ELH\_GFA} / \eta_{ELH\_GFA} \quad 7.8$$

$$P_{GFA\_GT1} + P_{GFA\_GT2} + P_{GFA\_GT3} + P_{GFA\_GT4} + P_{WT} - P_{GFA\_ELZ} - P_{GFA\_GFB} - P_{GFA\_GFC} - P_{dem\_GFA} - P_{ELH\_GFA} = 0 \quad 7.9$$

$$P_{GFA\_ELZ} = P_{ELZ} + P_{ds} + P_{cmp} \quad 7.10$$

Additionally, power transmission between GFA and GFC ( $P_{GFA\_GFC}$ ) and GFA to GFB ( $P_{GFA\_GFB}$ ) involves energy loss due to distance. Approximately 11% loss is factored in for transmission between GFA and GFC, while for GFA to GFB, a 5.4% power loss is considered.

In addition to power and heat conservation, ensuring hydrogen conservation is crucial, especially for supplying GTs. Constraints are applied to manage hydrogen content, as indicated in Eq. 7.11.

$$(m_{H_2,GFA-GT1})_{t_i} < (M_{HyT})_{t_0} + \sum_{t_0}^{t_i} M_{H_2,produced} - M_{H_2,consumed} \quad 7.11$$

The detailed explanations of these equations can be found in Paper VII. The study evaluates two distinct approaches to microgrid operation management; the “condition-based” approach, which follows predefined rules based on declared demands and available wind power, and the “optimization” approach, involving predicting demands and renewable production. Both approaches are thoroughly explored, with the research emphasizing the potential of the optimization approach to enhance overall microgrid operation, achieving more efficient and cost-effective energy management compared to the condition-based approach.

### 7.4.1 Scenario 1: Condition-Based Operation

In this scenario, the Gullfaks microgrid's operation follows predefined rules, providing immediate operational guidance based on real-time demand and wind turbine power generation. These rules adhere to key principles:

1. **Localized Power Production:** Platforms with GTs (GFA and GFC) prioritize local power production over importing from interconnected platforms to minimize unnecessary power transport and transmission losses.
2. **Optimized GT Operation:** Platforms aim to minimize the number of concurrently operating GTs. If a platform's demand can be met by two turbines instead of three, the two turbines operate at a higher load for enhanced engine efficiency.
3. **Balanced Operation:** When multiple engines are required, the load is evenly distributed to ensure balanced operation.
4. **Heat Utilization:** Platforms primarily meet heat requirements through GT-generated heat, considering it more cost-effective than using additional power for electric heaters. Electric heaters engage when GT heat falls short.
5. **Electrolyzer Activation:** The electrolyzer is powered only when wind turbine-generated power exceeds the combined demand of platforms GFA and GFB, ensuring surplus renewable power is directed towards hydrogen production.
6. **Hydrogen Consumption Priority:** In cases where hydrogen is available, its consumption is prioritized, contingent on hydrogen reserve availability.

Based on these principles, the condition-based operation calculates the required power for platform GFB (Eq. 7.1 to Eq. 7.3) and subsequently determines the power output of each GFC GT and the power transfer value between GFC and GFA following the flowchart in Figure 7.2. The power allocation for GTs on the GFA platform and the electrolyzer is then decided according to the flowchart in Figure 7.3.

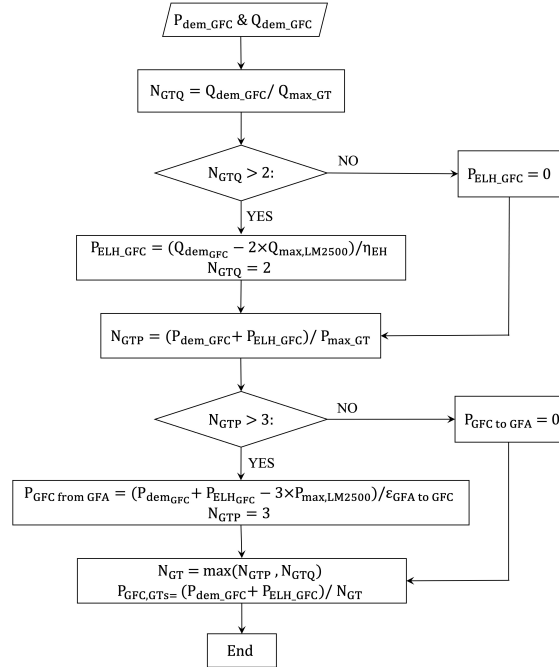


Figure 7.2 Condition-based operation flowchart for GFC.

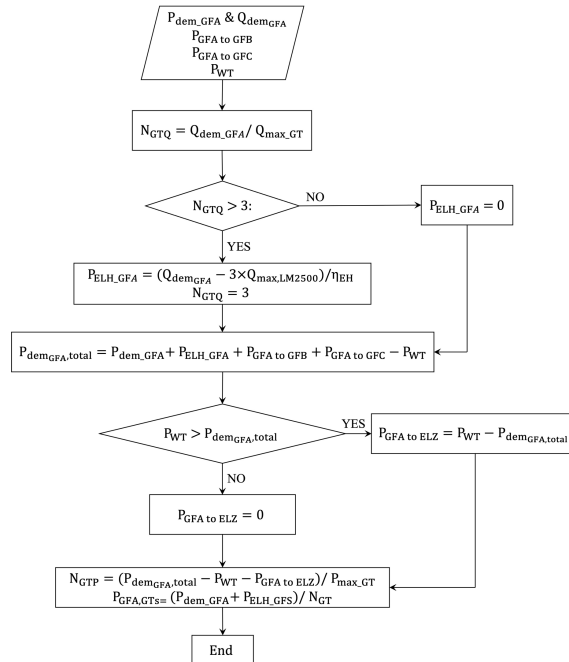


Figure 7.3 Condition-based operation flowchart for GFA.

### 7.4.2 Scenario 2: Optimized Operation

Integrating an optimization code enhances the microgrid’s predictive abilities by anticipating variables like wind availability, and optimizing energy storage and usage. This proactive approach maximizes renewables, reducing reliance on conventional sources. Unlike platform-specific methods, the optimizer considers all assets, resources, and demands system-wide, optimizing the interplay of components. This iterative process tests various scenarios, balancing energy requirements with costs and emissions to identify the optimal solution that minimizes both.

The optimizer employs AI techniques for swift and precise predictions. Robust forecasting modules predict variations in wind availability and demand patterns. ANNs model responsive microgrid subsystems, like GTs and wind turbines, with nonlinear behavior. A Bayesian technique, using Gaussian process models as detailed in section 5.3.5, fine-tunes the hyperparameters of ANN models. Input and output parameters for GTs, wind turbines, and the electrolyzer are outlined in Table 7.1. The optimized configuration of ANN models, presented in

Table 7.2, specifies the number of neurons in each layer and activation functions.

Table 7.1 Inputs and outputs of microgrid subsystem models.

	Input parameters	Output parameters
Gas turbine	$P_{MGT,dem}, FHR, T_{amb}$	$\dot{m}_f$
Wind turbine	$T_{amb}, P_{amb}, S_W, D_W$	$P_{WT}$
Electrolyzer	$P_{ELZ}$	$\dot{m}_{H_2}$

Table 7.2 ANN models optimized configuration.

	No. of neurons			Activation function			Learning rate
	layer 1	layer 2	layer 3	layer 1	layer 2	layer 3	
Gas turbine	42	17	-	Sigmoid	ReLU	-	0.72
Wind turbine	45	100	22	SELU	ReLU	Linear	0.57

The models' accuracy is evaluated using maximum absolute error (mAE), MAE, and MAPE, defined in Eq. 5.5 to Eq. 5.7. Table 7.3 presents the results, highlighting the high accuracy achieved by the developed models. Visual representations of the models' accuracy are available in Paper VII in the appendix.

Table 7.3 Models prediction error.

	mAE	MAE	MAPE
Gas turbine	0.017 [kg/s]	0.004 [kg/s]	0.21%
Wind turbine	0.801 [MW]	0.152 [MW]	0.61 %
Electrolyzer	1.6e-5 [kg/s]	1.2e-5 [kg/s]	0.05%

#### 7.4.2.1 Optimization Parameters and Objective Function

Determining power set-points for all seven GTs, selecting the optimal hydrogen/natural gas blend for GFA-GT1, and setting the power input for the electrolyzer constitute the tasks involved in the optimization process. The optimization window is defined as a day of operation, and decisions for dispatchable units are made at a 1-hour time step, totaling 216 parameters ( $9 \times 24$  hours). Each parameter adheres to upper and lower limits based on specific physical characteristics.

The GTs' power setpoints are constrained between 9 to 22 MW (Eq. 7.12), while the hydrogen/natural gas blend for GFA-GT1 is bounded by the LM2500 GT's tolerance of a maximum 75% hydrogen volume (Eq. 7.13). The fuel blend is defined based on the heating value ratios as previously presented by Eq. 6.1. The power allocated to the electrolyzer is restricted to not exceed its operational limit of 90 MW (Eq. 7.14).

$$P_{GT} = [P_{GT,1}, P_{GT,2}, \dots, P_{GT,24}], \quad P_{GT,\min} < P_{GT,i} < P_{GT,\max} \quad 7.12$$

$$\begin{aligned} FHR_{GT} &= [FHR_{GT,1}, FHR_{GT,2}, \dots, FHR_{GT,24}], \\ 0.516 &< FHR_{GT,i} < 1 \end{aligned} \quad 7.13$$

$$\begin{aligned} P_{GFA\_to\_ELZ} &= [P_{GFA\ to\ ELZ,1}, P_{GFA\ to\ ELZ,2}, \dots, P_{GFA\ to\ ELZ,24}], \\ 0 &< P_{GFA\ to\ ELZ,i} < 90 \end{aligned} \quad 7.14$$



The primary objective of the optimization process is to minimize the total cost of operation (Eq. 7.15). This includes factors such as the cost of purchasing natural gas ( $Cost_{NG}$ ), taxes on  $CO_2$  and  $NO_x$  emissions ( $Cost_{NG,tax}$  and  $Cost_{NO_x,tax}$ ), and maintenance costs for GTs and electrolyzation components ( $Cost_{GT,maint}$  and  $Cost_{ELZ}$ ).

$$Cost_{total} = Cost_{NG} + Cost_{NG,tax} + Cost_{NO_x,tax} + Cost_{GT,maint} + Cost_{ELZ} \quad 7.15$$

The cost of purchasing natural gas ( $Cost_{NG}$ ) is calculated based on the daily fuel price, while  $C_{NG,tax}$  represents the specific tax imposed by the Norwegian government on natural gas consumption. The tax for  $NO_x$  emissions ( $Cost_{NO_x,tax}$ ) is computed based on the  $NO_x$  emitted from the engines, correlated with power output. Maintenance costs for GTs, electrolyzer, compressor, and water desalination system are derived from reported values [144].

The objective function extends beyond total cost to include the preservation of hydrogen in the tank. Incentivizing hydrogen preservation, the estimation of the saved hydrogen's value for the next day is calculated using Eq. 7.16.

$$Inc_{HyT} = m_{HyT} \times \frac{LHV_{H_2}}{LHV_{NG}} \times (Cost_{NG} + Cost_{NG,tax}) \quad 7.16$$

The objective value to be minimized by the optimizer becomes:

$$OV = Cost_{total} - Inc_{HyT} \quad 7.17$$

This modification ensures that the optimizer not only minimizes immediate costs but also considers the future value of preserved hydrogen, encouraging more sustainable and forward-thinking energy management.

#### 7.4.2.2 Hybrid Optimization Approach

Addressing the intricate challenges associated with optimizing a complex system featuring numerous parameters and interrelated

constraints, a novel hybrid optimization approach has been proposed. This innovative strategy seeks to streamline the optimization process while ensuring strict compliance with all constraints, including the intricate hydrogen fuel conservation constraint outlined in Eq. 7.11.

The hydrogen conservation constraint stipulates that hydrogen consumption at each time step should not surpass the available amount in the tank. This dependency on both the hydrogen produced (related to  $P_{\text{GFA to ELZ}}$ ) up to that time step and the hydrogen consumed (linked to  $P_{\text{GFA-GT1}}$  and FHR) up to that time step introduces complexities in the optimization process, as indicated in Eq. 7.18.

for  $1 \leq i \leq 24$ :

$$\psi(\text{FHR}_1, \text{FHR}_2, \dots, \text{FHR}_i, P_{\text{GFA-GT1,1}}, P_{\text{GFA-GT1,2}}, \dots, P_{\text{GFA-GT1,i}}, P_{\text{GFA to ELZ,1}}, P_{\text{GFA to ELZ,2}}, \dots, P_{\text{GFA to ELZ,i-1}}) \leq 0 \quad 7.18$$

The introduced hybrid optimization approach operates at two distinct levels to effectively manage these complexities. At the field optimization level (outer optimization loop), the primary focus is on searching for optimal power transfer values between various platforms, such as GFA and GFC, and between GFA and ELZ. This level leverages the efficiency of the GA for decision-making.

Once the power transfer values are determined, the optimization process shifts to the platform optimization level (inner loop). Here, the objective is to optimize the operation of GTs on each platform, considering power balance requirements derived from each platform's demand and the previously determined power transfers. To minimize computational costs, this level employs a simplified approach, utilizing a pre-prepared database of platform operations and a table look-up to identify cost-effective combinations.

This two-level structure significantly reduces the number of optimization parameters, mitigating challenges associated with

high-dimensional optimization. The outer loop, dealing with field-level optimization, utilizes GA, while the inner loop, focusing on platform-level optimization, functions as a table look-up process, minimizing computational time.

The overall functionality of the hybrid optimization approach is illustrated in Figure 7.4 providing a visual representation of its operation. This approach not only streamlines the optimization of the offshore microgrid but also enables rapid decision-making, facilitating real-time adjustments for optimal power balance and platform operations.

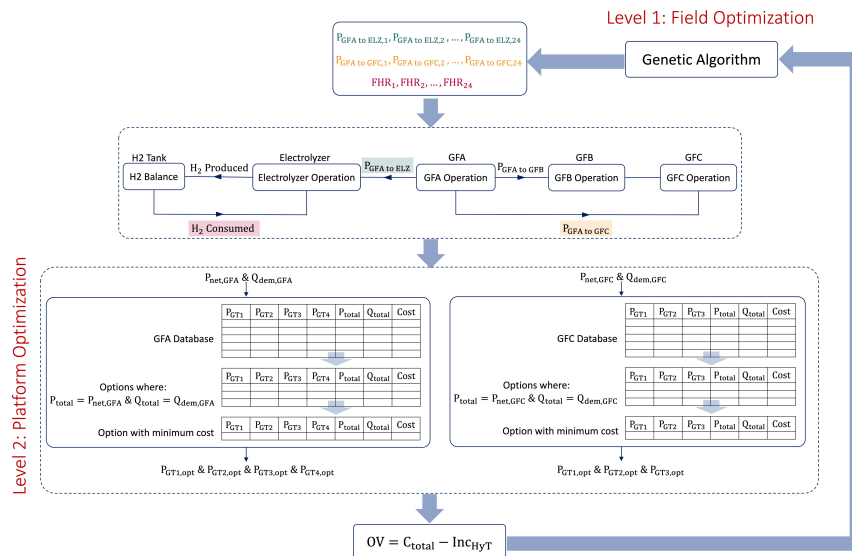


Figure 7.4 Hybrid optimization approach with outer loop for power transfer and fuel ratios and inner loop for platform operations.

## 7.5 Results

The integrated microgrid of the Gullfaks field and Hywind Tampen, coupled with an electrolyzer, underwent a comprehensive simulation to assess its performance over a week, from January 24<sup>th</sup>, 2022, to January 30<sup>th</sup>, 2022. The simulation encompassed both condition-based and optimization approaches, each offering unique insights into the system’s dynamics. This discussion

provides a condensed overview of the simulation results and technical insights; detailed analysis and insights are provided in Paper VII.

In the simulation, a daily optimization window with a 1-hour time step was utilized to examine hourly operational variations. Weather forecast data from the previous day's 18:00 update were employed to estimate wind farm power. Understanding platform demand patterns is crucial for effective microgrid optimization. Due to the lack of a detailed demand dataset for the Gullfaks platforms, the study relied on average values and common variations, generated using random distributions. The forecasted demand was adjusted with a maximum deviation of 7% and a mean of 5%, considering a deliberately higher error margin for a conservative approach.

Throughout the week, the combined power demand from the platforms was 59,20 GJ, with a total heat demand of 11,97 GJ. Wind farm power generation fell short by 3,83 GJ to meet power demand or 15,80 GJ when considering both heat and power requirements. Figure 7.5 visually highlights the wind power deviation from total power demand, emphasizing three distinct periods of low wind power generation.

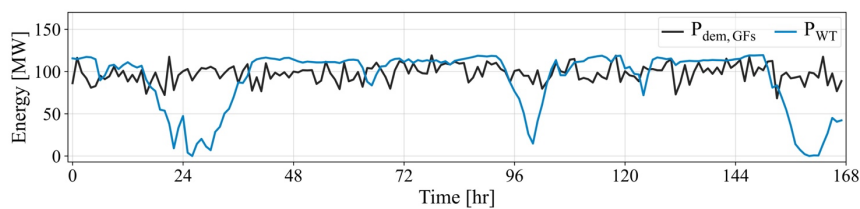


Figure 7.5 Total power demand from three Gullfaks platforms in comparison to the power generated by the wind farm.

The simulation began with an empty hydrogen tank, comparing the condition-based method, hourly analyzed throughout the week using actual data, and the optimization process, run seven times, each taking about one hour of run time. The optimizer employs forecast data for optimization, yet its evaluation depends on real-

world data to simulate practical scenarios. Any differences in forecasted and actual demand or wind power production are addressed online, through condition-based operations for remaining imbalances. This approach aligns with the methodology in Figure 9 of Paper VI.

The total power generated by all the GTs, as depicted in Figure 7.6, showed that the optimizer managed to operate the microgrid with considerably less power production from the GTs. However, there were time spans where the power production of the GTs was nearly the same for both scenarios, coinciding with periods of wind power deficiencies (Figure 7.5).

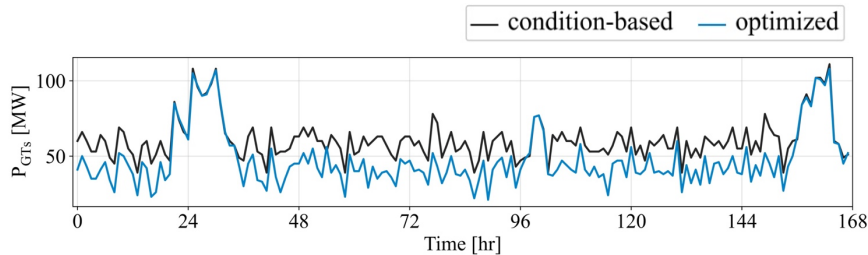


Figure 7.6 The total power produced by the seven GTs on the three Gullfaks platforms.

Figure 7.7 and Figure 7.8 provide a detailed breakdown of the total power produced by each platform. Interestingly, GFA demonstrated slightly higher power output from the GTs in the optimized scenario compared to the condition-based scenario, while the opposite trend was observed for GFC. In both scenarios, the GT production in GFA remained below the total demand, primarily because wind power contributed to fulfilling a portion of the demand.

In GFC, the condition-based scenario effectively balanced GT production with demand, while the GTs in optimized operation struggled to meet demand. Figure 7.9 illustrates the optimizer's dynamic allocation strategy, directing power from GFA to GFC to compensate for shortfalls, responding to varying wind power conditions. Despite the power loss penalty during transmission, the

optimizer strategically selects instances where this trade-off is economically justified.

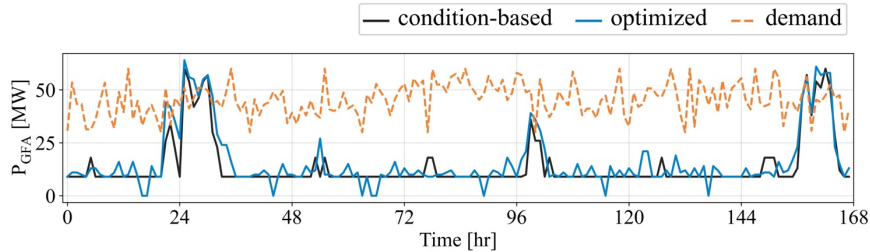


Figure 7.7 The total power produced by the four GTs on the GFA platform.

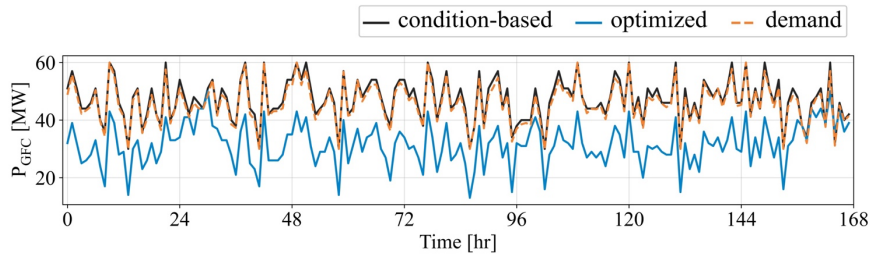


Figure 7.8 The total power produced by the three GTs on the GFC platform.

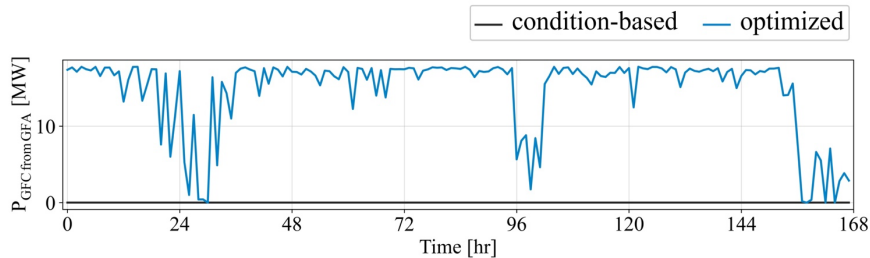


Figure 7.9 The power received by GFC from GFA.

Notably, there is a distinct contrast in hydrogen production and consumption patterns between scenarios as shown in Figure 7.10 and Figure 7.11. The condition-based operation consistently generated surplus power from wind turbines, while the optimizer often directed it to GFC (Figure 7.9), resulting in fewer GTs running on GFC (Figure 7.8). The condition-based approach exhibited a steady hydrogen consumption pattern, with minimal fluctuations except during wind deficiency periods. Conversely,

the optimized scenario displayed greater variability in hydrogen usage, reflecting the optimizer’s decision-making process and its impact on cost across optimization windows.

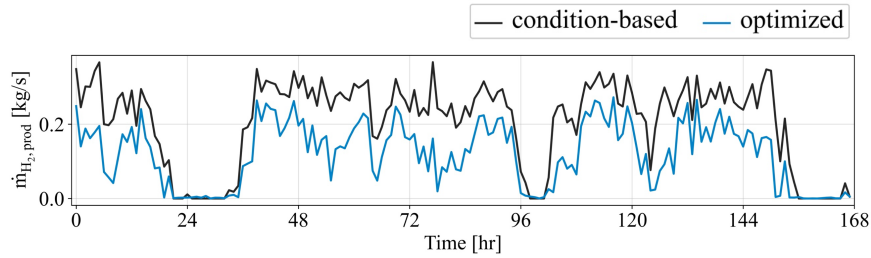


Figure 7.10 The rate of hydrogen production.

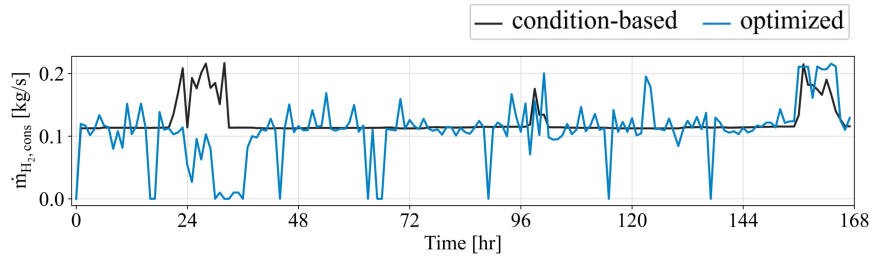


Figure 7.11 The rate of hydrogen consumption.

A comprehensive overview of the total hydrogen balance for both scenarios, presented in Table 7.4, highlighted a relative difference in hydrogen production, consumption, and reserves.

Table 7.4 Comparison of hydrogen balance after a week of operation by different scenarios.

	H <sub>2</sub> prod.	H <sub>2</sub> cons.	H <sub>2</sub> res.
CB	124.98 [t]	73.40 [kg]	51.58 [t]
OPT	72.89 [t]	65.79 [kg]	7.10 [t]
Relative difference	-41.68%	-10.37%	-86.23%

The economic and environmental implications of both scenarios were also assessed in Table 7.5. The optimized scenario demonstrated a decrease of about 16% in total costs compared to the condition-based approach. This cost reduction was attributed to the optimizer’s efficient utilization of wind power and strategic power transfer between platforms. The hydrogen saved in the tank

for the next week also has a potential value that is calculated based on Eq. 7.16. Based on this value, the total costs of the operations are modified and the results show about 12% improvement by the optimizer, compared to the condition-based operation.

Table 7.5 Overview of grid mode operation of the microgrid.

	NG cons.	NOx prod.	Total cost	H <sub>2</sub> res. cost red.	Total Cost-mod
	t	t	€	€	€
CB	2684.3	4.4	1136109	59657	1076452
OPT	2243.7	4.4	950741	8213	942529
Relative difference	-16.4%	0.9%	-16.3%	-86.2%	-12.4%

While the optimized scenario showcased reduced natural gas consumption by more than 16%, it experienced a slight increase of 0.9% in NOx emissions compared to the condition-based operation. It is expected that introducing an increasing coefficient for NOx tax could guide the optimizer toward more effective NOx reduction strategies if the emphasis on minimizing NOx emissions increases.

## 7.6 Conclusion

In this chapter, the integration and optimization of an offshore microgrid for a petroleum field with three platforms, a floating wind farm, and a green hydrogen production and storage system were focused on. A smart microgrid management system was developed using accurate models and real operational data, considering two approaches: a predefined condition-based method and an optimization. Over the course of a week, the optimized scenario exhibited a 16% reduction in costs compared to the condition-based operation, accompanied by a simultaneous decrease in natural gas consumption and emissions. The study presented a hybrid optimization approach, streamlining processes for real-world offshore microgrid systems, highlighting advanced energy management's potential for environmental responsibility in maritime energy. Further details can be found in Paper VII in the appendix.



## 8 Concluding Remarks

In the pursuit of advancing clean energy technologies and seamlessly integrating renewables into existing power systems, this thesis has undertaken a comprehensive exploration. As this research journey concludes, the importance of the study will be reflected upon, key findings summarized, and potential avenues for future research outlined.

### 8.1 Overview of the Conducted Study

Introducing a hydrogen-fueled MGT and advocating for the widespread adoption of hydrogen as a viable fuel option, the research advanced clean energy technologies. The integration of renewables, facilitated by advanced AI management tools, aimed to address the challenges posed by intermittency, fostering a stable and reliable energy grid. Moreover, the broader implications of this research align with various sustainable development goals, including affordable and clean energy, climate action, and industry innovation and infrastructure.

The literature review emphasized the extensive research conducted to integrate hydrogen into MGTs. While theoretical and laboratory advancements have been substantial, the lack of reported operational instances of MGTs running with hydrogen highlighted the need for practical implementations. The transition from theoretical advancements to real-world applications was essential for unlocking the full potential of hydrogen as a fuel source in MGTs.

The dual-modeling approach discussed in the literature, transitioning from white-box to black-box models, was identified as crucial. In early design phases, white-box models rooted in physics provided a theoretical understanding, while black-box

## Concluding Remarks

---

models, driven by empirical data, proved crucial in operational phases for real-time adaptability.

The literature on microgrid operation control and optimization underscored the transition to automated and adaptive frameworks, particularly in the smart grid evolution. The integration of transformative technologies, such as the energy hub concept and advanced modeling using ANNs and GA, showcased the potential for efficient real-time decision-making.

In the development of the hydrogen-powered MGT, challenges related to combustion stability, emissions control, and excessive combustor temperatures were extensively addressed. Modifications in combustor design and operational adjustments were highlighted, emphasizing the need for real-world testing.

The physics-based MGT model, employing a dual-strategy paradigm, demonstrated its adaptability to diverse operational scenarios. The dynamic model demonstrated proficiency in capturing both steady state and transient responses, while the steady state model accurately replicated the engine's behavior in stable operational conditions.

These models validated through empirical data, serve as useful tools for optimizing fuel-flexible MGT systems. Notably, the steady state model exhibited a faster response, making it particularly suitable for finding proper coefficients to adapt the models to experimental data. The adaptation process minimized differences between the model and experimental outcomes, enhancing the model's accuracy and applicability.

Utilizing ANNs for steady state modeling and NARX models for transient behavior, the data-driven model showcased a robust framework for MGT modeling. Achieving high accuracy was facilitated through systematic hyperparameter optimization. Its infrastructural versatility went beyond MGT applications, contributing to the foundational framework for advancements in renewable energy contexts.

## Concluding Remarks

---

The chapter on microgrid integration and optimization presented the development of a smart management system for a microgrid featuring wind turbines, an MGT, and an electrolyzer for energy storage. The use of an optimizer showcased its efficiency in finding the most cost-effective operation scenario.

In response to Norway's imperative to reduce emissions from offshore oil and gas operations, this research extended its scope to optimize GT operations within integrated systems. The research's adaptability was showcased by transitioning from onshore microgrids with MGTs to offshore scenarios with larger GTs, demonstrating the transformative and generalizable capacity of its methodologies and insights. The offshore microgrid integration and optimization chapter delved into the complexities of a real-world scenario—a petroleum field with three platforms, a floating wind farm, and introducing a green hydrogen production and storage setup. The implementation of a smart integrated microgrid management system, integrating actual operational data, showcased reductions in cost and natural gas consumption over a week of operation. The hybrid optimization approach efficiently employed GA alongside a rapid database search, providing enhanced efficiency without an exorbitant need for computing resources.

## 8.2 Additional Studies Conducted During the PhD Program

In addition to the research documented in this thesis, several studies were conducted during the course of this PhD program, contributing to the broader field of sustainable energy solutions. While these studies were not included in the main body of the thesis, their outcomes and methodologies align with the infrastructural approach employed here, emphasizing transferrable

## Concluding Remarks

---

skills and adaptable codes for similar research endeavors. The following provides an overview of these additional studies:

1. Optimizing Micro Gas Turbine Operation in a Microgrid System With Natural Gas and Hydrogen Fuel: An AI-Based Approach [145], [146]:

This study marks the author's initial contribution to the optimization of microgrids featuring hydrogen-compatible MGT. Although the paper covers the same content expounded in detail in Chapter 6, it specifically focuses on grid mode operation, omitting the discussion of island mode. Furthermore, the definition of "condition-based" operation presented in the paper is refined in Chapter 6. Essentially, the paper represents the preliminary stage of the research, paving the way for more mature and comprehensive work detailed in Chapter 6. The work was presented at the ASME Turbo Expo conference and was subsequently selected by the committee for publication in the associated ASME journal.

2. Techno-economic Analysis of a Biogas-Fueled Micro Gas Turbine Cogeneration System with Seasonal Thermal Energy Storage [147]:

In this study, a comprehensive analysis was undertaken to evaluate the techno-economic aspects of an integrated energy system designed for a small hotel's electricity and heating requirements. The system featured a biogas-fueled MGT, seasonal thermal energy storage with a borehole heat exchanger, and a ground source heat pump. The study, building upon the foundation laid by the PhD research, focused on the development and validation of intricate models, including a sophisticated data-driven MGT model utilizing feed-forward neural networks.

Utilizing the data-driven model introduced in Chapter 5, this paper exemplifies the transformative essence of the PhD work by demonstrating the effectiveness of such models in integrated energy system analyses.

## Concluding Remarks

---

### 3. Optimizing Building Heating Efficiency: A Data-Driven Approach for Cost and Energy Savings [148]:

Utilizing the data-driven modeling codes and infrastructure explained in Chapter 5, along with the MPC approach demonstrated in Chapter 6, this study introduced an innovative approach to enhance building heating control. The goal was to optimize the heating system while maintaining comfort levels. The proposed method integrates advanced tools based on building data and weather forecasts for predictive control, optimizing heating system operation using the infrastructural programs developed in Chapters 5 and 6 of this thesis.

### 4. Using Artificial Neural Networks to Gather Intelligence on a Fully Operational Heat Pump System in an Existing Building Cluster [149]:

This article introduced an innovative method that employed ANNs for developing heat pump models based on measured data from a municipal building cluster in Stavanger, Norway. The complexity and integration challenges of heat pumps were addressed, emphasizing an understanding of system intricacies. High accuracy in predicting energy-related parameters was demonstrated by ANN models.

The ANN model development code discussed in Chapter 5 played a main role in cleaning data and optimizing the structure of the ANN model. Future enhancements were considered, such as evaluating higher sampling resolutions and incorporating external temperature sensors for model refinement.

### 5. Artificial Neural Network Model for Predicting CO<sub>2</sub> Heat Pump Behavior in Domestic Hot Water and Space Heating Systems [150]:

This paper focused on advancing small-scale CO<sub>2</sub> heat pump technology through the development and optimization of control models using tailored ANNs. The ANN model constructing code from Chapter 5, contributing to data cleaning and structural

## Concluding Remarks

---

optimization, played a vital role. The study successfully predicted outlet temperatures, heat production, and electricity consumption based on measurable parameters. Acknowledging challenges in achieving precision under variable conditions, the aim was to minimize mean absolute percentage error in the models.

### 6. Optimal Operating Scenario and Performance Comparison of Biomass-Fueled Externally-Fired Microturbine [151]:

This paper focused on determining the optimal operating scenario for an Externally-fired MGT (EFMGT) using gas produced by biomass gasification. The ANN model for MGT developed in Chapter 5 was instrumental in the analysis, specifically for the natural-gas-fired MGT configuration. The optimization process resulted in an externally-fired performance of 77.9 kW electrical power and 20.3% efficiency, showcasing a 31.5% improvement over average current externally-fired demonstrated efficiencies.

### 7. On The Potential of Biomass-fueled Externally-fired Micro Gas Turbines in the Energy Transition: Off-design Performance Analysis [152]:

This paper explored substituting natural gas with biomass gasification syngas in an EFMGT for CHP generation. The developed model for the AE-T100 engine in Chapter 5 facilitated the comparison of the EFMGT with a reference natural-gas-fired MGT. The correlations and adaptations developed for the physics-based model of AE-T100 in Chapter 4 were employed for modeling the EFMGT. The analytical thermodynamic model validated using an ANN, demonstrated improved electricity efficiency at part-load conditions, reaching a maximum relative value of 110% compared to nominal conditions.

### 8. Streamlining Multi-Hole Probe Calibration Using Artificial Neural Networks [153]:

This study focused on the efficient calibration of multi-hole probes using ANNs. Traditional calibration processes for multi-hole pressure probes are time-consuming and require costly equipment

## Concluding Remarks

---

due to manufacturing imperfections affecting measuring accuracy. The research introduced a novel approach employing ANNs, known for their adaptability and generalization capabilities. Specifically, an ANN calibration model for a 5-hole probe was developed, and optimized through automated hyperparameter optimization, utilizing the programs presented in Chapter 5. The study demonstrated the ANN model's accuracy and successful application to new probes with minimal calibration data, showcasing its potential to streamline the calibration process with reduced data requirements.

### 8.3 Future Research

Concluding this doctoral study, several avenues for future research come to the forefront, representing the conclusion of the exploration while also signaling unexplored directions in this study:

- **Implementation of Hydrogen-Fueled GTs in Real-world Scenarios:** Although the research underscores the significance of green hydrogen as an energy storage solution, its actual application in hydrogen-compatible GT units is limited. Particularly for offshore microgrids, numerous challenges need to be addressed for the effective use of hydrogen in platform GTs.
- **Advanced Machine-Learning Models:** Future investigations should delve into cutting-edge machine-learning techniques, expanding the application and implications of advanced models like reinforcement learning and ensemble methods. This exploration holds promise for enhancing their pivotal role in optimizing energy systems.
- **Validation in Diverse Contexts:** While the research framework and models demonstrate efficacy, validating proposed solutions in diverse contexts remains essential. Future studies should extend the validation process to different geographical,

## Concluding Remarks

---

climatic, and operational contexts. This ensures the robustness and generalizability of the developed models, considering variations in environmental conditions and energy infrastructure.

- **Enhanced Techno-Economic Analysis for Microgrid Design:** Extending its scope beyond the operational phase, forthcoming research endeavors should concentrate on refining the accuracy of techno-economic analysis during the design phase of microgrids. The integration of advanced AI models into the design process holds promise for augmenting predictions of energy demand, optimizing component sizing, and facilitating more precise cost-benefit analyses. By adopting a data-driven approach, an improved assessment of operational risk analysis becomes feasible. This allows for the proactive addressing of critical issues such as reliability, lifetime, and energy balance during the design phase. Consequently, strategic component arrangement and the inclusion of buffer elements can be optimized to effectively mitigate potential challenges.
- **Real-Time Discrepancy Mitigation in Microgrid Optimization:** Addressing the difference between prediction and reality in microgrid optimization is crucial. Future studies should explore innovative solutions to mitigate real-time discrepancies between predicted and actual energy demand, especially concerning renewable energy sources like wind power. Improved methods for condition-based adjustments can contribute to more accurate and adaptive optimization.
- **Emphasizing Interconnected Microgrids and Collaborative Data Utilization:** The future trajectory of research should explore the integration of microgrids, fostering collaborative data-sharing practices. Leveraging operational data from diverse microgrids can provide valuable insights for enhanced control strategies. Addressing challenges such as big data handling and ensuring data security will be pivotal in



## Concluding Remarks

---

optimizing the collective performance and resilience of interconnected microgrids.

- **Real Integration Challenges:** While the emphasis of this PhD has been on modeling actual energy systems, particularly with data-driven models derived from real-world data, the integration process has been conceptual. The practical integration of these models into real-life systems remains unexplored and holds potential challenges.

Notably, at the Risavika Research Center in Stavanger, a genuine integrated system with MGT, electrolyzer, and reformer is under construction and is expected to be operational in 2025. However, this real-world integration did not align with the timeline of this PhD study.

## 8.4 Conclusion

In conclusion, this thesis contributed to the field of clean energy technologies, emphasizing the practical use of data and AI in operational management. The development of a hydrogen-fueled MGT, physics-based modeling, and data-driven approaches, offered a comprehensive understanding of challenges and opportunities in the realm of MGTs. The onshore and offshore microgrid integration cases highlighted effective data and AI utilization in operational management, showcasing the applicability of the developed models and systems.

Looking ahead, the identified areas for future research lay the groundwork for ongoing advancements in sustainable energy solutions, underscoring the continued relevance of data-driven approaches. The potential impact of this research extends beyond theory, influencing the practical implementation of clean energy technologies for a more sustainable, resilient, and eco-friendly energy future.

## References

- [1] “Next Generation of Micro Gas Turbines for High Efficiency, Low Emissions and Fuel Flexibility.” 2020.
- [2] A. Ali, W. Li, R. Hussain, X. He, B. Williams, and A. Memon, “Overview of Current Microgrid Policies, Incentives and Barriers in the European Union, United States and China,” *Sustainability*, vol. 9, no. 7, p. 1146, Jun. 2017, doi: 10.3390/su9071146.
- [3] The official website of the European Union, “2030 climate & energy framework | Climate Action.” Accessed: Jan. 25, 2021. [Online]. Available: [https://ec.europa.eu/clima/policies/strategies/2030\\_en](https://ec.europa.eu/clima/policies/strategies/2030_en)
- [4] International Energy Agency, “Renewables 2022 - Analysis and forecast to 2027,” 2022.
- [5] J. Romankiewicz, C. Marnay, N. Zhou, and M. Qu, “Lessons from international experience for China’s microgrid demonstration program,” *Energy Policy*, vol. 67, pp. 198–208, Apr. 2014, doi: 10.1016/j.enpol.2013.11.059.
- [6] T. S. Ustun, C. Ozansoy, and A. Zayegh, “Recent developments in microgrids and example cases around the world - A review,” *Renewable and Sustainable Energy Reviews*, vol. 15, no. 8, pp. 4030–4041, Oct. 2011, doi: 10.1016/j.rser.2011.07.033.
- [7] I. Renewable Energy Agency, “IRENA, Global Renewables Outlook: Energy Transformation 2050,” 2020.
- [8] International Energy Agency, “CO2 Emissions in 2022,” Mar. 2023. Accessed: Jul. 18, 2023. [Online]. Available: <https://iea.blob.core.windows.net/assets/3c8fa115-35c4-4474-b237-1b00424c8844/CO2Emissionsin2022.pdf>
- [9] International Energy Agency, “Energy Technology Perspectives 2014 Harnessing Electricity’s Potential.”

## References

---

- [10] M. Hamidieh and M. Ghassemi, “Microgrids and Resilience: A Review,” *IEEE Access*, vol. 10, pp. 106059–106080, 2022, doi: 10.1109/ACCESS.2022.3211511.
- [11] G. Brauner *et al.*, “Electrical Power Vision 2040 for Europe,” EUREL, 2012.
- [12] K. Oshiro and S. Fujimori, “Role of hydrogen-based energy carriers as an alternative option to reduce residual emissions associated with mid-century decarbonization goals,” *Appl Energy*, vol. 313, p. 118803, May 2022, doi: 10.1016/j.apenergy.2022.118803.
- [13] C. M. Colson and M. H. Nehrir, “A review of challenges to real-time power management of microgrids,” in *2009 IEEE Power and Energy Society General Meeting, PES '09*, 2009. doi: 10.1109/PES.2009.5275343.
- [14] M. Soshinskaya, W. H. J. Crijns-Graus, J. M. Guerrero, and J. C. Vasquez, “Microgrids: Experiences, barriers and success factors,” *Renewable and Sustainable Energy Reviews*, vol. 40, pp. 659–672, Dec. 2014, doi: 10.1016/j.rser.2014.07.198.
- [15] S. N. Bhaskara and B. H. Chowdhury, “Microgrids - A review of modeling, control, protection, simulation and future potential,” in *IEEE Power and Energy Society General Meeting*, 2012. doi: 10.1109/PESGM.2012.6345694.
- [16] eurostat Data Browser, “Final energy consumption by sector.”
- [17] M. A. Cañete, “Commission Recommendation (EU) 2016/1318,” 2016.
- [18] J. Arbon, M. Allington, J. Lonsdale, O. Brajterman, M. Jamieson, and Y. Verstraeten, *Energy Performance of Buildings Directive (EPBD)*. Publications Office, 2015. doi: 10.2833/281509.

## References

---

- [19] S. Gros, D. Jakus, J. Vasilj, and M. Zanon, “Day-ahead scheduling and real-time economic MPC of CHP unit in microgrid with smart buildings,” *IEEE Trans Smart Grid*, vol. 10, no. 2, pp. 1992–2001, Mar. 2019, doi: 10.1109/TSG.2017.2785500.
- [20] Disaggregated final energy consumption in households - quantities, “Disaggregated final energy consumption in households - quantities,” Eurostat Data Browser.
- [21] K. A. Kelly, M. C. McManus, and G. P. Hammond, “An energy and carbon life cycle assessment of industrial CHP (combined heat and power) in the context of a low carbon UK,” *Energy*, vol. 77, pp. 812–821, Dec. 2014, doi: 10.1016/j.energy.2014.09.051.
- [22] J. Chilvers *et al.*, “Realising transition pathways for a more electric, low-carbon energy system in the United Kingdom: Challenges, insights and opportunities,” *Proceedings of the Institution of Mechanical Engineers, Part A: Journal of Power and Energy*, vol. 231, no. 6, pp. 440–477, Sep. 2017, doi: 10.1177/0957650917695448.
- [23] A. Facchini, “Distributed energy resources: Planning for the future,” *Nat Energy*, vol. 2, no. 8, pp. 1–2, Aug. 2017, doi: 10.1038/nenergy.2017.129.
- [24] J. Chilvers *et al.*, “Realising transition pathways for a more electric, low-carbon energy system in the United Kingdom: Challenges, insights and opportunities,” *Proceedings of the Institution of Mechanical Engineers, Part A: Journal of Power and Energy*, vol. 231, no. 6, pp. 440–477, Sep. 2017, doi: 10.1177/0957650917695448.
- [25] B. Fais, N. Sabio, and N. Strachan, “The critical role of the industrial sector in reaching long-term emission reduction, energy efficiency and renewable targets,” *Appl Energy*, vol. 162, pp. 699–712, Jan. 2016, doi: 10.1016/j.apenergy.2015.10.112.

## References

---

- [26] C. Jägemann, M. Fürsch, S. Hagspiel, and S. Nagl, “Decarbonizing Europe’s power sector by 2050 - Analyzing the economic implications of alternative decarbonization pathways,” *Energy Econ*, vol. 40, pp. 622–636, Nov. 2013, doi: 10.1016/j.eneco.2013.08.019.
- [27] L. Björnebo, S. Spatari, and P. L. Gurian, “A greenhouse gas abatement framework for investment in district heating,” *Appl Energy*, vol. 211, pp. 1095–1105, Feb. 2018, doi: 10.1016/j.apenergy.2017.12.003.
- [28] J. H. Williams *et al.*, “The technology path to deep greenhouse gas emissions cuts by 2050: The pivotal role of electricity,” *Science (1979)*, vol. 335, no. 6064, pp. 53–59, Jan. 2012, doi: 10.1126/science.1208365.
- [29] K. Tokimatsu, R. Yasuoka, and M. Nishio, “Global zero emissions scenarios: The role of biomass energy with carbon capture and storage by forested land use,” *Appl Energy*, vol. 185, pp. 1899–1906, Jan. 2017, doi: 10.1016/j.apenergy.2015.11.077.
- [30] O. US EPA, “Catalog of CHP Technologies.”
- [31] P. O. Kaplan and J. W. Witt, “What is the role of distributed energy resources under scenarios of greenhouse gas reductions? A specific focus on combined heat and power systems in the industrial and commercial sectors,” *Appl Energy*, vol. 235, pp. 83–94, Feb. 2019, doi: 10.1016/j.apenergy.2018.10.125.
- [32] Resource Dynamics Corporation, “Cooling, Heating, and Power for Industry: A Market Assessment,” 2003.
- [33] M. Liu, Y. Shi, and F. Fang, “Combined cooling, heating and power systems: A survey,” *Renewable and Sustainable Energy Reviews*, vol. 35. Elsevier Ltd, pp. 1–22, Jul. 01, 2014. doi: 10.1016/j.rser.2014.03.054.
- [34] “Microturbine Systems Market Analysis,” Apr. 2022.

## References

---

- [35] E. Konečná, S. Y. Teng, and V. Máša, “New insights into the potential of the gas microturbine in microgrids and industrial applications,” *Renewable and Sustainable Energy Reviews*, vol. 134, p. 110078, Dec. 2020, doi: 10.1016/j.rser.2020.110078.
- [36] European Turbine Network (ETN), “Micro Gas Turbine Technology Research and Development for European Collaboration,” ETN Micro Gas Turbine Technology Summary.
- [37] Y. Zhang, D. Davis, and M. J. Brear, “The role of hydrogen in decarbonizing a coupled energy system,” *J Clean Prod*, vol. 346, p. 131082, Apr. 2022, doi: 10.1016/J.JCLEPRO.2022.131082.
- [38] Y. Sun *et al.*, “Effect of hydrogen addition on the combustion and emission characteristics of methane under gas turbine relevant operating condition,” *Fuel*, vol. 324, p. 124707, Sep. 2022, doi: 10.1016/J.FUEL.2022.124707.
- [39] K. Minakawa, T. Miyajima, and S. Yuasa, “Development of a hydrogen-fueled micro gas turbine with a lean premixed combustor,” in *33rd Joint Propulsion Conference and Exhibit*, American Institute of Aeronautics and Astronautics Inc, AIAA, 1997, pp. 1–6. doi: 10.2514/6.1997-3388.
- [40] H. H. W. Funke, N. Beckmann, J. Keinz, and A. Horikawa, “30 Years of Dry-Low-NO<sub>x</sub> Micromix Combustor Research for Hydrogen-Rich Fuels - An Overview of Past and Present Activities,” *J Eng Gas Turbine Power*, vol. 143, no. 7, Jul. 2021, doi: 10.1115/1.4049764/1096348.
- [41] J. D. Morris, R. A. Symonds, F. L. Ballard, and A. Banti, “Combustion Aspects of Application of Hydrogen and Natural Gas Fuel Mixtures to MS9001E DLN-1 Gas Turbines at Elsta Plant, Terneuzen, The Netherlands,” in *Proceedings of the ASME Turbo Expo*, Stockholm:

## References

---

- American Society of Mechanical Engineers Digital Collection, Dec. 1998. doi: 10.1115/98-GT-359.
- [42] I. A. Waitz, G. Gauba, and Y.-S. Tzeng, “Combustors for Micro-Gas Turbine Engines,” *J Fluids Eng*, vol. 120, no. 1, pp. 109–117, Mar. 1998, doi: 10.1115/1.2819633.
- [43] W. D. York, W. S. Ziminsky, and E. Yilmaz, “Development and Testing of a Low NO<sub>x</sub> Hydrogen Combustion System for Heavy-Duty Gas Turbines,” *J Eng Gas Turbine Power*, vol. 135, no. 2, Feb. 2013, doi: 10.1115/1.4007733.
- [44] H. Y. Shih and C. R. Liu, “A computational study on the combustion of hydrogen/methane blended fuels for a micro gas turbines,” *Int J Hydrogen Energy*, vol. 39, no. 27, pp. 15103–15115, Sep. 2014, doi: 10.1016/J.IJHYDENE.2014.07.046.
- [45] A. Cappelletti and F. Martelli, “Investigation of a pure hydrogen fueled gas turbine burner,” *Int J Hydrogen Energy*, vol. 42, no. 15, pp. 10513–10523, Apr. 2017, doi: 10.1016/J.IJHYDENE.2017.02.104.
- [46] B. A. Imteyaz, M. A. Nemitallah, A. A. Abdelhafez, and M. A. Habib, “Combustion behavior and stability map of hydrogen-enriched oxy-methane premixed flames in a model gas turbine combustor,” *Int J Hydrogen Energy*, vol. 43, no. 34, pp. 16652–16666, Aug. 2018, doi: 10.1016/J.IJHYDENE.2018.07.087.
- [47] P. Rajpara, R. Shah, and J. Banerjee, “Effect of hydrogen addition on combustion and emission characteristics of methane fuelled upward swirl can combustor,” *Int J Hydrogen Energy*, vol. 43, no. 36, pp. 17505–17519, Sep. 2018, doi: 10.1016/J.IJHYDENE.2018.07.111.
- [48] A. Pappa, L. Bricteux, P. Bénard, and W. De Paepe, “Can Water Dilution Avoid Flashback on a Hydrogen-Enriched Micro-Gas Turbine Combustion?—A Large Eddy

## References

---

- Simulations Study,” *J Eng Gas Turbine Power*, vol. 143, no. 4, Apr. 2021, doi: 10.1115/1.4049798.
- [49] A. Horikawa *et al.*, “Combustor Development and Engine Demonstration of Micro-Mix Hydrogen Combustion Applied to M1A-17 Gas Turbine,” in *Volume 3B: Combustion, Fuels, and Emissions*, American Society of Mechanical Engineers, Jun. 2021. doi: 10.1115/GT2021-59666.
- [50] J. Lu, Z. Fu, J. Liu, and W. Pan, “Influence of air distribution on combustion characteristics of a micro gas turbine fuelled by hydrogen-doped methane,” *Energy Reports*, vol. 8, pp. 207–216, May 2022, doi: 10.1016/j.egy.2021.11.027.
- [51] H. Liu, Z. Zeng, and K. Guo, “Numerical analysis on hydrogen swirl combustion and flow characteristics of a micro gas turbine combustor with axial air/fuel staged technology,” *Appl Therm Eng*, vol. 219, p. 119460, Jan. 2023, doi: 10.1016/j.applthermaleng.2022.119460.
- [52] A. Horikawa, K. Okada, M. Wirsum, H. H.-W. Funke, and K. Kusterer, “100% hydrogen dry low NO<sub>x</sub> combustor developments for 2MW class gas turbine,” in *The Proceedings of the International Conference on Power Engineering (ICOPE)*, The Japan Society of Mechanical Engineers, 2021. doi: 10.1299/JSMEICOPE.2021.15.2021-0222.
- [53] M. Henke, T. Monz, and M. Aigner, “Introduction of a New Numerical Simulation Tool to Analyze Micro Gas Turbine Cycle Dynamics,” *J Eng Gas Turbine Power*, vol. 139, no. 4, Apr. 2017, doi: 10.1115/1.4034703.
- [54] M. Henke, N. Klempf, M. Hohloch, T. Monz, and M. Aigner, “Validation of a T100 Micro Gas Turbine Steady-State Simulation Tool,” in *Volume 3: Coal, Biomass and Alternative Fuels; Cycle Innovations; Electric Power;*



## References

---

- Industrial and Cogeneration*, American Society of Mechanical Engineers, Jun. 2015. doi: 10.1115/GT2015-42090.
- [55] A. Traverso, “TRANSEO code for the dynamic performance simulation of micro gas turbine cycles,” in *Proceedings of the ASME Turbo Expo*, American Society of Mechanical Engineers Digital Collection, Nov. 2005, pp. 45–54. doi: 10.1115/GT2005-68101.
- [56] T. Zornik, T. Monz, and M. Aigner, “Performance analysis of the micro gas turbine Turbec T100 with a new FLOX-combustion system for low calorific fuels,” *Appl Energy*, vol. 159, pp. 276–284, Dec. 2015, doi: 10.1016/j.apenergy.2015.08.075.
- [57] M. Cristina Cameretti and R. Tuccillo, “Combustion features of a bio-fuelled micro-gas turbine,” *Appl Therm Eng*, vol. 89, pp. 280–290, Oct. 2015, doi: 10.1016/j.applthermaleng.2015.05.057.
- [58] R. Calabria, F. Chiariello, P. Massoli, and F. Reale, “CFD Analysis of Turbec T100 Combustor at Part Load by Varying Fuels,” *Proceedings of the ASME Turbo Expo*, vol. 8, Aug. 2015, doi: 10.1115/GT2015-43455.
- [59] S. M. Camporeale, B. Fortunato, and M. Mastrovito, “A Modular Code for Real Time Dynamic Simulation of Gas Turbines in Simulink,” *J Eng Gas Turbine Power*, vol. 128, no. 3, pp. 506–517, Jul. 2006, doi: 10.1115/1.2132383.
- [60] W. I. Rowen, “Simplified mathematical representations of heavy-duty gas turbines,” *J Eng Gas Turbine Power*, vol. 105, no. 4, pp. 865–869, Oct. 1983, doi: 10.1115/1.3227494.
- [61] A. Hussain and H. Seifi, “Dynamic Modeling of a Single Shaft Gas Turbine,” *IFAC Proceedings Volumes*, vol. 25, no. 1, pp. 43–48, Mar. 1992, doi: 10.1016/S1474-6670(17)50427-9.

## References

---

- [62] “Dynamic models for combined cycle plants in power system studies,” *IEEE Transactions on Power Systems*, vol. 9, no. 3, pp. 1698–1708, 1994, doi: 10.1109/59.336085.
- [63] L. N. Hannett, G. Jee, and B. Fardanesh, “A governor/turbine model for a twin-shaft combustion turbine,” *IEEE Transactions on Power Systems*, vol. 10, no. 1, pp. 133–140, 1995, doi: 10.1109/59.373935.
- [64] B. E. Ricketts, “Modelling of a gas turbine: a precursor to adaptive control,” in *IEE Colloquium on Adaptive Controllers in Practice '97*, IEE, 1997, pp. 7–7. doi: 10.1049/ic:19970954.
- [65] G. Crosa, F. Pittaluga, A. Trucco, F. Beltrami, A. Torelli, and F. Traverso, “Heavy-duty gas turbine plant aerothermodynamic simulation using simulink,” *J Eng Gas Turbine Power*, vol. 120, no. 3, pp. 550–556, Jul. 1998, doi: 10.1115/1.2818182.
- [66] P. Ailer, I. Sánta, G. Szederkényi, and K. M. Hangos, “NONLINEAR MODEL-BUILDING OF A LOW-POWER GAS TURBINE | Periodica Polytechnica Transportation Engineering,” *PERIODICA POLYTECHNICA TRANSPORTATION ENGINEERING*, vol. 29, 2001.
- [67] S. Abdollahi and A. Vahedi, “Dynamic Modeling of Micro-Turbine Generation Systems Using Matlab/Simulink,” *Renewable Energy and Power Quality Journal*, vol. 1, Mar. 2005, doi: 10.24084/repq03.243.
- [68] Q. Z. Al-Hamdan and M. S. Y. Ebaid, “Modeling and simulation of a gas turbine engine for power generation,” *J Eng Gas Turbine Power*, vol. 128, no. 2, pp. 302–311, Apr. 2006, doi: 10.1115/1.2061287.
- [69] L. Garborg, “Physical Modeling of a Turbec T100 Microturbine,” 2010.
- [70] C. Bang-Møller, M. Rokni, and B. Elmegaard, “Exergy analysis and optimization of a biomass gasification, solid

## References

---

- oxide fuel cell and micro gas turbine hybrid system,” *Energy*, vol. 36, no. 8, pp. 4740–4752, Aug. 2011, doi: 10.1016/J.ENERGY.2011.05.005.
- [71] W. Rachtan and L. Malinowski, “An approximate expression for part-load performance of a microturbine combined heat and power system heat recovery unit,” *Energy*, vol. 51, pp. 146–153, Mar. 2013, doi: 10.1016/j.energy.2012.12.037.
- [72] L. Malinowski and M. Lewandowska, “Analytical model-based energy and exergy analysis of a gas microturbine at part-load operation,” *Appl Therm Eng*, vol. 57, no. 1–2, pp. 125–132, Aug. 2013, doi: 10.1016/j.applthermaleng.2013.03.057.
- [73] P. Shaw, F. Zabihian, and A. S. Fung, “Gas turbine-based combined cycle power plant modeling and effects of ambient temperature,” in *ASME 2013 7th Int. Conf. on Energy Sustainability Collocated with the ASME 2013 Heat Transfer Summer Conf. and the ASME 2013 11th Int. Conf. on Fuel Cell Science, Engineering and Technology, ES 2013*, American Society of Mechanical Engineers Digital Collection, Dec. 2013. doi: 10.1115/ES2013-18256.
- [74] A. di Gaeta, F. Reale, F. Chiariello, and P. Massoli, “A dynamic model of a 100 kW micro gas turbine fuelled with natural gas and hydrogen blends and its application in a hybrid energy grid,” *Energy*, vol. 129, pp. 299–320, Jun. 2017, doi: 10.1016/j.energy.2017.03.173.
- [75] J. Nelson, N. G. Johnson, P. Doron, and E. B. Stechel, “Thermodynamic modeling of solarized microturbine for combined heat and power applications,” *Appl Energy*, vol. 212, pp. 592–606, Feb. 2018, doi: 10.1016/j.apenergy.2017.12.015.
- [76] S. Giorgetti, A. Parente, L. Bricteux, F. Contino, and W. De Paepe, “Optimal design and operating strategy of a carbon-

## References

---

- clean micro gas turbine for combined heat and power applications,” *International Journal of Greenhouse Gas Control*, vol. 88, pp. 469–481, Sep. 2019, doi: 10.1016/j.ijggc.2019.07.003.
- [77] A. Arsalis, “Thermodynamic modeling and parametric study of a small-scale natural gas/hydrogen-fueled gas turbine system for decentralized applications,” *Sustainable Energy Technologies and Assessments*, vol. 36, p. 100560, Dec. 2019, doi: 10.1016/j.seta.2019.100560.
- [78] G. B. de Campos, C. Bringhenti, A. Traverso, and J. T. Tomita, “Thermoeconomic optimization of organic Rankine bottoming cycles for micro gas turbines,” *Appl Therm Eng*, vol. 164, p. 114477, Jan. 2020, doi: 10.1016/j.applthermaleng.2019.114477.
- [79] F. Reale and R. Sannino, “Numerical Modeling of Energy Systems Based on Micro Gas Turbine: A Review,” *Energies (Basel)*, vol. 15, no. 3, p. 900, Jan. 2022, doi: 10.3390/en15030900.
- [80] P. Lin, X. Du, Y. Shi, and X.-M. Sun, “Modeling and controller design of a micro gas turbine for power generation,” *ISA Trans*, vol. 124, pp. 411–426, May 2022, doi: 10.1016/j.isatra.2020.05.050.
- [81] H. Asgari, X. Chen, and R. Sainudiin, “Considerations in modelling and control of gas turbines: A review,” in *The 2nd International Conference on Control, Instrumentation and Automation*, IEEE, Dec. 2011, pp. 84–89. doi: 10.1109/ICCIAutom.2011.6356635.
- [82] F. Jurado, “Hammerstein-model-based predictive control of micro-turbines,” *Int J Energy Res*, vol. 30, no. 7, pp. 511–521, Jun. 2006, doi: 10.1002/er.1166.
- [83] N. Chiras, C. Evans, and D. Rees, “Global Nonlinear Modeling of Gas Turbine Dynamics Using NARMAX

## References

---

- Structures,” *J Eng Gas Turbine Power*, vol. 124, no. 4, pp. 817–826, Oct. 2002, doi: 10.1115/1.1470483.
- [84] M. Fast, M. Assadi, and S. De, “Development and multi-utility of an ANN model for an industrial gas turbine,” *Appl Energy*, vol. 86, no. 1, pp. 9–17, Jan. 2009, doi: 10.1016/j.apenergy.2008.03.018.
- [85] M. Fast, T. Palmé, and M. Genrup, “A novel approach for gas turbine condition monitoring combining cusum technique and artificial neural network,” in *Proceedings of the ASME Turbo Expo*, American Society of Mechanical Engineers Digital Collection, Feb. 2009, pp. 567–574. doi: 10.1115/GT2009-59402.
- [86] C. M. Bartolini, F. Caresana, G. Comodi, L. Pelagalli, M. Renzi, and S. Vagni, “Application of artificial neural networks to micro gas turbines,” *Energy Convers Manag*, vol. 52, no. 1, pp. 781–788, Jan. 2011, doi: 10.1016/j.enconman.2010.08.003.
- [87] H. Nikpey, M. Assadi, and P. Breuhaus, “Development of an optimized artificial neural network model for combined heat and power micro gas turbines,” *Appl Energy*, vol. 108, pp. 137–148, Aug. 2013, doi: 10.1016/j.apenergy.2013.03.016.
- [88] M. Ben Rahmoune, A. Hafaiifa, A. Kouzou, X. Chen, and A. Chaibet, “Gas turbine monitoring using neural network dynamic nonlinear autoregressive with external exogenous input modelling,” *Math Comput Simul*, vol. 179, pp. 23–47, Jan. 2021, doi: 10.1016/j.matcom.2020.07.017.
- [89] I. Aslanidou, M. Rahman, T. Olsson RISE SICS tomasolsson, rise Västerås, and S. G. Konstantinos Kyprianidis, “TOWARDS AN INTEGRATED APPROACH FOR MICRO GAS TURBINE FLEET MONITORING, CONTROL, AND DIAGNOSTICS,” in

## References

---

- Global Power and Propulsion Forum 2018, Zurich, Switzerland*, 2018.
- [90] A. D. Fentaye and K. G. Kyrianiadis, “An intelligent data filtering and fault detection method for gas turbine engines,” *MATEC Web of Conferences*, vol. 314, p. 02007, 2020, doi: 10.1051/matecconf/202031402007.
- [91] S. S. Talebi, A. Madadi, A. M. Tousi, and M. Kiaee, “Micro Gas Turbine fault detection and isolation with a combination of Artificial Neural Network and off-design performance analysis,” *Eng Appl Artif Intell*, vol. 113, p. 104900, Aug. 2022, doi: 10.1016/j.engappai.2022.104900.
- [92] Z. Liu and I. A. Karimi, “Gas turbine performance prediction via machine learning,” *Energy*, vol. 192, p. 116627, Feb. 2020, doi: 10.1016/j.energy.2019.116627.
- [93] C. Li, O. B. Fosso, M. Molinas, Y. Jingpeng, and P. Raboni, “Defining Three Distribution System Scenarios for Microgrid Applications,” in *2020 IEEE 4th Conference on Energy Internet and Energy System Integration (EI2)*, 2020, pp. 982–987. doi: 10.1109/EI250167.2020.9347144.
- [94] E. Hossain, E. Kabalci, R. Bayindir, and R. Perez, “Microgrid testbeds around the world: State of art,” *Energy Convers Manag*, vol. 86, pp. 132–153, Oct. 2014, doi: 10.1016/J.ENCONMAN.2014.05.012.
- [95] C. Wang, H. Nehrir, F. Lin, and J. Zhao, “From hybrid energy systems to microgrids: Hybridization techniques, configuration, and control,” *IEEE PES General Meeting, PES 2010*, 2010, doi: 10.1109/PES.2010.5589628.
- [96] M. Geidl and G. Andersson, “Optimal Power Flow of Multiple Energy Carriers,” *IEEE Transactions on Power Systems*, vol. 22, no. 1, pp. 145–155, 2007, doi: 10.1109/TPWRS.2006.888988.
- [97] K. Orehounig, R. Evins, and V. Dorer, “Integration of decentralized energy systems in neighbourhoods using the

## References

---

- energy hub approach,” *Appl Energy*, vol. 154, pp. 277–289, 2015, doi: <https://doi.org/10.1016/j.apenergy.2015.04.114>.
- [98] A. Maroufmashat *et al.*, “Modeling and optimization of a network of energy hubs to improve economic and emission considerations,” *Energy*, vol. 93, pp. 2546–2558, 2015, doi: <https://doi.org/10.1016/j.energy.2015.10.079>.
- [99] R. Mallol-Poyato, S. Salcedo-Sanz, S. Jiménez-Fernández, and P. Díaz-Villar, “Optimal discharge scheduling of energy storage systems in MicroGrids based on hyper-heuristics,” *Renew Energy*, vol. 83, pp. 13–24, 2015, doi: <https://doi.org/10.1016/j.renene.2015.04.009>.
- [100] Y. Zhang, T. Zhang, R. Wang, Y. Liu, and B. Guo, “Optimal operation of a smart residential microgrid based on model predictive control by considering uncertainties and storage impacts,” *Solar Energy*, vol. 122, pp. 1052–1065, 2015, doi: <https://doi.org/10.1016/j.solener.2015.10.027>.
- [101] J. Ma, F. Yang, Z. Li, and S. J. Qin, “A renewable energy integration application in a MicroGrid based on model predictive control,” in *2012 IEEE Power and Energy Society General Meeting*, 2012, pp. 1–6. doi: [10.1109/PESGM.2012.6344641](https://doi.org/10.1109/PESGM.2012.6344641).
- [102] J. Reynolds, Y. Rezgui, and J.-L. Hippolyte, “Upscaling energy control from building to districts: Current limitations and future perspectives,” *Sustain Cities Soc*, vol. 35, pp. 816–829, Nov. 2017, doi: [10.1016/j.scs.2017.05.012](https://doi.org/10.1016/j.scs.2017.05.012).
- [103] J. Reynolds, M. W. Ahmad, Y. Rezgui, and J.-L. Hippolyte, “Operational supply and demand optimisation of a multi-vector district energy system using artificial neural networks and a genetic algorithm,” *Appl Energy*, vol. 235, pp. 699–713, 2019, doi: <https://doi.org/10.1016/j.apenergy.2018.11.001>.

## References

---

- [104] F. Tooryan, H. HassanzadehFard, E. R. Collins, S. Jin, and B. Ramezani, "Optimization and energy management of distributed energy resources for a hybrid residential microgrid," *J Energy Storage*, vol. 30, p. 101556, Aug. 2020, doi: 10.1016/j.est.2020.101556.
- [105] A. N. Abdalla, M. S. Nazir, Z. Tiezhu, M. Bajaj, P. Sanjeevikumar, and L. Yao, "Optimized Economic Operation of Microgrid: Combined Cooling and Heating Power and Hybrid Energy Storage Systems," *J Energy Resour Technol*, vol. 143, no. 7, Jul. 2021, doi: 10.1115/1.4050971.
- [106] X. Wang, W. Song, H. Wu, H. Liang, and A. Saboor, "Microgrid operation relying on economic problems considering renewable sources, storage system, and demand-side management using developed gray wolf optimization algorithm," *Energy*, vol. 248, p. 123472, Jun. 2022, doi: 10.1016/j.energy.2022.123472.
- [107] S. Mansouri, F. Zishan, O. D. Montoya, M. Azimizadeh, and D. A. Giral-Ramírez, "Using an intelligent method for microgrid generation and operation planning while considering load uncertainty," *Results in Engineering*, vol. 17, p. 100978, Mar. 2023, doi: 10.1016/j.rineng.2023.100978.
- [108] R. H. Perry, D. W. Green, and J. O. Maloney, *Perry's chemical engineers' handbook*, 7th ed. New York: McGraw-Hill, 1997.
- [109] S. Verhelst and T. Wallner, "Hydrogen-fueled internal combustion engines," *Prog Energy Combust Sci*, vol. 35, no. 6, pp. 490–527, Dec. 2009, doi: 10.1016/J.PECS.2009.08.001.
- [110] D. N. Anderson, "EFFECT OF HYDROGEN INJECTION ON STABILITY AND EMISSIONS OF AN



## References

---

- EXPERIMENTAL PREMIXED PREVAPORIZED PROPANE BURNER ,” Oct. 1975.
- [111] S. Davazdah Emami, R. M. Kasmani, M. D. Hamid, C. R. Che Hassan, and K. M. Mokhtar, “Kinetic and dynamic analysis of hydrogen-enrichment mixtures in combustor systems - A review paper,” *Renewable and Sustainable Energy Reviews*, vol. 62, pp. 1072–1082, Sep. 2016, doi: 10.1016/J.RSER.2016.05.029.
- [112] Z. Wei, Z. He, H. Zhen, X. Zhang, Z. Chen, and Z. Huang, “Kinetic modeling investigation on the coupling effects of H<sub>2</sub> and CO<sub>2</sub> addition on the laminar flame speed of hydrogen enriched biogas mixture,” *Int J Hydrogen Energy*, vol. 45, no. 51, pp. 27891–27903, Oct. 2020, doi: 10.1016/J.IJHYDENE.2020.07.119.
- [113] Y. He *et al.*, “Kinetic incentive of hydrogen addition on nonpremixed laminar methane/air flames,” *Int J Hydrogen Energy*, vol. 46, no. 27, pp. 14813–14823, Apr. 2021, doi: 10.1016/J.IJHYDENE.2021.01.230.
- [114] E. v. Jithin, R. J. Varghese, and R. K. Velamati, “Experimental and numerical investigation on the effect of hydrogen addition and N<sub>2</sub>/CO<sub>2</sub> dilution on laminar burning velocity of methane/oxygen mixtures,” *Int J Hydrogen Energy*, vol. 45, no. 33, pp. 16838–16850, Jun. 2020, doi: 10.1016/J.IJHYDENE.2020.04.105.
- [115] S. Benaissa, B. Adouane, S. M. Ali, and A. Mohammad, “Effect of hydrogen addition on the combustion characteristics of premixed biogas/hydrogen-air mixtures,” *Int J Hydrogen Energy*, vol. 46, no. 35, pp. 18661–18677, May 2021, doi: 10.1016/J.IJHYDENE.2021.02.225.
- [116] V. Kumar Yadav, A. Ray, and M. R. Ravi, “Experimental and computational investigation of the laminar burning velocity of hydrogen-enriched biogas,” *Fuel*, vol. 235, pp. 810–821, Jan. 2019, doi: 10.1016/J.FUEL.2018.08.068.

## References

---

- [117] C. K. Law, *Combustion physics*, vol. 9780521870528. Cambridge University Press, 2006. doi: 10.1017/CBO9780511754517.
- [118] J. L. Toof, “A Model for the Prediction of Thermal, Prompt, and Fuel NO<sub>x</sub> Emissions From Combustion Turbines,” *J Eng Gas Turbine Power*, vol. 108, no. 2, pp. 340–347, Apr. 1986, doi: 10.1115/1.3239909.
- [119] S. Candel, “Combustion dynamics and control: Progress and challenges,” *Proceedings of the Combustion Institute*, vol. 29, no. 1, pp. 1–28, Jan. 2002, doi: 10.1016/S1540-7489(02)80007-4.
- [120] J. Wu, P. Brown, I. Diakunchak, A. Gulati, M. Lenze, and B. Koestlin, “Advanced Gas Turbine Combustion System Development for High Hydrogen Fuels,” in *Proceedings of the ASME Turbo Expo*, American Society of Mechanical Engineers, May 2007, pp. 1085–1091. doi: 10.1115/GT2007-28337.
- [121] M. Ditaranto, T. Heggset, and D. Berstad, “Concept of hydrogen fired gas turbine cycle with exhaust gas recirculation: Assessment of process performance,” *Energy*, vol. 192, p. 116646, Feb. 2020, doi: 10.1016/J.ENERGY.2019.116646.
- [122] K. K. Venkataraman, L. H. Preston, D. W. Simons, B. J. Lee, J. G. Lee, and D. A. Santavicca, “Mechanism of Combustion Instability in a Lean Premixed Dump Combustor,” *J Propuls Power*, vol. 15, no. 6, pp. 909–918, May 2012, doi: 10.2514/2.5515.
- [123] P. Chiesa, G. Lozza, and L. Mazzocchi, “Using Hydrogen as Gas Turbine Fuel,” *J Eng Gas Turbine Power*, vol. 127, no. 1, pp. 73–80, Jan. 2005, doi: 10.1115/1.1787513.
- [124] C. Tang, Y. Zhang, and Z. Huang, “Progress in combustion investigations of hydrogen enriched hydrocarbons,”

## References

---

- Renewable and Sustainable Energy Reviews*, vol. 30, pp. 195–216, Feb. 2014, doi: 10.1016/J.RSER.2013.10.005.
- [125] S. C. Gülen, *Gas turbines for electric power generation*, 1st ed. Cambridge University Press, 2019.
- [126] D. G. Goodwin, H. Moffat, and R. L. Speth, “Cantera: An Object-oriented Software Toolkit for Chemical Kinetics, Thermodynamics, and Transport Processes. Version 2.2.1,” 2016.
- [127] T. Zornek, T. Mosbach, and M. Aigner, “Optical Measurements of a Lower Calorific Values-Combustor Operated in a Micro Gas Turbine With Various Fuel Compositions,” *J Eng Gas Turbine Power*, vol. 141, no. 4, Apr. 2019, doi: 10.1115/1.4040908.
- [128] Ansaldo Energia, “ANSALDO ENERGIA. AE-T100NG Product Specifications.” Accessed: Feb. 08, 2022. [Online]. Available:  
<https://www.ansaldoenergia.com/PublishingImages/Microturbines/AE-T100NG.pdf>
- [129] A. Gaitanis, A. Laterre, F. Contino, and W. De Paepe, “Towards real time transient mGT performance assessment: effective prediction using accurate component modelling techniques,” *Journal of the Global Power and Propulsion Society*, vol. 6, pp. 96–105, Jul. 2022, doi: 10.33737/jgpps/150359.
- [130] Ansaldo Energia, “AE-T100.” Accessed: Oct. 08, 2022. [Online]. Available:  
<https://www.ansaldoenergia.com/offering/equipment/turbo-machinery/microturbines/ae-t-100>
- [131] P. Wolfe, “The secant method for simultaneous nonlinear equations,” *Commun ACM*, vol. 2, no. 12, pp. 12–13, 1959.
- [132] A. Y. Alanis, N. Arana-Daniel, and C. Lopez-Franco, *Artificial Neural Networks for Engineering Applications*.

## References

---

- Elsevier Science, 2019. [Online]. Available: <https://books.google.no/books?id=OtuGDwAAQBAJ>
- [133] “Wind Technik Nord GmbH - WTN250.” Accessed: Dec. 27, 2022. [Online]. Available: <http://www.windtechniknord.de/ENGLISH/PRODUCTS/WTN250/>
- [134] M. Sánchez, E. Amores, L. Rodríguez, and C. Clemente-Jul, “Semi-empirical model and experimental validation for the performance evaluation of a 15 kW alkaline water electrolyzer,” *Int J Hydrogen Energy*, vol. 43, no. 45, pp. 20332–20345, Nov. 2018, doi: 10.1016/j.ijhydene.2018.09.029.
- [135] A. Liponi, A. Baccioli, L. Ferrari, and U. Desideri, “Techno-economic analysis of hydrogen production from PV plants,” *E3S Web of Conferences*, vol. 334, p. 01001, Jan. 2022, doi: 10.1051/e3sconf/202233401001.
- [136] Norwegian Petroleum Directorate, “Emissions to Air.”
- [137] Q. Zhang, R. M. Ogren, and S.-C. Kong, “Thermo-economic analysis and multi-objective optimization of a novel waste heat recovery system with a transcritical CO<sub>2</sub> cycle for offshore gas turbine application,” *Energy Convers Manag*, vol. 172, pp. 212–227, 2018, doi: <https://doi.org/10.1016/j.enconman.2018.07.019>.
- [138] R. S. Haszeldine, S. Flude, G. Johnson, and V. Scott, “Negative emissions technologies and carbon capture and storage to achieve the Paris Agreement commitments,” *Philosophical Transactions of the Royal Society A: Mathematical, Physical and Engineering Sciences*, vol. 376, no. 2119, p. 20160447, May 2018, doi: 10.1098/rsta.2016.0447.
- [139] S. M. Watson, “Greenhouse gas emissions from offshore oil and gas activities — Relevance of the Paris Agreement, Law of the Sea, and Regional Seas Programmes,” *Ocean*

## References

---

- Coast Manag*, vol. 185, p. 104942, Mar. 2020, doi: 10.1016/j.ocecoaman.2019.104942.
- [140] International Renewable Energy Agency (IRENA), “Climate Change and Renewable Energy National Policies and the Role of Communities, Cities and Regions,” 2019. Accessed: Aug. 26, 2023. [Online]. Available: <https://www.mofa.go.jp/files/000498436.pdf>
- [141] G. Durakovic, P. C. del Granado, and A. Tomasgard, “Powering Europe with North Sea offshore wind: The impact of hydrogen investments on grid infrastructure and power prices,” *Energy*, vol. 263, p. 125654, Jan. 2023, doi: 10.1016/j.energy.2022.125654.
- [142] Adrian Hjellestad, “Offshore wind power and hydrogen for oil and gas platform electrification,” Masters, University of Bergen, Bergen, Norway, 2022.
- [143] S. Dokhani, M. Assadi, and B. G. Pollet, “Techno-economic assessment of hydrogen production from seawater,” *Int J Hydrogen Energy*, vol. 48, no. 26, pp. 9592–9608, 2023, doi: <https://doi.org/10.1016/j.ijhydene.2022.11.200>.
- [144] G. Tilocca, D. S´anchez, M. Torres Garc´ia, and A. Escamilla Perejon, “A Methodology to Quantify Product Competitiveness and Innovation Requirements for Micro Gas Turbine Systems in Hydrogen Backup Applications,” in *ASME Turbo Expo 2023: Turbomachinery Technical Conference and Exposition*, Boston: ASME Turbo Expo, Jun. 2023.
- [145] R. Banihabib, S. Skaug Fadnes, M. Assadi, and B. Bensmann, “Optimizing Micro Gas Turbine Operation in a Microgrid System with Natural Gas and Hydrogen Fuel: An AI-Based Approach,” in *Proceedings of ASME Turbo Expo 2023*, Boston: ASME, Jun. 2023.
- [146] R. Banihabib, F. Skaug Fadnes, M. Assadi, and B. Bensmann, “Optimizing Micro Gas Turbine Operation in a

## References

---

- Microgrid System With Natural Gas and Hydrogen Fuel: An Artificial Intelligence-Based Approach,” *J Eng Gas Turbine Power*, vol. 146, no. 2, Feb. 2024, doi: 10.1115/1.4063423.
- [147] Q. Zhang, R. Banihabib, F. S. Fadnes, T. A. S. Sazon, N. Ahmed, and M. Assadi, “Techno-economic analysis of a biogas-fueled micro gas turbine cogeneration system with seasonal thermal energy storage,” *Energy Convers Manag*, vol. 292, p. 117407, Sep. 2023, doi: 10.1016/j.enconman.2023.117407.
- [148] R. Banihabib, F. S. Fadnes, and M. Assadi, “Optimizing Building Heating Efficiency: A Data-driven Approach for Cost and Energy Savings,” in *2023 IEEE 11th International Conference on Smart Energy Grid Engineering (SEGE)*, IEEE, Aug. 2023, pp. 212–217. doi: 10.1109/SEGE59172.2023.10274593.
- [149] F. S. Fadnes, R. Banihabib, and M. Assadi, “Using Artificial Neural Networks to Gather Intelligence on a Fully Operational Heat Pump System in an Existing Building Cluster,” *Energies (Basel)*, vol. 16, no. 9, p. 3875, May 2023, doi: 10.3390/en16093875.
- [150] F. S. Fadnes, R. Banihabib, and M. Assadi, “Artificial neural network model for predicting CO2 heat pump behaviour in domestic hot water and space heating systems,” *IOP Conf Ser Mater Sci Eng*, vol. 1294, no. 1, p. 012054, Dec. 2023, doi: 10.1088/1757-899X/1294/1/012054.
- [151] K. Bollas, R. Banihabib, M. Assadi, and A. Kalfas, “Optimal Operating Scenario And Performance Comparison of Biomass-Fueled Externally-Fired Microturbine,” *Energy*, 2024.
- [152] K. Bollas, R. Banihabib, M. Assadi, and A. Kalfas, “On the potential of biomass-fueled externally-fired micro-gas

## References

---

- turbines in the energy transition: off-design performance analysis,” *Appl Therm Eng*, 2024.
- [153] R. Banihabib, H. Hoenen, and M. Assadi, “Streamlining Multi-Hole Probe Calibration using Artificial Neural Networks,” *Flow Measurement and Instrumentation*, 2024.

# Paper I

The Role of Micro Gas Turbines in Energy Transition

R. Banihabib and M. Assadi.

Energies, vol. 15, no. 21, p. 8084, Oct. 2022, doi:  
10.3390/EN15218084.



# The Role of Micro Gas Turbines in Energy Transition

Reyhaneh Banihabib  and Mohsen Assadi \* 

Faculty of Science and Technology, University of Stavanger, 4016 Stavanger, Norway

\* Correspondence: mohsen.assadi@uis.no

**Abstract:** In the progressively rising decentralized energy market, micro gas turbines (MGT) are seen with great potential owing to their low emissions, fuel flexibility, and low maintenance. The current transformation in the landscape of electricity supply with an increasing share of fluctuant renewable energy resources and increasing complexity requires a reliable and energy-efficient power generation source to support the grid. In this scenario, small-scale power plants that are constructed based on micro gas turbines with up to 250 kW power range can play a substantial role in meeting the challenges of the modern electricity grid. Micro gas turbines provide a reliable and cost-effective power source with a quick load-following ability which can respond to demand peaks and compensate for intermittent renewable sources when they are not available. MGT units can work as a system together with renewables, or function as a stand-alone unit in off-grid operations. The features of micro gas turbines are compatible with the energy transition that is the carbon-free modern energy grid. The technology underlying MGTs offer hybridization with renewable energy sources, flexibility in operations and type of fuel, and promising low emission solutions that align with environmental concerns. However, there is a continuous need to improve energy efficiency with a pressing urge for reducing emissions. This paper provides a review of micro gas turbines' characteristics which promote their role in future power and heat generation systems. A brief overview of the challenges to improving operational flexibility, reliability, and availability of MGTs while maintaining low environmental impact and lowering the costs is presented. A model for an active monitoring and control system of the micro gas turbines is proposed which could improve the reliability of MGT operation in the grid by means of AI methods.

**Keywords:** micro gas turbine; energy transition; condition monitoring; performance improvement



**Citation:** Banihabib, R.; Assadi, M. The Role of Micro Gas Turbines in Energy Transition. *Energies* **2022**, *15*, 8084. <https://doi.org/10.3390/en15218084>

Academic Editor: Andrea De Pascale

Received: 31 August 2022

Accepted: 14 October 2022

Published: 31 October 2022

**Publisher's Note:** MDPI stays neutral with regard to jurisdictional claims in published maps and institutional affiliations.



**Copyright:** © 2022 by the authors. Licensee MDPI, Basel, Switzerland. This article is an open access article distributed under the terms and conditions of the Creative Commons Attribution (CC BY) license (<https://creativecommons.org/licenses/by/4.0/>).

## 1. Introduction

Centralized power generation exploiting fossil fuels or nuclear technology in largescale plants is no longer a vision of the future that climate change scientists, regulators, and growing majorities of voters approve of. Distributed energy generation (DEG) facilitates the use of different energy sources that are available for customers to choose from and install in small increments. These units provide the required power to meet the end-user demand. Distributed power is generated at or near the point of use with technologies such as gas turbines, fuel cells, diesel and gas reciprocating engines, solar panels, and wind turbines.

There are significant advantages that are associated with the replacement of centralized energy generation plants with a DEG system. The main environmental benefit of distributed systems is the reduction in carbon dioxide emissions from fossil fuels that is replaced by renewable sources such as solar power and wind. Long-term cost savings can be achieved as DEGs enable the governments and decision-makers in the utility division to avoid considerable capital investments in new fossil fuel-based power plants and build transmission and distribution infrastructure. DEG plants are situated near commercial, industrial, and residential users, which results in a reduction of energy losses that may occur due to inefficient power lines. Moreover, the short distance between generation and consumption enables access to small heat sources/sinks and provides the opportunity for

exploiting waste heat for cooling/heating purposes which is scarcely feasible in centralized power generation. DEG's location flexibility has a great positive effect on energy prices as well [1]. The distributed system provides diverse options for types of energy resources and fuels employing different technologies. Therefore, there is no need for a certain type of fuel more than others which can reduce fuel prices for customers [2].

Besides the economical benefits, DEGs have positive technical impacts on system operation such as improving voltage profile and power quality [3]. They can reduce the distribution networks' power losses by providing sufficient power relative to demand and reducing unnecessary power flow inside the transmission network [4].

DEGs can harness energy through a combined heat and power system, which might otherwise be wasted. Combined heat and power (CHP) units are more economical than conventional power generation systems [5]. They exploit waste heat for heating, cooling, or improving their efficiency by generating more power, which is not feasible in the sole utilization of centralized power generation [1].

The European Union (EU) energy system is shifting towards decentralized power and heat generation due to the availability of a vast share of renewable sources [6]. With an increasing number of units deploying solar, wind, and hydropower and small-scaled CHP plants connecting to the grid, the role of the utilities and independent power producers is evolving. Figure 1 displays the share of DEG in global power generation for the years 2000 and 2020 according to [7].

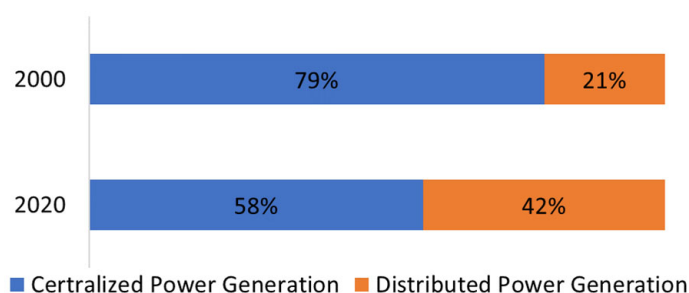


**Figure 1.** Share of DEG in the global power generation.

The current shift in the power generation industry towards more renewable and distributed generation strengthens the need for reliable and efficient small-scale dispatchable supply units. With increasing utilization of intermittent renewables such as solar and wind, a larger fluctuation in electricity input to the grid is introduced because of their non-dispatchable nature. They provide fluctuating and uncertain power outputs that are specific to certain locations. Therefore, supplementary systems and hybrid technologies are required to secure power outputs and meet demands. Micro gas turbines can provide fast and reliable power to compensate for renewable oscillations and guarantee smooth outputs to meet energy demands.

A decentralized power generation scenario integrating MGTs with wind turbines, solar systems, biomass plants, fuel cells, and energy storage would provide a secure, stable, efficient, economical, and environmentally friendly energy production system, close to consumption points, which provides the heat and electricity without major transportation and conversion losses [6]. Figure 2 gives an overview of different technologies in DEG and the position of MGT in the mix. It is worthful to note that the fuel flexibility of MGTs provides carbon-free and carbon-neutral choices of fuel such as hydrogen and biogas, which is not shown in the figure.

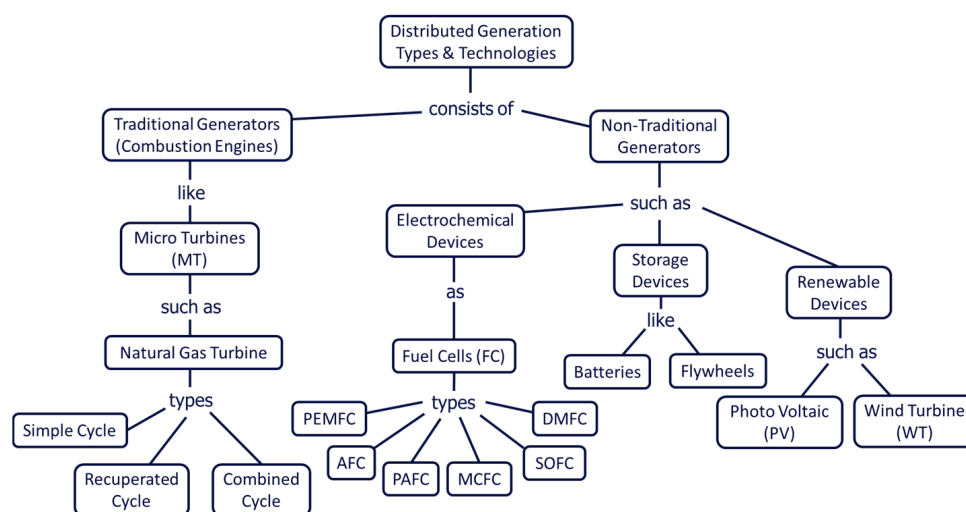


**Figure 2.** Distributed generation types and technologies [8].

MGTs have reliable operations [9] and have well-known technology, can start up rapidly, and require less maintenance due to their simple design [10]. An economic lifetime of up to 80,000 operating hours can be achieved in micro gas turbines with a maintenance interval of 4000–8000 h of operation, which is longer than most internal combustion engines [11]. They have been commonly used in many engineering fields and have already been proven to be reliable, work satisfactorily [9], and are suitable for integration with other systems or as a subsystem in a larger energy system [6].

They have lower capital costs than other DEG technologies with the potential for low-cost mass production [12]. Opportunities to utilize waste fuels (such as agricultural residues or organic waste) and energy recovery are other economic advantages of utilizing MGT systems. MGTs are very efficient with an overall efficiency (electricity + heat) up to 90% in case of using an economizer and have lower emissions compared to large-scale gas turbines [6].

Micro gas turbines that are used in co-generative applications have proven to be a promising technical solution for high-efficiency energy conversion. These comprise both combined heat and power and combined cooling/heating and power (CCHP). Exhaust gas out of the turbine in MGTs can be employed directly for heating or be recovered in a heat recovery unit (CHP application) or an absorption chiller (CCHP application) for cooling purposes. The utilization of MGTs in cogeneration mode improves their overall efficiency and operational flexibility, which makes them an attractive choice for applications that require a range of electrical to thermal output ratios [13]. These characteristics of MGTs have made them a transition technology for the EU's ambitious 2030 energy targets and a prime mover of the future for competitive, secure, and sustainable micro-scale poly-generation [6].

The structure of the paper is as follows: first, the environmental reasons that shape the energy roadmap are discussed in Section 2. In that section, the shift of power generation from a centralized to a decentralized scheme is reviewed. In Section 3 the position of heat and power cogeneration units in a decentralized system is discussed. Section 4 presents the micro gas turbine structure and its advantages over the competitors, followed by a brief history of MGT development in Section 5. Lastly, the challenges of improving MGT performance and suggestions for promoting them are provided by proposing an active condition monitoring and control system in Section 6.

## 2. Energy Policy

In this section, a brief review of the evolution of the electricity generation scheme is presented. The energy policy in the current world and associated studies are reviewed to illustrate the potential of MGTs in the near-future power generation system.

### 2.1. Climate Change and the Future of the Energy Framework

It is common knowledge that greenhouse gas (GHG) emissions are the main reason for the abnormal increase in the average surface temperature of the earth. National and international political bodies are discussing the “energy problem” and are pursuing possible solutions. The United Nations Framework Convention on Climate Change “COP21 Agreement” has given strength to the policies on climate change and the energy transition to a low-carbon energy scheme. In October 2014, the European Union agreed on vision 2030, to further increase the penetration of renewable energy technologies and improve the overall energy efficiency of electricity production with a reduction of GHG down to 40% (from 1990 levels), along with an ambitious target to reduce GHG by 95% until 2050 [14]. The vision is to keep the global temperature increase to well below 2 °C and pursue efforts to keep it to 1.5 °C [15].

According to the International Energy Agency projections, the average CO<sub>2</sub> intensity of electricity production needs to fall from 411 g per kilowatt-hour (g/kWh) in 2015 to 15 g/kWh by 2050 to achieve the goal of limiting the global increase in temperatures below 2 °C. While many studies confirm the feasibility of the goal, the development of a clear strategy and designing technical infrastructure is essential to achieve the new power market [16].

The key targets of the EU for 2030 were [15]:

- At least 40% reduction in greenhouse gas emissions (from 1990 levels), by decreasing emissions and increasing removals;
- At least 32.5% improvement in energy efficiency;
- At least 32% share for renewable energy.

As a part of the European Green Deal, in September 2020 the European Commission proposed to raise the 2030 greenhouse gas emission reduction target, to at least 55% compared to 1990 [15]. In December 2011, the European Commission communicated on the topic “Energy Roadmap 2050”. The EU is committed to reducing greenhouse gas emissions to 80–95% below 1990 levels, aiming to be climate-neutral (with net-zero GHG emissions) by 2050. Figure 3 depicts the EU energy targets. These targets aim to help the EU achieve a more competitive, secure, and sustainable energy system.

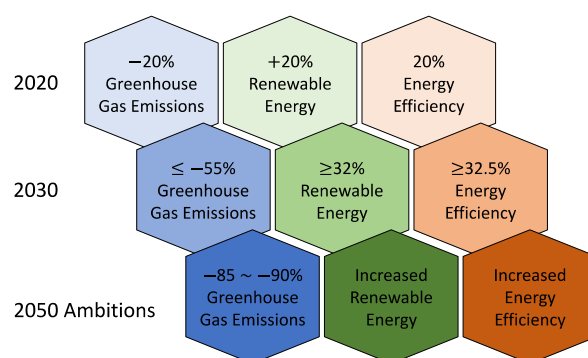


**Figure 3.** EU targets for renewable energy technologies penetration with GHG reduction [14] modified with new proposed targets [15].

One of the main challenges of the energy roadmap is the volatile feed-in from the solar and wind power plants. Electricity generation from wind and solar sources represents fluctuations that are inherited from their intermittent nature which affects the stability and reliability of the grid and could cause issues to a secure energy supply. This necessitates the development of energy backup systems to compensate for the fluctuations, consisting of storage methods for periods of oversupply, and flexible power production stations in episodes of low inputs from the renewable sources [17,18].

To provide secure, reliable, clean, and sustainable energy, a broad portfolio of energy conversion and storage technologies will be required. This is likely to include nuclear

power generation, concentrated-solar power plants, and hydrogen power plants, along with new technologies improving overall energy efficiency, as well as continued use of fossil fuels, ultimately with carbon capture and storage [19]. Due to the inevitable phases of low energy input from renewables, thermal power plants will be suitable for load control and backup power if sufficient storage capabilities are not available. The fossil power stations will be utilized only for the periods when wind and sun are absent. Utilizing large thermal power plants for standby functions will be accompanied by considerable operation costs.

Currently, the energy supplement in the world is dominated by fossil fuels and there are numerous functioning power plants and substantial fuel resources available. Therefore, even though they are the undesired sources for long-term ambitions of GHG reduction, it seems impossible for them to be phased out by the mid-century. According to recent research, 37% of the global CO<sub>2</sub> emissions are attributed to some industrial sectors such as iron, steel, and cement sectors. Therefore, fossil fuel-based power plants are difficult to eliminate [20]. Consequently, it is important to develop technologies that permit fossil-fueled plants to operate as low-emission power generators.

There are two main concepts to capture CO<sub>2</sub> from fossil fuel power plants: pre-combustion (CO<sub>2</sub> extraction from the synfuel) and post-combustion (CO<sub>2</sub> capture from exhaust gas) [21]. The CO<sub>2</sub> may be stored and disposed of in a distant geological storage site after capture. However, there is public and political opposition against geological storage sites on land in several European countries [22]. The carbon capture and storage (CCS) process costs about 10 to 14% of the production efficiency of a fossil-fuel plant [21] which is a considerable fraction of the whole establishment.

Another fuel resource for power plants is biomass, the most important renewable energy source which covered nearly 60% of renewable-based power production in Europe in 2016 [23]. On average, in industrialized countries, biomass contributes about 9–13% to the total energy supplies, but in developing countries, the proportion is less than 7% [21]. The electricity and heat producers of future power production systems must be able to function with carbon-neutral or carbon-free fuels, such as biofuels, hydrogen, or ammonia. While redeveloping large-scale fuel-flexible power plants is expensive, building small-scale power generation technologies which can operate with a range of fuels are technically and economically feasible.

It is anticipated that the future structure of power generation will appear in a similar layout as depicted in Figure 4. The power supply system will be a combination of big and small generators, where the small ones supply local power demands, and the big stations are for the system backup and are equipped with carbon capture and storage.

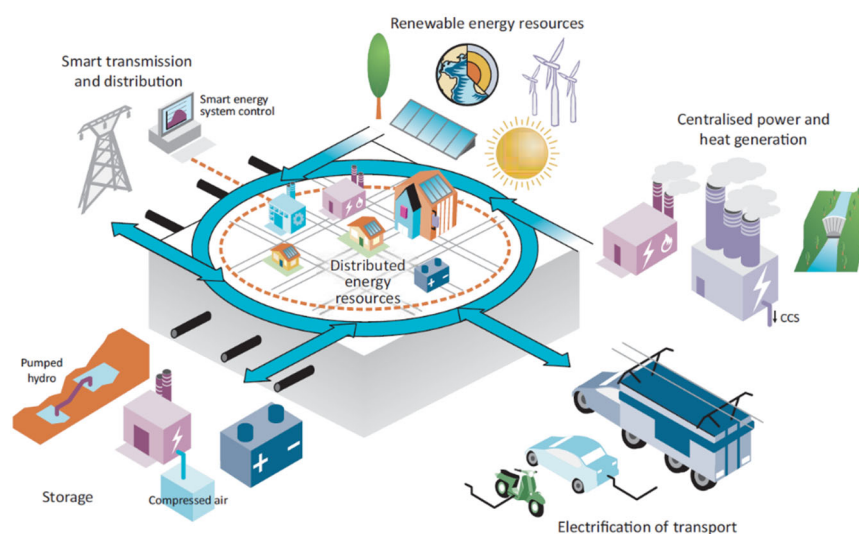


**Figure 4.** The integrated and intelligent electricity system of the future [24].



In the new scheme of power generation, the local power supply is called a microgrid (MG) which bind together to organize the local balance of the power system. If a microgrid cannot achieve the balance, then it will get power from the neighbor microgrid or the strong backup system to assure constant frequency [25].

Figure 4 shows a “smart grid”, a combination of local networks with active consumers and small storage, a strong backbone network, and powerful generators. The buildings, as one of the main consumers of electricity in today’s platform, will play an active role in the system, where they become flexible storage or even a supplier for the grid [26].

### 2.2. Option for Future Decentralized Microgrid Energy Structures

Microgrids are a group of interconnected loads and distributed energy resources within defined electrical boundaries, which act as a single controllable entity with respect to the grid. It can be connected and disconnected from the grid since it is capable of operating in both grid-connected and islanded modes [14]. Microgrids have been researched for decades [27], however, increasing penetration of distributed energy resources (DERs) into the existing power sector is raising the motive to develop advanced technologies for MG power generation units [28]. Besides the global warming effects, the increasing penetration of DER is attributed to fossil fuel shortage and political instability in the major energy-supplying countries [14]. Moreover, production costs for developing distributed energy resources declined due to technological improvements, hence the renewable energy sector has witnessed a boom in the past decade [14]. In the decentralized scheme, low power loss in the transportation of electricity due to the proximity of the production unit to the consumer is another attractive feature promoting it. Advanced MG systems will improve energy security and provide power that is efficient, reliable, and clean [18,29]. The international energy policies toward less GHG emissions are other key drivers for promoting renewable energy targets and DER, changing the MG role from a secondary energy source to a primary energy supply [27].

The rapidly increasing trend of microgrid integration into the electricity grid presents technical barriers and problems such as voltage stability, distribution system operation, control, and protection [30]. Technical challenges have been investigated for over a decade, and now can offer a stable and smoother energy supply [14]. However, the operation and maintenance of MG power units show improvement prospects for more reliable power generation.

### 2.3. Changing Role of Electric Power

The main sectors of the final energy consumption of EU-27 in 2018 were in the areas of residential (26.1%), transport (30.5%), and industry (25.8%) [31]. Figure 5 illustrates the share of different sectors in final energy consumption for EU-27 countries in 2018. The urbanization of the world is in progress which has a significant influence on energy demand. In developing countries, today more than 50% of the population are living in urban areas (Table 1), whereas in industrialized regions such as Europe already 77.5% has been reached. In industrialized countries, the electrification rate is more than 95% in urban areas (100% in the EU), but it is only about 60 to 70% in rural areas. One can say that urbanization is linked to electrification [21].

**Table 1.** Urbanization rate in percent of the total population in developing countries and industrialized countries [20].

	1950	1960	1970	1980	1990	2000	2010	2020	2030	2040
DC	18.0	21.7	25.3	29.6	35.1	40.2	45.3	50.5	56.0	61.6
IC	52.5	58.7	64.6	68.8	71.2	73.1	75.0	77.5	80.6	83.5

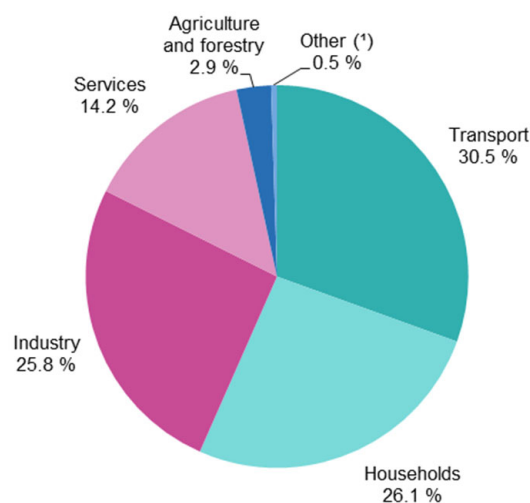


**Figure 5.** Final energy consumption by sector, EU-27, 2018 [31].

Electricity represents clean energy and is the ideal form of supply for densely populated urban areas. The building sector is crucial for achieving the EU’s energy and environmental goals. The EU “directive on the energy performance of buildings” provides the guidelines for the reduction of total energy consumption in the residential sector in the EU [32]. The aim of the directive is a “low-energy building” with a very high energy performance which improves the higher life quality of residents with additional economic advantages [33].

The microgrid concept for urban and residential households is a suitable solution for an increasing urban population, especially for operation in cogeneration mode [33]. A combined heat and power (CHP) generation mode of microgrids is an efficient solution for recovering the residual heat in the power generation unit to be exploited in proper form by the end-user. In centralized power generation mode, a part of the electrical power that is delivered to the residential sector is transformed and expended for heating or cooling purposes. Cogeneration units in DEG networks avoid inefficient heat to power and again power to heat conversion deficiencies.

### 3. Cogeneration of Heat and Power

Providing electricity and heat at the demanded location is the main purpose of the energy market. Even in today’s predominantly centralized power generation structure, heat generation is decentralized and produced near the end-user because of the high loss in heat distribution over long distances. The current shift in the electricity market towards a decentralized generation network corresponds with the current distributed heat generation scheme, particularly, a decentralized co-generation of power and heat will fulfill the new energy market structure.

Small-scale energy conversion units that can provide both electricity and heat to the customer are assumed to be the main elements of microgrids that correspond to the urban sector. Besides a reliable power supply, a micro-CHP unit provides the opportunity to exploit the remaining energy from the electricity generation process for heating or even cooling purposes, thus maximizing the level of fuel utilization and potentially decreasing carbon and air pollutant emissions by improving energy efficiency.

The European Union Cogeneration Directive sets down goals for “good quality” CHP to be a part of the delivered electricity [34,35]. However, these goals are yet to be reached. In the United States (U.S.), many states realized the value of DER and CHP to mitigate emissions and fuel consumption to fulfill environmental targets as well as achieve economic benefits [36]. Studies focusing on CHP systems and their role in meeting GHG reduction goals were investigated in different states of the U.S. [37,38], different countries in Europe [34,35,39,40], as well as on a global scale [41]. It was concluded through these

efforts that CHP is promoted as an economical and energy-efficient option for reducing air emissions, mitigating GHG emissions, and reducing reliance on grid electricity and hence enabling peak load shaving [42]. Industrial applications of CHP have been around for decades, converting 80 percent or more of the input fuel into an adequate type of energy, producing electricity and thermal energy onsite [43]. New thermally-driven cooling technologies are being developed and demonstrated that can potentially utilize the CHP heat output effectively for cooling purposes [43].

The U.S. Environmental Protection Agency (EPA) defines CHP as an efficient and clean approach for generating electricity and useful thermal energy from a single fuel source [20]. A typical CHP system operates by generating hot water or steam, deploying the recovered waste heat, and therefore, fulfilling the end-user's heat demand. The provided heat can also be directed to an absorption chiller where it can provide cooling which is called combined cooling, heating, and power.

With climate change and increasing temperature, the heating demand for the residential sector of energy consumers will decrease. Conversely, the cooling desires of household and commercial units will grow in which the CCHP mode of cogeneration will be desired. In today's marketplace, there is a variety of cooling technology options for the cogeneration of cooling, heating, and power. Absorption chillers are the most common technology that can be installed to utilize heat output to produce cooling [43].

The U.S. EPA CHP partnership gathered data and promoted the development of CHP in the industrial and commercial sectors in the U.S. and provided a thorough summary of the available existing prime mover technologies to drive a CHP system and a review of CHP systems around the world [44]. According to this effort, small CHP technologies or so-called micro-CHP technologies are the proper options for distributed generation (DG) [44]. Typically, DG is defined as power generation that is smaller than 50 MW with the unit output being used either on-site or close to where it is produced.

In one study, researchers evaluated a wide range of DG units to determine the potential for cooling, heating, and power in the U.S. industrial sector [43]. The study was focused on units by the year 2002, and included reciprocating engines, industrial turbines, microturbines, combined-cycle turbines, and fuel cells. The application of these units for electricity generation as well as cogeneration with heat and cooling were considered. The outcome of this research showed substantial market potential for CHP units in the U.S. industrial sector [43]. Market estimates show that almost three-quarters (73%) of the power market potential is for straight CHP applications, of which only one-third of the potential was available and in use in 2002 [43]. CHP with an absorber represents 15 percent of the potential, serving industries with substantial cooling demand, including the chemical and petroleum industries. The sole power generations showed only 11 percent of market potential. The research clearly shows the promising future for cogeneration on small scales in the U.S. [43].

In the same research, the authors investigated the market potential of CHP technologies variations by the size of the generating unit. In 2002, the U.S. market for small-size engines (under 1 MW) was dominated by reciprocating engines. Their combination of high efficiency and low installed cost made them a perfect choice. In the mid-range (1–20 MW), however, turbines were the prime movers, due to the large concentration of CHP-compatible sites in this size range. In large power sizes (20–50 MW), turbines offer economic potential with large combined cycles. The combined cycle applications were attractive in industries (such as steel) with relatively low steam demands.

The details of the investigation provide more insight into this market analysis with aspects such as the type of technology depicted in Figure 6. The analysis showed the dominance of micro gas turbines, industrial turbines, and reciprocating engines in 2002's CHP market. At that time, analyses showed that an adaptation of many high-efficiency features to turbine technology was to be expected which will take CHP's market share from other technologies, and even improve reciprocating engines. The same conclusion was made regarding the growing market for micro gas turbines in [45]. The reason behind this



was that the electrical efficiency improvements that were projected for micro and industrial turbines were much greater than those that were projected for reciprocating engines [43].

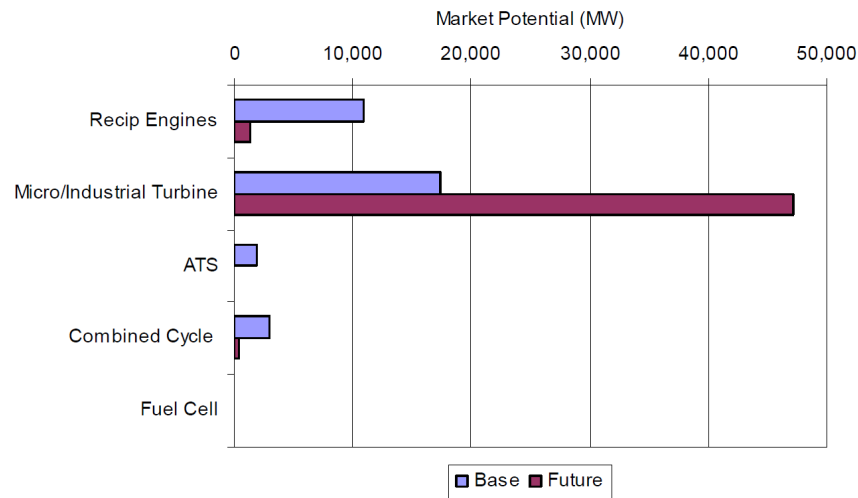


Figure 6. Market potential by technology, base data were collected in 2002 [43].

The investigations in [43] also showed that the turbine CHP market will expand and microturbines will take over in the under 1 MW applications, and larger (over 1 MW) turbines benefit from improved electrical efficiency and lower capital cost per unit power output [43]. Moreover, the low noise levels and NOx emissions of the micro gas turbines will be their other advantages over the rest of micro-CHP technologies [20]. The results are illustrated in Figure 7, showing the role of micro gas turbines with cogeneration capabilities in the future of energy production.

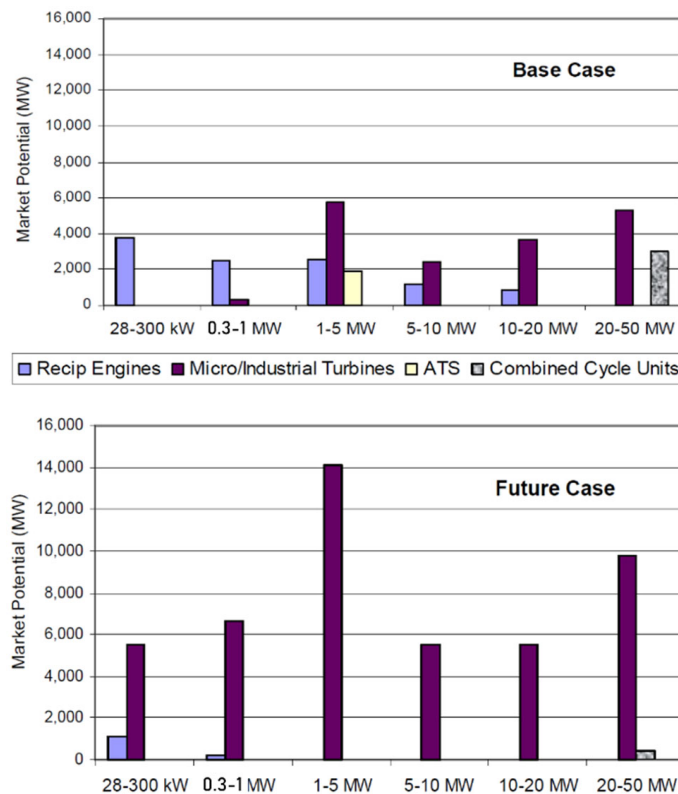


Figure 7. CHP technology market potential by unit size, base data is collected in 2002 [43].

To attain the high efficiency and reliable performance of MGTs as a CHP unit in future microgrids, further research, and development (R&D) is needed to promote these technologies and compete with more conventional options. CHP and thermal cooling technologies share the need for lower costs, increased efficiency, reduced maintenance, greater reliability, and lower emissions. While these needs vary by technology, the overall goal should be to support the industry in developing lower-cost CHP packages that improve industrial energy efficiency and reduce operating costs.

Currently, utilities and consumers are encouraged to move towards decentralized market structures and integrate with distributed small generators. With increasing power and heat demand due to the expansion of the urban sector, CHP technologies in compliance with microgrid networks will gain the most attention. As the study showed, micro gas turbines with cogeneration mode show the most potential as an economically beneficial market.

#### 4. Micro Gas Turbines

Micro gas turbines are basically small gas turbines with a power output range of 30 to 250 kW, operating on the same principle as open-cycle gas turbines. The setup consists of a compressor, a combustion chamber, and a turbine, forming a basic Brayton cycle. In this cycle, the air is compressed by the compressor then receives thermal energy by added fuel that is passing through the combustion chamber, thus leaving with a high-temperature gas. The high-pressure and-temperature gas enters the turbine where it expands and provides power to drive the compressor and the electric generator. For typical power ratings, the optimum rotational speed in micro gas turbines is between 60,000 to 120,000 rpm, a pressure ratio of 2:1 to 5:1, and turbine inlet temperature up to 1000 °C [46].

The single-shaft structure is the most common configuration of micro gas turbines [47], however, there are dual-shaft MGTs that are available in the market [46]. Single-stage centrifugal compressor and radial turbine are employed, which are manufacturing choices for compact sizes. Typical MGT employs a permanent magnet generator that is capable of compensating for the high rotational speed of MGTs which varies during the operation period [46]. Furthermore, microturbines usually employ variable-speed alternators generating a very high-frequency alternating current which must be first rectified and then converted to alternating current (AC) to match the required supply frequency [46].

The net electrical efficiency of a micro gas turbine in a basic Brayton cycle is usually low and about 17% [48] due to the small cycle pressure ratio. Moreover, the power output is also limited to turbine material constraints and cost limitations of the implementation of internal cooling systems on small scales such as micro gas turbines. The overall efficiency of MGTs is improved by preheating the compressed air to reduce fuel consumption. This pre-heating occurs in an air–air heat exchanger element called a recuperator that is placed in the way of exhaust hot gases to facilitate heat transfer between the hot exhaust gas and cold compressed air. The recuperator is, therefore, a vital element that increases the cycle efficiency to acceptable ranges. Fuel consumption in cycles that are equipped with recuperators is reduced and electrical efficiency of up to 30% can be achieved [48]. Furthermore, the low-pressure ratio in micro gas turbine cycles is advantageous for regenerative cycles since these cycles operate with higher efficiency in lower pressure ratios, as shown in Figure 8 [28]. For co-generation mode, the remaining heat in exhaust gas leaving the recuperator is transferred through another heat exchanger to provide hot water for heating purposes or be exploited in a chiller for cooling applications.

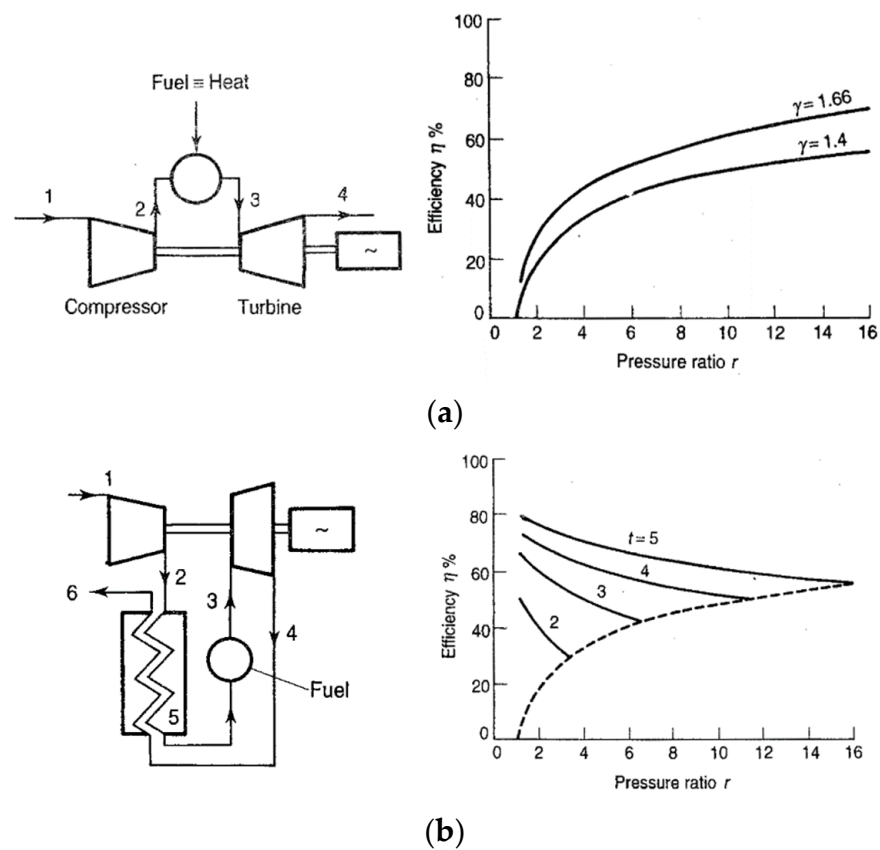


**Figure 8.** Cycle efficiency based on pressure ratio, (a) simple cycle, (b) regenerative cycle [49]. In schematic diagrams of gas turbine cycles in (a,b), the numbered locations are: 1. engine inlet, 2. compressor outlet, 3. combustor outlet, 4. turbine outlet. additional locations in (b): 5. recuperator outlet—cold-side and 6. recuperator outlet—hot-side. In efficiency diagram of (b)  $t$  is defined as ration of turbine inlet temperature to engine inlet temperature.

Figure 9 shows the simplified scheme of a micro gas turbine cycle arrangement with a recuperator and an economizer for co-generation.

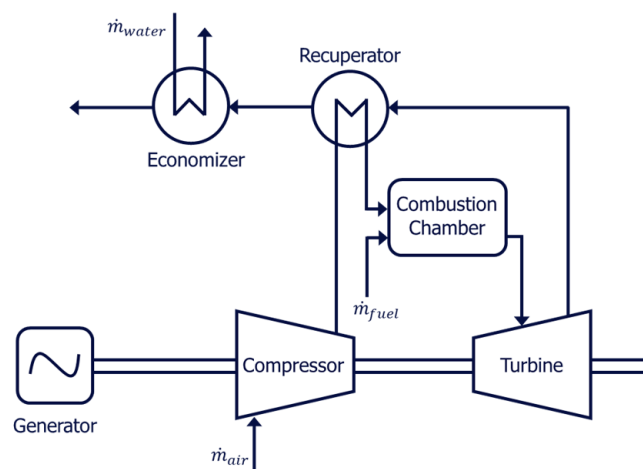


**Figure 9.** Typical MGT cycle with recuperator and economizer for combined heat and power generations.

An important advantage of micro gas turbines over other heat engines for decentralized power generation is their fuel flexibility, ranging from natural gas, diesel, liquefied petroleum gas (LPG), and hydrogen, to waste- and biomass-derived fuels. In fact, MGTs

can operate with fuels with low heating value without engine derating [6]. The combustion systems of micro gas turbines can also be designed in such a way that they can easily burn fuels with lower octane numbers as well as heavier hydrocarbon components [50]. The same is true for fuels containing hydrogen [51].

Relative to other technologies for small-scale power generation, micro gas turbines offer several advantages, including compact size, light weight, and low noise compared to other internal combustion engines (ICE) with similar power output ranges. They can be installed on-site with limited space. They have a small number of moving parts with small inertia (unlike large gas turbines with large inertia).

Another important advantage of micro gas turbines, over other ICEs such as reciprocating engines, is MGTs' low emissions [20]. Table 2 presents the baseload emissions for different micro gas turbine systems.

**Table 2.** Baseload emissions for different micro gas turbine systems [21].

	Capstone	Ansaldo	FlexEnergy	MTT
NO <sub>x</sub> [@ 15% O <sub>2</sub> ]	<9 ppm	<15 ppm	<5 ppm	<27 ppm (10 ppm with FLOX)
CO [@ 15% O <sub>2</sub> ]	<40 ppm	<15 ppm	<5 ppm	<50 ppm (10 ppm with FLOX)
UHC [@ 15% O <sub>2</sub> ]	<9 ppm	N/A	<5 ppm	N/A

A comprehensive survey was performed and reported in [20] and modified by Reinert [52] investigating the performance indicators, cost, and advantages of different cogeneration technologies towards one another. A summary of this investigation is reported in Tables 3 and 4, showing the advantages of MGT over the other technologies of the same power range.

**Table 3.** Comparison of CHP technologies: sizing, cost, and performance parameters—part 1 [20,52].

Technology		Steam Turbine	Gas Turbine	Microturbine
Capacity	MW	0.5 to several hundred	0.5–300	0.03–0.25
Power efficiency	Based on HHV	5–40+	24–36%	25–35%
Overall efficiency	Based on HHV	near 80%	66–71%	63–85%
Typical power–heat ratio	-	0.07–0.1	0.6–1.1	0.5–0.7
Part-load	-	ok	poor	ok
CHP installed costs	\$/kWe	670–1100	1200–3300	2500–4300
O&M cost	\$/kWe	0.006–0.01	0.009–0.013	0.009–0.013
Availability		72–99%	93–96%	98–99%
Hours to overhauls		>50,000	25,000–50,000	40,000–80,000
Start-up time		1 h–1 day	10 min–1 h	60 s
Fuels		all	natural gas, synthetic gas, landfill gas, fuel oils	natural gas, biogas, sour gas, liquid fuels
Noise		high	moderate	moderate
Uses of thermal output		process steam, district heating, hot water, chilled water	direct heat, hot water, LP & HP steam	direct heat, hot water, chiller
Power density	kW/m <sup>2</sup>	>100	20–500	5–70
NO <sub>x</sub>	lb/MMBtu	gas 0.1–0.2 wood 0.2–0.5 coal 0.3–1.2	0.036–0.05	0.015–0.036
NO <sub>x</sub>	lb/MWh total output	gas 0.4–0.8 wood 0.9–1.4 coal 1.2–5.0	0.52–1.31	0.14–0.49

Table 3. Cont.

Technology	Steam Turbine	Gas Turbine	Microturbine
Advantages	high overall efficiency, high temperature, high-quality heat any type of fuel may be used ability to meet more than one site heat grade requirement long working life and high reliability power–heat ratio can be varied	high reliability low emissions high-grade heat available no cooling required high-cost effectiveness	small number of moving parts compact size and light weight low emissions no cooling required
Disadvantages	slow start-up low power to heat ratio	require high-pressure gas or in-house gas compressor poor efficiency at low loading output falls as ambient temperature rises	high costs relatively low mechanical efficiency limited to lower temperature cogeneration applications

Table 4. Comparison of CHP technologies: sizing, cost, and performance parameters—part 2 [20,52].

Technology		Reciprocating Engine	Fuel Cell
Capacity	MW	0.005–10	200–2.8 commercial CHP
Power efficiency	Based on HHV	27–41%	30–63%
Overall efficiency	Based on HHV	77–80%	55–80%
Typical power–heat ratio	-	0.5–1.2	1–2
Part-load	-	ok	good
CHP installed costs	\$/kWe	1500–29,000	5000–6500
O&M cost	\$/kWe	0.009–0.025	0.032–0.038
Availability		96–98%	>95%
Hours to overhauls		30,000–60,000	32,000–64,000
Start-up time		10 s	3 h–2 days
Fuels		natural gas, biogas, propane, LPG, sour gas, industrial waste gas, manufactured gas	hydrogen, natural gas, propane, methanol
Noise		high	low
Uses of thermal output		space heating, hot water, cooling, LP steam	hot water, LP-HP steam
Power density	kW/m <sup>2</sup>	35–50	5–20
NOx	lb/MMBtU	0.013 rich burn 3-way cat. 0.17 lean burn	0.0025–0.0040
NOx	lb/MWh total output	0.06 rich burn 3-way cat. 0.8 lean burn	0.011–0.016
Advantages		high power efficiency with part-load operational flexibility fast start-up relatively low investment cost can be used in standalone mode and have good load following capability can be overhauled on-site with normal operators operate on low-pressure gas	low emissions low noise high efficiency good part-load behavior low maintenance
Disadvantages		low electrical efficiency	high costs low durability fuels requiring processing unless pure hydrogen is used start-up time

## 5. History

The development of micro gas turbines started in the early 1950s when most of the research was driven by the automotive industry viewing the possibility of using microturbines as alternatives to reciprocating piston engines [53]. This initiative was because of micro gas turbines' advantages regarding low emissions and operational and fuel flexibility. The technology became more suitable for utilization by introducing permanent magnets as high-speed generators in the early 1980s [54]. Permanent magnet generators are rotating electric machines in which permanent magnets prepare field excitation [46]. These high-speed generators offer small size, light weight, high reliability, high efficiency, and low maintenance which make them an advantageous choice to integrate with micro gas turbines [54]. However, even with permanent magnet generators, the technology of a hybrid-electric drivetrain was not mature enough and, therefore, microturbines did not achieve great success in the automotive segment [55].

The interest in micro gas turbines increased in the late 1980s and accelerated in the 1990s due to increased market interest in distributed power generation [55]. In the late 1990s, the market for hybrid vehicles started to expand and they also began to increase interest in micro gas turbines, integrating them with electric motors to generate propulsion force [46].

The deregulation of the electricity market began in late 1970s in the United States and several countries in Europe [46,56]. Breaking the monopoly in the electricity generation sector and increasing the expansion of decentralized power generation was another reason for the promotion of micro gas turbines. Micro gas turbines began to attract attention from the research and development sector due to their potential and place in the new decentralized electricity market. In the 1980s, a 50-kW gas turbine with a heat recovery system for cogeneration was under development under the Advanced Energy System (AES) program [46]. The program, however, was abandoned in the 1990s due to the high final cost of the product [46].

A Capstone turbine was incorporated in 1988 as NoMac Energy Systems started developing the micro gas turbine concept in the late 1980s, began field testing in 1997 for a 24-kW engine, and introduced the commercial product to the market in 1998 [53]. In the late 1990s micro gas turbines found acceptance in large quantities in the distributed power generation field [57]. In 2000, the state-of-the-art MGTs had electrical efficiency between 23% to 30% with an overall efficiency in cogeneration mode between 65% and 75% [58].

Other companies that were based in the United States, England, and Sweden have been introduced since then which offer a variety of power outputs to be installed in microgrids or for implementation in hybrid cars. Among these companies are Elliott Energy Systems, Capstone, Aurelia, Turbec (a spin-off of Volvo which was later purchased by Ansaldo Energia), AlliedSignal, Browman Power, and ABB Distributed Generation in a joint venture with Volvo Aero Corporation. A summary of the main features of MGTs in leading manufacturers is presented in Table 5 and a more elaborated history of micro gas turbine development could be found in [59].

**Table 5.** Technical characteristics of leading microturbine manufacturers [46].

Model	Manufacturers	Power Output	Set	Total Efficiency <sup>1</sup>	PR	TIT	NS
		kW		%	-	°C	rpm
-	AlliedSignal	75	single shaft	30 (HHV)	3.8	871	85,000
TA45	Elliott Energy System	45	single shaft	30	-	871	-
TA80	Elliott Energy System	80	single shaft	30	-	871	68,000
TA200	Elliott Energy System	200	single shaft	30	-	871	43,000
C30	Capstone	30	single shaft	28	-	871	96,000
C65	Capstone	65	single shaft	29	-	871	85,000
C200 HP	Capstone	200	single shaft	33	-	870	45,000
-	Power WorksTM	70	dual shaft	30 (HHV)	3	704	-
T100	Turbec	100	single shaft	30	4.5	950	70,000

<sup>1</sup> Total efficiency is calculated based on LHV unless it is specified otherwise.

## 6. Challenges and Opportunities

The MGT industry currently faces new challenges of increasing operational flexibility, reducing operating costs, and improving reliability and availability while mitigating environmental impact. The main concern when it comes to distributed generation is the ability to maintain performance and high availability while minimizing the operation and maintenance costs [60].

One of the main challenges that is raised in the MGT is the overall efficiency of the cycle in the operation range, including design point and part-load conditions. Even though cogeneration applications of MGT lead to higher thermodynamic efficiencies, there are episodes of poor matching between heat and power demand, which indicates that further investigations are required to attain more efficient performance schemes [60]. With an increasing number of passive houses, demand for heating will decrease which raises more challenges in the techno-economic aspects of MGT technology. However, the decrease of heat demand due to a paradigm shift in the structure of residential units and global warming effects will increase cooling demand, in which case the cooling application of MGTs will become more prevalent. For such applications, developing technologies for a more sophisticated operation of a micro gas turbine in cogeneration mode is essential.

Although performance improvements of gas turbine engines have been a subject of interest for decades, some features of micro gas turbines make them dissimilar to larger engines in several operating and system characteristics:

- The simple cycle form of micro gas turbines is less efficient than larger industrial gas turbines since the cycle pressure ratio in MGTs is considerably lower. The small size constraint in micro gas turbines imposes manufacturing complications to potential improvements of cycle parameters, such as pressure ratio and turbine inlet temperature. A recuperator helps with compensating for these deficiencies in MGT cycles which makes them an essential element of micro gas turbines, unlike large-scale engines.
- Micro gas turbines operate at significantly higher shaft speeds. With a smaller size, typical problems such as tip supersonic speeds or mechanical limits are delayed to even higher rotational speeds. Therefore, micro gas turbines can operate at speeds above 100,000 rpm whereas a larger gas turbine will typically operate in the range of 3000 to 20,000 rpm [6]. Moreover, with compensating generators connected to MGTs, the rotational speed can vary according to power demand, unlike most large-scale turbines that remain at a constant speed. This alteration of rotational speed leads to different optimization practices for performance improvements.
- MGT cycles operate with lower pressure ratios (2~5) and turbine inlet temperatures (typically less than 1000 °C) which make the part-load operation span of these systems different from large-scale gas turbines (with pressure ratios up to 25 and turbine inlet temperatures up to 1700 °C). The span of cycle parameter variations, especially with altering rotational speed, is smaller compared to large-scale gas turbines.
- Considering the low-pressure ratio as well as the small volumetric flow and small power rating, a single-stage radial compressor and turbine are usually used. Both components have different operational behavior from axial versions, which is the common configuration that is implemented in large-scale engines.
- If the micro gas turbine operates as a CHP or CCHP unit, the system includes a second heat exchanger that uses the remaining exhaust thermal energy after the recuperator. The available exhaust gas, typically around 300 °C, provides energy for water and space heating, cooling systems such as absorption chillers, and process heat applications. The implementation of an economizer adds more application flexibility as well as constraints to the cycle.
- The fuel flexibility of MGTs, although having environmental and financial advantages, poses certain challenges to MGT design and operation. For conventional cycles, the low calorific value of the fuels requires the implementation of a larger volumetric flow of fuel to achieve the design turbine inlet temperature. This will affect the original matching point with the compressor. Considering the common turbine



choking condition, the larger fuel flow rate results in lower demand for air from the compressor and, in general, an increase in compressor back-pressure and, therefore, lowering the surge margin [6]. On the other hand, a high air–fuel ratio within the primary combustion zone is required for achieving low emission levels at full-load conditions. Lean premix operation requires a large amount of air to be thoroughly mixed with fuel before combustion. This premixing of air and fuel enables clean combustion to occur at a relatively low temperature that is tolerated in uncooled turbines [61]. Therefore, some operational limitations are imposed on the fuel–air flow ratio considering the type of fuel that is injected into the engine.

All the above-mentioned aspects of MGTs lead to a different practice to improve theirs in comparison with large-scale gas turbines. MGTs and the MGT cycles need further development towards [6]:

- higher electrical efficiency;
- increased flexibility for integration with other systems;
- increased flexibility towards the utilization of various sources of energy.

Improving the efficiency, flexibility, and reliability of micro gas turbines could be pursued by two approaches:

- component level
- system level

The main components of the engine, namely the compressor, recuperator, combustor, and turbine, show great potential for improvement in MGTs. The recuperator is responsible for a significant fraction of the electrical efficiency; therefore, its performance and limitations are additional parameters to be considered for improvements. On the other hand, the materials that are used in recuperators impose limitations on flow temperature at the turbine outlet (and the turbine inlet and hence the power output). Focusing on new designs and materials for recuperators could contribute to the efficiency of MGTs.

MGTs as a backup for the renewable-dominant power system of the future will operate in part-load conditions as frequently as in full-load conditions. Therefore, it is essential to improve the efficiency of the compressor and turbine in off-design conditions along with the design point.

Combustion in MGTs occurs with lower equivalence ratios; the typical fuel–air ratio in MGTs is about an order of magnitude smaller than large-scale gas turbines. This means that the variation of flow properties in the flue gas in the case of replacing natural gas with hydrogen is small and, therefore, fewer complications are to be expected. The reason behind this is that flue gas properties of pure methane and pure hydrogen combustion diverge from each other as the equivalence ratio increases, yet in very lean combustions the difference is small. Focusing on hydrogen-driven MGTs will lead to building dispatchable units with zero carbon dioxide emissions. While fuel flexibility is an established advantage of MGTs, burning hydrogen and hydrogen-blended fuel is a goal to be accomplished by focusing on new technologies for combustion chambers.

Besides the component improvements, the system level improvements which are associated with the engine cycle and control of its operation could have a significant effect. Although MGTs are designed to run in cogeneration mode, the operation strategy is not mature and works the same as large-scale engines with addendums for cogeneration. The common design philosophy of operation control is based on sole electricity generation with an additional option of heat production. The controller runs the engine by focusing on power output and placing heat demand as the second priority. To improve the performance and operation efficiency of MGTs, it is essential to increase the flexibility of their operation by modifying the control and by setting the same priority for both heat and power generation.

As elaborated in the previous sections, the MGTs' main role in the future power generation industry is to provide support for intermittent renewable energy sources. Therefore, continuously monitoring MGTs' condition is important to maintain a reliable operation



and avoid unpredicted shutdowns. Engine online monitoring is essential for tracking key parameters that are linked to the engine's health condition. Deterioration in engine performance has to be detected in the early stages, as well as signs of potential engine faults. Proper measures should be recommended based on the detections to prevent penalties on engine performance or even its life cycle in more severe cases.

A fault refers to a condition of an engine with a change of the form of its component(s) and hence its performance, from its original design or its initial operation. An engine fault can manifest itself by a change of the geometrical characteristics and/or integrity of the material of its parts, such as fouling, corrosion, erosion, etc., in a compressor or turbine. Monitoring the condition of the engine and its performance during operation and analyzing the observations and sensor measurements can help with detecting those possible faults. Engine faults can have other reasons such as bearings' wear, insufficient cooling of bearings, combustor malfunction, etc. Usually, non-performance-based monitoring methods such as vibration and oil samples can help with the detection of these faults.

To properly monitor the health condition of an MGT, an accurate model which represents healthy operation, and a condition monitoring platform that compares the engine and the model outputs are required. A precise computer model of the engine imitating the whole cycle performance in full-load and part-loads must be employed. The healthy engine model could be physics-based [62,63] or data-driven, either way, the accuracy and speed of their prediction are the essential characteristics.

To develop a predictive model of the MGT cycle when a physics-based approach is chosen, a reduced order (0D and in some cases 1D) model is sufficient, as long as the maps and correlations that are implemented inside the components match the behavior of the actual healthy engine. To this end, a generic model of an MGT must be ready which could be tuned and become "adapted" to the actual engine during the first maneuvers of the operation. Once this model is tuned, then it works as a representative of a healthy engine and could be utilized as the core of condition monitoring platform. In [64] a review on cycle modeling of MGTs is presented, and in [63] a full process of accurate MGT model adaptation to experimental data is presented. Figure 10 shows the adaptation process which is titled "learning period". The model should run by the same power setpoint as the actual engine and then the outputs of MGT and the model are compared and used for modifying the model's tuning parameters, which are basically the calibration factors of the maps and correlations. This process will continue until the difference between the engine outputs and model results are closer than acceptable tolerance. If the data-driven approach is chosen for building the model, the process will be replaced by simple data-based model training, by the means of machine learning methods.

After the learning period is completed, the model must be utilized to provide inputs for the condition monitoring platform. In Figure 10, in the section "operation period", a structure for intelligent monitoring and control of MGT is proposed. The structure has three main poles: engine model, condition monitoring, and optimizer. The model is adapted to the healthy engine during the learning period, based on the initial operating hours of the MGT when it was assumed healthy. Then, a condition monitoring platform plays its role, which receives data from the engine as well as the model predictions.

The data-based condition monitoring can help with improving the reliability of the engine and reducing maintenance and operational expenditure by preventing harmful damages to the engine and avoiding unscheduled shutdowns. The advent of Industry 4.0 and the digitalization era provides the infrastructure for online collection and fast analysis of sensors' data to infer the condition of parts of the engine without dismantling the engine or getting direct access to its parts.

Artificial intelligence (AI) has demonstrated a powerful capacity in detecting and diagnosing faults of gas turbine engines [65]. Monitoring through AI is proven to be an effective method for shifting from classical "fail and fix" practices to a "predict and prevent" methodology. Enhanced analytics and AI-enabled algorithms can help identify out-of-band behavior to improve efficiency and help with keeping the balance between

energy supply and energy demand. AI techniques are quite useful when the problem is highly non-linear and a functional relationship between inputs and outputs is not easy to set up, or a quick response is required for real-time applications. Since physical problems of gas turbines have nonlinear and multidimensional characteristics, efforts to apply AI to performance prediction and fault detection and diagnosis of gas turbines have increased during the past decade [65,66].

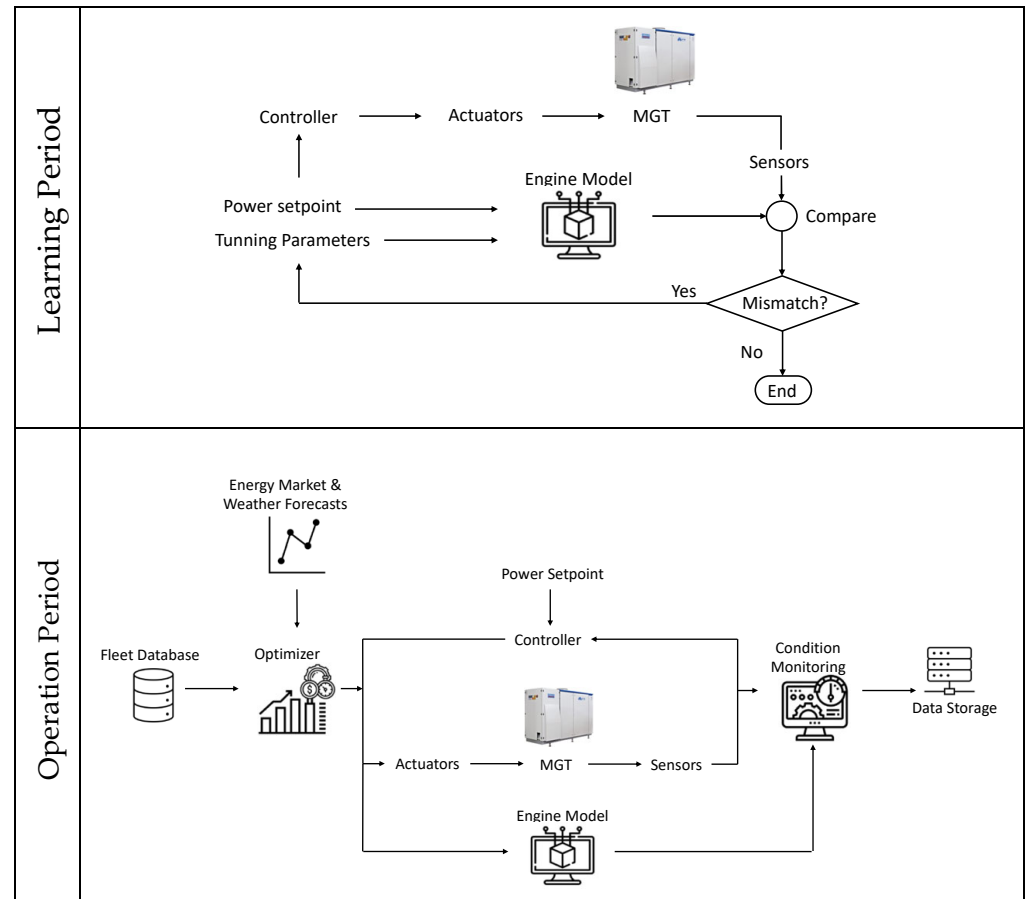


**Figure 10.** Micro gas turbine fleet control based on online condition monitoring.

The collected data in the condition monitoring platform of Figure 10 will be recorded and analyzed to estimate the health status of the MGT, which could improve the machinery maintenance strategy by employing statistical machine performance data and operational experience and hence prevent unexpected failure in the system. Online condition monitoring helps with predictive model improvements and, therefore, finding more optimized solutions for engine performance, which is the main role of the third pole of the system, the optimizer. Realizing the actual health condition of components of the engine, an adaptive control scheme can be employed to compensate for the effect of deterioration. The component degradation level is assessed by the variations in the available measurements; then the information about engine health conditions is employed to adopt modified control strategies that guarantee a safe operation and limit the reduction in performance efficiency.

The function of the optimizer is tied to the controller of the micro gas turbine. The controller's function is to command the engine to operate with a specific fuel flow rate and specific rotational speed, that generates the demanded power while keeping the engines' components safe. The controller parameters, however, are constant and usually designed based on the engine operating at its absolute healthy status. If the condition monitoring platform could provide information that indicates the engine's deviation from its initial health, these control parameters could be modified by the optimizer and lead to higher

efficiency and lifetime of the MGT. This flexibility of operation and increasing efficiency could be enhanced furthermore by adding flexibility to the cogeneration mode, as discussed previously. Inputs from weather and energy market forecast will be also beneficial to find the optimum operational strategy. The weather condition not only affects the fuel prices but also affects the amount and type of demand (i.e., electricity or heat).

It is useful to put the data from one engine into a database of the fleet of micro gas turbines, where the diagnosis information of each engine could be available for others. The changes in controller parameters and their effect on performance will be useful and provide guidelines. Other than diagnostics of the micro gas turbine, sharing information among the engines could be beneficial for prognostic purposes. In Figure 10, the data from condition monitoring are collected and stored in the fleet database which is called by the optimizer. With a sophisticated infrastructure to organize the data, the prospect of employing more intelligent operation strategies will be increased.

## 7. Conclusions

Micro gas turbines provide a reliable and cost-effective power source with a quick load-following ability which can respond to demand peaks and compensate for intermittent renewable sources when they are not available. MGT units can work as a system together with renewables, or function as a stand-alone unit in off-grid operations. MGTs are fuel flexible which can offer cost-effective electricity and heat production, especially with fluctuating fuel prices. As a small power plant that is utilized in private households or public buildings, MGTs offer low noise, easy operation, and highly reliable power generation units, which are the most important requirements for decentralized energy systems.

Combined heat and power systems based on MGTs have a higher share than micropower generators in the market due to the decentralized foundation of heat production. Moreover, the cogeneration of heat and power increases thermal energy conversion efficiency and reduces costs.

In this paper, the increasing role of micro gas turbines in the future of energy transition was investigated. The characteristics of micro gas turbines which make them a perfect choice as dispatchable standby unit for a renewable-dominant power generation scheme is reviewed. The challenges and places for further improvements that could accelerate the promotion of micro gas turbine was explained. Finally, a model for an active monitoring and control system of the micro gas turbine was proposed which could benefit from AI techniques to improve the reliability of micro gas turbines.

The continuous development and implementation of diagnostics can significantly reduce both the financial losses that are caused by system breakdown and the costs that are attributed to unnecessary repair and replacement of components. Moreover, the condition monitoring assessments could be provided to an optimizer that changes the operational strategy of the MGT controller, seeking higher efficiencies, a longer lifetime, or both. The integration of MGT cycle data with smart tools based on AI techniques can potentially increase the useful operational hours and thus higher investment returns. Digitalization based on intelligent tools is, therefore, needed to conduct real-time analysis, considering the key parameters such as components' conditions, power demand patterns, and market prices to identify a smart combination and deliver high efficiency from existing installations [60].

**Author Contributions:** Funding acquisition, M.A.; Supervision, M.A.; Writing an original draft, R.B.; Writing—review and editing, M.A. All authors have read and agreed to the published version of the manuscript.

**Funding:** This project has received funding from the European Union's Horizon 2020 research and innovation program under the Marie Skłodowska-Curie grant agreement No. 861079, "NextMGT"—Next Generation of Micro Gas Turbines for High Efficiency, Low Emissions and Fuel Flexibility.

**Conflicts of Interest:** The authors declare no conflict of interest.

## References

1. Alvarado, F.L. Locational Aspects of Distributed Generation. *IEEE Power Eng. Soc. Winter Meeting. Conf. Proc.* **2001**, *1*, 140. [CrossRef]
2. Silvestri, A.; Berizzi, A.; Milano, P. Distributed Generation Planning Using Genetic Algorithms. In *PowerTech Budapest 99. Abstract Records*; IEEE: Piscataway, NJ, USA, 1998; p. 257. [CrossRef]
3. Barker, P.P.; de Mello, R.W. Determining the Impact of Distributed Generation on Power Systems: Part 1—Radial Distribution Systems. In Proceedings of the 2000 Power Engineering Society Summer Meeting (Cat. No.00CH37134), Seattle, WA, USA, 16–20 July 2000; pp. 1645–1656.
4. Generation, A. Dispersed generation impact on distribution networks. *IEEE Comput. Appl. Power* **1999**, *12*, 22–28.
5. Ilic, M. The information technology (IT) role in future energy generation, distribution, and consumption. In *The Power Engineering Society Winter Meeting IEEE*; IEEE: Piscataway, NJ, USA, 2001; pp. 196–198.
6. *European Turbine Network (ETN) Micro Gas Turbine Technology, ETN Micro Gas Turbine Technology Summary*; ETN: Brussels, Belgium, 2018; Available online: [etn.globa](http://etn.globa) (accessed on 15 October 2022).
7. Owens, B.Y.B. The Rise of Distributed Power, General Electric Company. 2014. Available online: [legacy-assets.eenews.net](http://legacy-assets.eenews.net) (accessed on 15 October 2022).
8. El-Khattam, W.; Salama, M. Distributed generation technologies, definitions, and benefits. *Electr. Power Syst. Res.* **2004**, *71*, 119–128. [CrossRef]
9. Hanssen, J.; Riikonen, A.; Karlsson, G.; Stokholm, R.; Veland, B.J.; Pedersen, A. Operating Experiences from 18 Microturbine Applications for CHP and Industrial Purposes. *Engineering* **2004**, 1–20. Available online: <https://www.semanticscholar.org/paper/OPERATING-EXPERIENCES-FROM-18-MICROTURBINE-FOR-CHP-Hanssen-Riikonen/6aa7aeea2f6788359cad78e86c1a436c4a4af880> (accessed on 15 October 2022).
10. Suter, M. Active Filter for a Micro Turbine. In Proceedings of the Twenty-Third International Telecommunications Energy Conference INTELEC, Edinburgh, UK, 18 October 2001; pp. 162–165. [CrossRef]
11. Biomass Combined Heat and Power Catalog of Technologies. 2007. Available online: [www.epa.gov/chp](http://www.epa.gov/chp) (accessed on 15 October 2022).
12. Joh, L.; Del Monaco, P.E. The role of distributed generation in the critical electric power infrastructure. In Proceedings of the IEEE 2001 Winter Power Meeting, Columbus, OH, USA, 28 January–1 February 2001; pp. 144–145.
13. Paepe, W.D.e.; Delattin, F.; Bram, S.; Ruyck, J.D.e. Steam injection experiments in a microturbine—A thermodynamic performance analysis. *Appl. Energy* **2012**, *97*, 569–576. [CrossRef]
14. Ali, A.; Li, W.; Hussain, R.; He, X.; Williams, B.; Memon, A. Overview of Current Microgrid Policies, Incentives and Barriers in the European Union, United States and China. *Sustainability* **2017**, *9*, 1146. [CrossRef]
15. The Official Website of the European Union. 2030 Climate & Energy Framework | Climate Action. Available online: <https://ec.europa.eu> (accessed on 15 October 2022).
16. *ETN R&D Recommendation Report*; ETN Global: Brussels, Belgium, 2018. Available online: <https://etn.global/wp-content/uploads/2018/10/RD-Recommendation-Report-October-2018.pdf> (accessed on 15 October 2022).
17. Romankiewicz, J.; Marnay, C.; Zhou, N.; Qu, M. Lessons from international experience for China’s microgrid demonstration program. *Energy Policy* **2014**, *67*, 198–208. [CrossRef]
18. Ustun, T.S.; Ozansoy, C.; Zayegh, A. Recent developments in microgrids and example cases around the world—A review. *Renew. Sustain. Energy Rev.* **2011**, *15*, 4030–4041. [CrossRef]
19. Renewable Energy Agency I; IRENA. Global Renewables Outlook: Energy Transformation 2050, Abu Dhabi United Arab Emirates. 2020. Available online: [www.irena.org](http://www.irena.org) (accessed on 15 October 2022).
20. US EPA O. Catalog of CHP Technologies. September 2017. Available online: <https://www.epa.gov/chp/catalog-chp-technologies> (accessed on 15 October 2022).
21. Brauner, G.; D’Haeseleer, W.; Gehrler, W. Electrical Power Vision 2040. In *A Document from The EUREL Task Force*; EUREL: Brussels, Belgium, 2012; Available online: [www.eurel.org](http://www.eurel.org) (accessed on 15 October 2022).
22. Oltra, C.; Upham, P.; Riesch, H. Public Responses to CO<sub>2</sub> Storage Sites: Lessons from Five European Cases. *Energy Environ.* **2012**, *23*, 227–248. [CrossRef]
23. International Energy Agency. Energy Technology Perspectives 2014 Harnessing Electricity’s Potential. Available online: <http://www.iea.org> (accessed on 15 October 2022).
24. European Commission. Joint Research Centre, Brief on Biomass for Energy in the European Union. 2019. Available online: <https://data.europa.eu/doi/10.2760/546943> (accessed on 15 October 2022).
25. Lasseter, R.H. MicroGrids. In Proceedings of the 2002 IEEE Power Engineering Society Winter Meeting (Cat. No.02CH37309), New York, NY, USA, 27–31 January 2002; pp. 305–308. [CrossRef]
26. Aslanidou, I.; Rahman, M.; Zaccaria, V.; Kyprianidis, K.G. Micro Gas Turbines in the Future Smart Energy System: Fleet Monitoring, Diagnostics, and System Level Requirements. *Front. Mech. Eng.* **2021**, *7*, 51. [CrossRef]
27. Soshinskaya, M.; Crijns-Graus, W.H.; Guerrero, J.M.; Vasquez, J.C. Microgrids: Experiences, barriers and success factors. *Renew. Sustain. Energy Rev.* **2014**, *40*, 659–672. [CrossRef]
28. Bohn, D. *Micro Gas Turbine and Fuel Cell: A Hybrid Energy Conversion System with High Potential*; von Kármán Institute: Rhode-St-Genèse, Belgium, 2004; NATO Research & Technology Organisation, Report number: RTO-EN-AVT-131.



29. Colson, C.M.; Nehrir, M.H. A review of challenges to real-time power management of microgrids. In Proceedings of the IEEE Power and Energy Society General Meeting, PES '09, Calgary, Canada, 26–30 July 2009. [CrossRef]
30. Bhaskara, S.N.; Chowdhury, B.H. Microgrids—A review of modeling, control, protection, simulation, and future potential. In Proceedings of the IEEE Power and Energy Society General Meeting, San Diego, CA, USA, 22–26 July 2012. [CrossRef]
31. Energy Statistics—An Overview. 2018. Available online: <https://ec.europa.eu> (accessed on 15 October 2022).
32. Commission Recommendation (EU). 2016/1318 of 29 July 2016 on Guidelines for the Promotion of Nearly Zero-Energy Buildings and Best Practices to Ensure That, by 2020, all New Buildings are Nearly Zero-Energy Buildings, OJ L 208 02.08.2016. p. 46. Available online: <http://data.europa.eu/eli/reco/2016/1318/oj> (accessed on 15 October 2022).
33. Gros, S.; Jakus, D.; Vasilj, J.; Zanon, M. Day-ahead scheduling and real-time economic MPC of CHP unit in microgrid with smart buildings. *IEEE Trans Smart Grid* **2019**, *10*, 1992–2001. [CrossRef]
34. Kelly, K.A.; McManus, M.C.; Hammond, G.P. An energy and carbon life cycle assessment of industrial CHP (combined heat and power) in the context of a low carbon UK. *Energy* **2014**, *77*, 812–821. [CrossRef]
35. Chilvers, J.; Foxon, T.J.; Galloway, S. Realising transition pathways for a more electric, low-carbon energy system in the United Kingdom: Challenges, insights, and opportunities. *Proc. Inst. Mech. Eng. Part A J. Power Energy* **2017**, *231*, 440–477. [CrossRef]
36. Facchini, A. Distributed energy resources: Planning for the future. *Nat. Energy* **2017**, *2*, 17129. [CrossRef]
37. Björnebo, L.; Spatari, S.; Gurian, P.L. A greenhouse gas abatement framework for investment in district heating. *Appl. Energy* **2018**, *211*, 1095–1105. [CrossRef]
38. Williams, J.H.; DeBenedictis, A.; Ghanadan, R. The technology path to deep greenhouse gas emissions cuts by 2050: The pivotal role of electricity. *Science* **2012**, *335*, 53–59. [CrossRef]
39. Fais, B.; Sabio, N.; Strachan, N. The critical role of the industrial sector in reaching long-term emission reduction, energy efficiency, and renewable targets. *Appl. Energy* **2016**, *162*, 699–712. [CrossRef]
40. Jägemann, C.; Fürsch, M.; Hagspiel, S.; Nagl, S. Decarbonizing Europe’s power sector by 2050—Analyzing the economic implications of alternative decarbonization pathways. *Energy Econ.* **2013**, *40*, 622–636. [CrossRef]
41. Tokimatsu, K.; Yasuoka, R.; Nishio, M. Global zero emissions scenarios: The role of biomass energy with carbon capture and storage by forested land use. *Appl. Energy* **2017**, *185*, 1899–1906. [CrossRef]
42. Kaplan, P.O.; Witt, J.W. What is the role of distributed energy resources under scenarios of greenhouse gas reductions? A specific focus on combined heat and power systems in the industrial and commercial sectors. *Appl. Energy* **2019**, *235*, 83–94. [CrossRef] [PubMed]
43. Resource Dynamics Corporation. *Cooling, Heating, and Power for Industry: A Market Assessment*; Resource Dynamics Corporation: Vienna, Austria, 2003.
44. Liu, M.; Shi, Y.; Fang, F. Combined cooling, heating and power systems: A survey. *Renew. Sustain. Energy Rev.* **2014**, *35*, 1–22. [CrossRef]
45. Zampilli, M.; Bidini, G.; Laranci, P.; D’Amico, M.; Bartocci, P.; Fantozzi, F. Biomass Microturbine Based EFGT and IPRP Cycles: Environmental Impact Analysis and Comparison. In Proceedings of the ASME Turbo Expo. Vol. 3. American Society of Mechanical Engineers Digital Collection, Charlotte, NC, USA, 26–30 June 2017. [CrossRef]
46. Nascimento, M.A.R.D.; de, L.; dos Santos, E.C.; Gomes, E.E.B.; Goulart, F.L.; Velsques, E.I.G.; Miranda, R.A. Micro Gas Turbine Engine: A Review. In *Progress in Gas Turbine Performance*; Ernesto, B., Ed.; IntechOpen: London, UK, 2013. [CrossRef]
47. Ismail, M.S.; Moghavvemi, M.; Mahlia, T.M.I. Current utilization of microturbines as a part of a hybrid system in distributed generation technology. *Renew. Sustain. Energy Rev.* **2013**, *21*, 142–152. [CrossRef]
48. Saravanamuttoo, H.; Rogers, C.; Cohen, H.; Straznicky, P. *Gas Turbine Theory*, 6th ed.; Prentice Hall: Hoboken, NJ, USA, 2009.
49. Rodgers, C.; Watts, J.; Thoren, D.; Nichols, K.; Brent, R. *Microturbines. Distributed Generation: The Power Paradigm for the New Millennium*; Borbely, A.M., Kreider, J.F., Eds.; CRC Press: Boca Raton, FL, USA, 2013; pp. 119–150.
50. Lammel, O.; Schmitz, G.; Aigner, M.; Krebs, W. FLOX<sup>®</sup> Combustion at High Power Density and High Flame. *ASME J. Eng. Gas Turbines Power* **2010**, *132*, 121503. [CrossRef]
51. Lücknerath, R.; Meier, W.; Aigner, M. FLOX combustion at high pressure with different fuel compositions. *ASME Turbo Expo 2007 Power Land Sea Air* **2007**, *1*, 1–9. [CrossRef]
52. Reinert, N. Combined Heat and Power-Technology Review and Analysis for a Residential Building. Master’s Thesis, University of Tennessee at Chattanooga, Chattanooga, TN, USA, 2012.
53. Goldstein, L.; Hedman, B.; Knowles, D.; Freedman, S.I.; Woods, R.; Schweizer, T. *Gas-Fired Distributed Energy Resource Technology Characterizations*; National Renewable Energy Lab.: Golden, CO, USA, 2003. [CrossRef]
54. Chan, T.F.; Lai, L.L. Permanent-magnet machines for distributed power generation: A review. In Proceedings of the 2007 IEEE Power Engineering Society General Meeting, Tampa, FL, USA, 24–28 June 2007; pp. 1–6. [CrossRef]
55. Liss, W.E. Natural Gas Power Systems for The Distributed Generation Market. In Proceedings of the Power-Gen International 99 Conference, Burlingame, CA, USA, 25–28 July 1999.
56. Leal-Arcas, R.; Rios, J.A.; Akondo, N. Energy Decentralization in the European Union. *Georget. Environ. Law Rev.* **2019**. Available online: [https://papers.ssrn.com/sol3/papers.cfm?abstract\\_id=3333694](https://papers.ssrn.com/sol3/papers.cfm?abstract_id=3333694) (accessed on 15 October 2022).
57. McDonald, C.F. Low-cost compact primary surface recuperator concept for microturbines. *Appl. Therm. Eng.* **2000**, *20*, 471–497. [CrossRef]
58. Pilavachi, P.A. Mini- and micro-gas turbines for combined heat and power. *Appl. Therm. Eng.* **2002**, *22*, 2003–2014. [CrossRef]

59. Kolanowski, B.F. Introduction and History of the Microturbine. In *Guide to Microturbines*; River Publishers: Gistrup, Denmark, 2004; pp. 1–12. Available online: <https://ieeexplore.ieee.org/document/9558413> (accessed on 15 October 2022).
60. Next Generation of Micro Gas Turbines for High Efficiency, Low Emissions, and Fuel Flexibility. 2020. Available online: <https://cordis.europa.eu/project/id/861079> (accessed on 15 October 2022).
61. Corporation, C.T. Capstone Low Emissions MicroTurbine Technology, White Paper Capstone Corporation, California USA, 6 March 2000. Available online: [www.bioturbine.org](http://www.bioturbine.org) (accessed on 15 October 2022).
62. Banihabib, R.; Assadi, M. *Dynamic Modelling and Simulation of a 100 kW Micro Gas Turbine Running with Blended Methane/Hydrogen Fuel*; ASME Turbo Expo: Rotterdam, The Netherlands, 2022.
63. Banihabib, R.; Obrist, M.J.; Assadi, M.; Jansohn, P. *Micro Gas Turbine Modelling and Adaptation for Condition Monitoring*; Global Power and Propulsion: Chania, Greece, 2022.
64. Pinelli, M.; Suman, A.; Casari, N.; Reale, F.; Sannino, R. Numerical Modeling of Energy Systems Based on Micro Gas Turbine: A Review. *Energies* **2022**, *15*, 900. [[CrossRef](#)]
65. Kanelopoulos, K.; Stamatis, A.; Mathioudakis, K. Incorporating neural networks into gas turbine performance diagnostics. In *ASME 1997 International Gas Turbine and Aeroengine Congress and Exhibition. Volume 4: Manufacturing Materials and Metallurgy*; IGTI Scholar Award: Orlando, FL, USA, 1997. [[CrossRef](#)]
66. Volponi, A.J.; Sundstrand, H.; Ganguli, R.; Daguang, C. The Use of Kalman Filter and Neural Network Methodologies in Gas Turbine Performance Diagnostics: A Comparative Study. In *Power for Land, Sea, and Air. Volume 4: Manufacturing Materials and Metallurgy*; Diagnostics and Instrumentation Education: Munich, Germany, 2000. [[CrossRef](#)]

## Paper II

Development and testing of a 100 kW fuel-flexible micro gas turbine running on 100% hydrogen

R. Banihabib, T. Lingstädt, M. Wersland, P. Kutne, and M. Assadi.

International Journal of Hydrogen Energy, vol. 49, pp. 92–111, Jan. 2024, doi: 10.1016/j.ijhydene.2023.06.317.

Available online at [www.sciencedirect.com](http://www.sciencedirect.com)

ScienceDirect

journal homepage: [www.elsevier.com/locate/hydro](http://www.elsevier.com/locate/hydro)

# Development and testing of a 100 kW fuel-flexible micro gas turbine running on 100% hydrogen

Reyhaneh Banihabib<sup>a,\*</sup>, Timo Lingstädt<sup>b</sup>, Magnus Wersland<sup>a</sup>,  
Peter Kutne<sup>b</sup>, Mohsen Assadi<sup>a</sup>

<sup>a</sup> Faculty of Science and Technology, University of Stavanger, Stavanger, Norway

<sup>b</sup> German Aerospace Center (DLR), Germany

## HIGHLIGHTS

- Hydrogen's potential as an alternative, carbon-free fuel for micro gas turbines is assessed.
- The obstacles of utilizing hydrogen fuel in a micro gas turbine are addressed and the necessary modifications are presented.
- Data from successful tests of a micro gas turbine running on hydrogen blends ranging up to 100% hydrogen is presented.
- NOx emissions below the standard limits were achieved with the new setup.
- The study's outcomes could aid researchers and developers in incorporating hydrogen as a carbon-free energy carrier.

## ARTICLE INFO

### Article history:

Received 28 February 2023

Received in revised form

28 April 2023

Accepted 27 June 2023

Available online 13 July 2023

### Keywords:

Micro gas turbine

Hydrogen fuel

Development and test

Clean fuel

Energy transition

## ABSTRACT

Hydrogen, as a carbon-free energy carrier, has emerged as a crucial component in the decarbonization of the energy system, serving as both an energy storage option and fuel for dispatchable power generation to mitigate the intermittent nature of renewable energy sources. However, the unique physical and combustion characteristics of hydrogen, which differ from conventional gaseous fuels such as biogas and natural gas, present new challenges that must be addressed.

To fully integrate hydrogen as an energy carrier in the energy system, the development of low-emission and highly reliable technologies capable of handling hydrogen combustion is imperative. This study presents a ground-breaking achievement - the first successful test of a micro gas turbine running on 100% hydrogen with NOx emissions below the standard limits. Furthermore, the combustor of the micro gas turbine demonstrates exceptional fuel flexibility, allowing for the use of various blends of hydrogen, biogas, and natural gas, covering a wide range of heating values. In addition to a comprehensive presentation of the test rig and its instrumentation, this paper illuminates the challenges of hydrogen combustion and offers real-world operational data from engine operation with 100% hydrogen and its blends with methane.

© 2023 The Authors. Published by Elsevier Ltd on behalf of Hydrogen Energy Publications LLC. This is an open access article under the CC BY-NC-ND license (<http://creativecommons.org/licenses/by-nc-nd/4.0/>).

\* Corresponding author.

E-mail addresses: [Reyhaneh.Banihabib@uis.no](mailto:Reyhaneh.Banihabib@uis.no) (R. Banihabib), [Timo.Lingstaedt@dlr.de](mailto:Timo.Lingstaedt@dlr.de) (T. Lingstädt), [Magnus.Wersland@uis.no](mailto:Magnus.Wersland@uis.no) (M. Wersland), [Peter.Kutne@dlr.de](mailto:Peter.Kutne@dlr.de) (P. Kutne), [Mohsen.Assadi@uis.no](mailto:Mohsen.Assadi@uis.no) (M. Assadi).

<https://doi.org/10.1016/j.ijhydene.2023.06.317>

0360-3199/© 2023 The Authors. Published by Elsevier Ltd on behalf of Hydrogen Energy Publications LLC. This is an open access article under the CC BY-NC-ND license (<http://creativecommons.org/licenses/by-nc-nd/4.0/>).



## Nomenclature

### Alphanumeric Variables

$c_p$	Specific heat of gas at constant pressure (J/kg K)
$\dot{m}$	Mass flow rate (kg/s)
$N$	Relative rotational speed [%]
$P$	Power (kW)
$p$	Pressure [bar]
$T$	Temperature (K)
$V$	Valve position [%]

### Greek Symbols

$\rho$	Density (kg/m <sup>3</sup> )
$\phi$	Equivalence ratio

### Indices

comb	Combustor
f	Fuel
nom	Nominal
norm	Normalized

### Abbreviations

AF	Adiabatic Flame
LHV	Lower heating value
MGT	Micro gas turbine
TIT	Turbine inlet temperature
TOT	Turbine outlet temperature

## Introduction

Micro gas turbine (MGT) engines with a power output between 3 and 300 kW are instrumental in decentralized power generation, due to their reliability and ability to quickly respond to changes in load, making them an ideal backup option for intermittent renewables [1,2]. Their compact size, lightweight, and low installation and maintenance cost further strengthen MGT's position as a power generator in the future's distributed power system. Today's MGTs can run on a variety of fuels, from high-heating value fuels like methane and natural gas to lower-heating value fuels like biogas.

Despite the fuel-flexibility of MGTs providing a wide range of options, greenhouse gas emissions from carbon-based fuels continue to be a concern. Using carbon-free fuels, such as hydrogen, or carbon-neutral fuels is the most efficient way to achieve zero net CO<sub>2</sub> emissions in an MGT, given the difficulties associated with capturing CO<sub>2</sub> due to its low partial pressure [3]. The shift from the current power generation infrastructure, which primarily relies on carbon-based fuels, necessitates bridging technologies such as fuel-flexible MGTs that can work with blended fuels containing high levels of hydrogen [4].

Hydrogen fuel has the potential to significantly contribute to the shift towards a more sustainable and low-carbon energy system in the heat and power generation sector. The advantage of using hydrogen in power generation is its ability to significantly decrease greenhouse gas emissions and enhance air quality, as it only releases water vapor during combustion, in contrast to traditional fossil fuels like coal and natural gas, which emit harmful pollutants. By using

hydrogen as an energy storage solution, excess energy generated from renewable sources can be saved and utilized at a later time, ensuring a consistent and dependable energy supply even when renewable sources are unavailable [5].

Many research and development initiatives have been carried out on both large-scale and small-scale gas turbine units to address the challenges of using pure hydrogen or hydrogen-blended fuels. In 1998, Morris et al. published a paper [6] that presented their findings on incorporating hydrogen into heavy-duty gas turbines that were originally powered by natural gas. According to the authors, adding 10% hydrogen did not impact NO<sub>x</sub> emissions, but it reduced carbon monoxide production.

Shih et al. [7] conducted a study using computer simulation to evaluate the impact of hydrogen combustion in micro gas turbines. The authors employed computational fluid dynamics to examine the burning features of mixed fuels with different hydrogen volumetric fractions (ranging from 0 to 90%) in a can combustor that was initially designed for natural gas. Several case scenarios were tested to fuel the engine, and the results indicated steady combustion performance. However, the researchers found that modifications to the combustor design were necessary to tackle emissions since the original design was found to be insufficient [7].

In another study by Imteyaz et al. [8], a series of experiments were conducted to investigate the combustion behaviour of hydrogen-enriched methane fuel in a swirl-stabilized type gas-turbine combustor. The researchers increased the amount of hydrogen in the blended fuel up to 80% by volume and derived upper and lower limits for providing air to maintain stable combustion.

Rajpara et al. [9] performed both experimental and numerical investigations to assess the effect of hydrogen injection on a gas turbine with an upward swirl combustor running on methane fuel. The study found that increasing hydrogen content resulted in smaller flame dimensions but higher NO<sub>x</sub> emissions due to higher flame temperature, as well as a decrease in CO emissions.

Minakawa et al. [10] designed a prototype of a lean pre-mixed swirling flame combustor for a micro gas turbine to operate with pure hydrogen. The combustor was tested at atmospheric pressure and demonstrated high combustion efficiency and low NO<sub>x</sub> emissions. It was then installed on a micro gas turbine to assess its performance in actual conditions. During engine startup, flashbacks were observed which had not been seen in previous component tests. By controlling the airflow to the combustor, the flashbacks were prevented, and the engine achieved self-sustaining operation. The results of the study confirmed the excellent combustion performance of the micro gas turbine, including heat release rate, combustion efficiency, and low NO<sub>x</sub> emissions in lean conditions [10].

Cappelletti et al. [11] conducted a study to investigate the combustion of pure hydrogen in a lean premix burner using both experimental and numerical simulation methods. The experimental setup was based on a pre-existing burner from a heavy-duty gas turbine and was modified to allow for variable premixing levels. The study found that to avoid flame positioning inside the premix duct, high flow velocity was required during hydrogen combustion. The results indicated the potential for developing combustion technology using

pure hydrogen fuel while maintaining emissions within the regulated limits.

In May 2020, Kawasaki successfully tested an industrial gas turbine with hydrogen fuel using their dry low emission combustion technology. The combustor employs micro-mix combustion technology that utilizes ultra-small hydrogen-fueled flames and achieves low NO<sub>x</sub> combustion without the need for water or steam, which is beneficial in terms of cycle efficiency [12,13].

In this paper, the process of transforming a commercial micro gas turbine to run on blended methane/hydrogen fuel is outlined in detail. The project began in September 2021 in Stavanger, Norway, where a 100-kW micro gas turbine was modified to operate on a blend of hydrogen and methane. During the first phase, a hydrogen content of up to 30% on a volume basis was achieved, leading to unstable operation due to combustion instabilities at high power rates. The findings from phase 1 can be found in Ref. [14]. In the second phase, the combustion chamber and fuel control system were reengineered to handle higher hydrogen content and operate at higher power rates. All the modifications made to the system are described and illustrated in the paper. The engine was run on 100% hydrogen fuel and produced NO<sub>x</sub> emissions below regulatory standards, as demonstrated by the data collected from the sensors, which is presented in the paper.

In the following sections, first, the main challenges of the work are described, followed by the methods and approaches to overcome them. Lastly, the experimental results from running the MGT with a high hydrogen content of up to 100% are presented and discussed. Throughout the article, the content of hydrogen is presented as percentages of the whole fuel based on volume.

## Challenges of running an Mgt with hydrogen

The transformation of a gas turbine engine, including MGTs, to run on alternative fuels presents numerous challenges. The unique characteristics of hydrogen combustion require adjustments to both the combustor and other components of the system to ensure secure and stable operation while adhering to emission regulations. The difficulties associated with operating MGTs with hydrogen or hydrogen-blended fuels can be categorized into two distinct areas.

- The change in combustion properties of hydrogen compared to traditional fossil fuels, which affects the design and function of the combustor, i.e., challenges at the component level.
- Challenges related to the modification of the flow characteristics as a result of variations in combustion products and their impact on engine performance, i.e., challenges at the system level.

In this section, an overview of those challenges is provided.

### Component-level complications

Provided in Table 1 is an outline of the physical and chemical properties of hydrogen and methane, serving to contrast the

combustion characteristics of hydrogen fuel. Variations in these properties create differences in combustion characteristics between the two fuels, necessitating distinct combustor designs. Developing combustor technology for hydrogen combustion becomes even more complex when the objective is to operate with both pure hydrogen and hydrogen-blended fuels.

The hydrogen molecule has a light weight and a broad flammability range, which makes it suitable for use in gas turbine engines. It has the ability to burn in a mixture with an equivalence ratio of 0.1 in lean conditions, and up to 7.1 in rich conditions, allowing for a wide range of power outputs at different air-fuel ratios. The values presented in Table 1 are under atmospheric conditions, however, it is important to note that the lower limit of flammability increases under high-pressure conditions and decreases with higher temperatures. As a result of these opposing effects, the lower flammability limit of hydrogen in a micro gas turbine is higher than 0.1 but lower than methane under the same thermodynamic conditions, according to Ref. [16].

Hydrogen and methane have a significant difference in their minimum required ignition energy, with hydrogen being about 10 times lower in atmospheric conditions than methane. This high ignition temperature of methane and its slow flame propagation temperature can pose difficulties in ignition and maintaining stable combustion in low-load ranges of gas turbines. The addition of hydrogen holds the potential in enhancing combustion performance with regard to efficiency and stability as shown in studies [8,17–20]. It has been observed that an increase in the hydrogen share results in an increase in laminar burning velocity [21]. This is expected to result in a more stable flame, reducing the risk of flame-out in lean combustion conditions [22]. The broad flammability limits, high flame speeds, and low required ignition energy of hydrogen make it beneficial for hydrogen engine efficiency. Researchers have found that using hydrogen as a supplementary fuel to hydrocarbons can enhance the ignitability and flammability of lean premixed combustors and potentially allow for stable lean burn at lower temperatures [17,18]. Blending hydrogen with hydrocarbon fuels has the potential to improve flame stability in lean conditions with low temperatures, which in turn could help to reduce NO<sub>x</sub> emissions [18,19].

The laminar flame speed, which is an indicator of the burning rate, can have a significant impact on combustion

**Table 1 – Comparison of the properties of hydrogen and methane in atmospheric pressure and 300 K temperature [15].**

Property	Methane	Hydrogen
Molecular weight	16.04 g/mol	2.02 g/mol
Density	0.65 kg/m <sup>3</sup>	0.08 kg/m <sup>3</sup>
Lower heating value (per mass)	50 MJ/kg	120 MJ/kg
Stoichiometric air/fuel ratio	17.1 kg/kg	34.2 kg/kg
Minimum ignition energy	0.28 mJ	0.02 mJ
Flammability limits	0.5 ~ 1.67	0.1 ~ 7.1
Stoichiometric air-to-fuel ratio (kg/kg)	17.1	34.1
Stoichiometric air-to-fuel ratio (kmol/kmol)	59.7	2.4

efficiency and serves as the basis of turbulent combustion. In essence, the laminar flame speed represents the propagation rate of the flame front relative to the unburned mixture. Determining values for laminar flame speeds can provide validation targets for chemical kinetic models or be used in turbulent combustion models [20].

Zhou et al. [23] conducted numerical and experimental investigations to study the effect of fuel composition on combustion kinetics, for different equivalence ratios (0.6–1.5) and pressures (0.1–0.5 MPa), with a wide range of H<sub>2</sub>/CO/CH<sub>4</sub> compositions. Their research showed that increasing the H<sub>2</sub> content in the fuel significantly promotes fuel reaction activity, which in turn increases the laminar flame speed. Additionally, the study found that increasing pressure resulted in a reduction in flame speed.

The addition of hydrogen to the fuel mix also results in a change in the adiabatic flame temperature, which increases as the hydrogen content increases [23,24]. The temperature will rise with the equivalence ratio ( $\phi$ ) until reaching its peak, which occurs in slightly rich conditions ( $\phi \approx 1.05$ ). Beyond that point, the adiabatic flame temperature decreases as the mixture becomes richer because the specific heat value of the combustion products decreases at a faster rate than the heat release rate. The introduction of hydrogen into a methane mix will cause an increase in the adiabatic flame temperature [22] as hydrogen will speed up the reaction rate [25].

The production of toxic nitrogen oxides, also known as thermal NO<sub>x</sub> formation, is a concern in combustion processes with high flame temperatures. The oxidation of nitrogen molecules in the air occurs as the fuel burns at high temperatures, leading to the formation of NO<sub>x</sub>. Research has shown that a significant amount of NO<sub>x</sub> formation occurs around 1800 K and the rate of production increases rapidly with further temperature rise [26].

In gas turbines that use hydrocarbon-based fuels, the problem of high flame temperatures is addressed by premixing the fuel with air before combustion, thereby keeping the flame temperature below a certain value without affecting efficiency [27]. This approach is known as lean premixed burners or dry low NO<sub>x</sub> burners, which however, face several critical issues during fuel premixing, such as combustion instabilities, flashbacks, extinction, and thermo-acoustic instabilities [28,29].

The utilization of hydrogen or hydrogen-enriched fuels in gas turbines requires rethinking the design of the combustors, due to the large differences in flammability range and reaction rates between hydrogen and hydrocarbons [30]. The quick ignition of hydrogen before adequate premixing with air will result in high flame temperatures, promoting NO<sub>x</sub> formation.

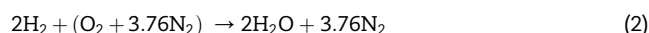
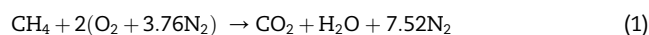
Another aspect to consider when examining the effects of hydrogen addition to fuel is its impact on CO emissions. Carbon monoxide production in a gas turbine is primarily a result of the incomplete combustion of hydrocarbon fuel and is therefore inversely proportional to the flame temperature [31]. It is believed that the addition of hydrogen to the fuel blend will result in a decrease in CO emissions because there will be fewer carbon elements present and the flame temperature will be higher in the presence of hydrogen, given that the equivalence ratios are the same in both cases [32].

## System-level complications

The properties of hydrogen and methane, which are distinct from each other, have an influence on the combustion behaviour as previously discussed. Variations in fuel flow rate are expected as a result of differences in heating value and density between the two fuels. In addition, the altered flow properties resulting from the different combustion products could potentially have an impact on the thermodynamics of the MGT cycle, as outlined in Refs. [33,34].

To assess the impact of the difference in properties between hydrogen and methane on the combustion characteristics, a comparative assessment is carried out based on the design point of the cycle. This assessment is performed by running the MGT at baseload and ISO conditions. The flue gas properties are analysed over a range of equivalence ratios for both methane and hydrogen combustion using Cantera software [35]. The air is mixed with the fuel in different equivalence ratios while keeping the pressure constant. This mixture equilibrates at 21% oxygen and 79% nitrogen, with a pressure of 4.3 bar and a temperature of 610 K. The results of these calculations are shown in Fig. 1, which illustrates the adiabatic flame temperature, the specific heat capacity at constant pressure, and the density of the flue gas for both fuels. The results show that the differences in flue gas properties between methane and hydrogen combustion become more pronounced as the mixture becomes richer.

In theory, the combustion process of methane will result in the production of steam and carbon dioxide which will then be mixed with the water and nitrogen content in the air, as described in Eq. (1). On the other hand, the combustion process of hydrogen will result in the production of only steam, as described in Eq. (2).



In reality, the combustion process of both methane and hydrogen fuels can result in the production of toxic nitrogen oxides, carbon monoxides, and other radicals, which can alter the composition and properties of the flue gas produced. To account for these factors, a computational tool known as Cantera is used to calculate the chemical potential of each element present in the flue gas [35]. The tool uses a mixture of fuel and air and sets it to a state of chemical equilibrium. It then employs a stoichiometric algorithm to determine the intermediate states that meet the constraints of each element, though they are not necessarily in a state of chemical equilibrium [35].

In Fig. 1, the differences in the flue gas properties are shown to be closely related to the equivalence ratio. To determine the conditions that exist in the current MGT, it is necessary to evaluate the value of the equivalence ratio. To produce 100 kW of power with 30% efficiency, the fuel flow rate is calculated based on the heat input required. Using 50 MJ/kg of lower heating value (LHV) for methane, 6.7 g/s of methane is needed and an equivalence ratio of 0.14 is achieved. The adiabatic flame temperature of the flue gas under these conditions is recorded as 1230.5 K, with a density of

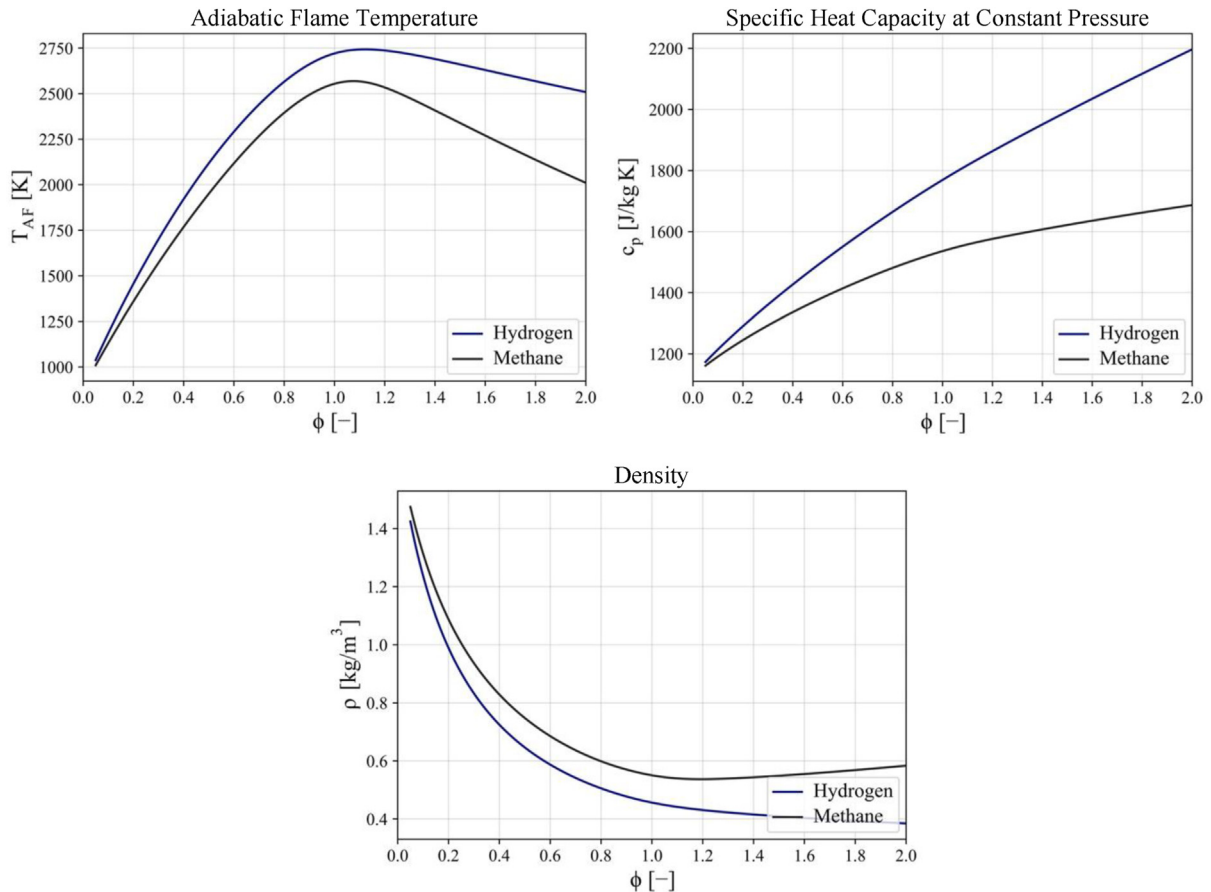


**Fig. 1** – Flue gas properties in different equivalence ratios for burning methane and hydrogen with air at 4.3 bar and 610 K.

1.21 kg/m<sup>3</sup> and a specific heat at a constant pressure of 1214.8 J/kg K.

To have an assessment of the case with pure hydrogen, first, it is assumed that the air enters the combustor with the same pressure and temperature. If the flue gas properties show a significant difference, it means the matching point will alter in a way that the original assumption was not correct.

The hydrogen fuel rate is calculated based on equal heat input and 120 MJ/kg of LHV. This leads to 2.8 g/s of hydrogen which with assumed 0.8 kg/s of the air inlet, an equivalence ratio of 0.12 will be realized. The adiabatic temperature will be 1236.51 K with 1.18 kg/m<sup>3</sup> density and 1228.8 J/kg K of specific heat. All these values and the composition of products are provided in [Table 2](#).

**Table 2** – Flue gas properties comparison for methane and hydrogen. Air with 21% O<sub>2</sub> and 79% N<sub>2</sub> at 4.3 bar and 610 K.

Property	Methane	Hydrogen
Fuel flow rate for nominal power output	6.7 g/s	2.8 g/s
Air flow rate	0.8 kg/s	0.8 kg/s
Flue gas mass flow rate	0.8076 kg/s	0.8028 kg/s
Flue gas density	1.2046 kg/m <sup>3</sup>	1.1815 kg/m <sup>3</sup>
Flue gas flow rate	0.67 m <sup>3</sup> /s	0.68 m <sup>3</sup> /s
Stoichiometric air fuel ratio	17.12	34.06
Actual air fuel ratio	120	288
Equivalence ratio	0.14	0.12
Adiabatic flame temperature	1230.52 K	1236.51 K
Flue gas heat capacity at constant pressure	1214.8 J/kgK	1228.8 J/kgK
Mass fraction of N <sub>2</sub>	0.75587	0.76423
Mass fraction of O <sub>2</sub>	0.17352	0.20459
Mass fraction of H <sub>2</sub> O	0.03138	0.03092
Mass fraction of CO <sub>2</sub>	0.03834	0.00000
Mass fraction of NO and NO <sub>2</sub> (sum)	< 0.001	< 0.001



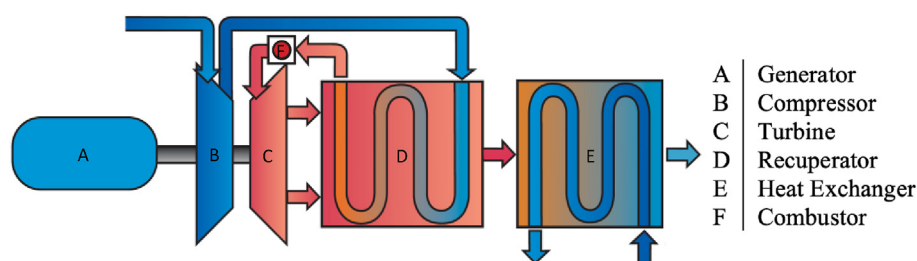


Fig. 2 – Schematic of the components in AE-T100 PH micro gas turbine.

Shifting the fuel from methane to hydrogen has increased the temperature by around  $6^\circ$  and with the changes in the density, the volumetric flow rate at the turbine is changed from  $0.67 \text{ m}^3/\text{s}$  to  $0.68 \text{ m}^3/\text{s}$  (a 1.5% increase). The specific heat capacity of the flue is increased by 1%. These minor changes are due to lean combustion ( $\phi < 0.15$ ) in the MGT, so the impact of fuel alteration on the composition of the flue gas is minor as the largest share of it is the excess air. For gas turbines with air to fuel ratios lower than MGTs, the variation of flow properties is expected to be higher [33].

Although the assessments were conducted using a reduced order model, it provides the basis for cycle evaluation, as they are also usually conducted by zero-dimensional or one-dimensional models. Even with this level of accuracy, it could be concluded that the fuel shift from methane to hydrogen will have a minor effect on the flow entering the turbine section and therefore only small variations in cycle points are expected thanks to the low fuel-air ratios in the MGT.

The following section presents an overview of the experimental setup of the micro gas turbine with details on the modifications implemented to enable running the engine with hydrogen blended fuel. Each of the challenges described previously has been addressed during the modifications described.

## Development of Mgt running with hydrogen fuel

### T100 PH micro gas turbine

The Turbec T100 PH micro gas turbine is a commercial engine used for the production of both power and heat. The engine consists of a single-stage centrifugal compressor, a single-stage radial turbine, and a single tubular combustor. It operates based on the regenerative Brayton cycle, where the heat from the hot gas that exits the turbine is transferred to the air entering the combustor via a recuperator. In addition to the recuperator, the engine is also equipped with a gas/water heat exchanger, which makes use of the remaining heat in the exhaust gas to warm up the recirculating water. The permanent magnet generator present in the engine enables it to run with a variable rotational speed.

To produce a desired power output, the controller of the T100 PH utilizes two main parameters: fuel flow rate and rotational speed. The engine is run to produce the demanded

power, while maintaining the turbine outlet temperature below the maximum allowed value to prevent damage to the hot components of the engine due to high temperatures.

The Turbec T100 PH micro gas turbine has the capability to produce 100 kW of power at ISO conditions with a pressure ratio of 4.3, a turbine inlet temperature of  $960^\circ\text{C}$ , and a rotational speed of 70,000 rpm. The engine operates within the range of power outputs and the controller manages this by adjusting the fuel flow rate and rotational speed. To ensure the endurance of the hot components in the engine, the turbine outlet temperature (TOT) must be maintained below a maximum allowed value of  $645^\circ\text{C}$ , which is the nominal load. A schematic representation of the main components of the T100 PH unit can be seen in Fig. 2.

A T100 PH unit has been installed in the Risavika gas centre located in Stavanger, Norway. This unit has been the subject of various research projects in the past. The most recent program aimed to expand the operation of the micro gas turbine to a wider range of fuel types, including hydrogen-enriched fuels and ultimately pure hydrogen. To achieve this goal, the program was divided into two phases. In the first phase, a hydrogen content of up to 30% was achieved, while in the second phase, the operation was successful with a hydrogen content of up to 100% while still maintaining emissions below regulated limits. The modifications made to the system to accommodate the project are depicted in Fig. 3 and mainly consisted of changes to the fuel system, combustor, and controller. To evaluate the performance of the



Fig. 3 – Turbec T100 PH unit with modified combustor and fuel train for flexible fuel operation.

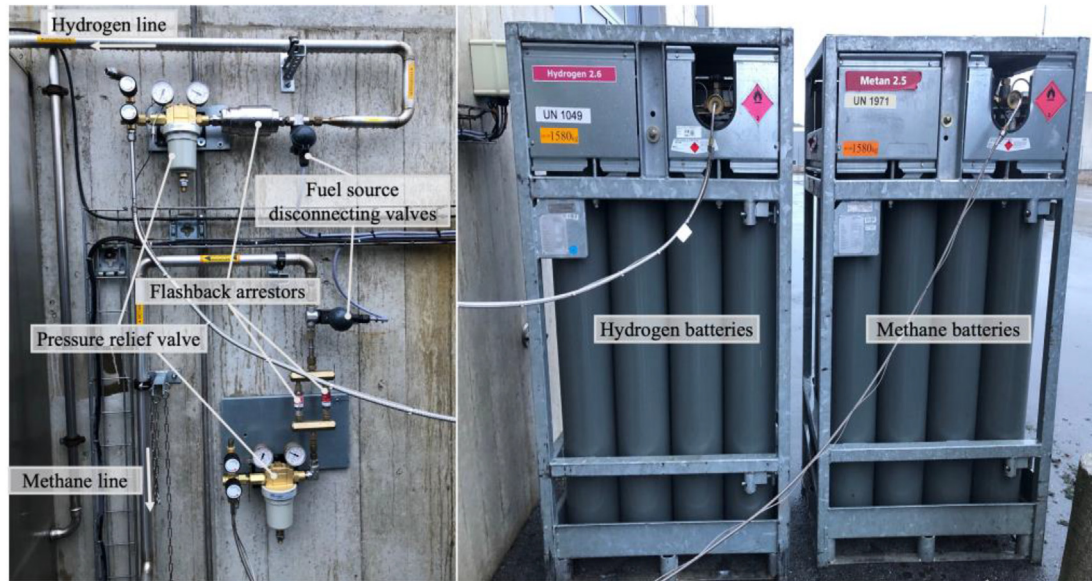


Fig. 4 – Fuel system arrangement outdoors, the valves left and fuel bottles right.

engine, numerous sensors were installed, and their readings were carefully monitored during the testing phase. Each of these modifications will be discussed in more detail in the sections that follow.

#### Fuel system

The original fuel system of the engines was designed to operate at low pressures, with an external compressor providing the necessary pressure boost. However, this system has been replaced with a new set-up that includes fuel sources such as methane and hydrogen batteries stored in a bundle structure. The pressure of the fuels is reduced using pressure relief valves and protected from flashbacks via arrestors. The fuel bundles and valves are located outside the building, with fuel disconnecting valves in place as a safety

measure to cut the fuel supply in the event of a leak. The fuel bundles and valves can be seen in Fig. 4.

The new fuel train system is temporarily installed on the MGT and is depicted in Fig. 5. The system consists of separate lines for methane and hydrogen which are combined to form a mixture that is delivered to the engine. The engine operator controls the mass flow rates of both fuels to regulate the fuel ratio. The mixing station has larger diameters than the rest of the system and is designed to allow for adequate mixing of the fuels. The mixed fuel then passes through a safety valve and is divided into main and pilot lines. Initially, two main valves were installed for increased flexibility in control, but the experiments showed that only one main valve and one pilot valve were needed to function properly. The fuel is transmitted into the combustor through two lines, with a pilot in the middle and the main burners surrounding it. The main

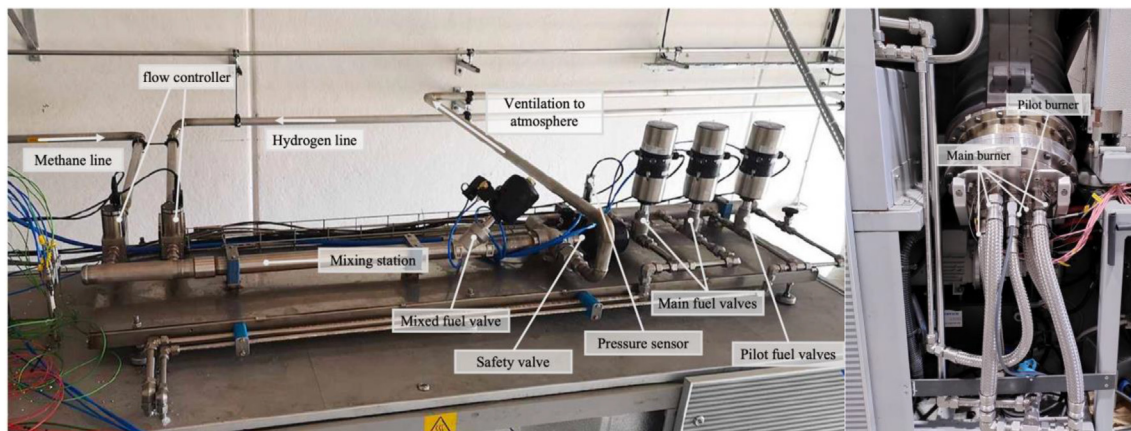


Fig. 5 – Fuel system indoors, the mixing station and fuel train installed on top of the MGT enclosure, left, and the combustor, right.

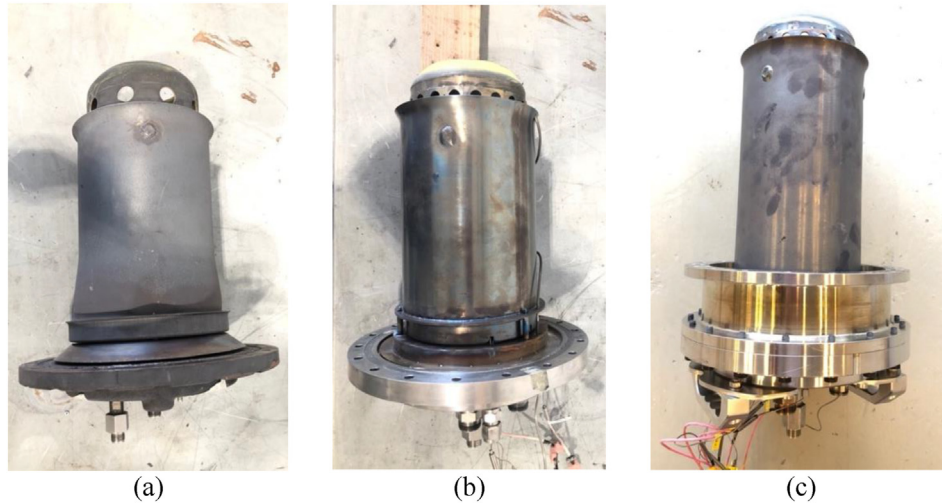


Fig. 6 – Evolution of combustion chambers, a) Turbec, b) F400s ver.01 and c) F400s ver.02.

burner is composed of 10 single-jet nozzles that are supplied by four lines.

### Combustor

The experiments utilized the F400s.3 combustion system developed by DLR, which consisted of two different flame tubes: ver.01, with the same length as the original combustor, and ver.02, with an extended flame tube. This combustion system was used as a replacement for the original Turbec swirl-type combustor. All of the experimental results reported in this work are based on variant (c) shown in Fig. 6.

Unlike the original combustor, the DLR F400's primary stage doesn't rely on swirl stabilization. Instead, it employs a stabilization principle that involves a combination of jet and recirculation, commonly referred to as the FLOX® concept. However, the pilot stage still uses the widely used swirl stabilization method. The swirler with annularly arranged air

and fuel orifices directs fuel tangentially and axially into the pilot stage, thus enhancing mixing.

In the main stage, the nozzles allow for good premixing and homogenization of the air-and fuel stream flow before reaching the flame zone. This, in turn, enhances combustion stability and reduces peak temperatures, thereby minimizing the chances of NO<sub>x</sub> formation.

Fig. 7 illustrates the FLOX® combustor, which features ten separate nozzles arranged in a circular pattern around the combustor cross-sectional area and pilot dome to inject main stage air axially with high momentum. Fuel is injected coaxially inside each nozzle to enable controlled premixing. The air jet mantle serves as a shield, reducing the risk of flashback and delaying ignition to achieve lean equivalence ratios and lower combustion temperatures.

Flame stabilization is ensured through a recirculation zone developed by the air jets, where hot exhaust gases are transported back toward the root of the flame with negative axial

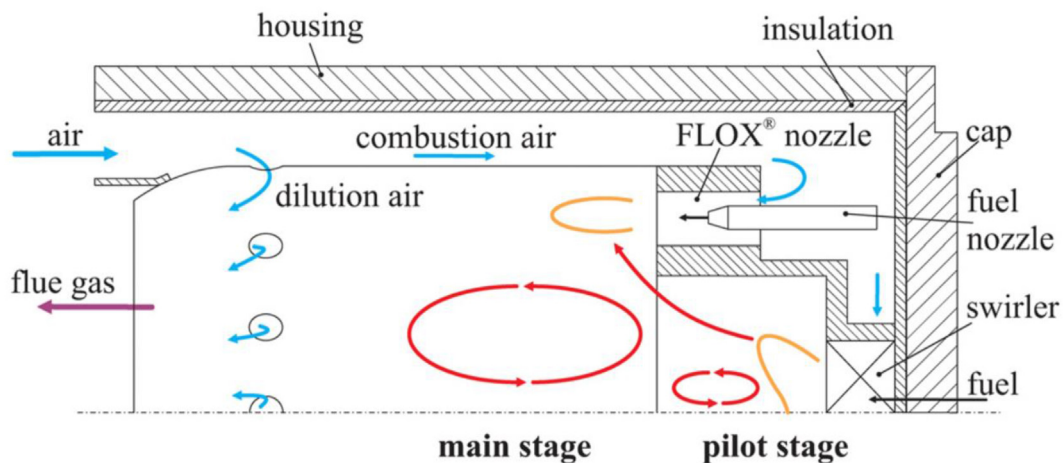
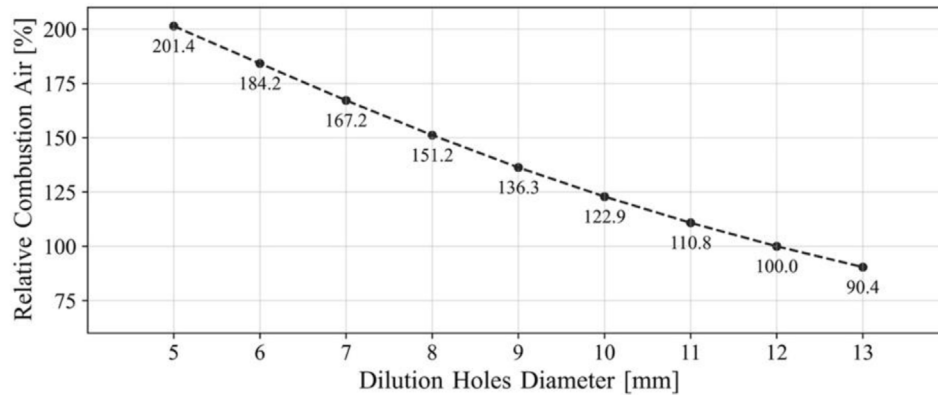


Fig. 7 – Schematic of the FLOX®-combustion principle [36].





**Fig. 8** – Expected relative combustion air over dilution hole diameter.

velocity. The developing flame is lifted off the combustor base to avoid excessive material stress inside the combustor head. More details about the combustor design and principle are available in Refs. [36,37].

The F400s.3 combustor is designed to operate with a range of fuels from low calorific synthesis gas up to natural gas. The combustor core underwent successful testing at DLR in an atmospheric test rig prior to the MGT test. The atmospheric tests were conducted with a gradual increase in hydrogen contents, up to pure hydrogen, to evaluate the fuel flexibility and performance of the optimized F400s combustor. To ensure that the velocity fields and jet velocities inside the combustor were comparable, the fuel input level and the supplied air were pressure-scaled. OH\* chemiluminescence and emissions measurements were performed to assess stability and functionality [37]. Results indicated that stable flames were achieved across the fuel composition range tested, and no flashback or material problems were observed during the investigations. The optimized combustor demonstrated fuel flexibility and an increased operating range concerning NOx emissions. Nevertheless, the increased pressure level and higher volumetric energy density in the operational environment introduce new factors that affect combustor behaviour and were not captured by the atmospheric investigations at DLR. The tests conducted in this work extend the experiences to the real-use case and demonstrate the feasibility of the optimized combustor under operational conditions.

In a recuperated MGT, a significant [37] amount of air is used as dilution air to cool down the exhaust gases after combustion, making them manageable for the turbine. When operating with high hydrogen content, the air split between combustor core air and dilution air was adjusted to accommodate the changed conditions. The diameter of the dilution holes downstream of the combustion zone, which distribute the supplied air inside the combustor, was adjusted to achieve this. The spot-welded dilution ring with defined holes was switched to four different configurations investigated according to Fig. 8: 9 mm (quite lean), 11 mm (slightly leaner), 12 mm (the original syngas configuration), and 13 mm (slightly richer). As the hydrogen content increases, better performance of the leaner variants is expected, but there is a higher

risk of a lean blowout of the flame. Optimal operating conditions for increased hydrogen content operation are expected to be much leaner compared to natural gas operation because the reactivity of hydrogen is significantly higher, along with the adiabatic and resulting flame temperature for a certain amount of air or equivalence ratio (see Fig. 1).

For all results approaching high hydrogen contents up to pure hydrogen, the 9 mm configuration was used, resulting in approximately 36% more air distributed to the combustion zone than in the original configuration. These values are based on rough estimations by resulting cross-sectional areas of the different significant holes or openings. This is expected to allow for low enough NOx emissions levels combined with sufficient flame stability margin.

### Controller system

In addition to the new combustor design, modifications to the fuel controller were necessary to ensure the safe operation of the MGT with the ability to vary power and maintain emissions below the regulated values [38]. To accommodate the MGT to run on blended fuels, a new fuel delivery system was installed to provide the user-specified fuel mixture for the engine. To minimize changes to the engine controller, an additional fuel controller was added upstream from the MGT controller, which manages the fuel system before the MGT controller takes over. The modifications to the MGT controller are limited to adjustments in controller parameters to minimize changes to the existing system.

Fig. 9 presents the schematics of the micro gas turbine unit designed to operate with fuels containing high levels of hydrogen. The methane and hydrogen fuels are stored in bottles under pressures of up to 250 bar. The pressure is then reduced to 12–15 bar, which is set manually by the operator, through pressure relief valves. The fuel flow is then directed to flow controllers, where the mass flow rate of methane and hydrogen is regulated by the fuel train controller, an additional system. The purpose of this system is to supply the desired fuel mixture in accordance with the operator's specifications.

The mixed fuel enters a series of valves which are pneumatically controlled by the MGT controller. The first valve is a



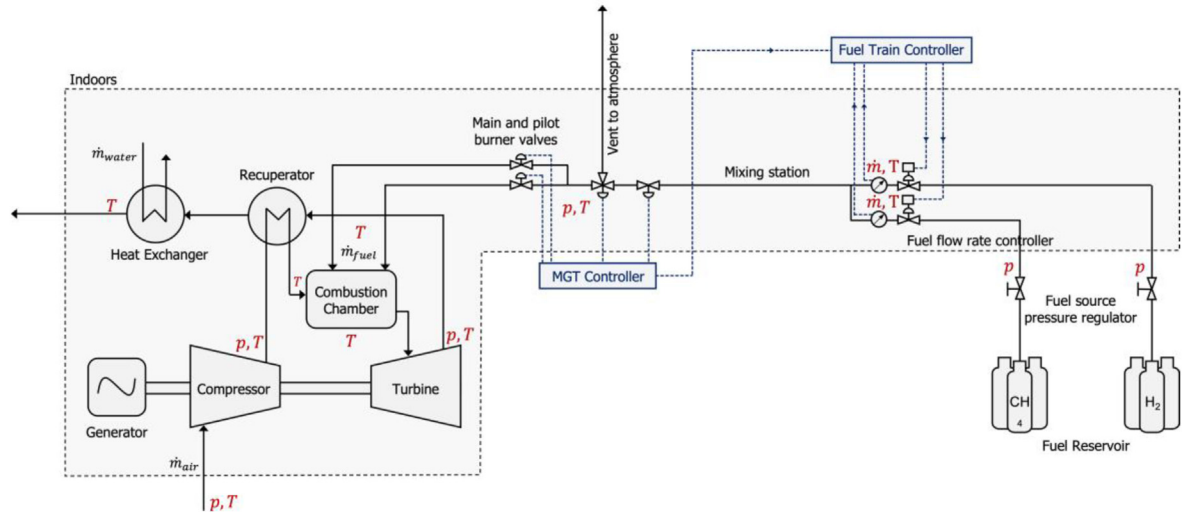


**Fig. 9 – Structure of micro gas turbine unit equipped with the new fuel train system, controllers, and measurement points.**

shutoff valve that connects the mixed fuel to the fuel train. After that, a 3-way valve is installed which provides a line to discharge the fuel to the atmosphere for safety reasons. The main path is divided into two separate lines and valves for the pilot and main fuel supply. The MGT controller regulates these valves to run the engine according to the operator's demand, the engine state (start-up, shut-down, steady, etc.), and the feedback from the engine sensors. Since the MGT controller has the primary control role, at the beginning of the operation it sends a signal to the fuel train controller to activate it. In Fig. 9 the connections between the controllers and valves are depicted. Moreover, the installed pressure, temperature, and flow rate sensors are also provided in red font. Some of these measurements are used by controllers and all of them are logged and collected for online monitoring of the operation and further post-process of the data.

The flammability range of hydrogen and methane poses a challenge in the fuel control system during the start-up. When

starting the engine, the combustor runs at pilot mode where the valve for the pilot burner permits a high flow rate and then reduces to a lower value that remains unchanged through the operation. The pilot valve opening is regulated by the controller based on a map, with respect to the reference TOT and rotational speed of the engine, which are set by the engine's state and power set point. In Fig. 10 (a) the original mapping of the valve is presented. This setting is suitable for fuel blends with low hydrogen content. However, for high hydrogen content, the flammability limit of the fuel is reduced, therefore modifications are implemented to permit a stable start-up. The new mapping is shown in Fig. 10 (b), where a smoother transition is provided which is the successful pattern derived from a try-and-error procedure during the tests.

To see the effect of a valve adjustment, the start-up diagram for the engine before and after the pilot valve adjustment is illustrated in Figs. 11 and 12. The maximum pilot valve

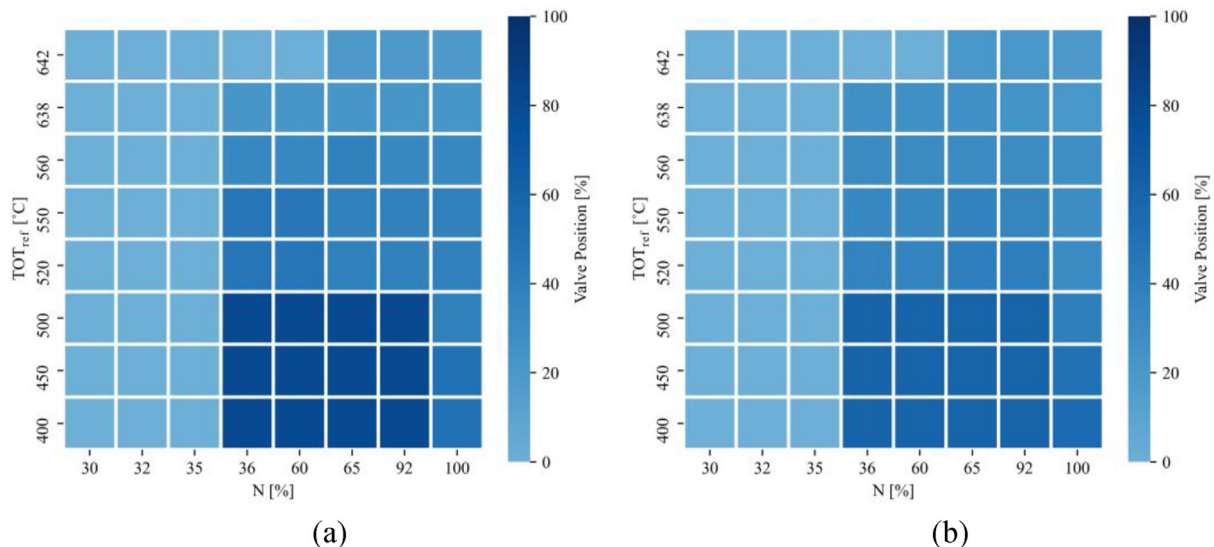


**Fig. 10 – Pilot valve setting, (a) the reference settings, (b) modified settings.**

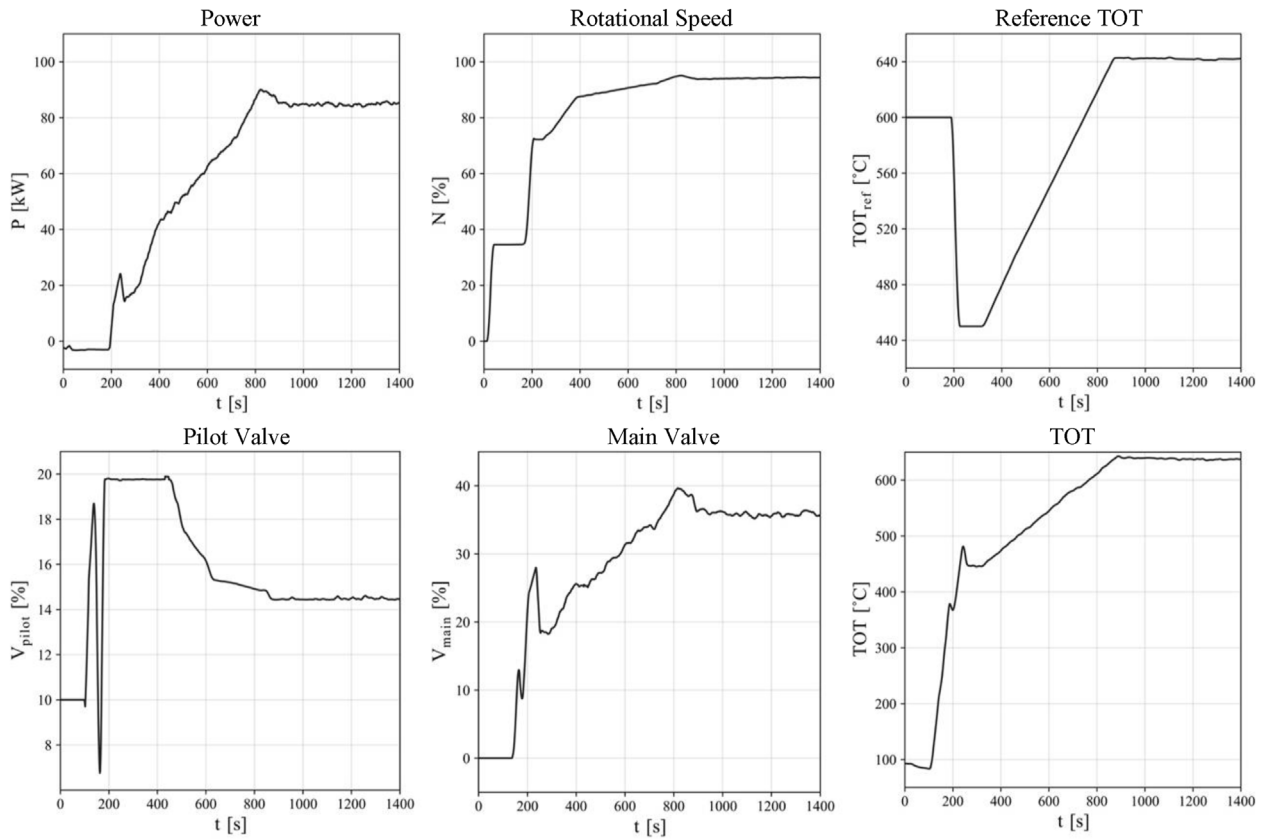


**Fig. 11** – Start-up diagram for MGT before pilot valve adjustment. The hydrogen content in the fuel is 55% and the ambient condition during the test is 14 °C and 1.03 bar.

opening was 20% in the original setting which is reduced to around 14.5% for steady opening. These values are reduced to 17% and 10% after the adjustment which is visible in Fig. 10 (b). The pattern of reference TOT and rotational speed is also presented in both cases which are the parameters that pilot maps are based on. With these minor modifications in the start-up controller, the ignition and initial acceleration of the MGT were achieved without any difficulties.

### Measurement system

To attain the most from the experiments, several additional sensors were installed at different locations of the engine. Sensors installed on the new fuel train are employed for controlling the fuel valves. Moreover, the combustion chamber as the new component of the engine is equipped with sensors so that its condition is constantly monitored during the test, trying to avoid high material temperatures. The pressure and temperature sensors inside the engine cycle are shown in Fig. 13 and a list of sensors measuring fuel properties is provided in Table 3. Hydrogen and methane properties are measured before and after mixing, as shown in Fig. 9. There is a thermocouple installed inside the combustor which measures the temperature of the fuel delivered to the combustor. The accuracy of sensors installed in the cycle and fuel system is presented in Table 4.

Out of 32 sensors listed in Figs. 13 and 6 sensors are built-in, and the rest are added for the purpose of the

experiments. The temperature at the turbine inlet is measured by the thermocouples installed on the combustor, close to the flue gas exit from the combustor (Fig. 14 (a)). Other than the flue gas temperature, the metal temperature on both sides of the liner is also measured to monitor the component's condition. An example of such measurement is shown in Fig. 14 (b). The number of sensors installed on the combustor and their type and accuracy are described in Table 5.

To evaluate the effect of hydrogen injection on CO and NO<sub>x</sub> emissions a gas analyser is installed to measure the concentration of different components. The analyser's probe is installed on the way of exhaust gas (location 9 in Fig. 13). During the measurement phase, the exhaust gas emissions (NO<sub>x</sub>, CO, CO<sub>2</sub>) are measured via the system shown in Fig. 15. The specification of the sensors in the analyser is provided in Table 6.

## Results and discussion

Experiments have been conducted to realize the influence of enriching methane fuel with hydrogen, on the performance of a micro gas turbine and to investigate the influence of different amounts of hydrogen blend on the emissions and the stability of the combustion.

An initial setting was chosen for the new fuel train system, and it was tested. During the test runs in phase 1, unstable operations were observed, during which a better controller

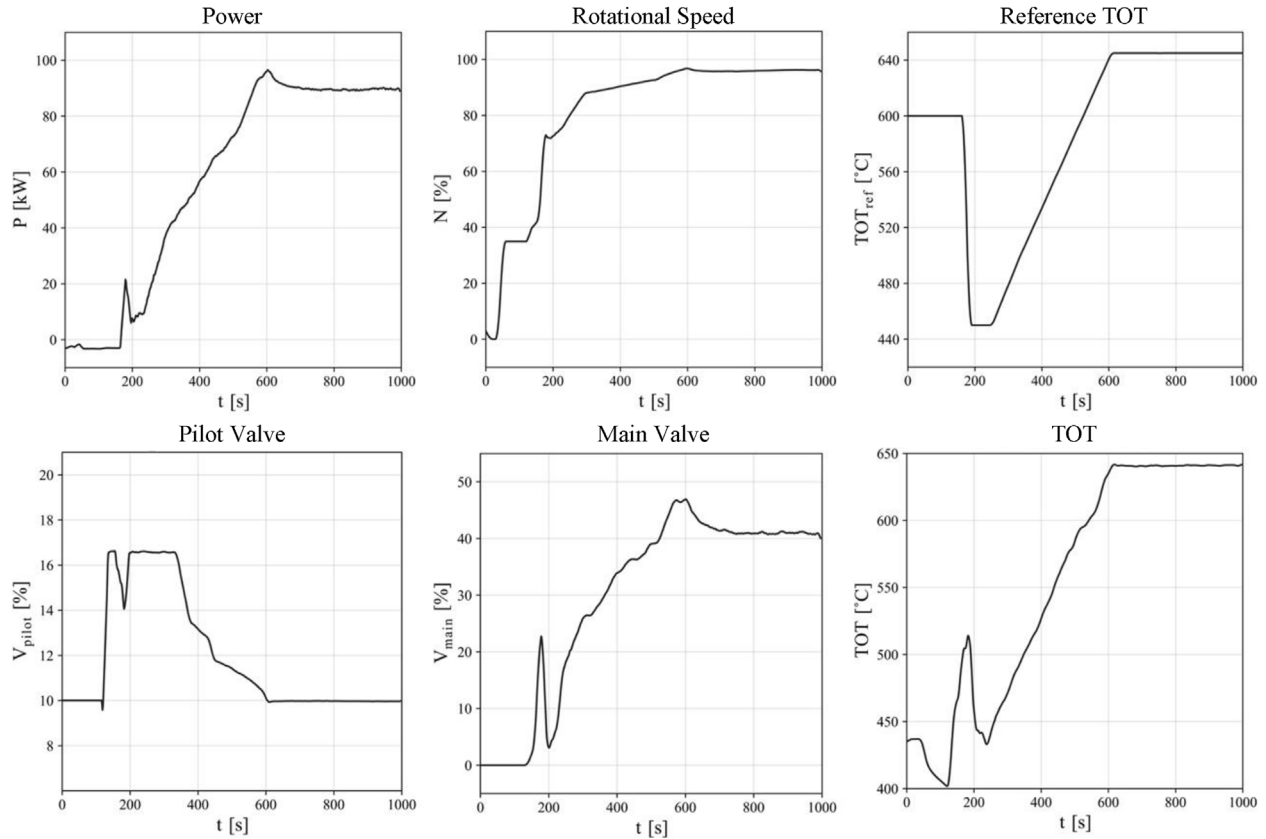


Fig. 12 – Start-up diagram for MGT before pilot valve adjustment. The hydrogen content in the fuel is 75% and the ambient condition during the test is 15 °C and 1.02 bar.

No.	Description	Temp.	Press.
1	Engine inlet	1	-
2	After inlet air filter	4	6
3	After compressor	3	3
4	After recuperator cold side	1	-
5	After combustor	2	-
6	After turbine	-	-
7	After diffuser	7	1
8	After recuperator hot side	-	-
9	Engine outlet	-	-
10	Before heat exchanger cold side	-	-
11	After heat exchanger cold side	4	-

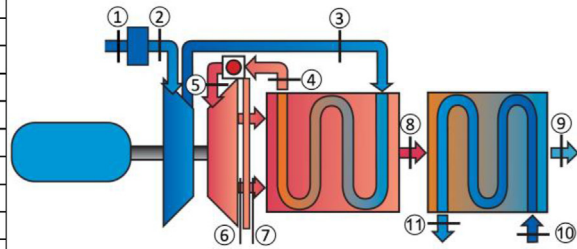


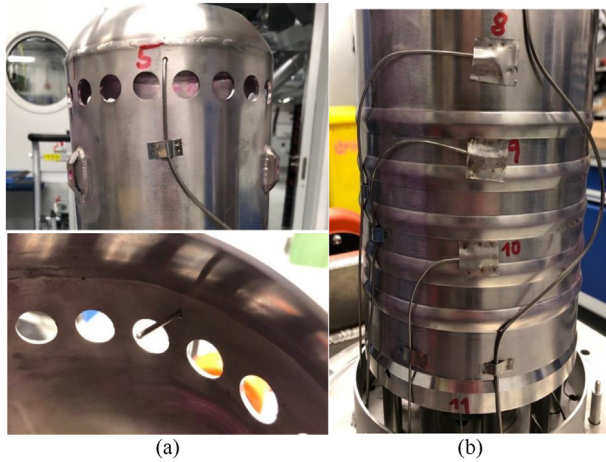
Fig. 13 – Cycle measurements, the table shows the number of installed sensors at each position.

Table 3 – Sensors installed on fuel system.

No.	Description	Temperature	Pressure	Mass flow rate
1	Methane fuel	1	1	1
2	Hydrogen fuel	1	1	1
3	Mixed fuel	1	2	–
4	Fuel in combustor	1	–	–

Table 4 – Performance of the installed sensors in the cycle and fuel system.

No.	Sensor	Accuracy
1	Temperature	$\pm 1.1$ °C - 2.2 °C
2	Pressure	$\pm 0.3\%$ of Full Scale
3	Mass flow rate	$\pm (0.4\%$ of Reading + 0.2% of Full Scale)



**Fig. 14 – Examples of sensors installed in the combustion chamber, (a) flow temperature and (b) metal temperature.**

setup was explored through a try-and-error manner. While this was effective for hydrogen content below 30%, for higher contents of hydrogen and especially in high power modes, the instabilities grew which were not controllable via fuel injection control.

During the second phase of the experiments, a modified version of the combustor was designed and manufactured by DLR, with smaller dilution holes to increase the airflow to the main burner and thereby imply more effective material cooling. Stable combustion was achieved in phase 2, thanks to the combustor setup. During a week of operation, blended fuel consisting of methane and hydrogen, with a high share of hydrogen (more than 50%) was fed to the engine, and different manoeuvres were conducted.

To illustrate the importance of the valve setting, operational results from the engine before and after valve adjustments are reported here. The normalized values reported in percentage points are calculated through the equations below, where  $P_{nom}$  and  $N_{nom}$  represent the power output and rotational speed of the engine at nominal conditions.  $T_{comb,max}$  represents the maximum allowed temperature in the combustor and  $T_{cooling\ air}$  is temperature of cooling air surrounding the combustion chamber.

$$P_{norm} = \frac{P}{P_{nom}} \quad (3)$$

$$N_{norm} = \frac{N}{N_{nom}} \quad (4)$$

$$T_{comb,norm} = \frac{T_{comb} - T_{cooling\ air}}{T_{comb,max} - T_{cooling\ air}} \quad (5)$$

**Table 5 – Sensors installed on the combustor.**

Description	No. Of sensors	Type	Accuracy
Metal temperature	9	Type N	±0.4%
Flue gas temperature	2	Type N	±0.4%
Inlet air temperature	1	Type N	±0.4%
Fuel temperature	1	Type N	±1.5 °C

**Table 6 – Sensors in the gas analyser.**

Item	Unit	Accuracy	Resolution	
1	O <sub>2</sub>	%	±0.8% of f.v.	0.01 vol%
2	CO	ppm	±2 ppm CO	1 ppm CO
3	NO	ppm	±2 ppm NO	0.1 ppm NO
4	NO <sub>2</sub>	ppm	±5 ppm NO <sub>2</sub>	0.1 ppm NO <sub>2</sub>
5	CO <sub>2</sub>	%	+1% of m.v.	0.01 vol% (0–25 vol%)
6	HC	ppm	±2% of m.v.	10 ppm

Fig. 16 displays the main operational parameters during a start-up and load variation test before the controller modifications were made. The test was run using a blended fuel consisting of approximately 55% hydrogen and 45% methane. A start-up to 85 kW was performed, and before reaching steady-state conditions, NO<sub>x</sub> emissions close to 18 ppm were observed and then reduced to 14.1 ppm at steady-state. When the power was increased to 100 kW, the NO<sub>x</sub> emissions rose to 15.7 ppm. The power was then reduced to 80 kW and increased again to 100 kW. During the second 100 kW load, the temperature of the flue gas was slightly higher and so were the NO<sub>x</sub> emissions. The fuel for the main burner was regulated by the main valve, which varied with the power output, while the opening of the pilot valve was almost constant throughout the operation. The shutdown from 100 kW was accompanied by changes in the fuel valve positions, and while the main valve was completely shut off, the pilot valve was reduced to 10%.

The experiments involving the micro gas turbine unit were conducted by increasing the hydrogen content in the fuel and running the engine at different power outputs. However, when the hydrogen content in the fuel exceeded 55%, instabilities during start-ups were observed along with high NO<sub>x</sub> emissions. To overcome this, modifications to the control parameters were made through a try-and-error process, which enabled safe operation in high hydrogen fuel mode with low emissions. The results from experiments with hydrogen content between 55% and 75% are missing due to a crash in the log system on one day and fuel leakage on another day. However, data from experiments with hydrogen content from 75% to 100% is available, and the effect of valve adjustments on the engine's performance is evident. Fig. 17 shows the engine's run with a hydrogen content of around 75%. The reason why the percentage of hydrogen is almost but not exactly equal to 75% is that the fuel controller is designed to receive hydrogen/methane mix ratios in mass bases, and the volume base mix depends on the density of the fuels, which can vary based on changes in pressure and temperature of the fuel.

The experiments continued by increasing the hydrogen content in the fuel and running the engine at different power levels. However, instabilities were observed during start-ups and high NO<sub>x</sub> emissions were recorded when the hydrogen content was above 55%. To address this, modifications to control parameters were made through a try-and-error process to allow safe operation in high hydrogen fuel mode with low emissions. The results from two days of runs with hydrogen content between 55% and 75% are missing due to a crash in the log system and fuel leakage. However, data from experiments with hydrogen content from 75% to 100% after





Fig. 15 – Exhaust gas composition measurements, probe installed on exhaust path in the left and analysing kit in the right.

the controller modifications are available. Fig. 17 shows the engine's run with approximately 75% hydrogen. During the manoeuvre, the engine was started successfully with 75% hydrogen and 90 kW power output, and the difference in operation with the new valve settings compared to before the controller adjustments (Fig. 16) was noticeable. The maximum pilot valve opening occurred during the start-up at 17% and was reduced to around 10% during the rest of the manoeuvre. The highest NOx emissions during the run were 14 ppm, which occurred during the power step up to 100 kW. This is

compared to the previous setup where the NOx emissions were 19 ppm during the overshoot for a 100-kW load (Fig. 16).

Other than transient conditions, the steady-state data from 80-, 90-, and 100-kW power outputs could be compared from two controller settings. At 80 kW the normalized flue gas temperature was 88.9% with 13.3 ppm of NOx production, while the same parameters are 89.2% and 8.1 ppm in the new controller arrangements. Although the trend of the temperature of flue gas close to the combustor outlet is consistent with the NOx emissions, it is worth mentioning that NOx

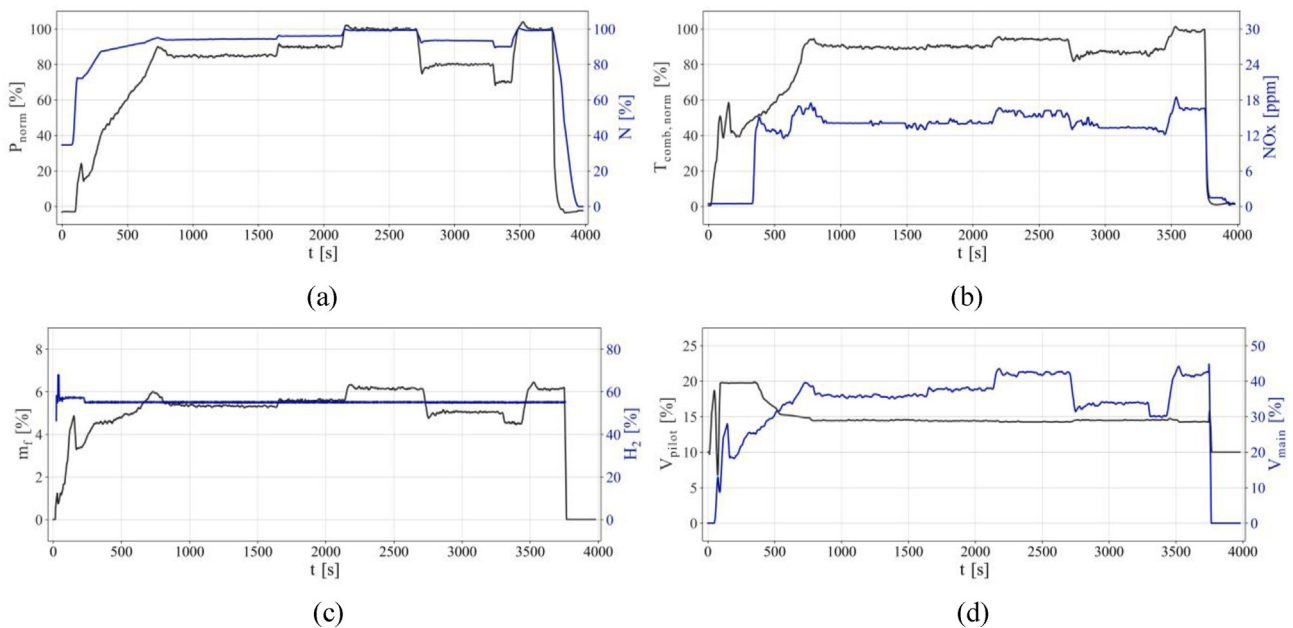
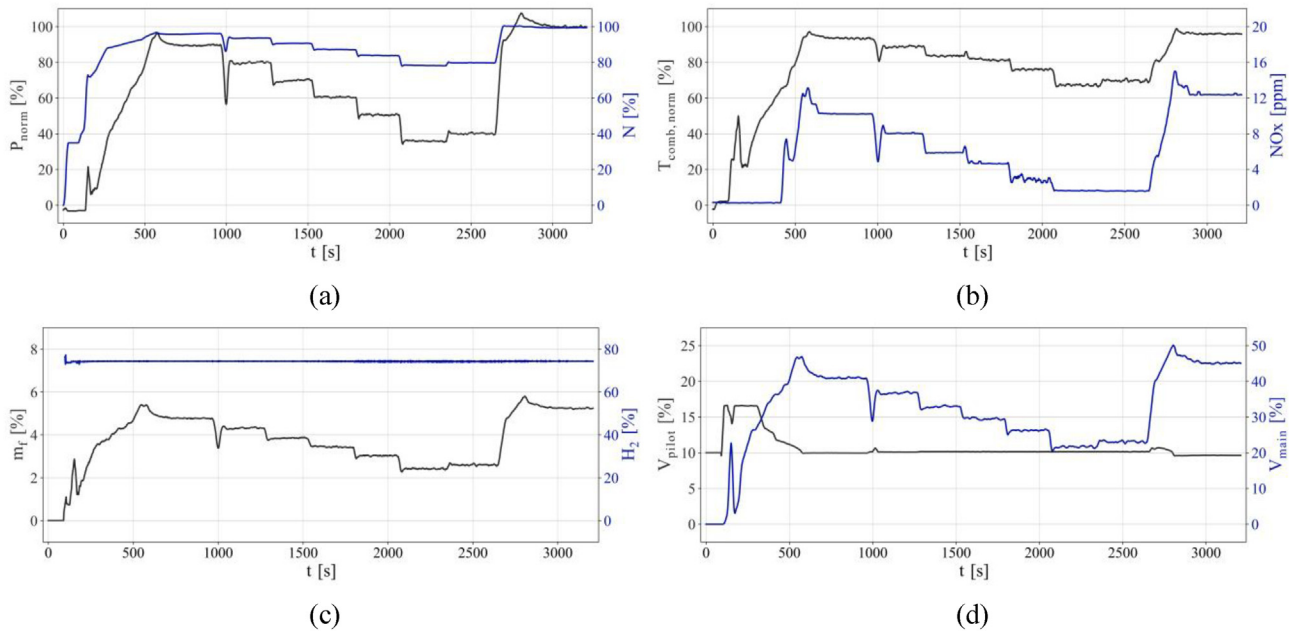
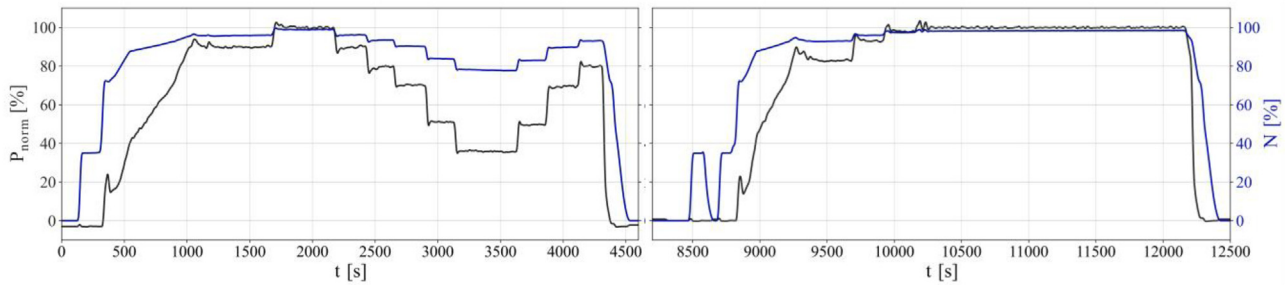


Fig. 16 – Start-up and power stepdown before adjusting the controller setup. The ambient temperature was 14 °C and the ambient pressure was 1.03 bar during the test.



**Fig. 17 – Power variation with F400-s ver02, modified controller setup. The ambient temperature was 15 °C and the ambient pressure was 1.02 bar during the test.**



**Fig. 18 – Power and rotational speed for manoeuvring with high hydrogen content.**

production is a local phenomenon and more correlated to temperature in different regions of the combustor. The flue gas temperature presented here is also a value measured at a specific location. However, it could be used as an indicator of temperature increase or decrease in the combustor. For 90- and 100-kW power outputs, the NO<sub>x</sub> emissions after controller adjustments are 10.2 and 12.3 respectively while in previous arrangements the values were 14.1 for 90 kW and

15.7 and 16.5 for 100 kW. The adjustment of the pilot valve has not only provided a stable start-up and ignition but also helped to significantly reduce the NO<sub>x</sub> produced during the combustion.

After reaching a suitable setup for the controller, a series of experiments were conducted with an increasing share of hydrogen in the fuel, up to 100%. The whole test included 2 start-ups and shutdowns which lasted for 3 h and 30 min. The

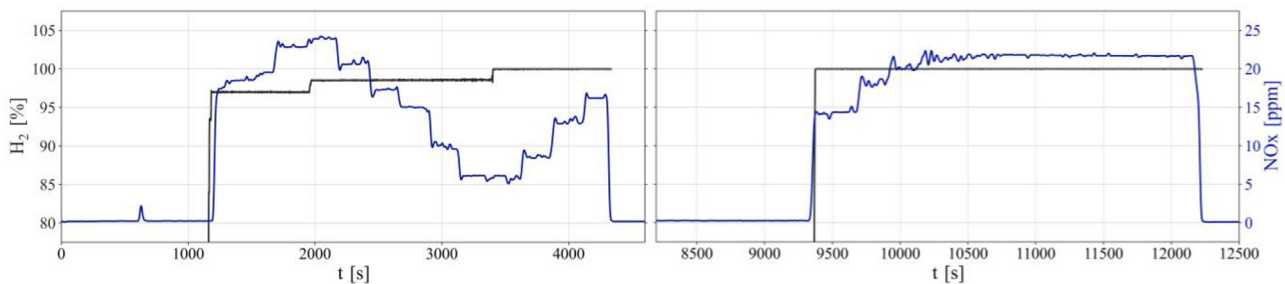


**Fig. 19 – Hydrogen content and NO<sub>x</sub> emissions for manoeuvring with 100% hydrogen.**

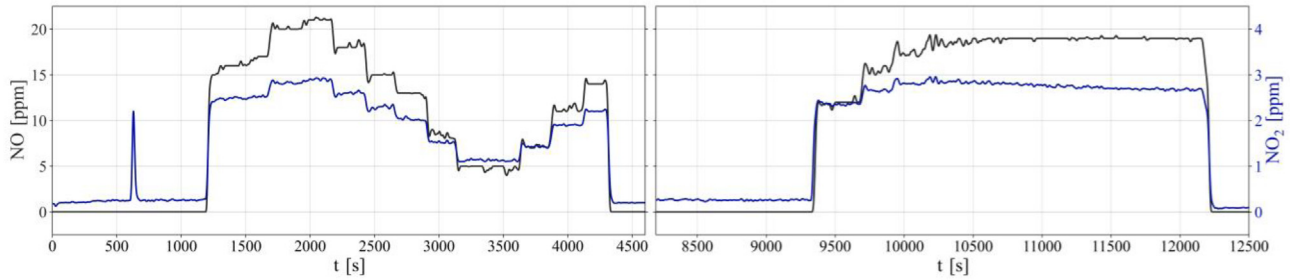


Fig. 20 – NO and NO<sub>2</sub> emissions for manoeuvring with 100% hydrogen.

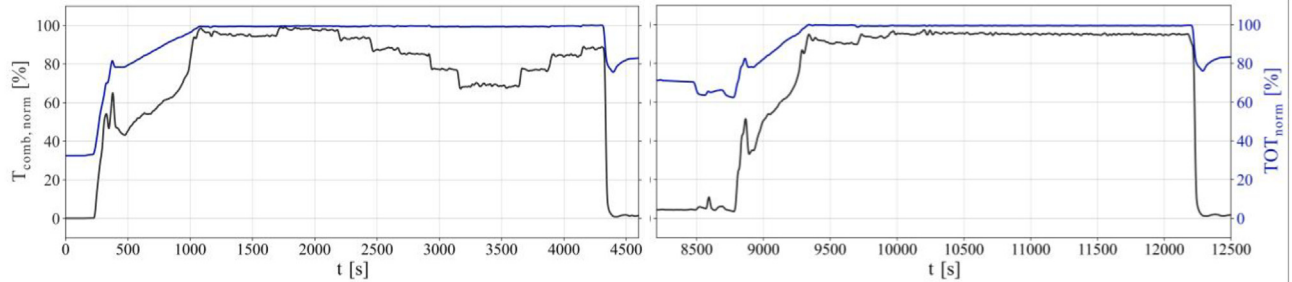


Fig. 21 – Combustor outlet temperature and turbine outlet temperature for manoeuvring with 100% hydrogen.

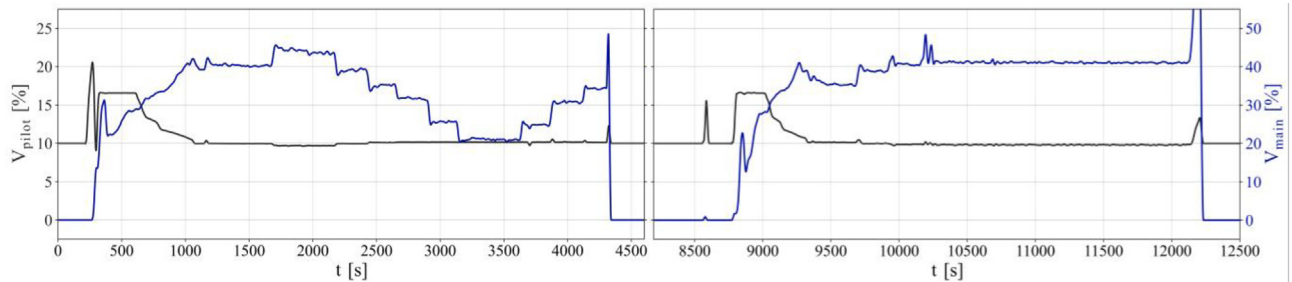


Fig. 22 – Fuel valves' position for manoeuvring with 100% hydrogen.

collected data are presented in Figs. 18–22. About an hour of data between two runs is eliminated in these figures, as it was only a cooling-down process for the engine. The initial ignition was successfully achieved with 90 kW of power with 97% hydrogen, with a smooth transition thanks to the optimized valves' positioning (Fig. 22). In about 10 min, the engine reached to 95.8% of its nominal rotational speed and produced 90 kW power with NO<sub>x</sub> productions of less than 20 ppm (Figs. 18 and 19). A 10 kW step-up was conducted after about 10 min to reach the maximum power of 100 kW. At this point, the rotational speed was elevated up to 98.9% of the nominal value and NO<sub>x</sub> emissions increased to 22.8 ppm (Figs. 18 and 19). Preserving the same power set point, hydrogen was added to the fuel to reach 98.5% concentration resulting 1.2 ppm increase in NO<sub>x</sub> emissions, presented in Fig. 19 and the share of NO and NO<sub>2</sub> production in NO<sub>x</sub> emissions is visible in Fig. 20.

After about 10 min of running at maximum power, the power was reduced to 35 kW in steps, without changing the

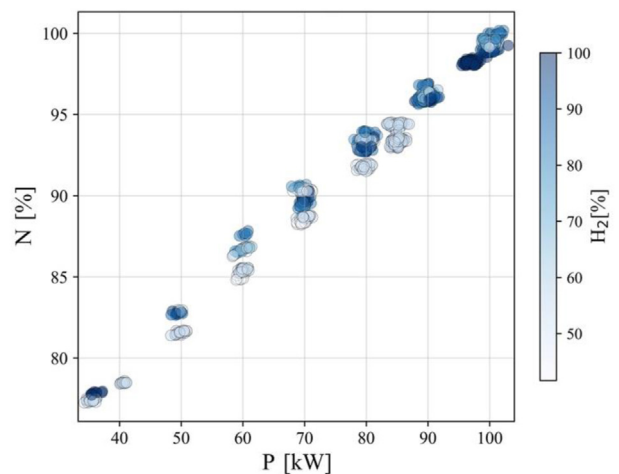


Fig. 23 – Engine rotational speed in different power output and different hydrogen content.

fuel blend. The NO<sub>x</sub> production was consequently reduced in steps to reach 6.1 ppm at 35 kW power. At this point, the hydrogen content was increased to 100% to examine the operation in low power output. The logged data presented in the figures show that only minor changes occurred in the engine when the hydrogen share was increased to 100%. With pure hydrogen, the power was increased to 50, 70, and 80, the same levels during the step-down with 98.5% hydrogen. Therefore, a comparison could be conducted; in all these three levels, NO<sub>x</sub> emissions were 1–2 ppm lower than pure hydrogen. The amount of produced NO<sub>x</sub> during the load increase with pure hydrogen is lower than step-downs with 98.5% hydrogen. According to Fig. 20, this behaviour was attributed to lower NO which could be due to hysteresis effects, since a step up in power (and with it increasing NO<sub>x</sub> values) was compared with a step-down manoeuvre, hence decreasing NO<sub>x</sub> values.

The MGT was shut down while producing 80 kW with pure hydrogen. After waiting for an hour for the engine to cool down, a start-up to 80 kW was initiated with pure hydrogen. In that case, NO<sub>x</sub> emissions were slightly lower than 80 kW power rates during two previous 80 kW hits which are due to lower NO production according to Fig. 20. Since a similar behaviour has been observed by the authors for hot restarts, this might be an indication of a short cool-down which entails hot-start settings for the engine controller.

With three small steps, the power is increased to 100 kW, where a stable operation is achieved with pure hydrogen with NO<sub>x</sub> emissions of 21.9 ppm. With time passing, the rate of NO<sub>2</sub> production decreased and the total NO<sub>x</sub> produced decreased to 21.7 ppm. After about 45 min of running the engine with pure fuel at maximum power, the engine was safely shut down. The value of TOT is normalized based on Eq. (6) below, where TOT<sub>nom</sub> is the turbine outlet temperature at nominal conditions (temperatures in Kelvin):

$$TOT_{\text{norm}} = \frac{TOT}{TOT_{\text{nom}}} \quad (6)$$

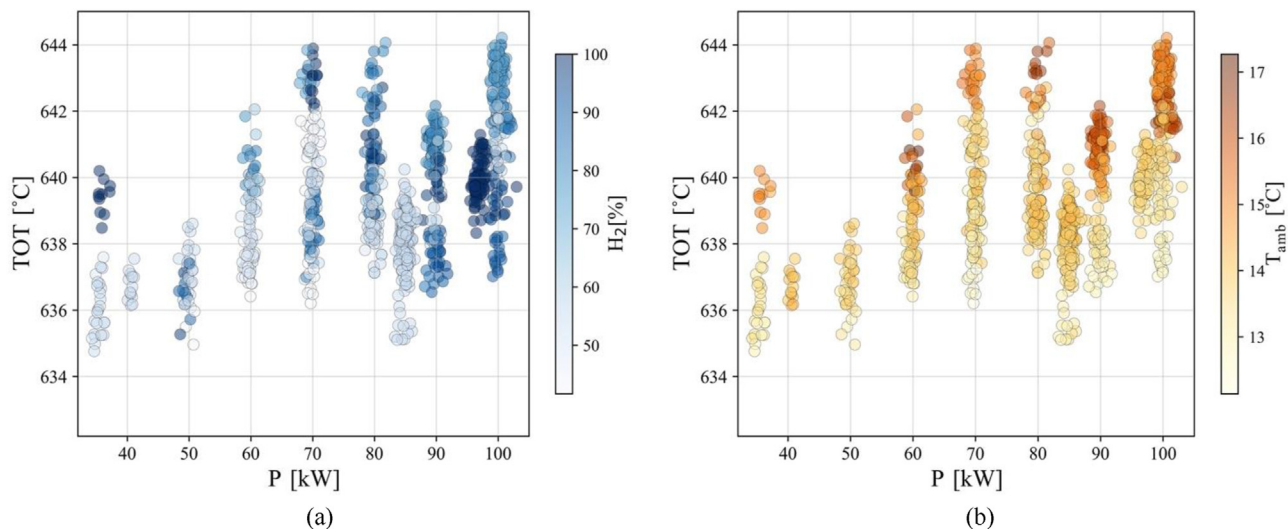


Fig. 24 – Turbine outlet temperature in different power output, (a) effect of hydrogen content and (b) effect of ambient temperature.

In Fig. 23, the relationship between rotational speed and power output is shown after the transient time spans were removed from the data collected from different engine manoeuvres. The TOT (total temperature of the cycle) of the engine is also considered in evaluating the effect of fuel variation on the engine's steady-state operation. The rotational speed of the engine at various power rates exhibits a linear relationship with power output, which is the expected pattern from the engine as previously observed when running on fossil fuels. The highest power output of 100 kW was reached with hydrogen content ranging from 55% to 100%, and as seen in Fig. 23, the range of fuel is almost at the same rotational speed. However, slight deviations in rotational speed can be observed in the figure, for instance at 60 kW, mainly due to the fact that they were collected from different experiments carried out on different days with varying ambient temperatures.

Another cycle parameter indicating the controller's performance is the steady-state condition in turbine outlet temperature, which is provided in Fig. 24, again from all manoeuvres by filtering the transient time spans. In Fig. 24 (a) the amount of hydrogen content in the fuel is presented by colour and as it is visible, the hydrogen content does not seem to have a correlation with TOT. Note that the relative share of hydrogen in the figures is calculated on a volume basis. For instance, at 100 kW higher hydrogen contents have resulted in lower TOT values while the opposite could be observed at 80 kW. This is also the effect of ambient temperature, as illustrated in Fig. 24 (b), higher TOT values are developed in the cycle when the environment was warmer.

The rate of NO<sub>x</sub> production in all power production rates with different hydrogen content is illustrated in Fig. 25. As it is evident from this figure, the rate of NO<sub>x</sub> emissions is directly correlated with an increase in hydrogen content and power rate, as both will increase the temperature in the combustion chamber. Therefore, moving to the upper right part of the graph, the darker the markers become, except for the data from 55% hydrogen which is not in compliance with this trend. The data from 55% hydrogen is from the experiments



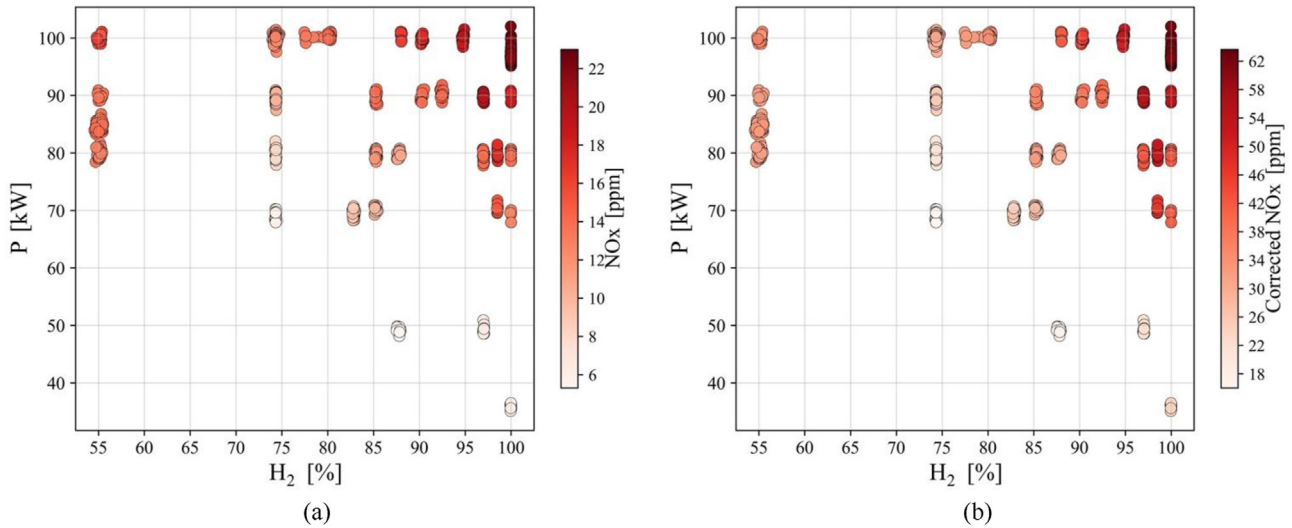


**Fig. 25** – Effect of hydrogen content on NOx emissions in different power output (a) measured values (b) corrected values based on 15% oxygen case.

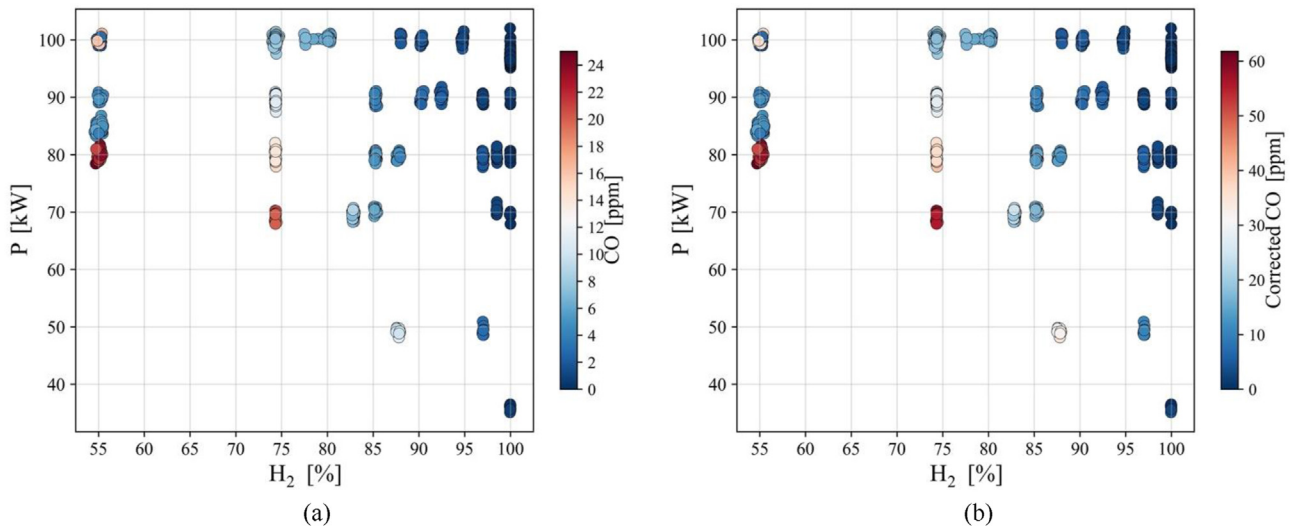


**Fig. 26** – Effect of hydrogen content on CO emission in different power output (a) measured values (b) corrected values based on 15% oxygen case.

before valve adjustments. Fig. 25 shows how the valve adjustments are essential to control the emissions; as the coloring suggests, the NOx emissions at 100 kW with 55% hydrogen before valve adjustments are close to the case of running with 87% hydrogen and producing 100 kW after optimizing the valve settings.

To be able to compare the emissions against different combustion systems, the concentration of NOx and CO is corrected based on the case with 15% O<sub>2</sub> in the exhaust gas, as a standard. For this purpose, the measured emissions are corrected using Eq. (3) and the corrected values are illustrated beside the actual values (Figs. 25 and 26).

$$X_{\text{corr}} = X_{\text{meas}} \left( \frac{20.95 - 15}{20.95 - O_{2,\text{meas}}} \right) \quad (3)$$

It is expected that increasing hydrogen content in the fuel will reduce the rate of CO and CO<sub>2</sub> production. The concentration of CO and CO<sub>2</sub> is measured in flue gas and presented in Figs. 26 and 27 over a range of experimented power output and fuel blends. With pure hydrogen combustion, concentrations of CO and CO<sub>2</sub> in the flue gas are zero. With less hydrogen content the rate of carbon monoxide and carbon dioxide production increases. Looking at Fig. 26, it can be realized that

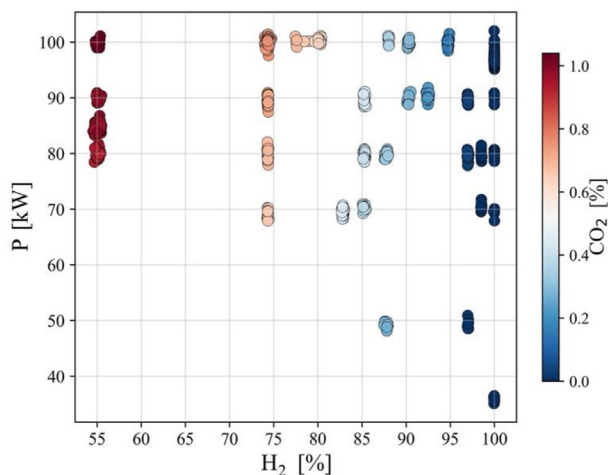


**Fig. 27 – Effect of hydrogen content on CO<sub>2</sub> emission in different power output.**

at constant fuel mix (for instance 75% hydrogen), the rate of CO production is higher at lower powers, which indicates nonideal combustion in low powers.

## Conclusions

In this paper, the objective was to explore the potential of using hydrogen as an alternative fuel for carbon-free power generation in gas turbines. The challenges of using hydrogen as fuel include its less stable combustion and a higher likelihood of flashbacks, as well as higher generation of NO<sub>x</sub> emissions due to its higher combustion temperatures. The study presented the process of modifying a micro gas turbine originally designed to run on natural gas, to run on hydrogen-enriched fuel, and eventually pure hydrogen. The modifications involved the combustor, fuel train, and controller components. These modifications enabled the safe operation of the turbine while ensuring the emissions remained below regulated values.

The micro gas turbine was developed to run on hydrogen-enriched fuel up to 100% pure hydrogen. To achieve stable operation throughout the full range of power outputs, modifications were made to the combustor, fuel train, and controller. During the tests, the volume-based hydrogen content in the fuel varied from 40% to 100%, and the results showed a steady operation of the micro gas turbine with NO<sub>x</sub> emissions below the regulated limits. The highest NO<sub>x</sub> emissions recorded for pure hydrogen and full-load operation was 22 ppm, which equates to 62 ppm of the corrected value based on a reference of 15% oxygen in the exhaust gas. The full range of operation results with different hydrogen contents is presented, demonstrating the stability of the micro gas turbine while meeting the regulatory NO<sub>x</sub> emission requirements.

## Declaration of competing interest

The authors declare that they have no known competing financial interests or personal relationships that could have appeared to influence the work reported in this paper.

## Acknowledgments

This project has received funding from the European Union's Horizon 2020 research and innovation program under the Marie Skłodowska-Curie grant agreement No. 861079 ("Next MGT"). The authors would like to express their sincere gratitude to Bjarte Ludvig Hetlelid for his exceptional contribution to the experiments conducted in this technical paper.



## REFERENCES

- [1] Little AD. Opportunities for micropower and fuel cell gas turbine hybrid systems in industrial applications - DOE report No. 85X-TA009V. 2000. Cambridge, Massachusetts 02140-2390 U.S.A., Jan. 2000.
- [2] Yang J, et al. Thermodynamic modelling and real-time control strategies of solar micro gas turbine system with thermochemical energy storage. *J Clean Prod Jul.* 2021;304:127010. <https://doi.org/10.1016/J.JCLEPRO.2021.127010>.
- [3] Best T, Finney KN, Ingham DB, Pourkashanian M. CO<sub>2</sub>-enhanced and humidified operation of a micro-gas turbine for carbon capture. *J Clean Prod Mar.* 2018;176:370–81. <https://doi.org/10.1016/J.JCLEPRO.2017.12.062>.
- [4] Tang C, Zhang Y, Huang Z. Progress in combustion investigations of hydrogen enriched hydrocarbons. *Renew Sustain Energy Rev Feb.* 2014;30:195–216. <https://doi.org/10.1016/J.RSER.2013.10.005>.
- [5] Zhang Y, Davis D, Brear MJ. The role of hydrogen in decarbonizing a coupled energy system. *J Clean Prod Apr.* 2022;346:131082. <https://doi.org/10.1016/J.JCLEPRO.2022.131082>.
- [6] Morris JD, Symonds RA, Ballard FL, Banti A. Combustion aspects of application of hydrogen and natural gas fuel mixtures to MS9001E DLN-1 gas turbines at elsta plant, Terneuzen, The Netherlands. In: Proceedings of the ASME turbo expo. Stockholm: American Society of Mechanical Engineers Digital Collection; Dec. 1998. <https://doi.org/10.1115/98-GT-359>.
- [7] Shih HY, Liu CR. A computational study on the combustion of hydrogen/methane blended fuels for a micro gas turbines. *Int J Hydrogen Energy Sep.* 2014;39(27):15103–15. <https://doi.org/10.1016/J.IJHYDENE.2014.07.046>.
- [8] Imteyaz BA, Nemitallah MA, Abdelhafez AA, Habib MA. Combustion behavior and stability map of hydrogen-enriched oxy-methane premixed flames in a model gas turbine combustor. *Int J Hydrogen Energy Aug.* 2018;43(34):16652–66. <https://doi.org/10.1016/J.IJHYDENE.2018.07.087>.
- [9] Rajpara P, Shah R, Banerjee J. Effect of hydrogen addition on combustion and emission characteristics of methane fuelled upward swirl can combustor. *Int J Hydrogen Energy Sep.* 2018;43(36):17505–19. <https://doi.org/10.1016/J.IJHYDENE.2018.07.111>.
- [10] Minakawa K, Miyajima T, Yuasa S. Development of a hydrogen-fueled micro gas turbine with a lean premixed combustor. In: 33rd joint propulsion conference and exhibit. American Institute of Aeronautics and Astronautics Inc, AIAA; 1997. p. 1–6. <https://doi.org/10.2514/6.1997-3388>.

- [11] Cappelletti A, Martelli F. Investigation of a pure hydrogen fueled gas turbine burner. *Int J Hydrogen Energy Apr.* 2017;42(15):10513–23. <https://doi.org/10.1016/J.IJHYDENE.2017.02.104>.
- [12] Horikawa A, Okada K, Wirsum M, Funke HH-W, Kusterer K. 100% hydrogen dry low NOx combustor developments for 2MW class gas turbine. In: The proceedings of the international conference on power engineering (ICOPE). The Japan Society of Mechanical Engineers; 2021. <https://doi.org/10.1299/JSMEICOPE.2021.15.2021-0222>.
- [13] Funke HHW, Beckmann N, Keinz J, Horikawa A. 30 Years of dry-low-NOx micromix combustor research for hydrogen-rich fuels - an overview of past and present activities. *J Eng Gas Turbines Power Jul.* 2021;143(7). <https://doi.org/10.1115/1.4049764/1096348>.
- [14] Banihabib R, Assadi M. Dynamic modelling and simulation of a 100 kW micro gas turbine running with blended methane/hydrogen fuel. In: Industrial and cogeneration; manufacturing materials and metallurgy; microturbines, turbochargers, and small turbomachines; oil & gas applications, vol. 7. American Society of Mechanical Engineers Digital Collection; Jun. 2022. <https://doi.org/10.1115/GT2022-81276>.
- [15] Perry RH, Green DW, Maloney JO. *Perry's chemical engineers' handbook*. 7th ed. New York: McGraw-Hill; 1997.
- [16] Verhelst S, Wallner T. Hydrogen-fueled internal combustion engines. *Prog Energy Combust Sci Dec.* 2009;35(6):490–527. <https://doi.org/10.1016/J.PECS.2009.08.001>.
- [17] Guo H, Smallwood GJ, Liu F, Ju Y, Gülder ÖL. The effect of hydrogen addition on flammability limit and NOx emission in ultra-lean counterflow CH<sub>4</sub>/air premixed flames. *Proc Combust Inst Jan.* 2005;30(1):303–11. <https://doi.org/10.1016/J.PROCI.2004.08.177>.
- [18] Frenillot JP, Cabot G, Cazalens M, Renou B, Boukhalfa MA. Impact of H<sub>2</sub> addition on flame stability and pollutant emissions for an atmospheric kerosene/air swirled flame of laboratory scaled gas turbine. *Int J Hydrogen Energy May* 2009;34(9):3930–44. <https://doi.org/10.1016/J.IJHYDENE.2009.02.059>.
- [19] Ren JY, Qin W, Egolpopoulos FN, Mak H, Tsotsis TT. Methane reforming and its potential effect on the efficiency and pollutant emissions of lean methane-air combustion. *Chem Eng Sci Mar.* 2001;56(4):1541–9. [https://doi.org/10.1016/S0009-2509\(00\)00381-X](https://doi.org/10.1016/S0009-2509(00)00381-X).
- [20] Chong CT, Ng J-H. Combustion performance of biojet fuels. In: *Biojet fuel in aviation applications*. Elsevier; 2021. p. 175–230. <https://doi.org/10.1016/B978-0-12-822854-8.00002-0>.
- [21] Jithin Ev, Varghese RJ, Velamati RK. Experimental and numerical investigation on the effect of hydrogen addition and N<sub>2</sub>/CO<sub>2</sub> dilution on laminar burning velocity of methane/oxygen mixtures. *Int J Hydrogen Energy Jun.* 2020;45(33):16838–50. <https://doi.org/10.1016/J.IJHYDENE.2020.04.105>.
- [22] Sun Y, et al. Effect of hydrogen addition on the combustion and emission characteristics of methane under gas turbine relevant operating condition. *Fuel Sep.* 2022;324:124707. <https://doi.org/10.1016/J.FUEL.2022.124707>.
- [23] Zhou Q, Cheung CS, Leung CW, Li X, Li X, Huang Z. Effects of fuel composition and initial pressure on laminar flame speed of H<sub>2</sub>/CO/CH<sub>4</sub> bio-syngas. *Fuel Feb.* 2019;238:149–58. <https://doi.org/10.1016/J.FUEL.2018.10.106>.
- [24] Amar H, Abdelbaki M, Fouzi T, Zeroual A. Effect of the addition of H<sub>2</sub> and H<sub>2</sub>O on the polluting species in a counter-flow diffusion flame of biogas in flameless regime. *Int J Hydrogen Energy Feb.* 2018;43(6):3475–81. <https://doi.org/10.1016/J.IJHYDENE.2017.11.159>.
- [25] Xiang L, Jiang H, Ren F, Chu H, Wang P. Numerical study of the physical and chemical effects of hydrogen addition on laminar premixed combustion characteristics of methane and ethane. *Int J Hydrogen Energy Aug.* 2020;45(39):20501–14. <https://doi.org/10.1016/J.IJHYDENE.2019.11.040>.
- [26] Toof JL. A model for the prediction of thermal, prompt, and fuel NOx emissions from combustion turbines. *J Eng Gas Turbines Power Apr.* 1986;108(2):340–7. <https://doi.org/10.1115/1.3239909>.
- [27] Cowell LH, Smith KO. Development of a liquid-fueled, lean-premixed gas turbine combustor. *J Eng Gas Turbines Power Jul.* 1993;115(3):554–62. <https://doi.org/10.1115/1.2906743>.
- [28] Ditaranto M, Heggset T, Berstad D. Concept of hydrogen fired gas turbine cycle with exhaust gas recirculation: assessment of process performance. *Energy Feb.* 2020;192:116646. <https://doi.org/10.1016/J.ENERGY.2019.116646>.
- [29] Venkataraman KK, Preston LH, Simons DW, Lee BJ, Lee JG, Santavicca DA. Mechanism of combustion instability in a lean premixed dump combustor. *J Propul Power May* 2012;15(6):909–18. <https://doi.org/10.2514/2.5515>.
- [30] Candel S. Combustion dynamics and control: progress and challenges. *Proc Combust Inst Jan.* 2002;29(1):1–28. [https://doi.org/10.1016/S1540-7489\(02\)80007-4](https://doi.org/10.1016/S1540-7489(02)80007-4).
- [31] Lee IB, Woo IS, Lee MC. Effects of nitrogen dilution on the NO<sub>x</sub> and CO emission of H<sub>2</sub>/CO/CH<sub>4</sub> syngases in a partially-premixed gas turbine model combustor. *Int J Hydrogen Energy Sep.* 2016;41(35):15841–51. <https://doi.org/10.1016/J.IJHYDENE.2016.04.131>.
- [32] Juste GL. Hydrogen injection as additional fuel in gas turbine combustor. Evaluation of effects. *Int J Hydrogen Energy Nov.* 2006;31(14):2112–21. <https://doi.org/10.1016/J.IJHYDENE.2006.02.006>.
- [33] Gülen SC. *Gas turbines for electric power generation*. 1st ed. Cambridge University Press; 2019.
- [34] Chiesa P, Lozza G, Mazzocchi L. Using hydrogen as gas turbine fuel. *J Eng Gas Turbines Power Jan.* 2005;127(1):73–80. <https://doi.org/10.1115/1.1787513>.
- [35] Goodwin DG, Moffat H, Speth RL. *Cantera: an object-oriented software toolkit for chemical kinetics, thermodynamics, and transport processes*. 2016. Version 2.2.1.
- [36] Zornek T, Mosbach T, Aigner M. Optical measurements of a lower calorific values-combustor operated in a micro gas turbine with various fuel compositions. *J Eng Gas Turbines Power Apr.* 2019;141(4). <https://doi.org/10.1115/1.4040908>.
- [37] Bower HE, Schwärzle A, Grimm F, Zornek T, Kutne P. Experimental analysis of a micro gas turbine combustor optimized for flexible operation with various gaseous fuel compositions. *J Eng Gas Turbines Power Mar.* 2020;142(3). <https://doi.org/10.1115/1.4044901>.
- [38] Funke HH-W, Keinz J, Börner S, Hendrick P, Elsing R. Testing and analysis of the impact on engine cycle parameters and control system modifications using hydrogen or methane as fuel in an industrial gas turbine, vol. 8; 2016. p. 409–26. <https://doi.org/10.1051/EUCASS/201608409>.

## Paper III


A Hydrogen-Fueled Micro Gas Turbine Unit for Carbon-Free Heat and Power Generation

R. Banihabib and M. Assadi

Sustainability, vol. 14, no. 20, 2022, doi: [10.3390/su142013305](https://doi.org/10.3390/su142013305).

## Article

# A Hydrogen-Fueled Micro Gas Turbine Unit for Carbon-Free Heat and Power Generation

Reyhaneh Banihabib and Mohsen Assadi \* 

Faculty of Science and Technology, University of Stavanger, 4021 Stavanger, Norway

\* Correspondence: mohsen.assadi@uis.no

**Abstract:** The energy transition with transformation into predominantly renewable sources requires technology development to secure power production at all times, despite the intermittent nature of the renewables. Micro gas turbines (MGTs) are small heat and power generation units with fast startup and load-following capability and are thereby suitable backup for the future's decentralized power generation systems. Due to MGTs' fuel flexibility, a range of fuels from high-heat to low-heat content could be utilized, with different greenhouse gas generation. Developing micro gas turbines that can operate with carbon-free fuels will guarantee carbon-free power production with zero CO<sub>2</sub> emission and will contribute to the alleviation of the global warming problem. In this paper, the redevelopment of a standard 100-kW micro gas turbine to run with methane/hydrogen blended fuel is presented. Enabling micro gas turbines to run with hydrogen blended fuels has been pursued by researchers for decades. The first micro gas turbine running with pure hydrogen was developed in Stavanger, Norway, and launched in May 2022. This was achieved through a collaboration between the University of Stavanger (UiS) and the German Aerospace Centre (DLR). This paper provides an overview of the project and reports the experimental results from the engine operating with methane/hydrogen blended fuel, with various hydrogen content up to 100%. During the development process, the MGT's original combustor was replaced with an innovative design to deal with the challenges of burning hydrogen. The fuel train was replaced with a mixing unit, new fuel valves, and an additional controller that enables the required energy input to maintain the maximum power output, independent of the fuel blend specification. This paper presents the test rig setup and the preliminary results of the test campaign, which verifies the capability of the MGT unit to support intermittent renewable generation with minimum greenhouse gas production. Results from the MGT operating with blended methane/hydrogen fuel are provided in the paper. The hydrogen content varied from 50% to 100% (volume-based) and power outputs between 35 kW to 100kW were tested. The modifications of the engine, mainly the new combustor, fuel train, valve settings, and controller, resulted in a stable operation of the MGT with NO<sub>x</sub> emissions below the allowed limits. Running the engine with pure hydrogen at full load has resulted in less than 25 ppm of NO<sub>x</sub> emissions, with zero carbon-based greenhouse gas production.



**Citation:** Banihabib, R.; Assadi, M. A Hydrogen-Fueled Micro Gas Turbine Unit for Carbon-Free Heat and Power Generation. *Sustainability* **2022**, *14*, 13305. <https://doi.org/10.3390/su142013305>

Academic Editors: Erol Kurt and Jose Manuel Lopez-Guede

Received: 30 August 2022

Accepted: 6 October 2022

Published: 16 October 2022

**Publisher's Note:** MDPI stays neutral with regard to jurisdictional claims in published maps and institutional affiliations.

**Keywords:** micro gas turbine; fuel flexible combustor; experimental data; hydrogen



**Copyright:** © 2022 by the authors. Licensee MDPI, Basel, Switzerland. This article is an open access article distributed under the terms and conditions of the Creative Commons Attribution (CC BY) license (<https://creativecommons.org/licenses/by/4.0/>).

## 1. Introduction

The global warming caused by CO<sub>2</sub> emissions from anthropogenic activities is threatening life on earth. Intermittent renewables, such as wind and solar energy, are foreseen to provide the largest increase in renewable power generation as the most important contributors to sustainable development. The paradigm change, from today's energy system to the future's carbon-free version based on intermittent renewables, can be formulated as the power will be generated when possible, not when needed. However, the intermittent nature of these energy sources is already causing grid instability, which will become even more severe when their share in the power mix will further increase in the near future. Therefore, fuel-flexible, dispatchable energy conversion technologies and energy storage



will be needed to bridge the gap caused by the intermittency of the renewables, such as wind and solar.

Distributed energy generation (DEG) facilitates the use of different energy sources. Since distributed power is generated at or near the point of use, transfer losses can be reduced, and small heat sinks close to end-users can be utilized resulting in considerable efficiency improvements and reduction in emissions. The characteristics of micro gas turbines, i.e., reliability and low maintenance, along with their fuel flexibility and load-following capability have made them an interesting option for combined heat and power generation and a prime mover for competitive, secure and sustainable micro-scale poly-generation [1]. In fact, MGTs can operate on a range of fuels, from high heating values such as methane to low heating value fuels such as biogas [2]. The combustion systems of micro gas turbines can also be designed so that they can burn fuels with lower octane numbers and heavier hydrocarbon components [3,4]. This applies also to fuels containing hydrogen [5].

Fuel flexible, distributed generation units that can utilize locally available resources to provide heat and power on demand, will be of paramount importance for the realization of sustainable energy solutions. Therefore, experimental studies for technology verification and the provision of data for model validation are needed to support this development. Utilizing hydrogen or hydrogen blends has become an important issue for carbon-free power generation. Various challenges are associated with developing and/or modifying the engine components to manage the variable volume flow of the fuel and the changing flame structure and kinetics due to hydrogen combustion [6,7]. However, evaluating the system operation with a large portion of the hydrogen in the fuel blend is a concern for which just a limited number of publications are available in the open literature.

The journey of driving gas turbines with hydrogen-enriched fuels began decades ago. In 1939, Hans von Ohain tested a prototype of a gas turbine that was supplied with hydrogen from an externally pressurized source. The smooth and fast combustion of hydrogen was observed while metal burnout was reported as an obstacle [7]. A combustor prototype for a micro gas turbine was developed by Minakawa et al. [8] to run with pure hydrogen. The combustor was a lean premixed swirling type, and it was tested in atmospheric pressure conditions, resulting in efficient combustion and low NO<sub>x</sub> emissions. The prototype was later assembled on an MGT which resulted in flashbacks during the startup. This issue, which was unforeseen during the component test, was addressed by modifying the air inlet to the combustor [8]. One of the first publications reporting the measurements of hydrogen injection into a heavy-duty gas turbine was provided by Morris et al. [9] in 1998. An immediate reduction in CO emissions and a slight increase in NO<sub>x</sub> production were observed by hydrogen injection up to 10% in the fuel.

With the development of computers over the years, researchers pursued modeling and simulation of combustion with hydrogen to reduce experimental costs and attain a deep understanding of the phenomena. Combustion of hydrogen/methane-blended fuels in a micro gas turbine was studied by Shih et al. utilizing computational fluid dynamic (CFD) methods [10]. In their research, the effect of hydrogen on flame structure and emissions were investigated by adding hydrogen from 0 to 90% on volume bases. The authors concluded that although simulation results indicate a stable combustion performance, modifications to the original combustor will be required to address the emissions of the combustor with a high hydrogen content [10]. Experiments, as well as numerical investigations, were conducted by Rajpara et al. [11] to assess the effect of hydrogen injection on a gas turbine burning methane, upstream of the swirl combustor. Increasing hydrogen content resulted in smaller flame dimensions with an increase in NO<sub>x</sub> emissions due to higher flame temperature but a decrease in CO emissions. Cappelletti et al. [12] investigated the combustion of pure hydrogen in a lean premix burner with experimental and numerical simulations. The experimental setup was built based on an existing burner from a heavy-duty gas turbine, which was modified to enable variable premixing levels. With hydrogen combustion, high flow velocity was required to avoid the flame positioning inside the pre-

mixer duct. The results of their work confirmed the possibilities of developing combustion technology with pure hydrogen fuel while keeping the emissions below the regulated limits. Binesh et al. [13] performed a series of experiments to investigate the combustion behavior of hydrogen-enriched methane fuel in a swirl-stabilized model gas-turbine combustor. The amount of hydrogen in the blended fuel was increased up to 80% in volume and during their test, the upper and lower limits of air to maintain stable combustion were derived.

In May 2020, Kawasaki announced a successful test of an industrial gas turbine with hydrogen fuel, through their dry low emission combustion technology. The combustor applies micro-mix combustion technology, which features ultra-small hydrogen-fueled flames and achieves low NO<sub>x</sub> combustion without using water or steam, which is beneficial in terms of cycle efficiency [14,15].

This paper presents the experimental setup of a test rig in Stavanger, Norway, utilizing a T100 micro gas turbine in combined heat and power (CHP) mode. As the reviewed literature shows, the goal of operating micro gas turbines has been pursued for decades, however, the successful operation of a micro gas turbine with high (up to 100%) content of hydrogen was not achieved before. In fact, burning high hydrogen content fuels was investigated in two ways, either numerical or experiments with combustor test rigs to focus on combustion phenomena. The stable combustion was achieved in most of the combustor test rigs at the atmospheric condition which fails to imitate the real pressure conditions in an engine. Furthermore, a test rig that is specified for a combustor, fails to simulate the interaction between the combustor and other components, different operating conditions of the engine, the transitions, and how they all affect the combustion of the hydrogen-enriched fuel.

This paper provides insights into the application of hydrogen-enriched fuel on a commercial micro gas turbine. The complications of running the engine in part-loads and base-load operations have been addressed. The transitions between loads are crucial situations in the engine, where the varying fuel flow rate and rotational speed in the engine will impact the air/fuel ratio in the combustor and the main flow rate through the engine as well. The complications of hydrogen combustion have a destructive effect on the performance of the engine, which has been encountered during the current endeavor and undertaken via design modifications and controller optimization.

The structure of the paper is as follows: first, an overview of the main challenges with hydrogen combustion is provided. Secondly, the engine setup is presented, with a focus on technology modifications, overcoming the issues of hydrogen combustion. The preliminary results from engine operation with various mixtures of methane and hydrogen are also presented which verifies the presented technology.

## 2. Problem Formulation

Developing a gas turbine engine to run with hydrogen is accompanied by numerous challenges; especially when the goal is to accommodate the variable content of the hydrogen blend with carbon-based fuels. The difference in characteristics of hydrogen and hydrocarbon (in this case, methane) leads to different combustion characteristics which must be considered during the designing process of the combustor and fuel delivery system. Reviewing numerous studies on combustion with hydrogen, a summary of these characteristics is provided in the following subsections.

### 2.1. Combustion Kinetics

Hydrogen has higher flammability and a lower ignition temperature. In fact, the low ignition temperature of hydrogen together with the high flame propagation speed and high flame temperature could improve the conditions for maintaining stable combustion in low-load ranges of gas turbines operation, also lower the risk of flame-out in lean combustion conditions [16–20]. The higher speed of hydrogen flame in comparison with methane can cause flashbacks, in which the flame sits in unwanted locations and could result in component damage. Part-load operations are more prone to flashbacks, therefore

careful consideration for controlling the airflow during the operation is required to avoid flashbacks [21].

## 2.2. Flame Temperature

The adiabatic flame temperature of hydrogen combustion is higher than methane and their differences increase as the combustion becomes richer [22,23]. Adding hydrogen to methane will also increase the adiabatic flame temperature since hydrogen will accelerate the reaction rate [16,24]. In Figure 1, the adiabatic flame temperature of burning methane and hydrogen is compared with each other. The air/fuel mixture in the calculation is assumed to be at 4.3 bar pressure and 630 K temperature, which is the condition of the air entering the combustor when the MGT is running at the baseload. As it is evident from the figure, the richer the combustion is, the larger the difference between the adiabatic flame temperature of methane and hydrogen becomes. However, in very lean air/fuel mixes, the adiabatic temperature of methane and hydrogen are very close to each other.

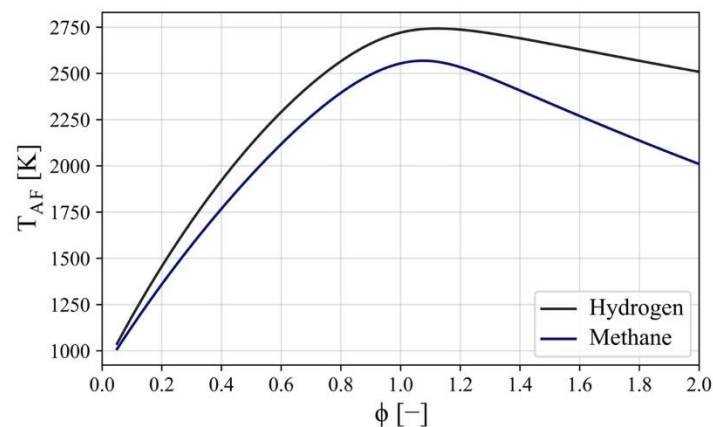


**Figure 1.** Adiabatic flame temperature for burning methane and hydrogen.

## 2.3. NOx Emissions

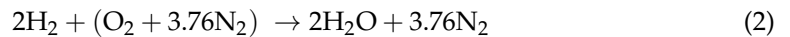
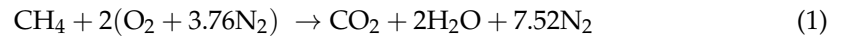
One of the main concerns of hydrogen combustion is the production of toxic nitrogen oxides due to high temperatures. The nitrogen molecule present in the air reacts with oxygen in high temperature conditions. The NOx production begins when the temperature reaches above 1000 °C and the rate of production increases rapidly with further increase in the temperature [25]. One of the common ways of preventing NOx emissions in gas turbines is to use lean premixed burners or dry low NOx burners, where the fuel is premixed with the air prior to the combustion, to keep the flame temperature below a certain value [26]. The main concerns with lean premixed burners are providing stable conditions for combustion, avoiding flashbacks, and thermo-acoustic instabilities [27,28]. These issues become more complicated when using hydrogen and methane blends. The established technology designed for hydrocarbon-based fuels is not adequate for hydrogen blends, especially with high hydrogen contents. With a big difference in flammability range and reaction rates of hydrogen from hydrocarbons, the ignition in combustors will occur before the fuel is adequately mixed with air which results in high temperatures and promotes NOx emissions. Dilution with steam and water is another method employed in gas turbines to alleviate the combustion temperature and NOx production, which is not the best solution since it has a destructive effect on cycle efficiency because of the evaporation of water spray in the hot combustion gas. Besides, dilution with water and steam could cause thermal stress which affects the material integrity of the components. Moreover, high quality water will be required which will increase the costs.

## 2.4. Different Combustion Products

The replacement of carbon atoms with hydrogen when hydrogen is added to the fuel will result in different combustion products. Burning methane will produce carbon



dioxide and water, while the products of hydrogen combustion will be only water (steam). Therefore, hydrogen combustion will result in a higher content of water (steam) in flue gas than when methane is combusted. Burning the fuels with air assuming the two main components of it (nitrogen and oxygen) will be as described in Equations (1) and (2):



This is when we are assuming complete combustion, however, the reality includes other products as the combustion is not complete. Carbon monoxide, nitrogen oxides, and even radicals could be in the product mix. Adding hydrogen to the fuel could improve the combustion efficiency and reduce the share of these products, as it increases the flame temperature [29].

To evaluate the effect of adding hydrogen to a methane–fuels combustor, two different approaches were conducted by the authors in [11]. Once, the hydrogen injection was performed while keeping the heat input constant, and secondly, the volume flow rate was kept constant. Both mechanisms that resulted in the reduction of CO in the products were observed in these two scenarios.

A numerical approach was taken by the authors of [16], where CO emissions for combustion at different pressure and temperature conditions with variant hydrogen content were simulated. According to their work, once the hydrogen share in the fuel reaches 80% of the whole fuel flow, CO emissions decreased to the half value of when there is no hydrogen in the mix. This result was somewhat true regardless of the pressure and temperature conditions. The simulations show that even a small quantity of hydrogen in the primary zone of combustion could contribute to CO reduction, because of both mechanisms discussed [30].

The destructive effect of premix on combustion efficiency and CO and HC emissions could be lessened by injecting small quantities of hydrogen (up to 4%) to lean primary zones, without affecting NO<sub>x</sub> production [31].

Developing combustor technology for hydrogen combustion becomes more complex when the goal is to operate with pure hydrogen as well as hydrogen-blended fuels. Blended fuels of methane and hydrogen should be applicable to small-scale heat and power generation units, such as micro gas turbines, with the option to vary the mixture ratio [32].

The difference in the heating value and density of the fuels is another variation that must be considered. This will lead to variations in the fuel flow rate and therefore flue gas flow rate. Moreover, with the difference in flue gas composition, the thermodynamic cycle of the MGT could be altered, as the matching point could be moved [33]. Assuming the same condition for the air entering the combustion chamber, the engine baseload condition is compared between methane and hydrogen. For the micro gas turbine to receive the required heat input, 6.7 g/s methane (pure methane case) and 2.8 g/s of hydrogen (pure hydrogen case) should be provided. The air has 4.3 bar and 610 K after passing through the compressor and the recuperator.

The equivalence ratio of the combustion mix could be calculated, assuming that the airflow inlet to the engine is 0.8 kg/s at the baseload. For pure methane, the equivalence ratio is 0.14 and for hydrogen it is 0.12, both indicating lean combustion. This difference will cause a 6 °C increase in the adiabatic flame temperature of hydrogen in comparison with methane. The volumetric flow rate of the flue gas entering the turbine will increase by 1.5% due to the alteration of the density and mass flow rate. The specific heat capacity in flue gas with hydrogen will be 1% higher compared to methane. All of these minor changes are due to the fact that the combustion mix at the baseload is very lean, so the difference in the properties is relatively small. This situation is very different from large-scale gas turbines, where the fuel-to-air ratio is an order of magnitude higher compared to MGTs. The flue gas properties are reported in Table 1 for pure methane and pure hydrogen combustion in the MGT.

**Table 1.** Flue gas properties comparison burning methane and hydrogen. Air composition is 21% O<sub>2</sub> and 79% N<sub>2</sub> with 4.3 bar pressure and 610 K temperature.

Property	Methane	Hydrogen
Lower heating value (per mass)	50 MJ/kg	120 MJ/kg
Fuel flow rate for nominal power output	6.7 g/s	2.8 g/s
Air flow rate	0.8 kg/s	0.8 kg/s
Flue gas flow rate	0.67 m <sup>3</sup> /s	0.68 m <sup>3</sup> /s
Stoichiometric air–fuel ratio (mass-based)	17.12	34.06
Actual air–fuel ratio (mass-based)	120	288
Equivalence ratio	0.14	0.12
Adiabatic flame temperature	1230.52 K	1236.51 K
Flue gas heat capacity at constant pressure	1214.8 J/kgK	1228.8 J/kgK

In the following section, an overview of the experimental setup with the main modifications and redeveloped items are explained which were essential to solve the challenges explained.

### 3. Test Rig Description

The test rig was based on a commercial Turbec T100 unit (T100PH) Series 2 micro gas turbine. T100PH is a single shaft micro gas turbine designed to work both in power generation mode and in cogeneration mode for combined heat and power generation. The T100 is equipped with a recuperator that preheats the air before the combustion chamber by transferring heat from the turbine exhaust gas. There is also a heat exchanger, exploiting the remaining heat in the exhaust gas to warm up the circulating water.

The power generating unit consists of a single-stage centrifugal compressor, a single-stage radial turbine, a tubular combustor, and a high-speed permanent magnet generator. The compressor and the turbine work with a pressure ratio of about 4.3 and a turbine inlet temperature of around 950 degrees Celsius. At nominal operating conditions (with ISO ambient conditions), the unit can produce 100 kW of electrical power at a rotational speed of 70,000 rpm and electrical efficiency of 30%, thanks to the recuperator which is compensating for the low-pressure ratio and low turbine-inlet temperature. In cogeneration mode, the total efficiency (fuel utilization factor) increases to 80%. The test rig, modified for fuel flexible operation is presented in Figure 2.



**Figure 2.** Turbec T100 unit with modified combustor and fuel train for flexible fuel operation.

During the past few years, numerous modifications have been made to the engine to enable research and development activities, exploring the fuel flexibility of the unit. Recently, the original engine was modified to enable running with hydrogen-enriched fuels, by replacing the original combustor with a new design. The fuel train was also modified to enable different fuel blends in terms of hydrogen content. Over 50 sensors have been installed in different locations of the engine for a comprehensive overview of the engine condition during a test run. In this section, an overview of the main modifications implemented on the engine is provided.

Hydrogen and methane fuel is provided by bundles, each comprising high-pressure interconnected bottles. The bundles are connected to the fuel train via a pressure regulator, to reduce the pressure from over 200 bars to below 20 bars. There are also flashback arrestors and disconnecting valves in the circuit which protect the line. The disconnecting valves are controlled by a leakage sensor inside the building. The bundles and regulator are shown in Figure 3.



**Figure 3.** Fuel bundles and regulators.

To enable seamless fuel mixing and to accommodate for the changing volume flow of the fuel blend, the fuel train and the gas mixing station have been modified. The system consists of two separate flow controllers for methane and hydrogen, a mixing station, two main valves, and a pilot valve to supply fuel to the MGT. The mixing station is a wide and long pipe that provides enough space so that methane and hydrogen mix well together, preventing hydrogen pockets and local high temperatures inside the combustor which could result in thermal damage and NO<sub>x</sub> production. The mixed fuel rate is determined by the MGT controller, which has a PID system that finds the adequate fuel flow rate that provides enough heat input to the system at each power set point. The amount of each fuel type is however defined and regulated by the additional controller provided for the fuel train, working based on the ratio of the fuel types defined by the operator.

In Figure 4, the fuel train temporarily installed on top of the MGT enclosure is shown with a schematic diagram of the system. Originally, two main valves were installed to increase the flexibility during the operation, however, one of them remained closed since it was not required. A three-way valve that provides discharge to the atmosphere is also included in the system for safety reasons.

The combustion chamber and fuel system of the MGT test rig have been replaced with a new design to accommodate various fuel mixtures of hydrogen and hydrocarbon-based fuels. The original combustor has been replaced by a fuel-flexible combustor designed and manufactured by the German Aerospace Centre (DLR) to investigate the performance of the engine in different load conditions. To evaluate the unit's performance and cyclic behavior, additional pressure and temperature sensors have been installed.

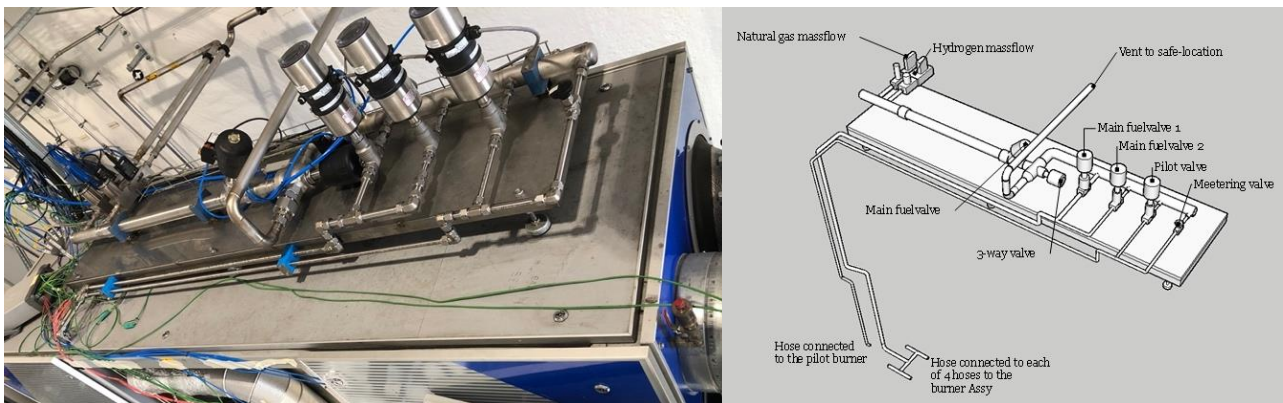


**Figure 4.** Fuel train for hydrogen/methane fuel supply and mixing.

The test rig is equipped with an F400s FLOX<sup>®</sup> combustor (see Figure 5). It is a low NO<sub>x</sub>, flameless combustor with proven fuel flexibility, capable of running on hydrogen [3,5]. The combustor was tested on an atmospheric test rig with up to 100% hydrogen, but its hydrogen capability in real conditions inside a gas turbine was verified during the current experiments. An overview of the original combustor's geometry could be found in [34].



**Figure 5.** The original combustor was installed on T100 (left) compared to the F400s fuel flexible combustor installed on the test rig (right).

The baseline engine is equipped with sensors, that measure the flow properties, rotational speed, power output, and a few other parameters mainly for controlling the engine operation. The test rig has been equipped with over 50 additional sensors to enable detailed condition monitoring and performance analysis. Figure 6 shows the position of the sensors at different locations. These sensors can be divided into four different categories:

1. Cycle measurements: Pressure and temperature sensors are placed in different locations to provide operational data;
2. Fuel measurement: Pressure, temperature, and mass flow sensors are providing comprehensive information about the fuel at every operational condition;
3. Metal temperature measurement: The metal temperature is measured inside the combustor for lifetime assessments;
4. Emissions measurement: Measuring the concentration of the exhaust gas components.



No.	Description	Temperature	Pressure
1	Engine inlet	1	-
2	After the inlet air filter	4	6
3	After compressor	3	3
4	After recuperator cold side	1	-
5	After combustor	2	-
6	After turbine	-	-
7	After diffuser	7	1
8	After recuperator hot side	-	-
9	Engine outlet	-	-
10	Before the heat exchanger cold side	-	-
11	After the heat exchanger cold side	4	-

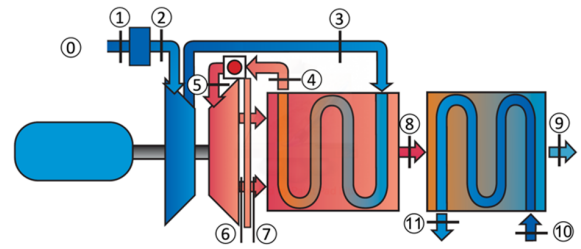


**Figure 6.** Cycle measurements.

Among the 32 sensors listed in the table of Figure 6 are 6 Turbec built-in sensors and 26 are additionally installed. It is worth mentioning that two thermocouples have been installed in position 5, where the working flow has the highest temperature in the cycle. These sensors are located inside the combustor, measuring the temperature of the flow close to the combustion and dilution zone. The temperature of the inlet air to the combustor is also measured (see Figure 7).

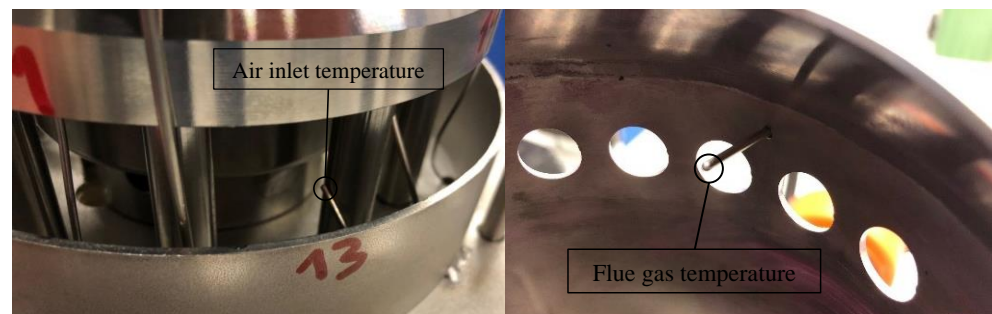


**Figure 7.** Flow measurements installed in the combustor.

The measurements related to the fuel system are presented in Table 2, providing detailed information about fuel conditions, before and after mixing. The sensors listed in rows 1 to 3 are installed in the fuel train (Figures 3 and 4) and the fuel temperature in the combustor is measured by a thermocouple close to the combustion point.

**Table 2.** Number of fuel measurements in the fuel system.

Description	Temperature	Pressure	Mass flowrate
Methane fuel	1	1	1
Hydrogen fuel	1	1	1
Mixed fuel	1	1	-
Fuel in combustor	1	-	-

#### 4. Results

To investigate the transient performance of the engine running with high hydrogen content, a maneuver of the engine with increasing hydrogen content, from 85% to 90% was conducted without changing the controller's settings. The run was executed in 13 °C ambient temperature and 1.01 bar ambient pressure for which the logged data are presented in Figure 8. Snapshot data are extracted and presented in Table 3, where the performance parameters at each power step in steady-state conditions are presented. The hydrogen content in the fuel is calculated based on the volume flow rate. Power step-up was run with 88% hydrogen and at the maximum load it was increased to 90% and then a step-down

was conducted. These data provide the bases for comparison as it was collected from less than an hour's run, however, the ambient temperature during the run gradually increased by one degree.

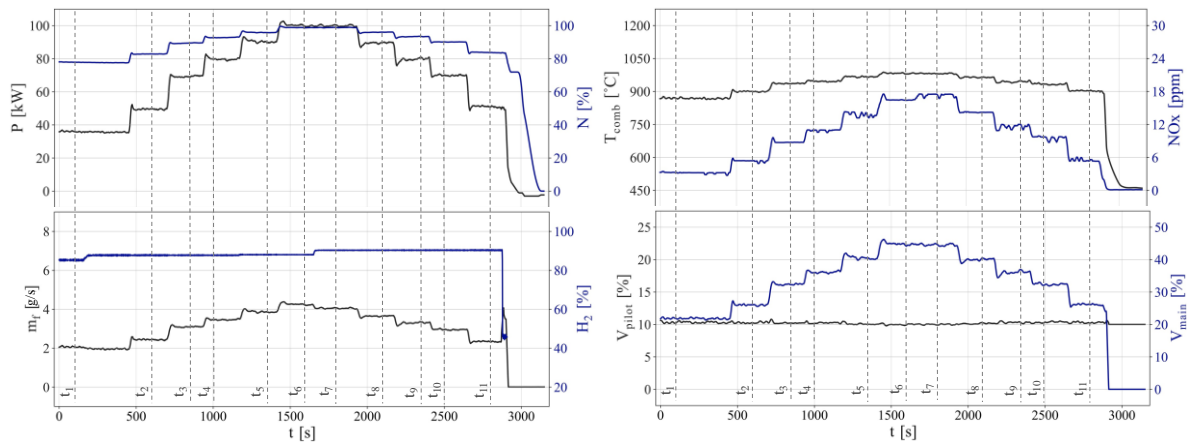


**Figure 8.** Power variation with F400-s ver02, modified controller setup. The ambient condition during the test is 13 °C and 1.01 bar.

**Table 3.** Data extracted from steady-state spans from a test run depicted in Figure 8.

	Elapsed time	P (kW)	N (%)	$\dot{m}_f$ (g/s)	H <sub>2</sub> (%)	T <sub>comb</sub> (°C)	NOx (ppm)	V <sub>pilot</sub> (%)	V <sub>main</sub> (%)
t <sub>1</sub>	100	35	77.9	2.1	85.1	869.8	3.3	10.3	20.6
t <sub>2</sub>	600	50	82.9	2.4	87.7	899.7	5.4	10.5	25.1
t <sub>3</sub>	850	70	89.5	3.1	87.6	934.5	8.7	9.8	31.5
t <sub>4</sub>	1000	80	92.7	3.5	87.7	948.1	11.0	10.3	35.0
t <sub>5</sub>	1350	90	95.8	3.9	88.1	966.3	13.9	10.6	39.5
t <sub>6</sub>	1600	100	98.7	4.2	87.9	979.2	16.4	9.9	43.3
t <sub>7</sub>	1800	100	98.8	4.1	90.4	980.5	17.5	10.2	43.9
t <sub>8</sub>	2100	90	96.0	3.7	90.4	964.6	14.2	10.2	39.2
t <sub>9</sub>	2350	80	93.5	3.3	90.3	947.8	12.0	10.2	35.8
t <sub>10</sub>	2500	70	90.2	2.9	90.3	933.5	9.7	10.2	31.3
t <sub>11</sub>	2800	50	83.7	2.3	90.0	902.6	5.3	9.9	24.9

At 100 kW the increase in hydrogen resulted in less than 2 °C increase in flue gas temperature and more than 1 ppm increase in NOx emissions. The same difference in the temperature and emissions could be observed for other power rates as well. The difference in NOx emission rate is due to the higher temperature in the combustor, previously discussed in the section "flame temperature." The variation in combustion temperature is illustrated in Figure 8 and according to the data reported in Table 3, less than 2 °C could be observed in flue gas temperature. This change is measured by the thermocouple shown in Figure 7 which is installed inside the combustor and closed to the dilution holes. Therefore, the measured temperature could only be an indicator of the increase in combustion temperature, since it is a local measurement after cooling and the actual value of the increase in combustion temperature is not clear. Other than the 100 kW case, the comparison for other power rates shows that NOx production is 1 ppm higher due to a 3% increase in hydrogen content.

The rotational speed of the engine for the same power outputs is slightly (less than 1% relative to the nominal speed) higher with increased hydrogen content, however, the ambient temperature is higher during the second half of the operation and that has a direct impact on the rotational speed. In general, when weather is warmer, the engine rotates at higher speeds.

The position of the pilot and main valves is also presented in Figure 8, where the pilot valve position is almost constant throughout the operation. The main valve provides

variations in fuel flow rate for the maneuver. The pilot opening for the steady-state operation was originally set to 14%, which is a value appropriate for methane and blended methane/hydrogen fuel with small share of hydrogen. With increasing the amount of hydrogen, the pilot valve is recalibrated to a lower value which keeps the NO<sub>x</sub> emissions below the regulated amount and also stabilizes the combustion.

Other than the discussed maneuvers, several runs with different hydrogen content have been conducted. Using the data post-processing tool, the steady-state period data are extracted which can provide insights into the influence of hydrogen injection on the MGT performance parameters. In Figure 9, the NO<sub>x</sub> emissions in different power outputs with various hydrogen content are presented. The general trend taken from the figure suggests that the production of NO<sub>x</sub> increases as the share of hydrogen in the fuel increases. There are a few points in Figure 9 that are from the runs with a hydrogen content of around 55% (white circles) which do not follow the general behavior. The reason is that, during that test, the original valve setting was used which led to high NO<sub>x</sub> emissions. The high temperatures in the combustor encouraged modifying the valves' settings which led to the lower opening of the pilot valve. All other points are from the maneuvers after recalibration of the valves.

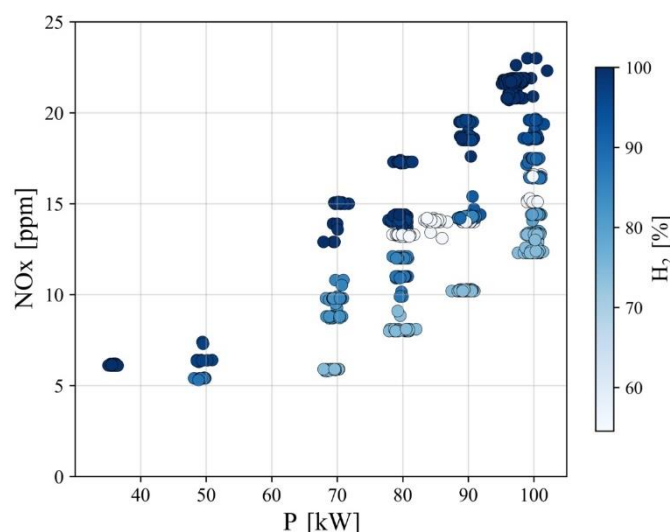


**Figure 9.** NO<sub>x</sub> production in a range of power outputs with respect to hydrogen content in the fuel.

The impact of hydrogen injection on the efficiency of the engine cycle is investigated in Figure 10. The performance of the engine in terms of electrical efficiency for a range of hydrogen contents is similar to each other and increases with the power output. There is a slight difference in the efficiency of the cycle at a constant power output, but the main reason is the effect of ambient conditions; as the engine inlet temperature increases, the efficiency of the engine reduces [35].

The main reason for replacing carbon-based fuels with hydrogen is to reduce the production of carbon oxides. As discussed, adding hydrogen fuel will contribute to the reduction in the greenhouse gases that result in global warming, both by replacement of carbon atoms with hydrogen and by promoting combustion efficiency and complete combustion. This effect is illustrated in Figure 11, where a higher content of hydrogen has resulted in lower CO emissions and zero CO emissions are evident for pure hydrogen. The only points that are not compliant with the trends are, once again, the experiment with 55% hydrogen. The run of that case included trials and errors to ensure a stable operation with NO<sub>x</sub> emissions below the regulated values, so different arrangements for pilot valves were tried. The results of these tests led to different combustion efficiencies and therefore CO emission rates.

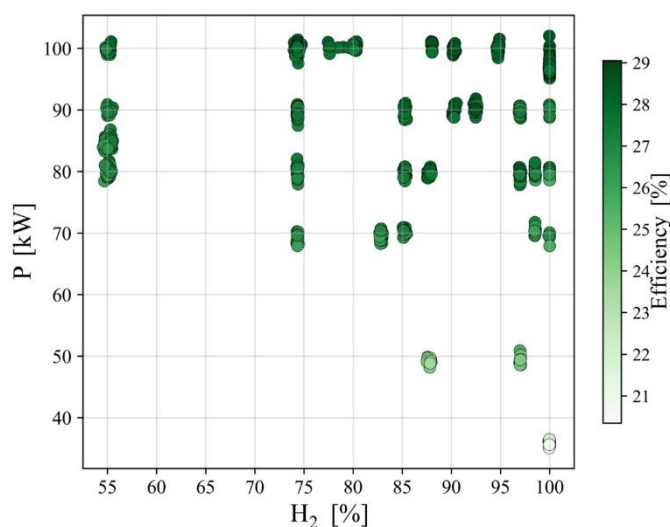


**Figure 10.** Electrical efficiency of the engine in a range of power output and hydrogen content in the fuel.

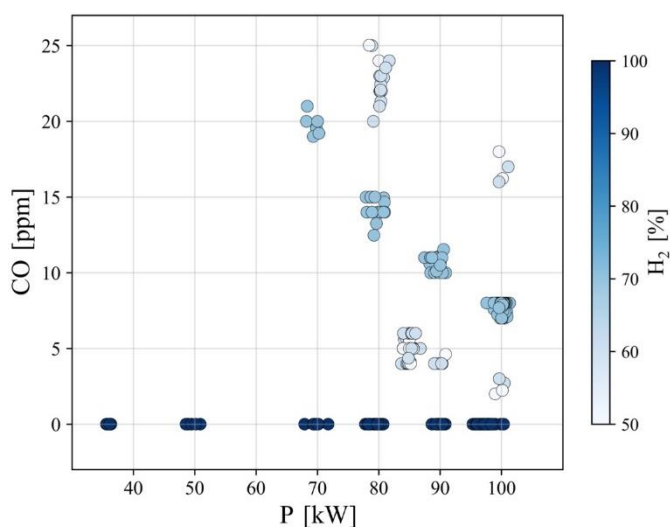


**Figure 11.** CO emission in a range of power output with different hydrogen content in the fuel.

## 5. Conclusions

In this paper, the process of redeveloping a commercial micro gas turbine to operate with blended methane/hydrogen fuel is presented. Previous studies have shown that a small amount of hydrogen injection into gas turbines is tolerated, however, as the share of hydrogen increases, combustion temperatures and therefore NO<sub>x</sub> emissions increase. Moreover, using the same combustion system will result in unstable combustion and the risk of flashbacks, because of the difference between the combustion characteristics between hydrogen and methane (or natural gas).

During a collaboration between the university of Stavanger and the German Aerospace Centre (DLR), a modified version of the T100 PH micro gas turbine is provided, with minimum modifications required. A new combustor with an innovative design based on FLOX technology developed by DLR is used to accommodate combustion with high hydrogen content. The engine is also equipped with a new fuel train with an additional controller, so a range of fuel blends could be provided for the engine. The modifications to the main controller of the engine are kept to a minimum and confined only to the controller parameters in the software. With a smaller opening in the pilot valve, stable combustion with regulated NO<sub>x</sub> is realized.

Several maneuvers with different hydrogen contents are conducted for a range of power outputs. The maximum NO<sub>x</sub> emission is 25 ppm for running the engine at maximum



load with pure hydrogen. The corrected NO<sub>x</sub> emission based on the case with 15% O<sub>2</sub> is 64 ppm, which is lower than the regulated value. The electrical efficiency of the engine is not impaired by hydrogen injection into the system. The greenhouse gas emission is reduced by increasing the share of hydrogen in the fuel, by replacement of the carbon element with hydrogen, also by the improvement of combustion efficiency. Close to zero CO emissions are realized when the engine is derived with pure hydrogen.

**Author Contributions:** Data curation, R.B.; Funding acquisition, M.A.; Software, R.B.; Supervision, M.A.; Visualization, R.B.; Writing—original draft, R.B.; Writing—review and editing, M.A. All authors have read and agreed to the published version of the manuscript.

**Funding:** This project has received funding from the European Union’s Horizon 2020 research and innovation program under the Marie Skłodowska-Curie grant agreement No. 861079, “NextMGT”-Next Generation of Micro Gas Turbines for High Efficiency, Low Emissions and Fuel Flexibility.

**Institutional Review Board Statement:** Not applicable.

**Informed Consent Statement:** Not applicable.

**Conflicts of Interest:** The authors declare no conflict of interest.

## References

1. European Turbine Network (ETN). Micro Gas Turbine Technology Research and Development for European Collaboration. In *ETN Micro Gas Turbine Technology Summary*; ETN: Brussels, Belgium, 2018.
2. Pilavachi, P. Mini- and micro-gas turbines for combined heat and power. *Appl. Therm. Eng.* **2002**, *22*, 2003–2014. [[CrossRef](#)]
3. Lammel, O.; Schütz, H.; Schmitz, G.; Lückcrath, R.; Stöhr, M.; Noll, B.; Aigner, M.; Hase, M.; Krebs, W. FLOX<sup>®</sup> Combustion at High Power Density and High Flame Temperatures. *J. Eng. Gas Turbines Power* **2010**, *132*, 121503. [[CrossRef](#)]
4. Zornek, T.; Monz, T.; Aigner, M. Performance analysis of the micro gas turbine Turbec T100 with a new FLOX-combustion system for low calorific fuels. *Appl. Energy* **2015**, *159*, 276–284. [[CrossRef](#)]
5. Lückcrath, R.; Meier, W.; Aigner, M. FLOX combustion at high pressure with different fuel compositions. In Proceedings of the ASME Turbo Expo 2007: Power for Land, Sea and Air, Montreal, QC, Canada, 14–17 May 2007; pp. 1–9. [[CrossRef](#)]
6. Calabria, R.; Chiariello, F.; Massoli, P.; Reale, F. CFD Analysis of Turbec T100 Combustor at Part Load by Varying Fuels. In Proceedings of the ASME Turbo Expo 2015: Turbine Technical Conference and Exposition, Montreal, QC, Canada, 15–19 June 2015.
7. Langston, L.S. Hydrogen Fueled Gas Turbines. *Mech. Eng.* **2019**, *141*, 52–54. [[CrossRef](#)]
8. Minakawa, K.; Miyajima, T.; Yuasa, S. Development of a hydrogen-fueled micro gas turbine with a lean premixed combustor. In Proceedings of the 33rd Joint Propulsion Conference and Exhibit, Seattle, WA, USA, 6–9 July 1997; pp. 1–6. [[CrossRef](#)]
9. Morris, J.D.; Symonds, R.A.; Ballard, F.L.; Banti, A. Combustion Aspects of Application of Hydrogen and Natural Gas Fuel Mixtures to MS9001E DLN-1 Gas Turbines at Elsta Plant, Terneuzen, The Netherlands. In Proceedings of the ASME International Gas Turbine and Aeroengine Congress and Exhibition, Stockholm, Sweden, 2–5 June 1998. [[CrossRef](#)]
10. Shih, H.-Y.; Liu, C.-R. A computational study on the combustion of hydrogen/methane blended fuels for a micro gas turbines. *Int. J. Hydrogen Energy* **2014**, *39*, 15103–15115. [[CrossRef](#)]
11. Rajpara, P.; Shah, R.; Banerjee, J. Effect of hydrogen addition on combustion and emission characteristics of methane fuelled upward swirl can combustor. *Int. J. Hydrogen Energy* **2018**, *43*, 17505–17519. [[CrossRef](#)]
12. Cappelletti, A.; Martelli, F. Investigation of a pure hydrogen fueled gas turbine burner. *Int. J. Hydrogen Energy* **2017**, *42*, 10513–10523. [[CrossRef](#)]
13. Imteyaz, B.A.; Nemitallah, M.; Abdelhafez, A.A.; Habib, M.A. Combustion behavior and stability map of hydrogen-enriched oxy-methane premixed flames in a model gas turbine combustor. *Int. J. Hydrogen Energy* **2018**, *43*, 16652–16666. [[CrossRef](#)]
14. Horikawa, A.; Okada, K.; Wirsum, M.; Funke, H.H.-W.; Kusterer, K. 100% hydrogen dry low NO<sub>x</sub> combustor developments for 2MW class gas turbine. In Proceedings of the International Conference on Power Engineering (ICOPE), Yokohama, Japan, 17–21 October 2021; Volume 2021. [[CrossRef](#)]
15. Funke, H.H.-W.; Beckmann, N.; Keinz, J.; Horikawa, A. 30 Years of Dry-Low-NO<sub>x</sub> Micromix Combustor Research for Hydrogen-Rich Fuels—An Overview of Past and Present Activities. *J. Eng. Gas Turbines Power* **2021**, *143*. [[CrossRef](#)]
16. Sun, Y.; Zhang, Y.; Huang, M.; Li, Q.; Wang, W.; Zhao, D.; Cheng, S.; Deng, H.; Du, J.; Song, Y.; et al. Effect of hydrogen addition on the combustion and emission characteristics of methane under gas turbine relevant operating condition. *Fuel* **2022**, *324*, 124707. [[CrossRef](#)]
17. Anderson, D.N. *Effect of Hydrogen Injection on Stability and Emissions of an Experimental Premixed Pre-vaporized Propane Burner*; Report NASA TMX-3301; Lewis Research Center, National Aeronautics and Space Administration: Cleveland, OH, USA, October 1975.
18. Emami, S.D.; Kasmani, R.M.; Hamid, M.D.; Hassan, C.R.C.; Mokhtar, K.M. Kinetic and dynamic analysis of hydrogen-enrichment mixtures in combustor systems—A review paper. *Renew. Sustain. Energy Rev.* **2016**, *62*, 1072–1082. [[CrossRef](#)]

19. Wei, Z.; He, Z.; Zhen, H.; Zhang, X.; Chen, Z.; Huang, Z. Kinetic modeling investigation on the coupling effects of H<sub>2</sub> and CO<sub>2</sub> addition on the laminar flame speed of hydrogen enriched biogas mixture. *Int. J. Hydrogen Energy* **2020**, *45*, 27891–27903. [[CrossRef](#)]
20. He, Y.; Liang, M.; Liu, C.; Liao, S.; Yang, R.; Qin, L.; Jian, X.; Shao, Y. Kinetic incentive of hydrogen addition on nonpremixed laminar methane/air flames. *Int. J. Hydrogen Energy* **2021**, *46*, 14813–14823. [[CrossRef](#)]
21. Wu, J.; Brown, P.; Diakunchak, I.; Gulati, A.; Lenze, M.; Koestlin, B. Advanced Gas Turbine Combustion System Development for High Hydrogen Fuels. In Proceedings of the ASME Turbo Expo: Power for Land, Sea, and Air, Montreal, QC, Canada, 14–17 May 2007; Volume 2, pp. 1085–1091. [[CrossRef](#)]
22. Zhou, Q.; Cheung, C.; Leung, C.; Li, X.; Li, X.; Huang, Z. Effects of fuel composition and initial pressure on laminar flame speed of H<sub>2</sub>/CO/CH<sub>4</sub> bio-syngas. *Fuel* **2018**, *238*, 149–158. [[CrossRef](#)]
23. Amar, H.; Abdelbaki, M.; Fouzi, T.; Zeroual, A. Effect of the addition of H<sub>2</sub> and H<sub>2</sub>O on the polluting species in a counter-flow diffusion flame of biogas in flameless regime. *Int. J. Hydrogen Energy* **2018**, *43*, 3475–3481. [[CrossRef](#)]
24. Xiang, L.; Jiang, H.; Ren, F.; Chu, H.; Wang, P. Numerical study of the physical and chemical effects of hydrogen addition on laminar premixed combustion characteristics of methane and ethane. *Int. J. Hydrogen Energy* **2019**, *45*, 20501–20514. [[CrossRef](#)]
25. Toof, J.L. A Model for the Prediction of Thermal, Prompt, and Fuel NO<sub>x</sub> Emissions from Combustion Turbines. *J. Eng. Gas Turbines Power* **1986**, *108*, 340–347. [[CrossRef](#)]
26. Cowell, L.H.; Smith, K.O. Development of a Liquid-Fueled, Lean-Premixed Gas Turbine Combustor. *J. Eng. Gas Turbines Power* **1993**, *115*, 554–562. [[CrossRef](#)]
27. Ditaranto, M.; Heggset, T.; Berstad, D. Concept of hydrogen fired gas turbine cycle with exhaust gas recirculation: Assessment of process performance. *Energy* **2020**, *192*, 116646. [[CrossRef](#)]
28. Venkataraman, K.K.; Preston, L.H.; Simons, D.W.; Lee, B.J.; Lee, J.G.; Santavicca, D.A. Mechanism of Combustion Instability in a Lean Premixed Dump Combustor. *J. Propuls. Power* **2012**, *15*, 909–918. [[CrossRef](#)]
29. Lee, I.B.; Woo, I.S.; Lee, M.C. Effects of nitrogen dilution on the NO<sub>x</sub> and CO emission of H<sub>2</sub>/CO/CH<sub>4</sub> syngases in a partially-premixed gas turbine model combustor. *Int. J. Hydrogen Energy* **2016**, *41*, 15841–15851. [[CrossRef](#)]
30. Schefer, R.W. Reduced Turbine Emissions Using Hydrogen-Enriched Fuels. In Proceedings of the 2002 US DOE Hydrogen Program Review, NREL/CP-610-32405, Golden, CO, USA, 6–10 May 2002.
31. Juste, G.L. Hydrogen injection as additional fuel in gas turbine combustor. Evaluation of effects. *Int. J. Hydrogen Energy* **2006**, *31*, 2112–2121. [[CrossRef](#)]
32. Tang, C.; Zhang, Y.; Huang, Z. Progress in combustion investigations of hydrogen enriched hydrocarbons. *Renew. Sustain. Energy Rev.* **2014**, *30*, 195–216. [[CrossRef](#)]
33. Chiesa, P.; Lozza, G.; Mazzocchi, L. Using Hydrogen as Gas Turbine Fuel. *J. Eng. Gas Turbines Power* **2005**, *127*, 73–80. [[CrossRef](#)]
34. Cadorin, M.; Pinelli, M.; Vaccari, A.; Calabria, R.; Chiariello, F.; Massoli, P.; Bianchi, E.C. Analysis of a Micro Gas Turbine Fed by Natural Gas and Synthesis Gas: MGT Test Bench and Combustor CFD Analysis. *J. Eng. Gas Turbines Power* **2012**, *134*, 071401. [[CrossRef](#)]
35. Technical Description Microturbine Turbec T100. Available online: [www.ensola.com](http://www.ensola.com) (accessed on 5 October 2022).

## Paper IV

Dynamic Modelling and Simulation of a 100 kW Micro Gas Turbine Running With Blended Methane/Hydrogen Fuel

R. Banihabib and M. Assadi.

Presented at ASME Turbo Expo, Rotterdam, Netherlands, June 2022, doi: 10.1115/GT2022-81276.

**DYNAMIC MODELLING AND SIMULATION OF A 100 KW MICRO GAS TURBINE RUNNING WITH BLENDED METHANE/HYDROGEN FUEL**

**Reyhaneh Banihabib**

Faculty of Science and Technology, University of Stavanger  
Stavanger, Norway

**Mohsen Assadi**

Faculty of Science and Technology, University of Stavanger  
Stavanger, Norway

**ABSTRACT**

The current shift from centralized to decentralized power generation with renewables as prime movers necessitates the integration of reliable small-scale power supply units to compensate for the intermittency of renewables. Micro gas turbines' (MGTs) characteristics such as high reliability and low maintenance, along with flexible operation and quick load-following capabilities have made them a dependable source for the modern power generation industry and for households. MGTs are small-scale gas turbine units with a power range lower than 500 kW that can operate with low-calorific fuels such as biofuels and syngas as well as conventional fossil fuels and zero-carbon fuels.

The utilization of MGTs in innovative cycle layouts or varying types of feeding fuels is increasing, which requires the evaluation of system dynamics to ensure the safe operation of the engine and its components. Moreover, the role of MGTs as a backup for the intermittent renewable inputs means that they operate under more transient conditions rather than constant power production mode. Therefore, a reliable dynamic model of an MGT is required to investigate the dynamic response of the engine under various transient modes to ensure safe operation. Moreover, utilizing a dynamic model is vital in the designing process of MGT-based cycles in order to evaluate the behaviour of coupled components in off-design conditions and to optimize the controller parameters. To that end, developing a dynamic model of the MGT cycle that is accurate enough to predict the dynamic response of the engine and its components and fast enough to be utilized in design iterations is necessary.

In this paper, a high-fidelity model for real-time simulation of an MGT, based on a lumped and nonlinear representation of gas turbine components is presented. The model for a recuperated T100 MGT was constructed in Simscape, the object-oriented environment of MATLAB for modelling physical systems. MGT components were modelled as lumped volumes

with dynamic equations of mass, momentum, and energy balance along with component-characteristic maps describing the evolution of the flow passing through them. Results from simulations were validated by experimental data collected from a real engine operating under different load conditions. Experimental tests and numerical simulations were conducted for pure methane as well as for blended methane/hydrogen as feeding fuels.

Keywords: micro gas turbine, dynamic modelling, simulation, controller system, transient manoeuvres, blended fuels, hydrogen

**NOMENCLATURE**

**Alphanumeric Variables**

$C$	Molecular composition vector
$c$	Specific heat (J/kg K)
$c_v$	Specific heat of gas at constant volume (J/kg K)
$c_p$	Specific heat of gas at constant pressure (J/kg K)
$E$	Total energy (J)
$D$	Diameter (m)
$e$	Total energy per unit mass (J/kg)
$f$	Function / friction factor
$g$	Acceleration of gravity ( $m/s^2$ )
$h$	Specific enthalpy (J/kg)
$k$	Thermal conductivity (W/mK)
$M$	Molar mass (g/mol)
$\dot{m}$	Mass flow rate (kg/s)
$Nu$	Nusselt number
$p$	Pressure (Pa)
$Pr$	Prandtl number
$Q$	Heat exchange (J)
$R$	Specific gas constant (J/kg K)
$Re$	Reynolds number
$T$	Temperature (K)
$t$	Time (s)

$\hat{u}$	Internal energy per unit mass (J/kg)
$V$	Volume (m <sup>3</sup> )
$\vec{v}$	Velocity (m/s)
$W$	Work exchange (J)
$x$	Weight coefficient (kg/kg)
$z$	Direction against gravity field, (m)

### Greek Symbols

$\eta$	Efficiency (-)
$\rho$	Density (kg/m <sup>3</sup> )
$\tau$	Time constant (s)
$\vec{\tau}$	Torque (N.m)
$\Phi$	Humidity ratio (kg/kg)
$\phi$	Energy flow rate (W)
$\omega$	Rotational velocity (rad/s)

### Indices

$a$	Air
$act$	actual
$ad$	adapted
$amb$	Ambient
$cc$	Combustion chamber
$cmp$	Compressor
$cr$	Critical
$e$	Electrical
$ec$	Energy conservation
$ex$	Excess
$f$	Fuel
$fl$	Flue
$HE$	Heat exchanger
$h$	Hydraulic
$in$	Inlet
$is$	Isentropic
$lam$	Laminar
$mc$	Mass conservation
$orig$	Original
$out$	Outlet
$p$	Pressure
$prod$	Product
$react$	Reactant
$ref$	Reference
$sat$	saturated
$T$	Temperature
$trb$	Turbine
$tur$	Turbulent
$v$	Vapor
$wf$	Working fluid, either air or flue gas

### Abbreviations

AF	Air/fuel ratio
CHP	Cogeneration of heat and power
LHV	Lower heating value
MGT	Micro gas turbine
PR	Pressure ratio
pu	Per unit
RH	Relative humidity

TOT Turbine outlet temperature

## 1. INTRODUCTION

Distributed energy generation facilitates the use of different energy sources that are available for customers to choose from and to install in small increments. These units provide the required power to meet the end-user demand. Distributed power is generated at or near the point of use with technologies such as gas turbines, fuel cells, diesel and gas reciprocating engines, solar panels, and small wind turbines.

The characteristics of micro gas turbines (MGTs) such as high reliability and low maintenance, along with flexible operation and quick load-following capabilities, have made them a dependable source of power generation and a prime mover for the future of competitive, secure, and sustainable micro-scale polygeneration [1].

An important advantage of MGTs over other heat engines for decentralized power generation is their fuel flexibility, ranging from natural gas, diesel, liquefied petroleum gas, and hydrogen to waste and biomass-derived fuels. In fact, MGTs can operate with fuels with low heating value without engine de-rating [2]. The combustion systems of MGTs can also be designed in such a way that they can easily burn fuels with lower octane numbers as well as heavier hydrocarbon components [3], [4]. The same is true for fuels containing hydrogen [5].

Modelling and simulation have significant importance in the design and manufacturing of gas turbines. These models provide a cost-effective solution for the inevitable design iterations of such complicated engines. High fidelity simulations of flow through gas turbine components provide insights into the details of component and flow interactions and thus enhance the knowledge about operations of the components. These models are usually three-dimensional and are performed with computational fluid dynamics and are widely employed by designers.

While high-fidelity models have a significant role in the world of design and manufacturing, the time-consuming simulations due to computational limitations of today's computers make them impractical for monitoring and controlling gas turbine engines. A rapid simulation of the whole gas turbine that can provide information about engine condition, narrowed to average flow properties at each main component entrance and exit, is sufficient and can be implemented for control and monitoring purposes.

A computer model that can mirror and simulate the operation of the power generation unit as a system of integrated components is called a digital twin, and manufacturers are using them for performance optimization and life cycle management, which have resulted in considerable savings for their customers [6]. The ability of the digital twin to predict the key variables of a healthy engine makes it suitable to be employed as a basis for condition monitoring systems, where any performance deviations from its calculations imply a fault.

Moreover, a substitute for the engine is essential for verifying the functionality of mechanics and electronic devices without taking any risks on the real engine's life. If a model were accurate enough, critical transients could be not only detected,

but predicted and avoided to protect the components of the engine. Because the models are faster than a real engine, they are useful for diagnostic and prognostic purposes [7].

Lumped models of gas turbine engine cycles consisting of time-dependent equations in individual elements have been proven to be reliable for dynamic simulations in previous studies [8]–[10]. Because the dynamic behaviour of the engine is inherently coupled and nonlinear [11], modifications are applied to the accurate equations in order to simplify the calculations and make them suitable for fast calculations. Moreover, empirical correlations are developed and utilized for some complex components to avoid unnecessary calculations.

Dynamic modelling of power-generating cycles based on MGTs has been pursued by researchers, but because of their complexity a number of assumptions and simplifications have been implemented. The developed dynamic models have mostly comprised steady-state models that are based on flow thermodynamics and component characteristics with additional adjacent elements representing the dynamic behaviour of each component [7], [12].

Abdollahi and Vahedi [13] developed a dynamic model of a single-shaft MGT in MATLAB/Simulink. Their model included the dynamic characteristics of the main components such as the turbine and the permanent magnet generator. Results of their work showed that the provided model can be used for dynamic simulation of MGT operation in various conditions. However, a validation of the developed model with experimental data was not reported in the paper.

Nikpey et al. [14] developed a thermodynamic model of two innovative cycles, Exhaust Gas Recirculation and Humid Air Turbine, based on a T100 MGT in the IPSEpro environment. The model was validated by experimental data, proving the accuracy of the model results. Because the model was not equipped with an engine controller system or with the dynamics of the components, it could not be used as an engine substitute for design or monitoring purposes; however, it could be utilized for comparative assessment of different cycle layouts. In another paper, Nikpey et al. [15] developed an artificial neural network model based on a T100 MGT driven by biogas. Pursuing a data-driven approach, the authors successfully overcame the dependency on “non-accurate” component maps by using measurement data for model development. The developed model can only be utilized for steady-state predictions because of the chosen artificial neural network layout and training data.

Rachtan and Malinowski [16] provided an approximate mathematical correlation for a heat recovery unit in an MGT cogenerating heat and power (CHP). The model was verified by experimental data for different part-load performances and proved to be reliable for modelling and design of micro-CHP plants. In another work, Malinowski and Lewandowska [17] developed an analytical model of a whole MGT for part-load operation. Exergy calculations were performed for all MGT components, and formulas were provided to overcome the problem of inadequate information about component maps due to the proprietary nature of the information for the manufacturer. The performance of the proposed model showed good agreement

with collected experimental data. The models provided in both publications were based on the thermodynamics of the system and therefore lacked the ability to predict the dynamic behaviour of the engine.

Nelson et al. [18] developed a quasi-steady physics-based model for a hybrid cycle consisting of a T100 MGT with a concentrating solar power tower. The tower was implemented to exploit solar energy for heating the air before it enters the combustion chamber. A range of electrical loads under varying ambient conditions was investigated to study the load-following and operation characteristics of the hybrid cycle. Moreover, sensitivity analyses were performed to investigate the performance of the hybrid cycle under various ambient conditions. The performance of the hybrid cycle was investigated based on the annual power demand for different cities in the US. The results of their work showed that the proposed hybrid cycle is capable of meeting the performance targets of an MGT working as its basic nonhybrid configuration. The authors also concluded that by utilizing this hybrid configuration fuel consumption can be reduced by 26% annually.

Two models were developed and presented by Roberts et al. to predict the performance of a T100 MGT that was modified in an experimental test rig [19]. One model was developed in MATLAB/Simulink and used time constants to simulate the dynamic behaviour of the components. In the second model, a plenum with time-dependent mass conservation was assumed to compensate for the dynamics of the engine. The data collected from the experiments showed agreement under steady-state conditions, where each modelling approach was more accurate than the other depending on which test and parameter was being investigated. Overall, the first approach based on time constants performed better at predicting the engine behaviour.

Another approach has been used for providing a dynamic model of MGTs inspired by Rowen’s model of gas turbines [20]. In these works, the transient behaviour of an MGT is assumed to be associated only with the dynamic response of the controller and the sensors [21]. The fluid-mechanical components of the MGT are replaced by simplified equations, and a time delay is associated with the large-sized components in the engine (e.g. the combustion chamber). While these models are very fast in simulations, they lack accuracy in predicting the conditions for the mechanical components of the engine such as the compressor and turbine. This problem can be augmented in engines with variable rotational speed (such as MGTs) where a broader range of performance is expected for the components.

In this paper a dynamic model of a 100 kW MGT, designed and manufactured by Turbec, is presented in which most of the components are represented with a zero-dimensional approach; however, the complete form of transient equations is solved without any simplifying assumptions or term negligence. We sought to overcome the limitations of the developed models in previous studies by constructing a fast and accurate dynamic model of an MGT that can be utilized as an engine substitute for performance evaluation and condition monitoring.

Using MATLAB Simscape facilitated physics-based modelling by providing a well-structured foundation while



preserving flexibility and a high degree of freedom for generating component models by programming.

In the following section, an overview of the T100 unit is presented, which was equipped with a modified combustor to enable the use of a fuel blend containing a large amount of hydrogen. This is followed by a comprehensive overview of the model development in Simscape, focusing on features for representing the dynamic behaviour as well as the fuel flexibility of the engine. Simulations were conducted to verify the performance of the model under varying loads and with different mixtures of hydrogen/methane fuel using measured data.

Utilizing hydrogen or hydrogen-mixed fuels has become a long-term goal for carbon-free power generation. Driving MGTs as one of the futurist micro-CHP generators is another ongoing topic for research and development. Various challenges are associated with developing and/or modifying the components to operate with high flame propagation speed as a result of hydrogen combustion [20], [21]. However, evaluating the whole system operating with hydrogen is another concern for which a limited number of publications are available in the open literature. In this work, the model construction was developed to be applicable for any fuel composition, which provided the ability to simulate the tested fuels with hydrogen mixtures. The model will enable the study of a range of engine setups and fuel mixtures for different purposes, such as predicting engine behaviour in expanding applications (e.g. innovative cycles or fuels), designing control logics, and monitoring the condition of the unit.

## 2. THE TURBEC T100 SYSTEM

The unit studied was a Turbec T100, which is a single-shaft MGT designed to work under power generation mode as well as the cogeneration of power and heat. This unit was installed at Risavika district, Stavanger, Norway, and the power and the heat produced by the unit is consumed locally. Numerous modifications and tests have been implemented on these engines during the past decade, enabling research and development on MGTs such as applications with simulated biogas and natural gas mixtures [15]. Recently, the combustion chamber and the fuel train system for one of the MGTs were replaced with a new design to enable the combustion of fuel mixtures with a high percentage of hydrogen.

The T100 in power mode (T100 P) works in the regenerative Brayton cycle to increase efficiency. The unit is equipped with a recuperator that preheats the air before the combustion chamber by transferring heat from the turbine exhaust gas. The T100 Power and Heat unit (T100 PH) is basically a T100 Power module combined with an exhaust gas heat exchanger, exploiting the remaining heat in the exhaust gas for heating the circulating water.

The power-generating unit consists of a single-stage centrifugal compressor, a single-stage radial turbine, a tubular combustor, a high-speed permanent magnet generator, and additional auxiliary units. The compressor and non-cooled turbine work with a pressure ratio of about 4.5 and a turbine inlet temperature of around 950°C. Under nominal operating conditions (with ISO ambient condition), the unit can achieve

100 kW of electrical power with a rotational speed of 70,000 rpm. The cycle electrical efficiency is 30% thanks to the recuperator that compensates for the low-pressure ratio and low turbine inlet temperature. In cogeneration mode, the total efficiency (fuel utilization factor) increases up to 80%. More details about this unit can be found in the technical description in [23].

The combustor was replaced by a fuel-flexible combustor designed and manufactured by the German Aerospace Centre to investigate the performance of the engine under different load conditions. The unit with the modified combustor and fuel train is shown in Figure 1. To evaluate the unit performance and cyclic behaviour, additional pressure and temperature sensors were installed in the unit under investigation.

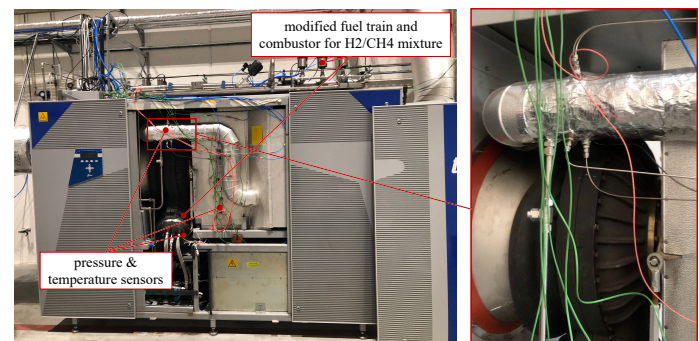


FIGURE 1: TURBEC T100 UNIT WITH MODIFIED COMBUSTOR AND FUEL TRAIN FOR A HYDROGEN/METHANE FUEL MIXTURE

The fuel is provided by bundles, each comprising 12 high-pressure interconnected bottles of hydrogen or methane. The bundles are connected to the fuel train within a pressure regulator to reduce the pressure to the proper value for the MGT. The fuel setting allows for running the engine with different percentages of hydrogen mixed with methane. Figure 2 shows the fuel system and the connecting valves.



FIGURE 2: HYDROGEN AND METHANE FUEL BUNDLES AND VALVES

## 3. DEVELOPED MODEL

Building a dynamic model of an MGT that encompasses the mechanics, thermodynamics, and control system of an MGT system can be best carried out in software that provides infrastructure for all those domains and the relations between them. MATLAB Simscape is a powerful tool developed for modelling physical systems that provides the foundation for all physical domains while preserving the freedom to define arbitrary components based on those domains.

Simscape was originally developed within the well-known Simulink environment with features that facilitate building models for physical systems. While the connections in Simulink components are defined based on equations, in Simscape they establish an actual physical connection between physical components, which results in a model that topologically matches the physical system, thus simplifying the construction of even complex physical networks [24].

Every Simscape model is constructed based on two elements: domains and components. Domains are the definitions of the physical fields of the system, e.g., electrical, gas, magnetic, etc., and are based on declaring “through” and “across” variables. A through-variable is referred to as a type of domain variable that imitates a flow in a domain, whereas a cross-variable is associated with a point in the domain. For instance, electrical current is a through-variable and voltage is an across-variable in the electrical domain. Another way of describing this is based on the way these variables can be measured. For a through-variable, a gauge must be installed in series (e.g., an ammeter for electric current) while an across-variable is measured by connecting in parallel (e.g., a voltmeter for measuring voltage) with one port of the gauge attached to the measurement point and the other port attached to the domain reference point (electrical ground).

Components represent the actual physical elements that are working in the defined domains. A resistor or capacitor is an example of a physical component. A physical system with a multi-domain background with components that are defined based on more than one domain can be constructed in Simscape. For instance, a DC motor can be defined in the mechanical, electrical, and thermal domains. Libraries of physical domains and components are available; however, custom domains and components can be defined as textual files. This is an advantage over most software in which components and domains are predefined and only changing parameters is permitted.

Because Simscape has been developed based on Simulink, it is worth describing the advantages of Simscape that make it suitable for modelling physical systems. A model that is constructed with Simscape easily reproduces the actual physical system layout, while in Simulink equations play the main role in constructing the system, which make them more difficult to interpret by people other than the model developer. Moreover, each connection line in Simulink transports a single variable that can be transferred in one direction, while connections in Simscape are capable of simulating bidirectional flow and transferring multiple through-variables in either direction. In addition, the equations and mathematical functions within the components allow acausal modelling and the ability to solve the equations implicitly. Simscape converts the entire network to equations and solves them simultaneously with no order expected. This clearly provides an undemanding method of component definition that is more flexible than Simulink’s explicit calculation approach.

A Simscape model can also connect to Simulink components by converting a physical signal to a Simulink signal

and vice versa, which enables the modelling of control systems in a physical system within the Simulink environment.

In this section, the developed model is presented while highlighting the approach for building an MGT model that is capable of running with various fuel mixtures.

### 3.1 Domain Definition

A model of the T100 PH engine was constructed in Simscape based on three domains – gas, rotational, and thermal. The through and across-variables of these domains are presented in Table 1. The thermal and rotational domains are predefined in Simscape, but a new version of the gas domain was defined for the current work, which has added variables and functions to enable the modelling of variations in flow properties due to internal combustion during the cycle.

**TABLE 1: DOMAINS AND CORRESPONDING VARIABLES EMPLOYED IN THE MGT MODEL**

Domain	Through variables	Across variables
Gas	$\dot{m}, \phi, \dot{m}_f$	$p, T, x_f$
Rotational	$\dot{\tau}$	$\omega$
Thermal	$\dot{Q}$	$T$

The gas domain is defined based on flowing variables, including the mass flow rate  $\dot{m}$ , energy flow rate  $\phi$ , and fuel flow rate  $\dot{m}_f$ . The across-variables are the pressure ( $p$ ), temperature ( $T$ ), and fuel concentration ( $x_f$ ) in the flow. The pressures and temperatures are defined based on stagnation values that are correlated with thermodynamic properties. The concentration of fuel inflow is correlated to the total mass flow rate and the fuel mass flow rate by Eq.1. Therefore, only one of them ( $x_f$  or  $\dot{m}_f$ ) is sufficient; however, both are defined because having equal numbers of through and across-variables in a domain improves the Simscape solver’s performance [25].

$$x_f = \frac{\dot{m}_f}{\dot{m}} \quad (1)$$

### 3.2 Flow Properties

The properties of the working fluid depend on the molecular composition, thermodynamic pressure, and thermodynamic temperature of the gas. For components mounted upstream of the combustion chamber, airflow is considered, while downstream of the combustion chamber the calculation for gas composition in the flue is performed. The model is capable of accepting different dry air compositions. The ambient conditions including pressure, temperature, and relative humidity are set as inputs to the model. The weight fraction of humid air molecules is calculated by calculating the vapor fraction.

$$Air = x_{O_2}O_2 + x_{N_2}N_2 + x_{Ar}Ar + x_{SO_2}SO_2 + x_{CO_2}CO_2 + x_{H_2O}H_2O + x_{He}He \quad (2)$$

$$Fuel = x_{CH_4}CH_4 + x_{H_2}H_2$$

The relative humidity of the air is defined as the ratio of the actual vapor pressure to the saturation vapor pressure:

$$RH = \frac{p_v}{p_{v,sat}} \quad (3)$$

The vapor pressure is calculated from the relative humidity and the saturated vapor pressure, which is available in



temperature-saturation pressure tables. The humidity ratio is defined as the ratio of vapor mass to dry mass:

$$\phi = \frac{m_v}{m_{a,dry}} \quad (4)$$

Assuming ideal gas status for both vapor and dry air, the relative humidity can be calculated from:

$$\Phi = \frac{M_v}{M_{a,dry}} \times \frac{p_v}{p_{a,dry}} \quad (5)$$

In the above equation,  $M_v$  is the molar mass of water (18.016 g/mol) and  $M_{a,dry}$  is calculated based on the dry air composition in the simulation. The dry air pressure in Eq.5 is simply calculated as:

$$p_{a,dry} = p_{amb} - p_v \quad (6)$$

The weight fraction of the vapor is calculated from the relative humidity, and the weight fraction of humid air is calculated based on the weight fraction of water in the air:

$$x_{H_2O} = \frac{\Phi}{1 + \Phi}, \quad x_{a,humid} = \frac{1}{1 - x_{H_2O}} \quad (7)$$

The weight fraction of all components of humid air can be calculated from their weight fraction in dry air and the weight fraction of humid air:

$$x_{a,component,humid} = \frac{x_{a,component,dry}}{x_{a,humid}} \quad (8)$$

The air composition vector is built from Eq.8, and for fuel the composition vector is prepared based on the elements included in the fuel:

$$\vec{C}_a = [x_{O_2} \ x_{N_2} \ x_{Ar} \ x_{SO_2} \ x_{CO_2} \ x_{H_2O} \ x_{He}] \quad (9)$$

$$\vec{C}_f = [x_{CH_4} \ x_{H_2}] \quad (10)$$

The working fluid in the cycle changes from air to flue gas in the combustion chamber and the downstream MGT components. The composition vector for flue is assumed to have similar components as defined for air in Eq.9 (because of combustion products elaborated later in section 3.6); however, the weight coefficients are different from air and must be calculated based on the air/fuel ratio:

$$\vec{C}_{fl} = \vec{C}_{fl}(\vec{C}_a, \vec{C}_f, AF) \quad (11)$$

Where  $AF$  is the ratio of air mass to fuel mass and can be calculated in the model based on the mass flow variables and is available for calculation from the across-variable  $x_f$ .

$$AF = \dot{m}_a / \dot{m}_f \quad (12)$$

It is worth noting that defining  $x_f$  (or  $\dot{m}_f$ ) as a variable in the domain provided the possibility to calculate the accurate flow composition at any point of the system and at any time of the simulation. By knowing the composition of the working fluid (air or flue gas) at the entrance of each MGT component, the properties of the gas are calculated based on the composition and thermodynamic state of the working fluid:

$$k = k(\vec{C}_{wf}, T), \quad c_p = c_p(\vec{C}_{wf}, T), \quad c_v = c_p - R \quad (13)$$

For density calculation, the ideal gas law is assumed:

$$M_{wf} = M_{wf}(\vec{C}_{wf}), \quad R = R(M_{wf}), \quad p = \rho RT \quad (14)$$

### 3.3 Principal Equations for Modelling Components

As discussed, the model is comprised of lumped components that are assumed to have uniform flow properties at their boundaries. Therefore, for all of the components running on a gas domain, basic thermodynamic equations are provided in the full time-dependent form. The balance of the mass flow is defined from:

$$V \frac{\partial \rho}{\partial t} + \sum_i (\dot{m})_{out} - \sum_i (\dot{m})_{in} = 0 \quad (15)$$

With ideal gas assumption (Eq.14), the mass conservation results in:

$$\frac{\partial \rho}{\partial t} = \frac{1}{RT} \frac{\partial p}{\partial t} - \frac{p}{T} \frac{1}{RT} \frac{\partial T}{\partial t} \quad (16)$$

Similarly, the conservation of energy for the component can be written:

$$dQ/dt - dW/dt = Vd(\rho e)/dt \quad (17)$$

$$+ \sum (h + 1/2|\vec{V}|^2 + gz)_{out} \dot{m}_{out}$$

$$- \sum (h + 1/2|\vec{V}|^2 + gz)_{in} \dot{m}_{in}$$

$Q$  and  $W$  are the heat and work exchange that contribute to the total energy variation,  $E$ , and  $e$  is the total energy per unit mass and consists of internal kinetic and potential energy:

$$e = \hat{u} + \frac{1}{2}|\vec{V}|^2 + gz \quad (18)$$

The sigma in Eq.16 and Eq.17 is to account for all inputs and all outputs of the component. For most of the components, there is only one inlet and one outlet because the leakages are neglected. Neglecting variation in velocity and level of flow in transient mode and with ideal gas assumption, the internal energy term will be left, which can be related to temperature as:

$$\hat{u} = c_v T \quad (19)$$

Therefore, the time derivative of the internal energy term can be calculated from the following equation:

$$\frac{d(\rho u)}{dt} = \rho c_v \frac{\partial T}{\partial t} + \rho T \frac{\partial c_v}{\partial T} + c_v T \frac{\partial \rho}{\partial t} \quad (20)$$

The  $c_v$  terms are rewritten using their relation to  $c_p$  (Eq.13), so the correlation between  $c_p$  and temperature and flow composition can be calculated:

$$\frac{dc_v}{dt} = \frac{dc_p}{dt} = \frac{\partial c_p}{\partial T} \frac{\partial T}{\partial t} \quad (21)$$

Rearranging Eq.16 and Eq.17 with respect to terms for the time derivative of pressure and temperature results in the full form of the time-dependent conservation equations as below:

$$\tau_{p,mc} \frac{\partial p}{\partial t} + \tau_{T,mc} \frac{\partial T}{\partial t} = \dot{m}_{out} - \dot{m}_{in} \quad (22)$$

$$\tau_{p,ec} \frac{\partial p}{\partial t} + \tau_{T,ec} \frac{\partial T}{\partial t} = \dot{m}_{out} c_{p,out} T_{out} - \dot{m}_{in} c_{p,in} T_{in} + \frac{\partial q}{\partial t} - \frac{\partial w}{\partial t} \quad (23)$$

In the above equations,  $\tau$  is the time constant for the time derivative terms in the mass and energy conservation equations:

$$\tau_{p,mc} = \frac{V}{RT}, \quad \tau_{T,mc} = -\frac{\rho V}{T}, \quad \tau_{p,ec} = \frac{c_v V}{R}, \quad \tau_{T,ec} = \rho TV(\partial c_p)/\partial T \quad (24)$$

The last three equations are implemented as common principal equations for modelling all main components of the

MGT, namely the compressor, turbine, combustor, and recuperator. In all components, except for the recuperator, these equations are written between the inlet and outlet of the component because they are treated as zero-dimensional components. For the recuperator, a one-dimensional approach is chosen and the same equations are employed but within each discretized cell. Other than principal laws of conservation, specific equations explaining the behaviour of each component are employed as demonstrated in the following sections.

After the model has been constructed, running the model requires the same inputs as the real engine. In an operating real-life engine, the following information is available, either imposed by the environment or chosen by the user:

- Ambient condition: pressure, temperature, and humidity (imposed by the environment)
- Fuel condition: pressure, temperature (imposed based on where and how the fuel is sourced) and mixture (chosen by the user as the volumetric ratio between different fuel types)
- Power set point (chosen by the user, constant, or varying)

The same information is required by the model, and once these are prepared, the model will run and provide all data, including flow properties throughout the engine cycle, in addition to rotational speed, fuel flow rate, and efficiency of the engine (the required inputs are summarized in Table 2).

The developed model for the T100 is depicted in Figure 3. As presented in the thermodynamic cycle shown in Figure 3(A), there are different physics domains that are distinguished by

color. Note that even though the model runs in the thermal domain, the thermal domain is not visible in the picture because it is only used inside the components and does not contribute to their connection points. In between every two connected components, a measuring component has been placed to extract all flow properties.

**TABLE 2: MODEL INPUTS**

Input			
Ambient condition	$p_{amb}$	$T_{amb}$	$RH_{amb}$
Fuel condition	$p_f$	$T_f$	CH4/H2 choice
Demand power	$P(t)$		

The input set for the model is shown In Figure 3(B), where mixture, pressure, and temperature constants are set for the fuel (which can be replaced with time-varying signals if required). For ambient conditions and for demand power, a signal builder is chosen that enables creating either constant or varying signals. In Figure 3(C), the power set by the user (created inside the signal builder) is shown, where the user has chosen a stepwise power set. This is the same way the engine user sets the input. The figures are from the first case discussed in section 4 of the paper. Air and fuel compositions are calculated as explained previously and then used as inputs together with the pressure and temperatures of the air and fuel reservoirs. The mass flow of fuel and rotational speed is defined by the controller, which is built in the Simulink environment. In the following sections the main components of the engine and the controller are described.

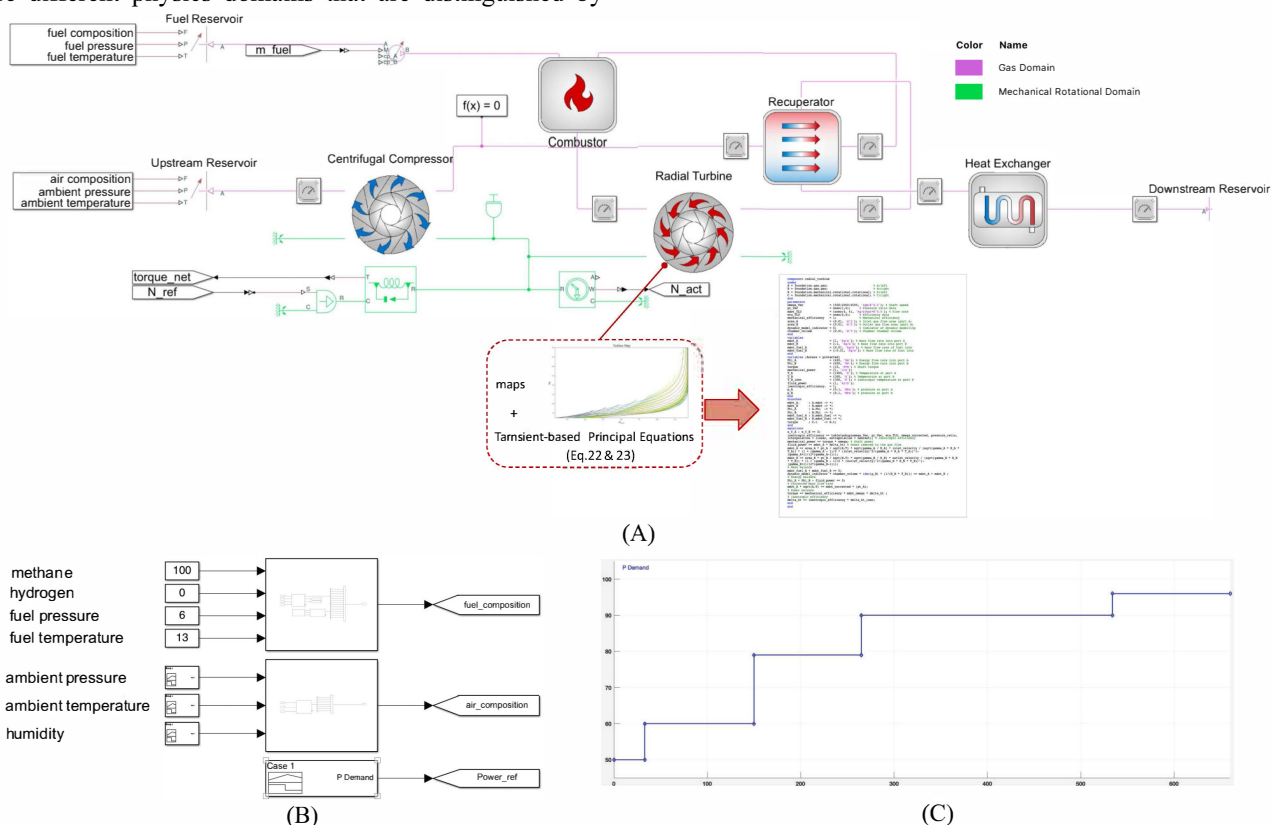


**FIGURE 3: DEVELOPED MODEL FOR A TURBEC T100 UNIT USING MATLAB SIMSCAPE. (A) THERMODYNAMIC CYCLE, (B) INPUTS REQUIRED FOR THE MODEL, (C) EXAMPLE POWER SET CHOSEN BY THE USER**

### 3.4 Compressor and Turbine

The turbo components are modelled based on the map data, which represent the correlation between the flow parameters of the components under a range of pressure ratios and rotational speeds. The maps are generated by test runs of each component under steady-state conditions. However, coupling them with dynamic equations for mass and energy balance (Eq.22 and Eq.23) results in the adequate dynamic response of the model [26]. The map parameters are normalized through Eq.25, and the maps reveal the correlation between the mass flow rate and the isentropic efficiency of the component and the imposed pressure ratio and rotational speed within these normalized forms (Eq.26).

$$\dot{m}^* = \frac{\dot{m} \sqrt{T_{in}}}{p_{in}}, N^* = \frac{N}{\sqrt{T_{in}}} \quad (25)$$

$$\dot{m}^*, \eta_{is} = f(PR, N^*) \quad (26)$$

Collecting measured values from the engine revealed that the operation points are slightly deviated from the map points. This might be due to the fact that component maps are usually generated by testing components separately while imposing several boundary conditions and using computer programs for other conditions that might be different from a component's actual behaviour when mounted in an engine [27]. Moreover, the components are prone to deviation from their original condition due to operation for several tens of thousands of hours over several years. For that reason, both the compressor and turbine maps are adapted as follows [27]:

$$MF_{\eta} = \eta_{act} / \eta_{map,original} \quad (27)$$

The adaptation of efficiency is possible because pressure and temperature are measured at the inlet and outlet of the compressor and turbine. The value of the modification factor  $MF$  is calculated by minimizing the results from the modified map and the measurements, at different pressure ratios, as demonstrated in Eq.28.

$$MF_{\eta} = \operatorname{argmin} \sum_{i=1}^m (T_{out,exp} - T_{out,map,ad}(PR_i, MF_{\eta} \times \eta_{map,orig}))^2 \quad (28)$$

The  $MF$  is calculated for both the compressor and turbine by an optimization algorithm in MATLAB (outside of the Simscape module) and is used for adapting both components' maps. These modified maps are used with linear interpolation between two points and with linear extrapolation for points outside of the map boundaries, which can occur in simulation iterations.

### 3.5 Recuperator

The recuperator of the T100 is a compact-type heat exchanger with dense arrays of wavy plates, enhancing the transfer of heat from the turbine outlet gas to the compressor outlet air. A single-pass arrangement is designed for both hot and cold flow, and both flow in a single direction [28]. The flow paths are perpendicular to each other as depicted in Figure 4, which creates a 2-dimensional temperature distribution on the separating sheets. Modelling the recuperator dynamic response is done by discretizing the flow path and metal sheets into uniform elements. Both metal and flow cells are provided with

time-varying governing equations to account for the dynamic response of the recuperator. Heat is transferred between neighbouring metal and flow cells, while heat and mass are transferred between neighbouring flow cells.

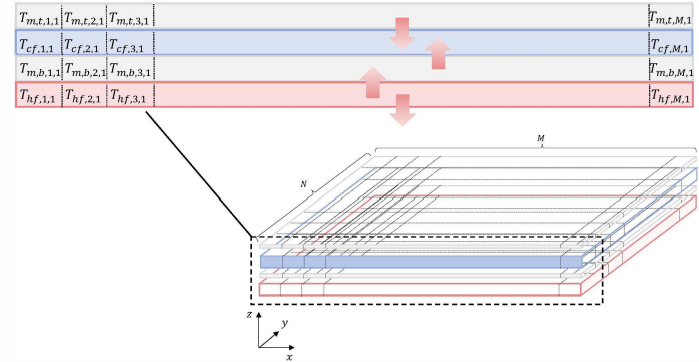


**FIGURE 4: DISCRETIZED RECUPERATOR MODEL. HOT GAS FLOWS IN THE X-DIRECTION, AND COLD AIR FLOWS IN THE Y-DIRECTION**

For the metal sheet cells, heat conduction along two dimensions parallel to the plate is assumed, and the temperature is assumed to be uniform in a perpendicular direction considering the sheets' thickness.

$$\frac{\partial^2 T}{\partial x^2} + \frac{\partial^2 T}{\partial y^2} = \frac{1}{\alpha} \frac{\partial T}{\partial t}, \quad \alpha = \frac{k}{\rho c} \quad (29)$$

For flow path cells, the rectangular duct is assumed to have a wall temperature imposed by adjacent sheets. The model is a constant volume of gas that accounts for viscous friction losses and convective heat transfer with the walls. Flow pressure and temperature evolve along the flow path based on the compressibility and thermal capacity of the gas (Eq.13 & Eq.14). Convective heat transfer imposed by wall temperature is imposed by calculating the Nusselt number for laminar and turbulent flow regimes [28]:

$$Nu_{lam} = 5.60 k_{lam}, \quad Re_{D_h} \leq Re_{cr} \quad (30)$$

$$Nu_{tur} = k_{tur} \frac{f/8(Re_{D_h} - 1000)Pr}{1 + 12.7(f/8)^{1/2} \left( Pr^{2/3} - 1 \right)}, \quad Re_{D_h} \geq Re_{cr} \quad (31)$$

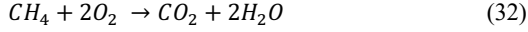
In the above equations,  $k_{lam}$  and  $k_{tur}$  are correction factors to account for the plates' wave pattern, which is extracted from experimental data while the unit is operating under steady-state conditions.

### 3.6 Combustor

The combustion chamber is modelled as a plenum with an inlet from the fuel source and air leaving the recuperator. The user sets the percentage of methane and hydrogen in the fuel source (which is the same as for the actual engine for which the operator chooses the combination). The molecular composition of dry air is also known and set with a default value, but it is modifiable if required. With ambient conditions (including pressure, temperature, and relative humidity) set by the user, the correct molecular composition of air is calculated (as demonstrated in section 3.2). The composition of the inlet mixture to the combustion chamber is therefore known, and from

there the thermophysical properties such as heat capacity are calculated using Eq.13 and Eq.14.

During combustion the composition of the flow changes due to the combustion of fuel, which is modelled with two reactions described in Eq.32 & Eq.33, considering complete combustion in all operational conditions, except for start-up, which is corrected by an efficiency value [12]. Other than oxygen, the remaining parts of the air will not take part in combustion, but they are included in the calculation of heat capacity for the flue gas and therefore affect the temperature of the flow at the inlet to the turbine.



To obtain the flue gas temperature, the enthalpy of formation is calculated, which is available at the reference temperature of 25°C. Thus, the heat transfer for a temperature change in the reactants relative to a reference temperature can be calculated. In Eq.34  $n_f$  is the number of fuel types, which is 2 for this case. For the air side, it is assumed that nitrogen in the air will not take part in combustion and therefore only oxygen is considered in the reactant side.

$$Q_{react,ref} = \sum_{i=1}^{n_f} \dot{m}_{f,i} \int_{T_{f,in}}^{T_{ref}} c_{p,f,i}(T) dT + \dot{m}_{\text{O}_2} \int_{T_{a,in}}^{T_{ref}} c_{p,\text{O}_2} dT \quad (34)$$

The combustion heat is then calculated by employing the difference in formation enthalpies between products and reactants:

$$Q_{reaction} = \sum_{i=1}^{n_{prod}} \dot{m}_{prod,i} h_{form,prod,i} - \sum_{i=1}^{n_{react}} \dot{m}_{react,i} h_{form,react,i} \quad (35)$$

From the above equations, the heat released from combustion is calculated and used for the calculation of the flue gas temperature. The flue gas consists of combustion products and excess air. Using the *AF* ratio, the weight ratio vector for the molecular composition of the exhaust gas can be calculated separately for the combustion product and excess air (Eq.11). The heat transfer coefficient can be calculated (Eq.13) and then used in Eq.37 to calculate the temperature of the flow leaving the combustion chamber. In Eq.37 the heat capacity terms are a function of temperature (Eq.13), and therefore the two equations are iteratively solved by initial guesses for the combustor outlet temperature.

$$\dot{m}_{a,ex} = \dot{m}_a - \dot{m}_{\text{O}_2,react} \quad (36)$$

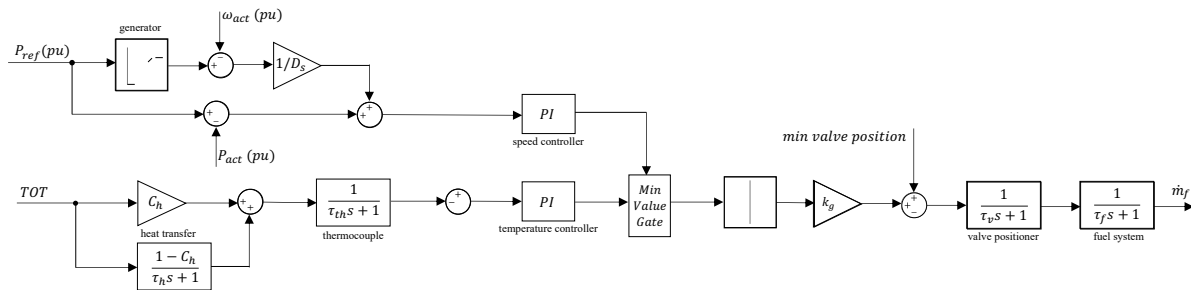


FIGURE 5: CONTROLLER FOR THE T100 MGT DEVELOPED IN SIMULINK

$$Q_{react,ref} + Q_{reaction} = \dot{m}_{prod} \int_{T_{ref}}^{T_{out}} c_{p,prod} dT + \dot{m}_{a,ex} \int_{T_{a,in}}^{T_{out}} c_{p,ex} dT \quad (37)$$

### 3.7 Heat Exchanger

The exhaust gas leaving the recuperator still contains useful energy, which is exploited by a gas/water heat exchanger. The component is modelled using an empirical correlation, indicating the relation between the pressure drop and the hot gas mass flow in the unit.

### 3.8 Controller

The unit is controlled by an automatic control system using inputs from the user (setpoints) and measurements from the engine. The built-in measurements used by the controller include turbine outlet temperature, rotor speed, and power output. For safety reasons the temperature of the oil and water that cool the generator and the vibration of the unit were also measured. The purpose of the control system is to achieve the demanded power while keeping the turbine outlet temperature (TOT) around a certain value that is below 645 °C. Limiting the TOT is necessary to protect components downstream of the turbine, such as the recuperator and the heat exchanger. Moreover, confining the TOT will constrain the turbine inlet temperature as well, which is less convenient to measure continuously. High turbine inlet temperatures run with the risk of damaging the combustor and the turbine.

Figure 5 shows the diagram of the controller used in the model. The main difference between MGT controllers and those of large-scale gas turbine power generators is the rotational speed, which has higher values and is more variable in operation in MGTs. The controller's purpose is to control the power output and TOT by changing the fuel mass flow and the rotational speed.

The controller for both TOT and power is equipped with proportional-integral regulators as presented in Figure 5. Abrupt changes in power are restricted and modified to acceptable rates in order to control the acceleration of the rotor, and a correlation between the reference rotational speed and the reference power is defined based on generator's characteristics. Moreover, the reference power (and hence the rotational speed) is kept below a maximum limit in order to protect the rotor. The operational limits also include low TOT, which has the prospect of high emissions, and thus is not included in the modelled controller because only practical operations were of interest in this work. Values of the parameters used in the controller are provided in Table 3.



**TABLE 3: CONTROLLER PARAMETERS**

controller section			
speed	$D_s = 0.05$	$k_p = 0.1$	$k_i = 0.5$
fuel	$k_g = 0.77$	$\tau_v = 0.05$	$\tau_f = 0.4$
temperature	$\tau_{th} = 5$	$k_p = 0.1$	$k_i = 0.5$
	$C_h = 0.8$	$\tau_h = 80$	

#### 4. RESULTS AND DISCUSSION

The described test rig was provided to investigate the overall behaviour of the unit under different operating conditions and with different concentrations of hydrogen in the fuel. From those tests, the main operational behaviour was extracted to evaluate the performance of the developed model. At the beginning phase of the test, only methane was used as the fuel from which the measured values were extracted under steady-state conditions. The model was tuned using these data by adapting the maps for the compressor and turbine (section 3.4) and by accounting for the mechanical loss in the engine. A series of transient manoeuvres were then conducted, and the collected data allowed us to analyse the dynamic response of the model.

The first transient manoeuvre was conducted with pure methane as the fuel. The ambient conditions were an atmospheric pressure of 1.0007 bar, an atmospheric temperature of 17.7°C, and a relative humidity of 78%. The fuel had a pressure of around 6 bar with an average temperature of 13°C (varying between 12°C and 14°C). The demanded power was increased gradually during the manoeuvre, which is visible in the power production plot presented in Figure 6.

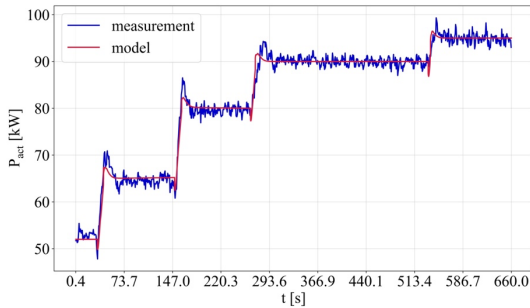


**FIGURE 6: COMPARISON OF GENERATED POWER FOR THE MGT RUNNING WITH PURE METHANE**

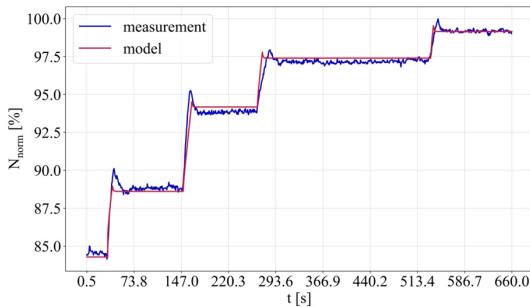


**FIGURE 7: COMPARISON OF ROTATIONAL SPEED FOR THE MGT RUNNING WITH PURE METHANE**

At the beginning the MGT was running in a steady-state and producing 55 kW of power, then the demanded power was increased in a stepwise manner to 65, 80, 90, and 95 kW. The

blue line in Figure 6 represents the measured values from the engine and the red line shows the model's prediction. As it is clear in Figure 6, the model imitated the engine's behavior under transient conditions, especially with rapid load fall-down and overshoots in stepping periods. Capturing these overshoots is important for identifying the critical conditions that occur under such transient load conditions. The rotational speed of the engine is presented in Figure 7, which shows fairly good agreement between the model predictions and the measured values. In these figures, the rotational speed of the engine is normalized by its nominal value (for design point) of 70,000 rpm. Although overshoots in speeds are captured by the model, their magnitudes are underestimated. The duration of simulation for this test was 49 seconds, which was about 7% of the whole run duration.

For the second manoeuvre, the MGT was operated with a mixture of methane and hydrogen with a volume ratio of 70/30. The test condition of this case included an ambient air temperature of 13.6°C with the same atmospheric pressure and humidity as before. The mixed fuel was provided with a pressure of 8 bar and a temperature of 12°C. The unit was initially running at 50 kW under steady state conditions and then underwent stepwise load ramp-ups by 10 kW steps up to 100 kW. The power produced by the engine and the model predictions are presented in Figure 8, which indicates that the model's transient behaviour was very similar to the engine up to 80 kW. However, for the last two steps certain deviations can be noticed. It seems that the operation of the engine with hydrogen-blended fuel is less stable at high power demands, which might be due to combustion instabilities that cannot be captured by this model.

The same behaviour was noticed in the rotational speed (Figure 9), which showed good agreement up to 80 kW, but at higher power demands the model predictions deviated from the measurements in terms of overshoot magnitudes and delay times. For this simulation, 63 seconds were consumed by the model, which is about 6% of the manoeuvre time.

As discussed in section 3.8, the logic behind the controller is to define the proper fuel mass flow rate and rotational speed for the engine in order to produce the demanded power while keeping the engine safe from high temperatures. This correlation is depicted in Figure 10. At a constant ambient temperature, both the rotational speed and fuel mass flow increased to produce higher power. Similar behaviour was observed for the engine running with a mixture of fuels, as shown in Figure 11.

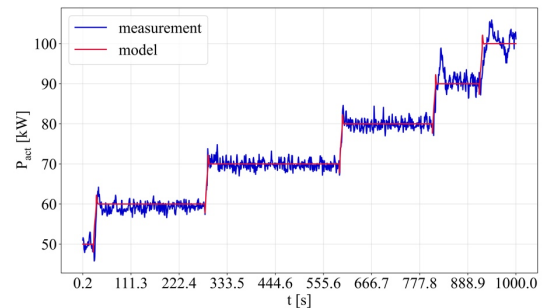


**FIGURE 8: COMPARISON OF GENERATED POWER FOR THE MGT RUNNING WITH MIXED METHANE/HYDROGEN FUEL**

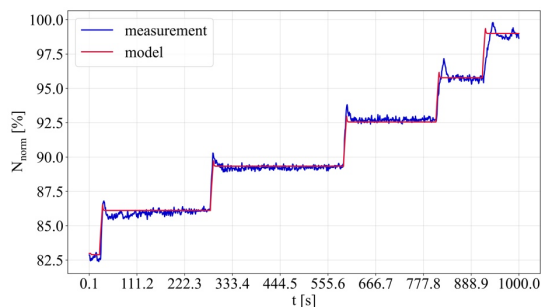


**FIGURE 9:** COMPARISON OF THE ROTATIONAL SPEED FOR THE MGT RUNNING WITH MIXED METHANE/HYDROGEN FUEL

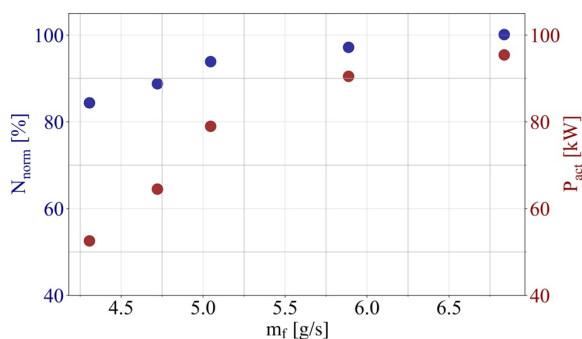


**FIGURE 10:** ROTATIONAL SPEED AND FUEL MASS FLOW RATE IN DIFFERENT POWER MODES BY THE MGT RUNNING ON PURE METHANE

It is worth noting that the rotational speeds for the same power outputs were different in the two manoeuvres. For instance, at 80 kW the engine driven with pure methane as fuel was rotating at 93.9% of its nominal value (predicted to be 94.2% by the model) as can be seen in Figure 10, while the engine running with mixed fuel rotated at 92.7% (Figure 11). This deviation was imposed by the controller and seems to be related to changes in ambient conditions rather than changes in the fuel composition. The same behaviour was noted with the engine running with the same fuel but at different ambient temperatures.

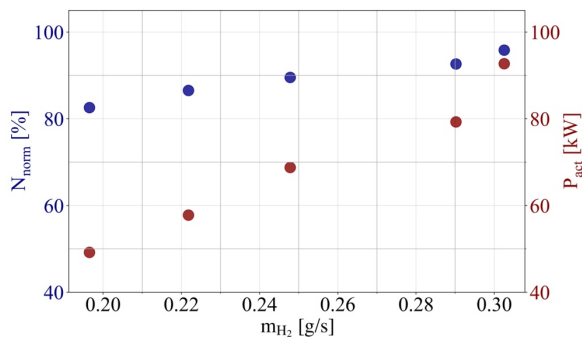


**FIGURE 11:** ROTATIONAL SPEED AND FUEL MASS FLOW RATE IN THE MGT RUNNING WITH MIXED METHANE/HYDROGEN FUEL

This variation in rotational speed was accompanied by changes in fuel flow rate, which was 5.06 g/s in the engine running with pure methane and 6.04 g/s in the blended fuel. This means that the total efficiency of the engine (Eq. 38) will

increase with increasing ambient temperature, which was presented in the technical description of the CHP unit and is shown in Figure 12.

$$\eta_{total} = \frac{W_e + Q_{HE}}{\dot{m}_f LHV} \quad (38)$$

As is shown in Figure 12, the heat output decreased with higher ambient temperatures, while the total efficiency seemed to increase. This means that electrical efficiency increased with increasing temperatures. As is shown in these experiments, with lower ambient temperature more fuel (even with higher heat value in the case of this study) was consumed to produce the same power output.

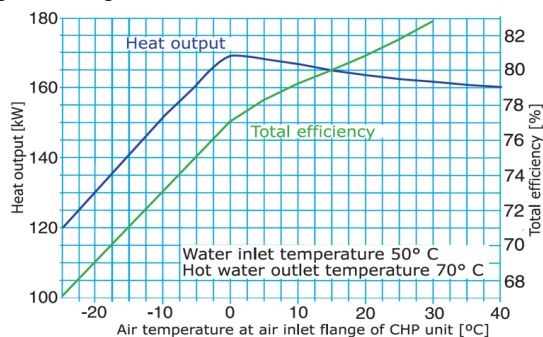


**FIGURE 12:** EFFECT OF AMBIENT TEMPERATURE ON HEAT OUTPUT AND TOTAL EFFICIENCY OF T100 PH [23]

A comparison between steady-state results is provided in Table 4 and Table 5. For all the variables, the error of the model prediction is calculated by Eq. 39:

$$Error [\%] = \frac{X_{model} - X_{measurement}}{X_{measurement}} \times 100 \quad (39)$$

**TABLE 4:** COMPARISON OF EXPERIMENTAL DATA AND MODEL PREDICTIONS IN AN MGT RUNNING ON PURE METHANE

Power	55 kW	65 kW	80 kW	90 kW	95 kW
$N_{norm}$ [%]	84.40	88.79	93.90	97.20	100.13
$N_{norm,model}$ [%]	84.28	88.61	94.18	97.40	99.16
Error [%]	-0.142	-0.203	0.298	0.206	-0.969
$\dot{m}_f$ [g/s]	4.31	4.72	5.06	5.89	6.84
$\dot{m}_{f,model}$ [g/s]	4.33	4.76	5.11	5.85	6.88
Error [%]	0.464	0.847	0.988	-0.679	0.585
$p_{cmp,out}$ [bar]	3.05	3.44	3.80	4.11	4.27
$p_{cmp,out,model}$ [bar]	2.98	3.51	3.78	4.19	4.32
Error [%]	-2.295	2.035	-0.526	1.946	1.171
$T_{cmp,out}$ [°C]	167	178	195	215	221
$T_{cmp,out,model}$ [°C]	164.23	180.12	194.07	214.01	220.57
Error [%]	-1.659	1.191	-0.477	-0.460	-0.195

The model seems to be accurate in the prediction of the variables, with less than 1% error in methane mass flow and rotational speed and 4.5% error for hydrogen mass flow. To assess the error margin in hydrogen mass flow, the 90 kW case is considered when there is a 0.01 g/s deviation in prediction. By

assuming 120,000 kJ/kg to be the lower heating value (LHV) of hydrogen, this deviation will cause a 1.2 kW difference in heat provided by the fuel, resulting in less than 0.1% deviation in the calculation of total efficiency of the engine at the design point (100 kW electrical power output with 30% electrical efficiency). Therefore, the hydrogen mass flow rate predictions are accurate enough for cycle performance assessments.

**TABLE 5: COMPARISON OF EXPERIMENTAL DATA AND MODEL PREDICTIONS FOR THE MGT RUNNING WITH MIXED METHANE/HYDROGEN FUEL**

Power	50 kW	60 kW	70 kW	80 kW	90 kW
$N_{norm}$ [%]	82.60	86.54	89.55	92.65	95.84
$N_{norm,model}$ [%]	82.98	86.11	89.34	92.57	95.78
Error [%]	0.460	-0.497	-0.235	-0.086	-0.063
$\dot{m}_{CH_4}$ [g/s]	4.03	4.49	4.96	5.75	5.97
$\dot{m}_{CH_4,model}$ [g/s]	4.05	4.53	5.01	5.77	6
Error [%]	0.496	0.891	1.008	0.348	0.503
$\dot{m}_{H_2}$ [g/s]	0.20	0.22	0.25	0.29	0.30
$\dot{m}_{H_2,model}$ [g/s]	0.21	0.23	0.26	0.30	0.31
Error [%]	4.545	4.000	3.448	3.333	4.545
$p_{cmp,out}$ [bar]	3.25	3.31	3.58	3.81	4.12
$p_{cmp,out,model}$ [bar]	3.15	3.40	3.62	3.86	4.09
Error [%]	-3.077	2.719	1.117	1.312	-0.728
$T_{cmp,out}$ [°C]	162.18	167.78	177.07	189.09	200.54
$T_{cmp,out,model}$ [°C]	160.01	166.98	176.34	189.76	199.86
Error [%]	-1.338	-0.477	-0.412	0.354	-0.339

## 5. CONCLUSION

This paper presents a comprehensive overview of a dynamic model for a fuel-flexible MGT that was developed in MATLAB Simscape. The infrastructures of the software for physics-based modelling were utilized to develop a model with fully transient forms of equations with minimal simplifying assumptions. The main points of the model construction process were presented including the measures undertaken to permit fuel-flexible simulations and adaptations of the component maps to the real engine. For high-fidelity purposes, in the mathematical calculation of the properties (such as thermal capacity) the flow composition is considered along with pressure and temperature. The controller of the engine is an important element and is modelled and described.

The performance of the model was examined by transient manoeuvres of the actual engine running with pure methane and methane/hydrogen mixtures. The time-dependent parameters of the simulation are presented along with measured values, proving the prediction accuracy of the model for steady-state operation as well as transient conditions. Fairly good agreements were observed between the model predictions and the experimental measurements. Other than for high power outputs in mixed fuel cases, the model was able to capture the dynamic response of the engine in transient mode. With the accuracy of the predictions and speed of the simulation (less than 8% of the

actual operation time), the model is assumed to be trustable for the process of cycle design or controller systems design, as well as for condition-monitoring purposes. In future work, the results from these experiments will be investigated to understand the effect of ingesting hydrogen on the behaviour of the engine at the component level.

## ACKNOWLEDGEMENTS

This project has received funding from the European Union's Horizon 2020 research and innovation program under the Marie Skłodowska-Curie grant agreement No. 861079.

## REFERENCES

- [1] European Turbine Network (ETN), "Micro Gas Turbine Technology Research and Development for European Collaboration," ETN Micro Gas Turbine Technology Summary.
- [2] P. A. Pilavachi, "Mini- and micro-gas turbines for combined heat and power," *Applied Thermal Engineering*, vol. 22, no. 18, pp. 2003–2014, Dec. 2002, doi: 10.1016/S1359-4311(02)00132-1.
- [3] O. Lammel, G. Schmitz, M. Aigner, and W. Krebs, "FLOX® Combustion at High Power Density and High Flame," *Journal of Engineering for Gas Turbines and Power*, vol. 132, no. December 2010, pp. 1–10, 2016, doi: 10.1115/1.4001825.
- [4] T. Zornik, T. Monz, and M. Aigner, "Performance analysis of the micro gas turbine Turbec T100 with a new FLOX-combustion system for low calorific fuels," *Applied Energy*, vol. 159, pp. 276–284, Dec. 2015, doi: 10.1016/j.apenergy.2015.08.075.
- [5] R. Lückert, W. Meier, and M. Aigner, "FLOX combustion at high pressure with different fuel compositions," in *ASME Turbo Expo 2007: Power for Land, Sea and Air*, 2007, pp. 1–9.
- [6] V. Zaccaria, M. Stenfelt, I. Aslanidou, and K. G. Kyprianidis, "Fleet Monitoring and Diagnostics Framework Based on Digital Twin of Aero-Engines," *Proceedings of the ASME Turbo Expo*, vol. 6, Aug. 2018, doi: 10.1115/GT2018-76414.
- [7] S. M. Camporeale, B. Fortunato, and M. Mastrovito, "A Modular Code for Real Time Dynamic Simulation of Gas Turbines in Simulink," *Journal of Engineering for Gas Turbines and Power*, vol. 128, no. 3, pp. 506–517, Jul. 2006, doi: 10.1115/1.2132383.
- [8] M. T. Schobeiri, M. Attia, and C. Lippke, "GETRAN: A generic, modularly structured computer code for simulation of dynamic behavior of aero- and power generation gas turbine engines," *Journal of Engineering for Gas Turbines and Power; (United States)*, vol. 116:3, no. 3, pp. 494–483, Jul. 1994, doi: 10.1115/1.2906847.
- [9] G. Crosa, F. Pittaluga, A. Trucco Martinengo, F. Beltrami, A. Torelli, and F. Traverso, "Heavy-Duty Gas Turbine Plant Aerothermodynamic Simulation Using Simulink," *American Society of Mechanical Engineers (Paper)*, pp. 1–8, Jan. 2015, doi: 10.1115/96-TA-022.
- [10] O. O. Badmus, K. M. Eveker, and C. N. Nett, "Control-Oriented High-Frequency Turbomachinery Modeling:

- General 1D Model Development,” *ASME 1993 International Gas Turbine and Aeroengine Congress and Exposition, GT 1993*, vol. 3C, Feb. 2015, doi: 10.1115/93-GT-385.
- [11] M. Jelali and A. Kroll, *Hydraulic Servo-systems: Modelling, Identification and Control*. Springer, 2003. Accessed: Jan. 26, 2021. [Online]. Available: [https://books.google.no/books/about/Hydraulic\\_Servo\\_sys\\_tems.html?id=AukHCAAQAQBAJ&printsec=frontcover&source=kp\\_read\\_button&redir\\_esc=y#v=onepage&q&f=false](https://books.google.no/books/about/Hydraulic_Servo_sys_tems.html?id=AukHCAAQAQBAJ&printsec=frontcover&source=kp_read_button&redir_esc=y#v=onepage&q&f=false)
- [12] M. Henke, T. Monz, and M. Aigner, “Introduction of a New Numerical Micro Gas Turbine Cycle Dynamics,” *Journal of Engineering for Gas Turbines and Power*, vol. 139, no. 4, Apr. 2017, doi: 10.1115/1.4034703/444282.
- [13] S. Abdollahi and A. Vahedi, “Dynamic Modeling of Micro-Turbine Generation Systems Using Matlab/Simulink,” *Renewable Energy and Power Quality Journal*, vol. 1, Mar. 2005, doi: 10.24084/repq03.243.
- [14] H. Nikpey, M. M. Majoumerd, M. Assadi, and P. Breuhaus, “Thermodynamic Analysis of Innovative Micro Gas Turbine Cycles,” *Proceedings of the ASME Turbo Expo*, vol. 3A, Sep. 2014, doi: 10.1115/GT2014-26917.
- [15] H. Nikpey, M. Assadi, P. Breuhaus, and P. T. Mørkved, “Experimental evaluation and ANN modeling of a recuperative micro gas turbine burning mixtures of natural gas and biogas,” *Applied Energy*, vol. 117, pp. 30–41, Mar. 2014, doi: 10.1016/j.apenergy.2013.11.074.
- [16] W. Rachtan and L. Malinowski, “An approximate expression for part-load performance of a microturbine combined heat and power system heat recovery unit,” *Energy*, vol. 51, pp. 146–153, Mar. 2013, doi: 10.1016/j.energy.2012.12.037.
- [17] L. Malinowski and M. Lewandowska, “Analytical model-based energy and exergy analysis of a gas microturbine at part-load operation,” *Applied Thermal Engineering*, vol. 57, no. 1–2, pp. 125–132, Aug. 2013, doi: 10.1016/j.applthermaleng.2013.03.057.
- [18] J. Nelson, N. G. Johnson, P. Doron, and E. B. Stechel, “Thermodynamic modeling of solarized microturbine for combined heat and power applications,” *Applied Energy*, vol. 212, pp. 592–606, Feb. 2018, doi: 10.1016/j.apenergy.2017.12.015.
- [19] R. A. Roberts, I. Rossi, and A. Traverso, “Dynamic Simulation of Energy Systems: Comparison of a Physics-Based Against Time Constant Based Approach Applied to a Microturbine Test Rig,” *Proceedings of the ASME Turbo Expo*, vol. 8, Aug. 2015, doi: 10.1115/GT2015-42651.
- [20] W. I. Rowen, “Simplified mathematical representations of heavy-duty gas turbines,” *Journal of Engineering for Gas Turbines and Power*, vol. 105, no. 4, pp. 865–869, Oct. 1983, doi: 10.1115/1.3227494.
- [21] H. Wei, Z. Jianhua, W. Ziping, and N. Ming, “Dynamic modelling and simulation of a micro-turbine generation system in the microgrid,” in *2008 IEEE International Conference on Sustainable Energy Technologies, ICSET 2008*, 2008, pp. 345–350. doi: 10.1109/ICSET.2008.4747029.
- [22] R. Calabria, F. Chiariello, P. Massoli, and F. Reale, “CFD Analysis of Turbec T100 Combustor at Part Load by Varying Fuels,” *Proceedings of the ASME Turbo Expo*, vol. 8, Aug. 2015, doi: 10.1115/GT2015-43455.
- [23] “Technical Description Microturbine Turbec T100.” [Online]. Available: [www.ensola.com](http://www.ensola.com)
- [24] T. M. MATLAB 2020b, “Basic Principles of Modeling Physical Networks - MATLAB & Simulink.” <https://www.mathworks.com/help/physmod/simscape/ug/basic-principles-of-modeling-physical-networks.html> (accessed Dec. 16, 2021).
- [25] “Declare Through and Across Variables for a Domain - MATLAB & Simulink.” <https://www.mathworks.com/help/physmod/simscape/lang/declare-through-and-across-variables-for-a-domain.html> (accessed Dec. 16, 2021).
- [26] M. T. Schobeiri, *Turbomachinery Flow Physics and Dynamic Performance*. Springer Berlin Heidelberg, 2012. doi: 10.1007/978-3-642-24675-3\_1.
- [27] A. Stamatis, K. Mathioudakis, and K. D. Papailiou, “Adaptive Simulation of Gas Turbine Performance,” *Journal of Engineering for Gas Turbines and Power*, vol. 112, no. 2, pp. 168–175, Apr. 1990, doi: 10.1115/1.2906157.
- [28] F. P. Incropera, D. P. DeWitt, T. L. Bergman, and A. S. Lavine, *Fundamentals of heat and mass transfer*. John Wiley & Sons, 2006.



## Paper V

Micro Gas Turbine Modelling and Adaptation for Condition Monitoring

R. Banihabib, M. J. Obrist, M. Assadi, and P. Jansohn.

Presented at Global Power and Propulsion, Chania, Greece, September 2022.

## GPPS-TC-2022-138

### MICRO GAS TURBINE MODELLING AND ADAPTATION FOR CONDITION MONITORING

**Reyhaneh Banihabib**  
**University of Stavanger**  
reyhaneh.banihabib@uis.no  
Stavanger, Norway

**Markus Josef Obrist**  
**Paul Scherrer Institute (PSI),**  
markus.obrist@psi.ch  
Villigen, Switzerland

**Mohsen Assadi**  
**University of Stavanger**  
mohsen.assadi@uis.no  
Stavanger, Norway

**Peter Jansohn**  
**Paul Scherrer Institute (PSI),**  
peter.jansohn@psi.ch  
Villigen, Switzerland

#### ABSTRACT

The future of decentralized power production with renewables as the main driver necessitates small-scale units such as micro gas turbines (MGTs) that are reliable and flexible in operation. Similar to large-scale gas turbines, MGTs operate based on the Brayton cycle, while providing added flexibility by variable rotational speed. To continuously monitor the condition of MGTs and maintain a reliable operation, an accurate model of the engine is required which predicts the expected operation of the engine in its healthy status.

This work aims to develop a model for individual MGTs that is fast and accurate enough to be utilized for condition monitoring purposes. Due to the role of MGTs in the power generation system as backup for renewables, they operate frequently in part-load conditions to provide the remaining required power for the electric grid. Therefore, the model should provide accurate predictions for both design and off-design operations. In this paper, the development of an engine model and the extensive adaptation process are presented during which the characteristics of the gas turbine components are modified in order to meet the experimental data within a range of operational conditions. The adaptive approach is validated by the experimental results extracted from a test rig of a MGT unit such that the model can be subsequently used as a reliable tool for condition monitoring of that MGT.

#### INTRODUCTION

To guarantee the availability of power generation units such as micro gas turbines, a condition monitoring (CM) system for assessing operational health of the engine is required (Tahan et al. 2017). Manufacturers are adopting CM approach to optimize maintenance intervals and avoid unwanted shutdowns. A CM system monitors the performance of the engine by collecting the sensors' data and assessing the health status of the components. The core element in a model-based CM system is a model of the so-called "healthy engine" that can predict the expected behaviour of the unit in which none of the components had endured any deteriorations (Cruz-Manzo et al. 2018). After the model is prepared, it will be implemented in the condition monitoring platform and deviations between model predictions and sensors' data from the unit will be investigated to assess the health status of the engine. In this procedure, the healthy-engine model should be able to operate by same inputs as the real engine and provide the same information that is available through the sensors.

Two main approaches are available to provide predictions for the healthy-engine: physics-based, and data-based. In physics-based approach, the engine is presented by component models connected to each other by applying the law of thermodynamics. Each component is modelled based on the characteristics of the components extracted from experiments (such as component maps) together with thermodynamic laws. In data-based approach, the model is constructed exclusively based on operational data extracted from the engine. In this approach, artificial intelligence methods will be used to construct and train the model, based on the data collected from the healthy engine.

Both physics-based and data-based models have their merits and shortcomings: the physics-based models are usually more complicated to construct as it is elaborated with models of each individual component. The components require characteristic curves or correlations that represents the behaviour of the flow passing through them. Whereas with data-based model, no information about the components' behaviour is required since the model is constructed based on black-box assumption of the whole system. The efforts to build a physics-based model is rewarded by providing insights to engine behaviour by providing flow properties at each component's inlet/outlet. Moreover, since predictions from the model are physics-informed, they can provide acceptable predictions for a range of operational conditions, while the data-based model fail to provide good predictions for the operational range that was not included in the training dataset.

Even with a detailed physics-based model, it is common to see deviations of model predictions from real life engine data. The main reason is imperfect component models due to mismatches between employed maps and correlations, and the actual behaviour of the components. To overcome this issue, the components' model should be tuned or "adapt" to real life components data.

The adaptation approach has been pursued by researchers during past decades, to overcome the mismatches between experimental data and modelling maps of gas turbine components. Stamatis et al. introduced a scaling method where the search for best scaling factors is conducted to minimize the difference between model predictions and the experimental data (Stamatis et al. 1990). While this scaling method showed great improvement of modelling accuracy, Kong et al. (Kong et al. 2003) proposed a new adaptation algorithm based on the conventional scaling method. In their approach, first the scaling parameters were calculated based on the data from a real engine and then new component maps were constructed based on mathematical models. The proposed method was tested on modelling a turboprop which showed significant increase in the accuracy of prediction in comparison with the model based on traditionally scaled maps.

A design-point adaptation approach was pursued by Li et al. (Li et al. 2006) to provide an accurate simulation of an industrial gas turbine by selection of parameters according to sensitivity analysis. The results of this work showed improvements in both simulation accuracy and reduction of the duration of adaptation. The work was further extended to perform multiple points adaptation of a model developed for a dual shaft aeroengine (Li et al. 2012b). While the results were satisfactory, it was declared that the outcome depended on defining proper range for each adaptation factors. Therefore, the adaptation process was improved by regression model between the prior scaling factors and off-design conditions. The regression coefficients were used to determine the search range for the multiple off-design point performance adaptation. The method was applied on a single shaft turboshaft which was proved to be accurate and faster than before since it avoided several try and errors, searching for correct parameter ranges (Li et al. 2012a).

A semi-automated procedure was introduced by Rompokos et al. (Rompokos et al. 2020) where integrated tuning methods for components' map were applied to adapt a computer model of a heavy-duty gas turbine in a range of operations. Other than map scaling, IGV corrections were applied, which resulted in increased accuracy in part-load conditions and providing trustable model for condition monitoring purposes.

Most of the adaptation algorithms employs map scaling methods which is proved to be practical and accurate for gas turbine modelling purposes. Pursuing more elaborated approach on component maps, numerous studies have been conducted to analytically express the turbo component maps which can represent the nonlinear behaviour of these components (Tsoutsanis et al. 2013; Tsoutsanis et al. 2015; Gaitanis et al. 2021). The advantage of this approach is that adapting the correlations to actual experimental data is not bound to scaling and provides higher degree of freedom depending on the complexity of the correlation.

In this paper, development of an accurate physics-based model of a micro gas turbine is presented. Empirical correlations are employed together with thermodynamic equations to provide components' model. Proper adaptation parameters are implemented inside the component's correlations and adaptation is performed to find the best set of parameters to increase the accuracy of the model in a range of operations.

The rest of the paper is structured as follows: first, the developed model for this work is presented including the correlations implemented in each component, followed by the adaptation procedure based on the parameters introduce in modelling section. Finally the results of the adapted model are compared to the data from an actual engine and the improvements are investigated.

## **DEVELOPED MODEL**

The developed model for the MGT system is a computer code written in Python language and is constructed based on connecting models for each of principal components of the engine. Each of the components are represented by the lumped assumption in which the flow condition at inlet and outlet are considered uniform. Required inputs for the solver are: demanded power and ambient conditions, namely: ambient pressure, ambient temperature and relative humidity.

Values for fuel flow rate and rotational speed is initially guessed by the solver, as well as air mass flow rate at inlet to the engine. Then the simulation is started by entering the first component with fully determined flow condition at inlet: pressure and temperature from defined ambient condition and the guessed mass flowrate. The outlet condition is calculated based on the thermodynamic equations and behavioural correlations/maps of the component, and is passed as input to the next component. After a complete course of calculation is performed from the first component to the last one, the outlet

pressure is compared to ambient value. According to the error in outlet pressure, the guessed air mass flowrate is modified until convergence in pressure is achieved. This is the innermost loop of the code. Two other loops are present in the code in which fuel flowrate and rotational speed are the modifying parameter and output power and turbine outlet temperature (TOT) is the controlling parameters respectively. At each modification step of these loops, the Secant method has been implemented which assures fast convergence.

The component models are defined as functions, in which flow properties at component inlets are input arguments, and the output arguments are outlet flow condition. Inside each component, principal thermodynamic equations are solved with steady-state assumption, together with the behaviour correlations. These correlations are often dependent on flow properties (e.g., heat capacity) which are functions of molecular composition as well as thermodynamic pressure and temperature. To accurately evaluate flow properties, the composition of the working fluid is evaluated inside each component.

The composition of working fluid is humid air before the combustion chamber. By defining relative humidity, the actual composition of air is calculated based on the dry air composition and the ambient pressure. Detail calculation and formula can be found in (Banihabib and Assadi 2022). Downstream of combustor, the working fluid is a mixture of combustion products and the excess air. The molecular composition depends on the fuel type (composition), air composition and air/fuel ratio. The air/fuel ratio depends on the operational point, which imposes different inlet air flow rate and different fuel flow rate. Therefore the concentration of the fuel is defined (Eq. 1) and calculated for each simulation point:

$$x_f = \frac{\dot{m}_f}{\dot{m}} \quad (1)$$

In above equation,  $\dot{m}$  is total mass flow rate. Knowing the air composition and the fuel concentration in the working fluid, the weight fraction of each element is calculated.

$$\vec{C}_{wf} = (x_{O_2}, x_{N_2}, x_{Ar}, x_{SO_2}, x_{CO_2}, x_{H_2O}, x_{He}) \quad (2)$$

The flow properties in each component are calculated based on the pressure and temperature of the flow:

$$k = k(\vec{C}_{wf}, T_s), \quad c_p = c_p(\vec{C}_{wf}, T_s), \quad c_v = c_p - R \quad (3)$$

$$M_{wf} = M_{wf}(\vec{C}_{wf}), \quad R = R(M_{wf}), \quad p_s = \rho R T_s \quad (4)$$

The thermodynamic equations inside components are well-known mass, momentum and energy conservation which is common among all components. However, characteristic curves (maps) and correlations are specific to each component which requires adaptation to each specific engine. The adaptation procedure (which will be covered in the next section) is in fact calibration of these characteristic curves and correlations to better match with experimental data.

The engine modelled in this work is AE-T100 which is a recuperated micro gas turbine manufactured by Ansaldo Energia. At design point, the engine produces 100 kW power with 30% electrical efficiency while running at 70,000 rpm. The cycle pressure ratio at this point is about 4.5 and the turbine inlet temperature is around 950°C. The engine is designed to operate with turbine outlet temperature not higher than 645°C. T100 PH version of this model is equipped with a bottoming heat exchanger which increases the total efficiency (fuel utilization factor) of the unit to 80%. More detailed information about this engine can be found in (Technical Description Microturbine Turbec T100).

A schematic figure of the engine with the main components are presented in Figure 1. The flow at different location of the engine is distinguished by a number, which will be used inside correlations in following sections. The correlations are empirically extracted from several studies conducted on the same engine and presented as functions of flow properties. Inside the correlations, the tuning parameters are differentiated from the original correlations by the symbol “\*”. Note that in all equations, the pressures and temperatures represent the total (stagnation) values, unless written with the index “s”, in which case the static (thermodynamic) value was intended.

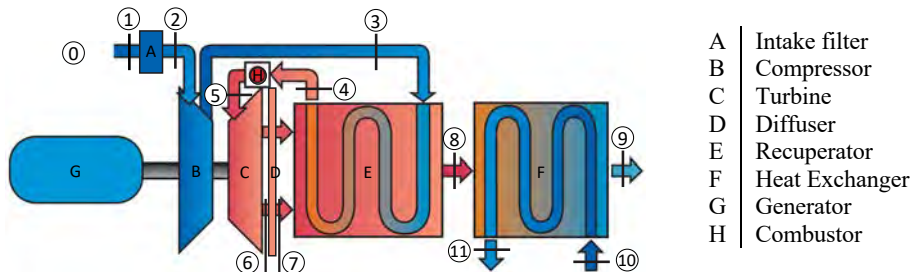


**Figure 1 Schematic of the components in AE-T100 (PH) micro gas turbine**

## Intake Air Filter

The air entering the engine passes through a filter to prevent small particles from entering to the compressor. This filter imposes a small pressure drop which can be correlated based on collected experimental data as a function of the pressure drop at design point (Björn Nyberg 2010), presented below:

$$\Delta p_{intk} = \Delta p_{coeff,intk} \times \frac{\dot{m}_1 \times \sqrt{T_1}}{p_1} \quad (5)$$

$$\Delta p_{coeff,intk} = \Delta p_{coeff,intk}^* \times \left( \Delta p_1 / \left( \frac{\dot{m}_1 \times \sqrt{T_1}}{p_1} \right) \right)_{des} \quad (6)$$

Incoming air circulates around the generator and the cooling water of auxiliary parts before entering the compressor, leading to temperature increase of the inlet air. A linear correlation between the air inlet temperature and increased value is extracted from the experiments, defined by the correlation below:

$$\Delta T_{intk} = \Delta T_{coeff,intk}^* \times \Delta T_{coeff,intk} T_1 + \Delta T_{incpt,intk}^* \times \Delta T_{incpt,intk} \quad (7)$$

Three adaptation coefficients are implemented to adjust the pressure drop and the temperature increase in the flow as described in Eq. 6 and 7.

## Turbo Components

The compression of the air in AE-T100 is conducted in a single stage centrifugal compressor, for which, characteristic behaviour of flow is presented through maps, represented with corrected physical parameters. The mass flow rate is corrected based on inlet pressure and inlet temperature, and the rotational speed is corrected based on the inlet temperature, as presented in Eq. 8. The maps are organized as isentropic efficiency based on pressure ratio and corrected mass flow rate. The rotational speed is illustrated with constant corrected speed lines. For adaptation purposes, two tuning factors are implemented as presented in Eq. 9 and 10. To implement the maps inside the developed computer model, the maps' data are provided through 2D tables in  $f_{\dot{m},cmp}(PR, N_{corr})$  and  $f_{\eta,cmp}(PR, N_{corr})$ .

$$\dot{m}_{2,corr} = \dot{m}_2 \sqrt{T_2} / p_2, \quad N_{corr,cmp} = N / \sqrt{T_2}, \quad PR_{cmp} = p_3 / p_2 \quad (8)$$

$$\dot{m}_{2,corr} = \dot{m}_{coeff,cmp}^* \times \dot{m}_{coeff,cmp} \times f_{\dot{m},cmp}(PR_{cmp}, N_{corr,cmp}) \quad (9)$$

$$\eta_{is,cmp} = \eta_{coeff,cmp}^* \times \eta_{coeff,cmp} \times f_{\eta,cmp}(PR_{cmp}, N_{corr,cmp}) \quad (10)$$

Similar correlations are employed for modelling single-stage radial turbine, in which the distribution of corrected mass flow rate and isentropic efficiency are provided via tabular data representing the performance map of the turbine. Two adaptation parameters to tune the turbine map are implemented as well (Eq. 12 and 13).

$$\dot{m}_{5,corr} = \dot{m}_5 \sqrt{T_5} / p_5, \quad N_{corr,trb} = N / \sqrt{T_5}, \quad PR_{trb} = p_5 / p_6 \quad (11)$$

$$\dot{m}_{5,corr} = \dot{m}_{coeff,trb}^* \times \dot{m}_{coeff,trb} \times f_{\dot{m},trb}(PR_{trb}, N_{corr,trb}) \quad (12)$$

$$\eta_{is,trb} = \eta_{coeff,trb}^* \times \eta_{coeff,trb} \times f_{\eta,trb}(PR_{trb}, N_{corr,trb}) \quad (13)$$

## Diffuser

The gas leaving the turbine section flows into a diffuser before entering the hot side of the recuperator. In diffuser the flow-path area increases gradually to lower the flow velocity that was previously increased by the turbine impeller. An empirical equation from (Björn Nyberg 2010) is employed to model the pressure drop in diffuser while the temperature is assumed to remain constant. The dynamic term of pressure after the diffuser is neglected. For diffuser no adaptation is considered.

$$p_7 = p_{s,7} = \Delta p_{coeff,diff} \times (p_6 - p_{s,6}) + p_{s,6} \quad (14)$$

$$\Delta p_{coeff,diff} = \left( \frac{p_{s,7} - p_{s,6}}{p_6 - p_{s,6}} \right)_{des} \quad (15)$$

## Recuperator

To model the recuperator, the cold side and hot sides are defined as two separated functions while the heat balance between two flow-paths is the connecting correlation between them. The effectiveness of the recuperator is defined based on the temperature increase in the cold side and the maximum temperature difference at inlets of the component:

$$\varepsilon_{rcp} = \frac{T_4 - T_3}{T_7 - T_3} \quad (16)$$

According to (Hohloch et al. 2010) the effectiveness of recuperator increases with rotational speed up to its maximum and then decreases. Here, instead of correlation with MGT rotational speed, same pattern but as a function of flow mass

flow rate is assumed, as the air flow rate to the engine has a linear dependency to the engine rotational speed. Based on the experimental data collected from same model of engine in (Hohloch et al. 2010), a conditional function is assumed for the recuperator effectiveness where there are two linear correlations, for mass flow rates below and above the optimum value:

$$\varepsilon_{rcp} = \begin{cases} \varepsilon_{opt,rcp}^* \times \varepsilon_{opt,rcp} - \varepsilon_{coeff1,rcp}^* \times \varepsilon_{coeff1,rcp} (\dot{m}_3 - \dot{m}_{opt,rcp}^* \times \dot{m}_{opt,rcp}), & \dot{m}_3 < \dot{m}_{opt,rcp} \\ \varepsilon_{opt,rcp}^* \times \varepsilon_{opt,rcp} + \varepsilon_{coeff2,rcp}^* \times \varepsilon_{coeff2,rcp} (\dot{m}_3 - \dot{m}_{opt,rcp}^* \times \dot{m}_{opt,rcp}), & \dot{m}_3 > \dot{m}_{opt,rcp} \end{cases} \quad (17)$$

Four adaptation parameters have been implemented in recuperator effectiveness correlations, two for the optimum mass flow rate and the effectiveness and two for the slope of the lines.

Temperature rise in the cold side is calculated based on the effectiveness, from which the amount of absorbed heat is defined. Extracted heat from hot side is equal to increase of the value in the cold side plus a fraction that is considered as wasted to the surrounding. The heat loss coefficient is equipped with an adaptation coefficient:

$$Q_{rcp,cs} = Q_{rcp,hs} (1 + Q_{loss,rcp}^* \times Q_{loss,rcp}) \quad (18)$$

The pressure loss on both cold and hot sides are calculated based on empirical correlations with dependency on mass flow rate, pressure and temperature, described below (Björn Nyberg 2010). Both correlations are tuned with adaptation coefficients.

$$p_4 = p_3 - p_3 \times \left(\frac{\dot{m}_3}{p_3}\right)^2 \times \frac{T_4^{1.55}}{T_3^{0.55}} \times \Delta p_{coeff,rcp,cs}^* \times \Delta p_{coeff,rcp,cs} \quad (19)$$

$$p_8 = p_7 - p_7 \times \dot{m}_7^2 \times T_7 \times \Delta p_{coeff,rcp,hs}^* \times \Delta p_{coeff,rcp,hs} \quad (20)$$

## Combustor

The pressure loss in the combustor is a function of mass flow rate, inlet pressure and inlet and outlet temperature of the gas in the component. The correlation below is extracted from the experimental data which counts for pressure loss due to both combustion air and dilution air (Björn Nyberg 2010):

$$p_5 = p_4 - (\Delta p_{coeff,cmb}^* \times \Delta p_{coeff,cmb} \times p_4 \times \left(\frac{\dot{m}_4 \sqrt{T_4}}{p_4}\right)^2 \times \left(1 + \Delta p_{const,cmb} \times \left(\frac{T_5}{T_4} - 1\right)\right)) \quad (21)$$

The outlet temperature of the combustion product is calculated via an energy balance, where the inlet heat is calculated based on fuel mass flow rate and the enthalpy of the inlet air to the combustor.

$$H_5 = (\dot{m}_f \times LHV + \dot{m}_4 \times h_4) \times (1 - Q_{loss,cmb}^* \times Q_{loss,cmb}) \quad (22)$$

To calculate the temperature at combustor outlet, the heat capacity of the flow is calculated based on the molecular composition of the combustion products (diluted by the excess air) and static temperature (Eq. 3). Hence, an iterative procedure is conducted to accurately calculate the turbine inlet temperature.

$$T_5 = \frac{H_5}{\dot{m}_5 \times c_p(\vec{C}_{wf,5}, T_{s,5})} \quad (23)$$

## Heat Exchanger

The temperature of the flow leaving the hot side of the recuperator is still high enough to warm-up water that can be utilized for district heating purposes. The pressure drop inside the gas-water heat exchanger is extracted from empirical data available from (Björn Nyberg 2010) which provides the pressure drop values versus gas mass flow rate.

## Shaft

The AE-T100 micro gas turbine is designed as a single-shaft unit in which mechanical components and generator rotate with same speed. Newton's 2<sup>nd</sup> law for the solid shaft results in balance of the torque imposed by mechanical components and the torque from generator in steady state conditions. A fraction of transmitted torque by turbo components is consumed to overcome losses such as friction:

$$T_{mech} = T_{trb} - T_{cmp} \quad (24)$$

$$T_{mech} - T_{elec} - T_{fric} = I\dot{\omega} = 0 \quad (25)$$

The loss of torque has been evaluated by the wasted power due to frictions and the unideal conversions in the generator:

$$T_{mech}\omega - T_{elec}\omega = T_{fric}\omega \quad (26)$$

$$P_{turbo} - P_{elec} = P_{loss} \quad (27)$$

According to (Henke et al. 2017) the power loss can be formulated by Eq. 29. For the adaptation purposes, only the value of intercept is multiplied by a tuning parameter.

$$P_{loss} = P_{fric} + P_{cnvr}, P_{fric} = P_{coeff,fric} \omega, P_{remain} = P_{turbo} - P_{fric} \quad (28)$$

$$P_{cnvr} = P_{coeff1,cnvr} P_{remain}^3 + P_{coeff2,cnvr} P_{remain}^2 + P_{coeff3,cnvr} P_{remain} + P_{incpt,cnvr}^* P_{incpt,cnvr} \quad (29)$$

All coefficients and constants of the empirical correlations are presented with their values in Table 1 and an overview of implemented adaptation parameters is provided in Table 2.

**Table 1 Components' modeling coefficients**

Component	Eq. #	Coefficients
intake	5, 7	$\Delta p_{coeff,intk} = 16.72 \times 10^5 \text{ ms}\sqrt{K}$ , $\Delta T_{coeff,intk} = 0.11$ , $\Delta T_{incpt,intk} = -30.46K$
diffuser	14	$\Delta p_{coeff,diff} = 0.64$
recuperator	17, 18	$\epsilon_{opt,rcp} = 0.93$ , $\dot{m}_{opt,rcp} = 0.63 \text{ kg/s}$ , $\epsilon_{coeff1,rcp} = 0.14 \text{ s/kg}$ , $\epsilon_{coeff2,rcp} = -0.4 \text{ s/kg}$ , $Q_{loss,rcp} = 0.02$
combustor	21	$\Delta p_{coeff,cmb} = 2 \times 10^7 \text{ 1/m}^2 \text{ s}^2 \text{ K}$ , $\Delta p_{const,cmb} = 0.2$ , $Q_{loss,cmb} = 0.015$
shaft	28, 29	$P_{coeff,fric} = 1.28 \text{ W/s}$ , $P_{coeff1,cnvr} = -4.48 \times 10^{-12} \text{ 1/W}^2$ , $P_{coeff2,cnvr} = 2.67 \times 10^{-7} \text{ 1/W}$ , $P_{coeff3,cnvr} = 0.0812$ , $P_{incpt,cnvr} = 3473W$

**Table 2 Adaptation parameters**

Component	Eq. #	No. of Parameters	Adaptation Parameters
intake	6, 7	3	$\Delta p_{coeff,intk}^*$ , $\Delta T_{coeff,intk}^*$ , $\Delta T_{incpt,intk}^*$
compressor	9, 10	2	$\dot{m}_{coeff,cmp}^*$ , $\eta_{coeff,cmp}^*$
turbine	12, 13	2	$\dot{m}_{coeff,trb}^*$ , $\eta_{coeff,trb}^*$
recuperator	17, 18, 19, 20	7	$\dot{m}_{opt,rcp}^*$ , $\epsilon_{opt,rcp}^*$ , $\epsilon_{coeff1,rcp}^*$ , $\epsilon_{coeff2,rcp}^*$ , $Q_{loss,rcp}^*$ , $\Delta p_{coeff,rcp,cs}^*$ , $\Delta p_{coeff,rcp,hs}^*$
combustor	21, 22	2	$\Delta p_{coeff,cmb}^*$ , $Q_{loss,cmb}^*$
shaft	29	1	$P_{incpt,cnvr}^*$

## METHODOLOGY OF ADAPTATION

While the developed model presented in previous section is capable of predicting engine behaviour, the accuracy of each prediction point is dependent on how the characteristic curves and correlations match the behaviour of the components in an actual engine. In most cases, the performance of the real engine shows deviation from those predefined characteristics which can be due to one or several of the reasons listed below:

1. Most of the characteristic maps and correlations are extracted from tests of isolated components. These results can be different from the integrated engine. One reason for such deviation is that even a sophisticated test stand fails to provide exact flow property distribution that occur in a real engine.
2. In some cases, the maps are generated by computer for the points where there is insufficient experimental data available. For such points, interpolation and extrapolations are employed which can be different from actual experimental results.
3. Some physical properties that are involved in the maps might be difficult to measure (e.g. high temperatures), in which calculation will be used to fill the gap and therefore causing calculation error.
4. The accuracy of measurements during the component tests can affect the accuracy of the generated map, which can lead to deviations.
5. If the characteristic maps are generated from measurements in an engine, some deviations can be observed compared to other engines, due to manufacturing tolerances.
6. Even if the maps were accurate at certain time, aging of the engine and several thousands hours of operation can cause small deformations which created deviation of performance from previously accurate map.

To utilize the model in condition monitoring platform, it is necessary to calibrate it with the experimental data from the healthy engine, to avoid misclassification of aforementioned deviations as engine faults. The calibration of components characteristics with actual engine data is called model adaptation.

Model adaptation can also be helpful in the cases that actual maps of the components (even imperfect version) are not available since they are considered proprietary to the manufacturer. In those cases, maps from similar components can be implemented in the model and then modified by proper adaptation procedure.

The process of adaptation starts with defining adequate adaptation coefficients in characteristics of different components. These coefficients must be able to calibrate the component behaviour while retaining the overall behavioural pattern. The adaptation parameters will be modified so that the prediction of the integrated model reach closer to the experimental data from the actual engine. Therefore, the whole process can be defined as an optimization problem:

$$X_{opt} = \underset{X}{\operatorname{argmin}} \left( \sum_{i=1}^m \frac{\alpha_i}{\Delta Y_{i,ref}} \sum_{j=1}^n |Y_{exp,j} - Y_{model,j}(X)| \right) \quad (30)$$

In the equation 30 above,  $X$  represents the set of adaptation parameters and  $Y$  includes the target properties to assess the adaptation of the model to experimental data. By definition of objective function as summation of errors on different target parameters, multiple objectives of the optimization (i.e. the multiple targets), are reduced to a single value. Mean absolute error (MAE) for each of target parameter extracted from the model and from different operation points ( $n$  points) are then normalized with a reference error value ( $\Delta Y_{i,ref}$ ). By implementing weights ( $\alpha_i$ ) for each target parameter, the importance of each target parameter is defined. The optimum set of adaptation parameters will minimize this objective function.

## RESULTS AND DISCUSSION

To examine the presented methodology, adaptation of the developed model to experimental data available from a test rig of AE-T100 is performed. The test rig is at Paul Scherrer Institute (PSI), Switzerland, which is installed and equipped with additional sensors for research purposes. The engine with principal flow-based components is presented in Figure 2. In Table 3, an overview of available data from the engine is presented, which shows the built-in measurements and the additional ones. The numbering of the parameters used is the same as in Figure 1.

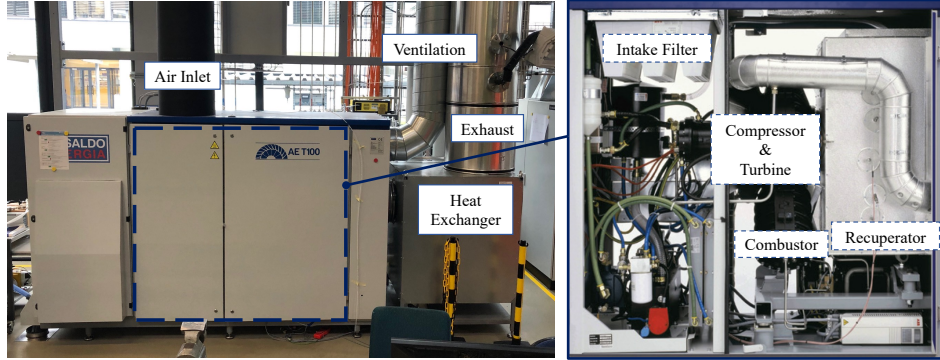


Figure 2 AT-T100 at PSI with components from outside (left), engine inside with components (right). The right picture is from (ANSALDO ENERGIA)

Table 3 Flow-path measurements in the MGT

Location	Description	Built-in Measurements	Additional Measurements
1	Engine inlet	$T_1$	$RH$
2	After inlet air filter	$\Delta p_{1-2}$	$p_2, T_2$
3	After compressor	-	$p_3, T_3$
4	After recuperator cold side	-	$T_4$
7	After diffuser	$T_7 (TOT)$	-
9	Engine outlet	$T_9$	-
10	Before heat exchanger cold side	$T_{10}$	-
11	After heat exchanger cold side	$T_{11}$	-

Other than main flow-path measurements provided in Table 3, cycle measurement are available from built-in sensor, such as shaft rotational speed ( $N$ ), produced power ( $P$ ) and fuel flow rate ( $\dot{m}_f$ ).

The data log from the engine includes a complete envelop of operation, from start-up to load changes and to shut down and hot restarts. Since the model of the engine is developed based on steady-state assumptions, only steady state data points from the experiments were extracted to be employed in model adaptation process. From all logs of sensors collected from running the engine over 24 days, about 10,800 operation points were proved to be steady state. Since running the model for all these points takes long time, a smaller subset was chosen randomly, which is representative for the whole dataset. The 100 data points chosen for adaptation purpose is well distributed in terms of power range and ambient conditions. The distribution for ambient condition is shown in Figure 3. The produced electrical power by engine is distributed between 70 kW to 110 kW. Note that over 100 kW electrical power production albeit in the data, the manufacturer does not recommend operating the engine with that power rate.

The adaptation is performed in two separate steps to avoid conducting high dimensional optimizations with high calculation costs. Since the models for recuperators cold side and hot side are convoluted with each other (Eq.16 & Eq.18), the only possible separating point is the outlet of the compressor. Intake and compressor are adapted in the first step (5 parameters) and the remaining 12 parameters are adapted in the second step.

For each adaptation parameter, proper bound is defined by verifying feasibility of the results from the model at max and min values. The first step is conducted with objective function, based on pressure and temperature after intake ( $p_2$  &  $T_2$ ) and compressor ( $p_3$  &  $T_3$ ), as shown in Eq. 31. For the second step, the temperature of air after cold side of the recuperator ( $T_4$ ), the turbine outlet temperature ( $TOT$ ) and the net power output ( $P$ ) is chosen as target parameters for the adaptation (Eq. 32). All errors are optimized with a normalized value and the weight factors. The weights are chosen based on the importance of each objective parameter and also through a try and error procedure, searching for the best weight set that guides the optimization to reduce the errors for each objective parameter down to their accepted tolerance. Since the data from experiment are noisy, even after noise cancelation, mean absolute error is chosen so that the objective function will be less affected by the presence of noise. The units used in equations below are kW for power, Celsius for temperatures and bar for pressure (absolute values). The optimization problem is solved with genetic algorithm embedded in SciPy library (Virtanen et al. 2019).



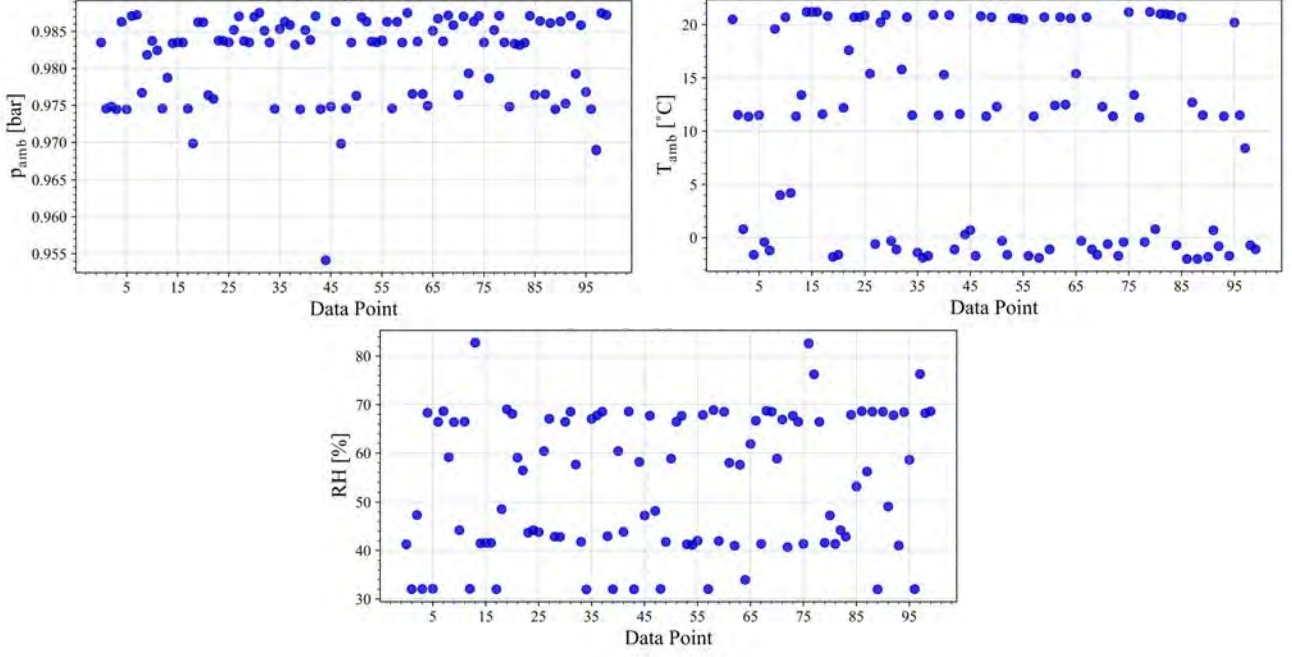


**Figure 3 Distribution of ambient pressure, ambient temperature and relative humidity in dataset used for adaptation**

$$OF_1 = \frac{0.05}{0.001 \times 100} \sum_{j=1}^{100} |(p_2)_{exp,j} - (p_2)_{model,j}| + \frac{0.1}{0.1 \times 100} \sum_{j=1}^{100} |(T_2)_{exp,j} - (T_2)_{model,j}| \quad (31)$$

$$+ \frac{0.5}{0.1 \times 100} \sum_{j=1}^{100} |(p_3)_{exp,j} - (p_3)_{model,j}| + \frac{0.15}{2.0 \times 100} \sum_{j=1}^{100} |(T_3)_{exp,j} - (T_3)_{model,j}|$$

$$OF_2 = \frac{0.1}{2 \times 100} \sum_{j=1}^{100} |(T_4)_{exp,j} - (T_4)_{model,j}| + \frac{0.2}{2 \times 100} \sum_{j=1}^{100} |(TOT)_{exp,j} - (TOT)_{model,j}| \quad (32)$$

$$+ \frac{0.2}{2 \times 100} \sum_{j=1}^{100} |(P)_{exp,j} - (P)_{model,j}|$$

To start the optimization process, initial population was chosen randomly, with 3 times the number of adaptation parameters. Mutation is imposed during the optimization to avoid convergence to local minimum. The evolution of objective function for the second step is shown in Figure 4 as an example. During each optimization step, uneven number of model runs have been conducted. For instance, at first optimization iteration, the simulation ran for 72 times over 100 data points, which means 7200 times of calling and running the model. Average time for model run is 0.3 seconds which resulted 36 minutes for the first iteration of optimization, however the number of model runs is decreased as the optimization proceeds. Duration of whole process was 8 hours and 27 minutes. For the first adaptation step only 7 iterations of optimization were conducted which took less than 3 hours, as there was only 5 parameters to optimize. In total, the model with 17 adaptation parameters was adapted with less than 11 hours of run.

The bounds specified for each of the adaptation parameters with their final adapted values are presented in Table 4. Since the final optimized values lie between the maximum and minimum bounds, adequacy of specification of the bounds is reassured.

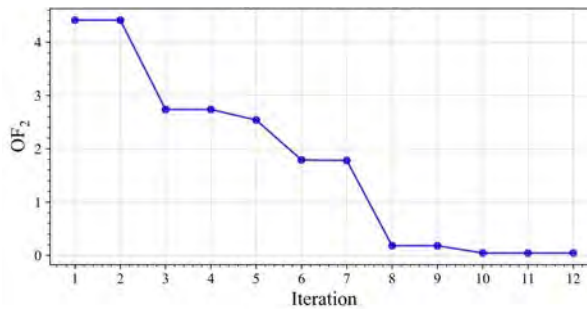


**Figure 4 Objective function during adaptation step 2.**

**Table 4 Adaptation parameters with bounds, associated objective function and optimum values**

No.	Parameter	Bound	Adapted value	Objective Function	No.	Parameter	Bound	Adapted value	Objective Function
1	$\Delta p_{coeff, intk}^*$	(0.50, 2.00)	1.735	$OF_1$	10	$\eta_{coeff1, rcp}^*$	(0.80, 1.20)	0.864	$OF_2$
2	$\Delta T_{coeff, intk}^*$	(0.50, 2.00)	1.051	$OF_1$	11	$\eta_{coeff2, rcp}^*$	(0.80, 1.20)	0.900	$OF_2$
3	$\Delta T_{incpt, intk}^*$	(0.50, 2.00)	1.503	$OF_1$	12	$Q_{loss, rcp}^*$	(0.05, 5.00)	2.612	$OF_2$
4	$\dot{m}_{coeff, cmp}^*$	(0.50, 2.00)	1.001	$OF_1$	13	$\Delta p_{coeff, rcp, cs}^*$	(0.50, 3.00)	2.901	$OF_2$
5	$\eta_{coeff, cmp}^*$	(0.50, 2.00)	0.977	$OF_1$	14	$\Delta p_{coeff, rcp, hs}^*$	(1.00, 3.00)	2.719	$OF_2$
6	$\dot{m}_{coeff, trb}^*$	(0.70, 1.20)	1.007	$OF_2$	15	$\Delta p_{coeff, cmb}^*$	(0.08, 1.70)	1.029	$OF_2$
7	$\eta_{coeff, trb}^*$	(0.70, 1.20)	1.046	$OF_2$	16	$Q_{loss, cmb}^*$	(0.10, 5.00)	2.769	$OF_2$
8	$\dot{m}_{opt, rcp}^*$	(0.80, 1.10)	1.04	$OF_2$	17	$P_{incpt, cnvr}^*$	(0.10, 2.00)	0.796	$OF_2$
9	$\eta_{opt, rcp}^*$	(0.80, 1.05)	1.030	$OF_2$					

To evaluate the performance of the adapted model, another set of 100 points were chosen from the steady state dataset, again assuring that it covers a good range of power and ambient condition by choosing randomly. An overview of model prediction errors (both MAE and maximum) for target parameters before and after adaptation is presented in Table 5. By looking at the error values associated with the adapted column, the maximum prediction error of power is less than 2 kW which is fairly accurate for an engine with 100 kW baseload power and minimum of 50 kW at part-load operation. Less than 5°C of maximum error is achieved for TOT, however the maximum error for  $T_4$  is close to 10°C. The reason behind this is the implemented correlation for heat transfer in the recuperator.

**Table 5 Model prediction error for target parameters before and after adaptation**

No.	Parameter	Original Model		Adapted Model	
		MAE	Absolute of Maximum Error	MAE	Absolute of Maximum Error
1	$p_2$	0.0025 bar	0.0027 bar	0.0010 bar	0.0012 bar
2	$T_2$	275.99 °C	330.83°C	0.16 °C	0.64 °C
3	$p_3$	0.0634 bar	0.1534 bar	0.043 bar	0.069 bar
4	$T_3$	1.74 °C	5.20 °C	0.27 °C	0.86 °C
5	$T_4$	269.69°C	323.07 °C	3.54 °C	9.74 °C
6	TOT	275.99 °C	330.83°C	1.79 °C	4.94 °C
7	$P$	30.60 kW	41.80 kW	0.66 kW	1.67 kW

As discussed in “Developed Model” section, the correlation employed for modelling the recuperator efficiency is inspired by the results presented in (Hohloch et al. 2010), shown in view (a) of Figure 5 with green markers. The effectiveness of the adapted recuperator is presented in view (b), which has a maximum value and two linear correlations with the mass flow, given the linear relation between rotational speed and air mass flow rate. In view (c) of Figure 5, the actual error for  $T_4$  is presented (model prediction minus experiment). It can be seen that the difference with experiment is low near the optimum mass flow rate but increases when the mass flow rate gets far from the optimum. This can be explained by looking at the data from view (a), where it seems that green marker points show parabolic behaviour on two sides of the optimum mass flow rate, while the model assumption is linear. It is anticipated that modifying the correlation to two parabolic correlations will increase the accuracy, however it will increase the number of adaptation parameters further and hence increases the time required for the optimization.

Figure 6 presents an overview of adaptation results, for target parameters of the second step of adaptation, namely power, temperature at outlet of the cold side of the recuperator and the turbine outlet temperature. As it is obvious from the left side figures, the model prediction was far from experimental data at the beginning. The adapted model predictions are depicted on the right side of Figure 6 which show a satisfactory compliance with experimental data. The results from before adaptation has high errors, mainly due to correlations for the components were extracted from different works and references, which were derived from using data collected from different engines. However, the configuration of the correlations was proper and compliant with the component behaviour since by tuning the coefficients, a high accuracy of prediction is achieved.

By looking at the errors reported in Table 5 and predicted values shown in Figure 6, accuracy of TOT prediction is higher than  $T_4$ , even though it is expected that errors of  $T_4$  prediction will be destructive for TOT as well. It seems that the adaptation of turbine maps compensated for high  $T_4$  errors. Even so, by looking at Figure 6 it is obvious that points with high  $T_4$  errors have led to high TOT errors as well (for example, the points for power output higher above 105 kW).

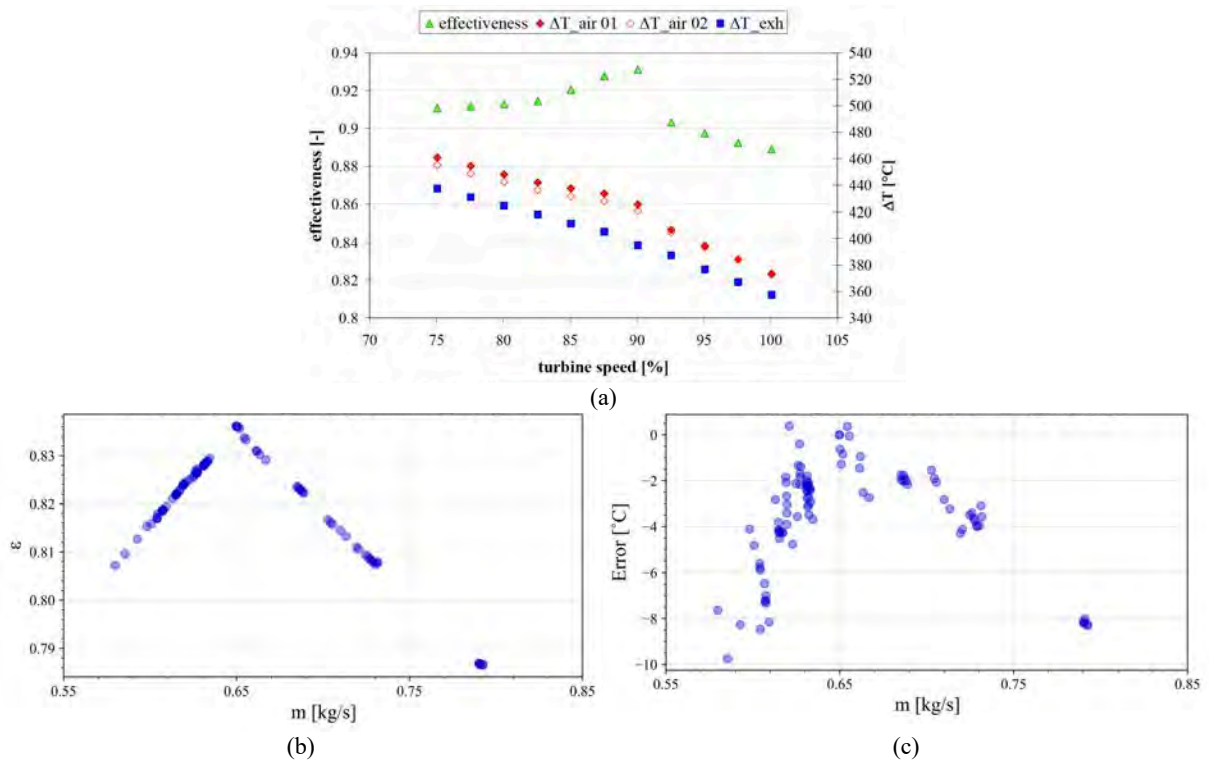


Figure 5 Temperature data and effectiveness of recuperator reported in (Hohloch et al. 2010) (a), effectiveness of adapted recuperator in the current work (b), error of  $T_4$  predict in current work (c).

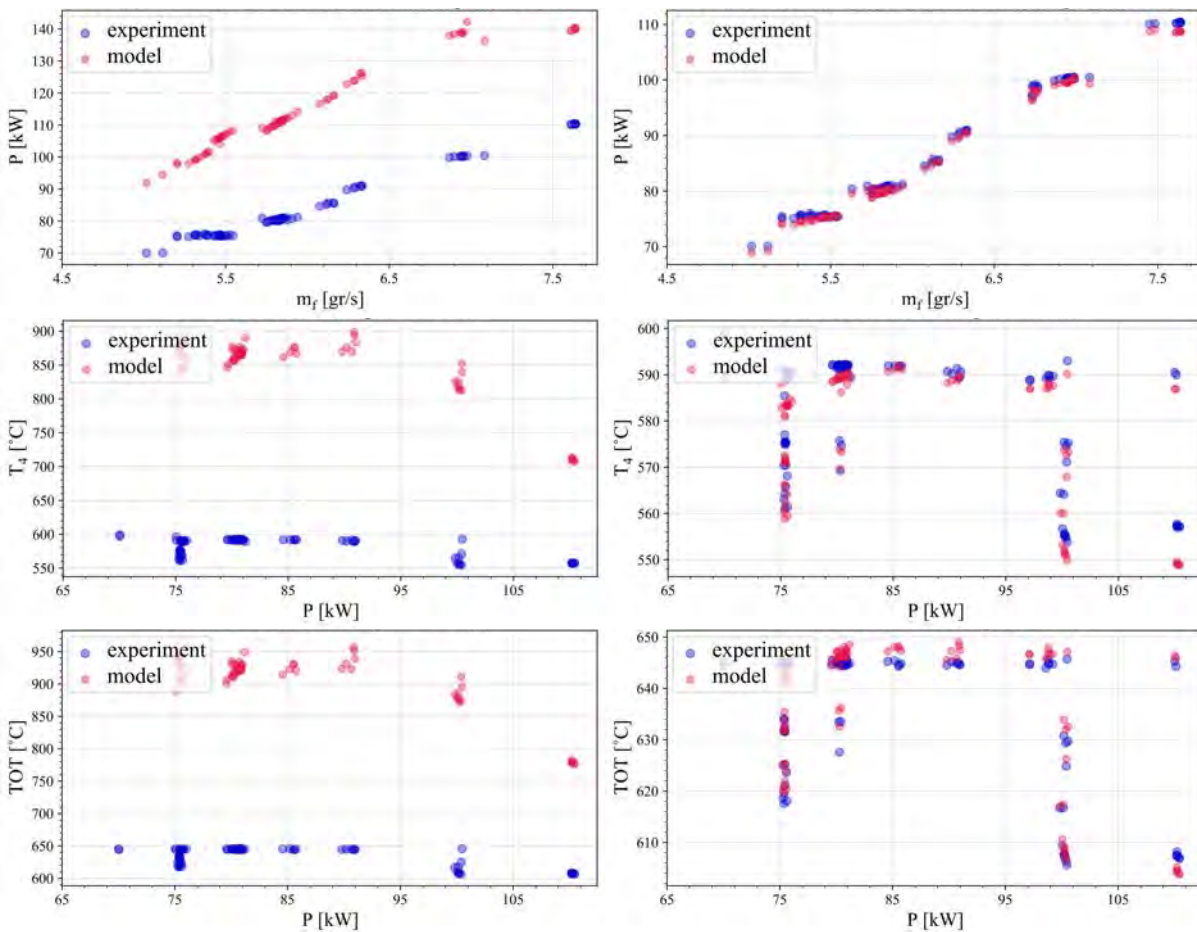


Figure 6 Model prediction and experimental data for power, TOT and  $T_4$ . Left figures are from the model before adaptation and right figures are from the adapted model.

## CONCLUSION

In this paper a comprehensive overview of the development of a computer model for a micro gas turbine operating in steady-state condition is provided. The code is constructed with lumped assumption for all of the principal gas turbine components, employing thermodynamic equations and empirical correlations to model each components behaviour. Proper adaptation parameters were implemented during the modelling which led to a total number of 17 adaptation parameters.

The adaptation process was conducted through two separate courses of optimization, employing a genetic algorithm method. At each course of optimization, a number of parameters were tuned to decrease the error between model predictions and experimental data collected from an MGT test rig. The results showed high accuracy of the adapted model which proves the suitability of the employed method, to provide an accurate model that can be utilized for condition monitoring purposes. For further improvements, a more flexible correlation for the modelling of the recuperator is expected to improve the accuracy of the predictions even more, however at the expense of increased computational cost.

## NOMENCLATURE

### Alphanumeric Variables

$C$	Molecular composition vector	$n$	Number of operation points
$c_v$	Specific heat of gas at constant volume (J/kg K)	$p$	Pressure (Pa)
$c_p$	Specific heat of gas at constant pressure (J/kg K)	$Q$	Heat exchange (J)
$h$	Specific enthalpy (J/kg)	$R$	Specific gas constant (J/kg K)
$k$	Thermal conductivity (W/mK)	$T$	Temperature (K)
$M$	Molar mass (g/mol)	$X$	Adaptation parameters
$m$	Number of target parameters for adaptation	$x$	Weight coefficient (kg/kg)
$\dot{m}$	Mass flow rate (kg/s)	$Y$	Measurements from the MGT
$N$	Absolute or relative rotational speed (rpm or %)		

### Greek Symbols

$\alpha$	Weight factor inside objective function	$\rho$	Density (kg/m <sup>3</sup> )
$\varepsilon$	Effectiveness (-)	$\omega$	Rotational speed (rad/s)
$\eta$	Efficiency (-)		

### Indices

$cmb$	Combustor	$hs$	Hot side
$cmp$	Compressor	$incpt$	Intercept
$cnvr$	Conversion	$is$	Isentropic
$coeff$	Coefficient	$intk$	Intake
$corr$	Corrected	$mech$	Mechanical
$cs$	Cold side	$opt$	Optimum
$des$	Design	$rcp$	Recuperator
$diff$	Diffuser	$ref$	Reference
$elec$	Electrical	$s$	Static
$f$	Fuel	$trb$	Turbine
$fric$	Friction	$wf$	Working fluid, either air or flue gas

### Abbreviations

CM	Condition monitoring	PR	Pressure ratio
LHV	Lower heating value	PSI	Paul Scherrer Institute
MAE	Mean absolute error	RH	Relative humidity
MGT	Micro gas turbine	TOT	Turbine outlet temperature
PH	Power and heat		

## ACKNOWLEDGMENTS

This project has received funding from the European Union's Horizon 2020 research and innovation program under the Marie Skłodowska-Curie grant agreement No. 861079 ("Next MGT").



## REFERENCES

ANSALDO ENERGIA. AE-T100NG Product Specifications. Available at: <https://www.ansaldoenergia.com/PublishingImages/Microturbines/AE-T100NG.pdf>.

- Banihabib, R. and Assadi, M. 2022. DYNAMIC MODELLING AND SIMULATION OF A 100 KW MICRO GAS TURBINE RUNNING WITH BLENDED METHANE/HYDROGEN FUEL. In: *ASME Turbo Expo*. Rotterdam
- Björn Nyberg 2010. *Fuel Flexible Prediction Model for T100 Gas Turbine*. Thesis for the Degree of Master of Science, Lund: Lund University.
- Cruz-Manzo, S., Panov, V. and Zhang, Y. 2018. Gas Path Fault and Degradation Modelling in Twin-Shaft Gas Turbines. *Machines* 6(4), p. 43. Available at: <https://www.mdpi.com/2075-1702/6/4/43/htm>.
- Gaitanis, A., Laterre, A., Contino, F. and de Paepe, W. 2021. TOWARDS REAL TIME TRANSIENT MGT PERFORMANCE ASSESSMENT: EFFECTIVE PREDICTION USING ACCURATE COMPONENT MODELLING TECHNIQUES. In: *Global Power & Propulsion Society*. Available at: [www.gpps.global](http://www.gpps.global).
- Henke, M., Monz, T. and Aigner, M. 2017. Introduction of a New Numerical Micro Gas Turbine Cycle Dynamics. *Journal of Engineering for Gas Turbines and Power* 139(4). Available at: [http://asmedigitalcollection.asme.org/gasturbinespower/article-pdf/139/4/042601/6175127/gtp\\_139\\_04\\_042601.pdf](http://asmedigitalcollection.asme.org/gasturbinespower/article-pdf/139/4/042601/6175127/gtp_139_04_042601.pdf).
- Hohloch, M., Zanger, J., Widenhorn, A. and Aigner, M. 2010. Experimental Characterization of a Micro Gas Turbine Test Rig. In: *Proceedings of the ASME Turbo Expo*. American Society of Mechanical Engineers Digital Collection, pp. 671–681. Available at: [http://asmedigitalcollection.asme.org/GT/proceedings-pdf/GT2010/43987/671/2689295/671\\_1.pdf](http://asmedigitalcollection.asme.org/GT/proceedings-pdf/GT2010/43987/671/2689295/671_1.pdf).
- Kong, C., Ki, J. and Kang, M. 2003. A New Scaling Method for Component Maps of Gas Turbine Using System Identification. *Journal of Engineering for Gas Turbines and Power* 125(4), pp. 979–985. Available at: <https://asmedigitalcollection.asme.org/gasturbinespower/article/125/4/979/477439/A-New-Scaling-Method-for-Component-Maps-of-Gas>.
- Li, Y.G., Ghafir, M.F.A., Wang, L., Singh, R., Huang, K., Feng, X. and Zhang, W. 2012a. Improved multiple point nonlinear genetic algorithm based performance adaptation using least square method. *Journal of Engineering for Gas Turbines and Power* 134(3). Available at: <https://asmedigitalcollection.asme.org/gasturbinespower/article/134/3/031701/455920/Improved-Multiple-Point-Nonlinear-Genetic>.
- Li, Y.G., Marinai, L., Gatto, E. lo, Pachidis, V. and Pilidis, P. 2012b. Multiple-Point Adaptive Performance Simulation Tuned to Aeroengine Test-Bed Data. *Journal of Propulsion and Power* 25(3), pp. 635–641. Available at: <https://arc.aiaa.org/doi/abs/10.2514/1.38823>.
- Li, Y.G., Pilidis, P. and Newby, M.A. 2006. An Adaptation Approach for Gas Turbine Design-Point Performance Simulation. *Journal of Engineering for Gas Turbines and Power* 128(4), pp. 789–795. Available at: <https://asmedigitalcollection.asme.org/gasturbinespower/article/128/4/789/465157/An-Adaptation-Approach-for-Gas-Turbine-Design>.
- Rompokos, P., Aretakis, N., Roumeliotis, I. and Mathioudakis, K. 2020. Application of an advanced adaptation methodology for gas turbine performance monitoring. In: *Global Power & Propulsion Society*. GPPS. doi: 10.33737/GPPS20-TC-92.
- Stamatis, A., Mathioudakis, K. and Papailiou, K.D. 1990. Adaptive Simulation of Gas Turbine Performance. *Journal of Engineering for Gas Turbines and Power* 112(2), pp. 168–175. doi: 10.1115/1.2906157.
- Tahan, M., Tsoutsanis, E., Muhammad, M. and Abdul Karim, Z.A. 2017. Performance-based health monitoring, diagnostics and prognostics for condition-based maintenance of gas turbines: A review. *Applied Energy* 198, pp. 122–144. doi: 10.1016/j.apenergy.2017.04.048.
- Technical Description Microturbine Turbec T100*. Available at: [www.ensola.com](http://www.ensola.com).
- Tsoutsanis, E., Li, Y.G., Pilidis, P. and Newby, M. 2013. Part-Load Performance of Gas Turbines: Part I — A Novel Compressor Map Generation Approach Suitable for Adaptive Simulation. *ASME 2012 Gas Turbine India Conference, GTINDIA 2012*, pp. 733–742. Available at: [http://asmedigitalcollection.asme.org/GTINDIA/proceedings-pdf/GTINDIA2012/45165/733/4240933/733\\_1.pdf](http://asmedigitalcollection.asme.org/GTINDIA/proceedings-pdf/GTINDIA2012/45165/733/4240933/733_1.pdf).
- Tsoutsanis, E., Meskin, N., Benammar, M. and Khorasani, K. 2015. Transient gas turbine performance diagnostics through nonlinear adaptation of compressor and turbine maps. *Journal of Engineering for Gas Turbines and Power* 137(9). Available at: <https://asmedigitalcollection.asme.org/gasturbinespower/article/137/9/091201/374016/Transient-Gas-Turbine-Performance-Diagnostics>.
- Virtanen, P. et al. 2019. SciPy 1.0--Fundamental Algorithms for Scientific Computing in Python. *ArXiv - Computer Science - Mathematical Software* 17(3), pp. 261–272. Available at: <http://arxiv.org/abs/1907.10121>.

## Paper VI

Techno-Economic Optimization of Microgrid Operation with Integration of Renewable Energy, Hydrogen Storage, and Micro Gas Turbine

R. Banihabib, F. S. Fadnes., M. Assadi.

Under review for Energy Conversion and Management.

**This paper is not included in the repository because it has not yet been published.**

## Paper VII

Towards a Low-Carbon Future for Offshore Oil and Gas Industry:  
A Smart Integrated Energy Management System with Floating  
Wind Turbines and Gas Turbines

R. Banihabib and M. Assadi.

Journal of Cleaner Production, vol. 423, p. 138742, Oct. 2023, doi:  
10.1016/j.jclepro.2023.138742.





# Towards a low-carbon future for offshore oil and gas industry: A smart integrated energy management system with floating wind turbines and gas turbines

Reyhaneh Banihabib<sup>\*</sup>, Mohsen Assadi

University of Stavanger, Stavanger, Norway

## ARTICLE INFO

Handling Editor: Panos Seferlis

### Keywords:

Decarbonization  
Offshore microgrid  
Floating wind turbines  
Hydrogen-compatible gas turbines  
Hybrid optimization  
Online optimization  
AI algorithms  
Operational efficiency  
Sustainable energy future  
Carbon-based emissions

## ABSTRACT

Decarbonizing offshore oil and gas fields is crucial in the global fight against climate change. To achieve this objective, the offshore oil and gas industry has embraced innovative energy systems, including microgrids that seamlessly integrate renewable energy sources like floating wind turbines. This study presents a comprehensive investigation into an integrated energy management system for an offshore microgrid, encompassing three platforms and a floating wind farm, along with green hydrogen production and storage facilities.

The operational decision-making process for such a complex microgrid, involving numerous assets, presents notable challenges. To address this, a sophisticated smart management system is employed, enabling efficient optimization with advanced forecasting capabilities to identify the most cost-effective and environmentally friendly version of the microgrid's operation. To overcome the intricacies of optimization and computational constraints, a novel hybrid optimization approach, with a platform-centric strategy, is utilized. Leveraging real-world operational data, the study harnesses an innovative online optimization method fortified with state-of-the-art AI algorithms.

The results of the optimization are benchmarked against a rule-based operation, wherein no formal optimization occurs, but the most economically viable decisions are made. The findings underscore the effectiveness of the developed optimization method, leading to a significant 16% reduction in operational costs and carbon-based emissions compared to the rule-based approach.

This study effectively demonstrates the real-world applicability of the developed method by applying and testing the smart management system on an actual offshore platform with minimal simplifications. The investigation provides valuable evidence of the method's adaptability to complex operational scenarios, highlighting its potential for practical implementation in the offshore oil and gas industry.

## 1. Introduction

The extraction and processing of fossil fuels significantly impact the release of greenhouse gases (GHGs), highlighting the urgency to find effective strategies for minimizing these emissions and achieving a carbon-neutral society. Offshore facilities rely heavily on gas turbines (GTs) for power generation, using natural gas or diesel oil as fuels, thereby being the primary sources of CO<sub>2</sub> and NO<sub>x</sub> emissions. According to a report, in 2022, GTs accounted for 81% of CO<sub>2</sub> emissions generated by petroleum activities in the Norwegian Continental Shelf (NCS) (Norwegian Petroleum Directorate, 2023). The power required on oil and gas (O&G) platforms ranges from 10 MW to several hundreds of

MW, depending on factors like temperature, pressure, and field properties (Polleux et al., 2022). To meet this demand GTs coupled with electric generators operate by burning natural gas or diesel oil (Zhang et al., 2018).

Dependence on GTs for power generation in offshore O&G facilities significantly amplifies environmental consequences. The continuous release of CO<sub>2</sub> intensifies the global issue of climate change (Hachem et al., 2022), setting off a series of effects. These include the gradual increase in global temperatures, rising sea levels, and disruptions to ecosystems. The long-term consequences of GHG emissions not only affect the local marine environments around offshore installations but also contribute to broader climate shifts (Grasso, 2019), underscoring

<sup>\*</sup> Corresponding author.

E-mail addresses: [Reyhaneh.Banihabib@uis.no](mailto:Reyhaneh.Banihabib@uis.no) (R. Banihabib), [Mohsen.Assadi@uis.no](mailto:Mohsen.Assadi@uis.no) (M. Assadi).

<https://doi.org/10.1016/j.jclepro.2023.138742>

Received 16 June 2023; Received in revised form 27 August 2023; Accepted 7 September 2023

Available online 12 September 2023

0959-6526/© 2023 The Authors. Published by Elsevier Ltd. This is an open access article under the CC BY-NC-ND license (<http://creativecommons.org/licenses/by-nc-nd/4.0/>).



the need for a comprehensive and globally oriented response ([International Energy Agency, 2020](#)). In response to environmental concerns, the offshore O&G industry is experiencing a transformative shift driven by evolving regulations, societal pressures, and a growing recognition of its environmental footprint. International efforts like the Paris Agreement illustrate the joint commitment to reducing emissions and controlling global warming ([Haszeldine et al., 2018](#)). The International Maritime Organization and its Energy Efficiency Existing Ship Index regulations demonstrate global initiatives to limit emissions in the maritime sector, which also influence offshore operations ([Watson, 2020](#)).

Norway has been a pioneer in promoting environmental awareness and reducing GHG from the O&G sector. In 1991, Norway introduced a CO<sub>2</sub> tax of approximately 40 €/ton. Over time, the implementation of this policy has resulted in operators on the NCS now facing a combined CO<sub>2</sub> tax of 52 €/ton, which is expected to increase to more than 70 €/ton by 2040 due to the tightening of regulatory frameworks in Europe ([Oliveira-Pinto et al., 2019](#)). The European Union Trading System (ETS), created in 2005, has also significantly promoted environmental awareness, with current ETS prices around 5 €/ton of CO<sub>2</sub> ([Oliveira-Pinto et al., 2019](#)). As a result, the increasing emissions of GHGs not only pose environmental concerns but also result in significant financial penalties. Therefore, improving the energy management of offshore facilities is becoming an economic driver for the industry ([Oliveira-Pinto et al., 2019](#)). Particularly in Norway, where the cost of CO<sub>2</sub> emissions stemming from natural gas utilization in petroleum fields is notably high at approximately 2400 NOK/ton of natural gas (equivalent to about 214 €/ton) under the 2023 regulatory framework (“[Tax rates in Norway](#)”), field operators have shown keen interest in exploring solutions to reduce O&G platform emissions.

One of the strategies embraced by O&G facilities in Norway to attain sustainability and decrease emissions is adopting onshore power sources. Given that a substantial portion of onshore power in Norway is derived from renewable sources ([International Energy Agency, 2022](#)), this approach is gaining momentum. Currently, 16 fields have either already implemented or are planning to use this technology ([Norwegian Petroleum Directorate Professor Olav Hanssens and vei, 2020](#)), which is projected to account for around 45% of total O&G production on the continental shelf ([Norwegian Petroleum Directorate Professor Olav Hanssens and vei, 2020](#)). This shift towards power from land solutions is expected to significantly reduce petroleum-related emissions in Norway, avoiding approximately 3.2 million tons of CO<sub>2</sub> emissions annually-equivalent to a quarter of the total emissions from the petroleum sector in 2019 ([Norwegian Petroleum Directorate Professor Olav Hanssens and vei, 2020](#)).

Another avenue showing promise in mitigating emissions within the offshore sector is CO<sub>2</sub> capture and storage (CCS) from turbine exhaust. Despite its potential, the practical implementation of this method on platforms presents intricate logistical challenges that necessitate careful consideration. The need for substantial infrastructure in proximity to the gas turbine, combined with spatial constraints on these platforms, complicates the approach ([Roussanaly et al., 2019](#)). Consequently, exploring innovative solutions characterized by compactness and reduced weight becomes essential, bypassing the hurdles posed by spatial limitations and heavy equipment installation ([Anekwe et al., 2023](#)). Despite the challenges, significant progress has been achieved in implementing CO<sub>2</sub> capture from turbine exhaust on offshore platforms, exemplified by the United Kingdom and Norway (“[Carbon capture and storage, 2023](#)”). This uptake validates the technology’s feasibility in the offshore environment. Other than Europe, the initiatives in offshore carbon dioxide storage in regions such as the United States, Japan, and Australia, underscore a commitment to safe and environmentally responsible storage, complemented by their respective regulations and policies ([Luo et al., 2023](#)).

The integration of renewable energy sources and alternative power supply methods is another avenue to address the challenges of

sustainable offshore operations. This approach offers a multifaceted solution to the challenges of sustainable offshore operations. Renewable energy sources, including wind, solar, and wave energy, have gained traction as effective tools to reduce the carbon footprint of offshore O&G platforms ([de Souza et al., 2022](#)). Wind turbines, in particular, stand out due to their suitability for offshore high wind speeds. Developing hybrid energy systems that combine renewable sources with conventional gas turbines aims to enhance offshore platform efficiency and sustainability, ensuring a consistent power supply to meet operational demands. This integration leads to substantial contributions to energy demand through renewables, resulting in emissions reduction and notable cost savings ([Watson, 2020](#)). While the shift to renewable energy sources may entail upfront expenses, the reduction in operational costs and avoidance of emissions-related taxes can lead to significant economic benefits ([International Renewable Energy Agency \(IRENA\), 2019](#)). Government incentives and regulatory support play a pivotal role in shaping the economic landscape of this transition ([International Renewable Energy Agency \(IRENA\), 2019](#)).

Insights into the growth of offshore wind in the Asia Pacific region and the policies implemented by various governments to promote this sector are provided in ([Cheng and Hughes, 2023](#)). The operation of a 4 × 5 MW offshore wind farm operating in parallel with GTs was studied by [Korpås et al. \(2012\)](#). The findings highlight the potential for significant cost savings and emissions reductions, validating the viability of offshore wind integration for sustainable and efficient power supply to O&G field centers. [Zhang et al. \(2021\)](#) explored the integration of wind power into offshore O&G field energy systems, assessing its economic and environmental performance. According to the authors ([Zhang et al., 2021](#)), introducing wind energy reduced carbon emissions by approximately 39.91% and lowered the total annual cost by about 2.57% ([Zhang et al., 2021](#)). Additionally, Panda et al. investigated an XAI-driven net-zero carbon roadmap for the petrochemical industry, considering stochastic scenarios of offshore wind energy, which demonstrated the potential for further advancements in cost reductions and emissions mitigation through the integration of renewable energy sources ([Panda and Das, 2021](#)).

Although the benefits of integrating renewable energy sources, particularly wind power, are evident, its intermittent nature introduces technical challenges causing system instability, potentially requiring a reliable backup power source ([Al-Shetwi, 2022](#)). To that end, the incorporation of energy storage and energy management systems becomes imperative in the integrated system. Notably, the offshore wind sector is undergoing rapid global expansion since it holds the dual promise of decarbonizing electricity and serving as a platform for hydrogen production, thus addressing energy storage needs ([Durakovic et al., 2023](#)). This concept involves generating green hydrogen through electrolysis technology by converting water into hydrogen using surplus renewable energy. The stored hydrogen can then serve as carbon-free fuel for gas turbine units. The utilization of hydrogen and hydrogen-based fuels has gained attention for gas turbines in recent decades and many original equipment manufacturers have shared information regarding the hydrogen compatibility of their engines ([Amin and Fors, 2020](#)), ([Goldmeier, 2019](#)).

Researchers have investigated the feasibility of producing and utilizing green hydrogen on offshore platforms by harnessing available wind power to run an electrolyzer, converting water, readily abundant in offshore fields, into hydrogen ([Dokhani et al., 2023](#)), ([Riboldi et al., 2020](#)). In ([Kumar et al., 2023](#)), the authors offered valuable insights into the symbiotic relationship between the green hydrogen sector and offshore industries. Their analysis of integrating offshore renewable energy systems with O&G sectors revealed the advantages, contributions, and safety considerations of green hydrogen in decarbonizing offshore industries ([Kumar et al., 2023](#)). [Giamperri et al. \(Giamperri et al., 2023\)](#) show that producing green hydrogen from offshore wind could achieve significant cost reduction by 2030 and 2050, making it competitive against grey and blue hydrogen. According to their study,

compressed hydrogen production offshore is the most cost-effective scenario for projects starting in 2025, while alternative strategies like liquefied hydrogen or methylcyclohexane may become more cost-effective for projects beginning in 2050 (Giampieri et al., 2023). Riboldi et al. compared three offshore energy supply models: standard gas turbines, a hybrid GT-wind turbine setup, and a hybrid energy system for offshore integrating GTs, WTs, and hydrogen storage (Riboldi et al., 2020). Results reveal the third approach's potential to notably cut CO<sub>2</sub> emissions (up to 40%) compared to conventional setups, supported by an optimization framework for sustainable offshore energy solutions (Riboldi et al., 2020).

To power offshore rigs sustainably, a hybrid energy system that combines offshore wind power, on-site gas turbines, and power-to-gas storing electrolyzers becomes a necessary solution. Integrating these diverse energy sources and technologies is imperative to transform various offshore drilling and production platforms into integrated energy microgrids (IEMs) that can interact effectively with offshore power plants (Li et al., 2022). The criteria for a microgrid include having a well-defined electrical boundary, a control system for resource management, and a generation capacity exceeding critical load to allow the microgrid to operate independently from the main grid (Li et al., 2020). Implementing smart IEM can optimize the use of diverse energy sources, minimize waste, and improve system reliability for the sustainable development of offshore O&G platforms. These advanced energy management systems facilitate decarbonization efforts, enable remote monitoring, reduce human intervention, and enhance overall safety.

The offshore microgrid concept has been extensively studied (Grainger et al., 2021; Adrian, 2022; Peters et al., 2020; Ventrelli, 2022), with most research concentrating on evaluating the feasibility and analyzing renewable integration in O&G fields. Some studies targeted power balancing for IEM systems and addressed the challenges of assuring power demand satisfaction (Anglani et al., 2020; Yu et al., 2020; Zare et al., 2023; Jing et al., 2022). The literature also addresses the significance of operational strategies and system integration involving offshore wind farms and gas turbines on platforms for achieving emission reductions (Svendsen et al., 2022).

This study goes beyond ensuring power demand and production balance, by introducing a smart energy management system that optimizes asset operation in the microgrid to reduce costs and emissions. Furthermore, the development of an online platform with highly accurate models for optimizing offshore microgrid operation is a novel practice, yet to be conducted as per the authors' knowledge. Additionally, while the concept of offshore microgrids in a theoretical context has been covered in the literature (Panda and Das, 2021), (Zare et al., 2023), (Li et al., 2023) this study delves into a real-world scenario, analyzing an actual case with verifiable data. In line with the challenges posed by hybrid integrated energy systems, the incorporation of advanced optimization techniques and control strategies, as highlighted in (Shezan et al., 2023), could potentially enhance the effectiveness of the proposed smart energy management system.

The paper is organized as follows: first, a description of the offshore platform under study is presented, followed by the methodology for operating the platform conventionally versus using smart management tools. Lastly, the results of the operation in both scenarios are presented for a week of operation, demonstrating the value of using smart management systems for offshore IEMs.

## 2. Case study description

### 2.1. Gullfaks platforms and Hywind Tampen

The Gullfaks O&G field is situated in the Norwegian sector of the North Sea, at a latitude of 61.21 and a longitude of 2.27. The field comprises three platforms - Gullfaks A (GFA), Gullfaks B (GFB), and Gullfaks C (GFC) - all of which were constructed in the 1980s. These platforms serve the dual purpose of drilling and production, as well as

accommodating personnel. Originally, these platforms were designed to operate using gas turbines; however, in line with the goal of reducing carbon emissions, Equinor, the field operator, has initiated a project to source a portion of the power needed for the platforms from a floating wind farm. Hywind Tampen is the first offshore wind farm that provides renewable energy to the offshore O&G field (Tampen - Equinor). The farm is designed to operate at a 125 km distance from the shore.

The floating wind farm consists of a total of 11 wind turbines, each of 8 MW capacity. Out of these 11 turbines, five are specifically allocated to generate power for the Gullfaks field, while the rest are intended to serve the Snorre field, another O&G field in the Norwegian sector of the North Sea (Norwegian Petroleum Directorate Professor Olav Hanssens and vei, 2020). The field operator has provided a visual representation, depicted in Fig. 1, to illustrate the positioning of the Hywind Tampen, Gullfaks, and Snorre fields. The field operator is currently exploring the feasibility of expanding the farm's capacity to 94.6 MW by upgrading the wind turbines.

Through the utilization of this floating wind farm to supply power to the Gullfaks and Snorre fields, it is projected that around 200,000 tons of CO<sub>2</sub> emissions and 1000 tons of NO<sub>x</sub> emissions can be omitted (Tampen - Equinor). Notably, the wind turbines will directly deliver electricity to the offshore oil platforms, without relying on any connections to the land. It is expected that these turbines will meet approximately 30–35% of the total energy demand across the five platforms (Adrian, 2022).

Hywind's design is based on a spar buoy, with a heavy sub-structure and a lighter upper structure to maintain stability. The Siemens SQT 8.0–154 turbine model has been chosen for the farm, featuring a hub height of 95 m, 3 blades with a diameter of 154 m, a nacelle weight of 480 tons, and a floater weight of 10,000 tons. Since Siemens has not disclosed the power curve for this specific model, the power curve for Vestas' V164–8.0 MW turbine was utilized. The relevant data for both Siemens and Vestas turbines are presented in Table 1 below. The similarity between the configuration and the operational parameters of these two models enables the use of operational data of V165–8.0 (available in (Desmond et al., 2016)) as a close estimation of SWT 8.0–154.

All the platforms are equipped with General Electric's LM2500 engines, which is an aero-derivative gas turbine with a power capacity of 22 MW. The GFA platform has four of these gas turbines installed, while the GFC platform has three. Each turbine, except one, on both platforms is equipped with a waste heat recovery unit (WHRU). GFB platform doesn't house any gas turbines and instead receives its required power from GFA through two sea cables, capable of transferring a maximum of 20 MW of power. GFA and GFC are also connected via a cable with the same power transmission limit. To supply power to the Gullfaks field using wind energy, there is a cable that connects the Hywind facility to GFA. Fig. 2 provides a visual representation of the fields and their interconnections.

The energy demand on the platforms encompasses essential needs such as lighting, heating for the accommodation spaces, accommodating 2–300 personnel, as well as computer and control systems responsible for platform management and communication. However, the primary power consumer is the O&G production process itself. Around 70% of the total onboard electrical power is dedicated to fulfilling the energy requirements of the production process consumers (Tangerås and Tveiten, 2018).

### 2.2. Adding storage system

Assuming the installed wind turbines cover 35% of the total demands on the platform, it is expected to reduce the emissions more with further installation of the wind turbines. However, a platform that could solely operate on wind farms is not feasible due to the intermittency of power generation from the wind. Adding a storage system, suitable to the condition and the environment, could mitigate problem. A microgrid serving as an integration of wind turbines, storage systems, and gas turbines could manage the demands of the field with the minimum



Fig. 1. The Hywind Tampen project and its connection to Gullfaks and Snorre fields (“Hywind Tampen approved by Norwegian”), (“Views from the industry”).

**Table 1**  
Comparison of wind turbine models (Tangerås and Tveiten, 2018).

Parameter	Siemens SWT 8.0–154	Vestas V164–8.0
Diameter [m]	154	164
Area [m <sup>2</sup> ]	18627	21124
No. of blades [-]	3	3
Cut-in wind speed [m/s]	3–5	4
Cut-out wind speed [m/s]	25	25
Nominal wind speed [m/s]	13–15	13
Nominal power [MW]	8	8

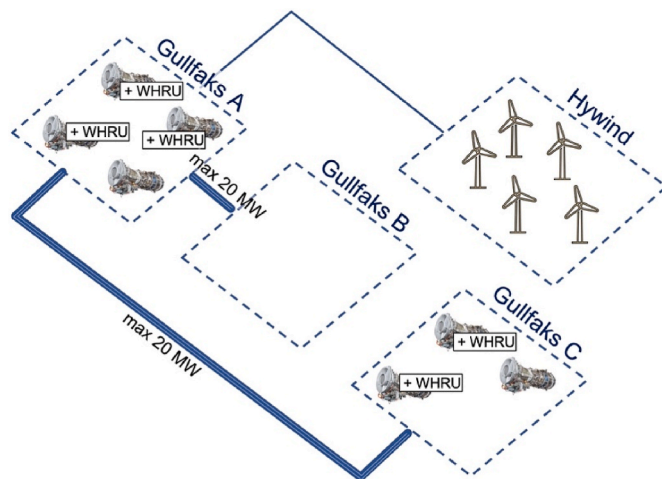


Fig. 2. Schematic view of Gullfaks platforms and Hywind wind farm with their connections.

emissions possible. The end goal is to reduce the operation of gas turbines with fossil fuel gas.

Various studies have extensively explored the feasibility and techno-economic aspects of green hydrogen production and local storage, specifically focusing on harnessing seawater and wind power (Dokhani et al., 2023), (Adrian, 2022). These investigations highlight the low cost associated with water desalination (Dokhani et al., 2023) and emphasized the economic viability of subsea storage of compressed hydrogen as a means to effectively store surplus wind power (Adrian, 2022).

To establish the necessary infrastructure for hydrogen production and storage, key components such as a saltwater desalination facility, feed water storage, electrolyzer, hydrogen compressor, hydrogen storage tanks, and the requisite transmission elements (including pipes and connections) between these components are essential (GREENSTAT). It is envisioned that a platform or floater will be required to accommodate the hydrogen production line, with the storage tanks positioned subsea. At present, the commercial availability of subsea hydrogen storage remains limited. However, ongoing initiatives led by Norwegian companies indicate promising developments in this field, with a focus on pressurized hydrogen tanks supported by a rigid structure capable of storing up to 12 tons of compressed hydrogen (“Hydrogen”).

Given the existing connection of GFA with the wind turbines and the two other platforms (GFB and GFC), GFA serves as a pivotal junction in the microgrid setup. Consequently, it is proposed that the platform or floater be constructed in close proximity to GFA, housing the subsea hydrogen storage tanks. For the planned system, a stack comprising 15 proton exchange membrane electrolyzers, each boasting 6 MW capacity is considered. Relevant data relating to the electrolyzers can be found in (Kopp et al., 2017), while Fig. 3 provides the performance curve for each electrolyzer.

Regarding hydrogen storage, a capacity of 100 tons is deemed economically viable and reliable, as demonstrated by (Adrian, 2022). Occupying approximately 580 m<sup>3</sup> of space on the seabed, the pressurized hydrogen storage will be connected to GFA, facilitating an alternative fuel source for the gas turbines. While all the gas turbines on the platform are of the same model, this study assumes that only one of the turbines will be modified to operate on hydrogen-blended fuel, and the remaining turbines will continue to utilize natural gas as their conventional fuel source.

### 3. Microgrid operation management

For the operation of the Gullfaks field with power productions from Hywind farm, the seven gas turbines installed on GFA and GFC platforms and the electrolyzer and hydrogen storage are considered within a microgrid operation, running in island mode. The wind farm is assumed to increase its capacity to cover 100% of the field’s operation and the storage system and gas turbines will help with mismatches of production and demand. Fig. 4 illustrates the Gullfaks microgrid’s layout. A comprehensive control system oversees all microgrid components and manages their operation. The gas turbines’ power output, the electrolyzer’s power supply, and the hydrogen consumption are determined by the control system, with one of the gas turbines assumed to run with a hydrogen blend. The controller has to assure the balance of the demand and production (both power and heat) at each time step of the operation.

The management system ensures that the combined power output from the gas- and wind turbines adequately meets the power demand of

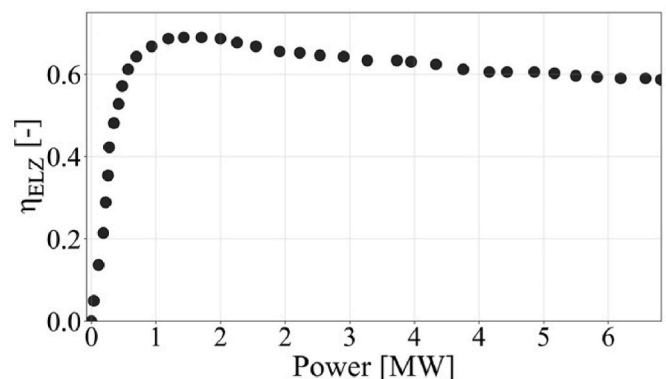


Fig. 3. The efficiency of hydrogen production as a function of the total power consumption of the electrolyzer (Kopp et al., 2017).



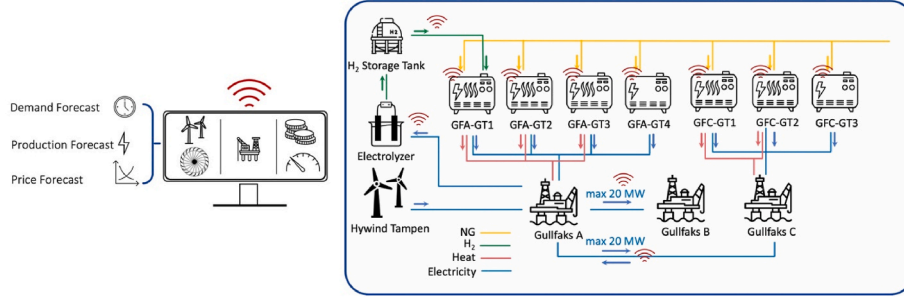


Fig. 4. Schematic diagram of the offshore microgrid and the smart management system.

each platform while also supplying power to the electrolyzer, in case of a surplus. The platforms require power and heat for essential operations and for running accommodations for personnel. The heating requirements of the facilities can be partially met by gas turbines equipped with WHRUs. Additionally, circulating water passes through an electrical heater to further warm it when the heating capacity of the gas turbines is insufficient or unavailable. For instance, on the GFB platform, which lacks a gas turbine, both the power and heat demands are fulfilled by GFA and transferred via a cable, since the heating demand on the GFB platform is addressed by an installed electrical heater.

At each time step, the operation decision made for the controllable units has to satisfy certain constraints regarding the conservation of power, heat, and hydrogen content. To write the energy balance for each platform, GFB could be conducted first as it has minimum connections to other platforms and has no energy production unit on it. The conservation of energy for platform GFB is shown in Eq. (1) to Eq. (3). All of the heat demand of GFB is provided by the electrical heater (Eq. (1)) and the power required to run it is calculated based on its efficiency (Eq. (2)), which is 85%. The power received from platform A should be equal to the demanded power and the power consumed by the electrical heater (Eq. (3)).

$$Q_{ELH\_GFB} - Q_{dem\_GFB} = 0 \quad (1)$$

$$P_{ELH\_GFB} = Q_{ELH\_GFB} / \eta_{ELH\_GFB} \quad (2)$$

$$P_{GFA\_GFB} - P_{dem\_GFB} - P_{ELH\_GFB} = 0 \quad (3)$$

The GFC platform also has a connection to GFA for which the power and heat conservation is written as below, in Eq. (4) to Eq. (6). The heat demands on GFC are met by the two gas turbines with WHRU, along with the utilization of an additional electrical heater on GFC (Eq. (4)). The electrical heater's power is calculated based on its efficiency (Eq. (5)). Finally the power balance of GFC is calculated, balancing the power generated by the gas turbines, the demanded power, the electrical heater's power, and the power transferred between GFA and GFC (Eq. (6)).

$$Q_{GFC\_GT1} + Q_{GFC\_GT2} + Q_{ELH\_GFC} - Q_{dem\_GFC} = 0 \quad (4)$$

$$P_{ELH\_GFC} = Q_{ELH\_GFC} / \eta_{ELH\_GFC} \quad (5)$$

$$P_{GFC\_GT1} + P_{GFC\_GT2} + P_{GFC\_GT3} + P_{GFA\_GFC} - P_{dem\_GFC} - P_{ELH\_GFC} = 0 \quad (6)$$

Lastly, the heat and power balance for GFA is analyzed by Eq. (7) to Eq. (9). The required heat demand is met by the implementation of three gas turbines equipped with WHRU, accompanied by an additional electric heater (Eq. (7)). The power consumption of the electrical heater is computed based on its efficiency (Eq. (8)), which is then integrated into the power balance equation (Eq. (9)). The power balance for GFA encompasses the generated power from the four gas turbines, the power supplied from the wind farm, and the consuming elements, including the electrolyzer's consumption, power transfers to GFB and GFC, as well as the power demand and electrical heater's consumption on the GFA

platform (Eq. (9)).

$$Q_{GFA\_GT1} + Q_{GFA\_GT2} + Q_{GFA\_GT3} + Q_{ELH\_GFA} - Q_{dem\_GFA} = 0 \quad (7)$$

$$P_{ELH\_GFA} = Q_{ELH\_GFA} / \eta_{ELH\_GFA} \quad (8)$$

$$\begin{aligned} P_{GFA\_GT1} + P_{GFA\_GT2} + P_{GFA\_GT3} + P_{GFA\_GT4} + P_{WT} - P_{GFA\_ELZ} - P_{GFA\_GFB} \\ - P_{GFA\_GFC} - P_{dem\_GFA} - P_{ELH\_GFA} \\ = 0 \end{aligned} \quad (9)$$

The power allocated to the electrolysis process ( $P_{GFA\_ELZ}$ ) serves multiple purposes, including water desalination, electrolysis operations, and pressurizing the stored hydrogen (Eq. (10)). To fulfill the desalination requirement of seawater, an energy input of 3.86 kJ per kilogram of seawater is considered (Lim et al., 2021). Additionally, with an adiabatic compression process and a compressor efficiency of 70%, the power consumed by the compressor amounts to 60 kJ per kilogram of hydrogen. Therefore, the complete process necessitates approximately 90 kJ of power for the production of 1 kg of hydrogen, which is obtained from 9 kg of seawater.

$$P_{GFA\_ELZ} = P_{ELZ} + P_{ds} + P_{comp} \quad (10)$$

An important aspect to consider is that the power transmission between GFA and GFC ( $P_{GFA\_GFC}$ ) is prone to power waste, due to the approximately 6 km distance between the platforms. While transmission in both directions is possible, around 0.11 MW are considered to be wasted for every megawatt of power leaving the platform. Therefore, when modeling and exploring different operation scenarios, special attention must be given to the direction of power transferred between GFA and GFC, as well as the value of the power term involved in the power balance of each platform. The power transferred from GFA to GFB ( $P_{GFA\_GFB}$ ), is also prone to 5.4% of waste due to the approximately 3 km distance between them. However, this power transfers in one direction, making it simpler to implement in the equations.

In addition to power and heat conservation, hydrogen conservation is also a critical consideration. Ensuring an adequate fuel supply for the gas turbines at the beginning of each time step is essential. Specifically, for GFA-GT1, the availability of hydrogen in the tank is crucial. Thus, the hydrogen required for consumption at each time step, denoted as  $t_i$ , must be less than the tank value accumulated from the initial condition to time step  $t_i$ . This constraint is represented by Eq. (11).

$$(m_{H_2, GFA-GT1})_{t_i} < (M_{HyT})_{t_0} + \sum_{t_0}^{t_i} M_{H_2, produced} - M_{H_2, consumed} \quad (11)$$

Ensuring heat and power conservation on each platform within the field is a constant requirement that must be met. However, variables such as the power output of gas turbines, the levels of hydrogen production and consumption, and the power transmission between platforms can fluctuate. These operational choices inherently lead to varying costs and emissions. There are two approaches to managing the operation:

- To follow certain rules which assure the balance of demand and production. This approach is called “condition-based”. At each time step, the demands (power and heat on each of the three platforms) are declared and the wind power is determined. According to the condition, a decision is made to control the microgrid’s operation.
- To predict the demands and renewable production ahead of time, and optimize the microgrid operation based on the forecasts. This approach is called “optimization”, which searches for the best operational solution with minimum costs and emissions while assuring the demands are met.

In this study, both operation scenarios are thoroughly investigated and discussed. It is important to note that the condition-based operation does not involve optimization or forecasting tools; yet, decisions are based on a set of rules which aims to minimize costs as much as possible. This aspect is crucial to ensure a fair comparison with the optimizer’s performance, as it would be unfair to compare it with an operator that does not make the best economical decision at each time step. The research demonstrates how the intelligent management system, i.e., the optimizer operation, can further enhance the overall operation compared to the already economical condition-based operation.

### 3.1. Scenario 1: condition-based operation

In this scenario, the Gullfaks microgrid follows a set of predefined rules to manage the assets. These rules provide immediate guidelines for operation based on real-time demand and the power generated by the wind turbine. The rules are designed with the following principles in mind:

- Platforms equipped with gas turbines (GFA and GFC) prioritize local power production over receiving power from connecting platforms. This approach minimizes unnecessary power transportation, which can lead to transmission losses.
- Each platform aims to minimize the number of gas turbines operating simultaneously. If the power demand of a platform can be met by two

gas turbines instead of three, the two engines will operate at a higher load. This decision is driven by the fact that higher loads result in increased engine efficiency (Brenntrø, 2016).

- When multiple engines are required to meet the demand of a platform, the load is distributed equally among them to ensure balanced operation.
- The heat demand of the platforms is primarily fulfilled by the heat generated by the gas turbines. Utilizing the excess heat from gas turbines is more economical than using additional power for electrical heaters. In cases where the heating capacity is insufficient, an electrical heater is utilized to supplement the heat supply.
- The electrolyzer is only supplied with power if the power generated by the wind turbine exceeds the combined demand of platforms GFA and GFB. This ensures that excess renewable power is utilized for hydrogen production.
- If hydrogen is available, its consumption takes priority, limited to the availability of hydrogen reserves.

According to these principles, the condition-based operation will be pursued by calculating the power required to be delivered to platform GFB (Eq. (1) to Eq. (3)). Afterwards, calculations for GFC are considered by following the flowchart (a) in Fig. 5. From GFC’s operation, the power output of each GFC gas turbine is determined, as well as the value of power transfer between GFC and GFA. Lastly, the decision for the GFA platform’s gas turbine power and the power allocated for the electrolyzer is determined according to the flowchart (b) in Fig. 5.

The flowcharts are strategically designed to adhere to economic efficiency rules. The number of gas turbines involved is determined by both the heat demand ( $N_{GTQ}$ ) and the power demand ( $N_{GTP}$ ). The electrical heater is utilized only if the gas turbines cannot meet the requirements adequately. Referring to diagram (a) in Fig. 5, GFC requests power from GFA only when all gas turbines are unable to fulfill the demands. Similarly, the same principles are applied to GFA (diagram (b) in Fig. 5), with an additional condition involving the electrolyzers’ power, which is determined by comparing wind power to the aggregated demand on GFA.

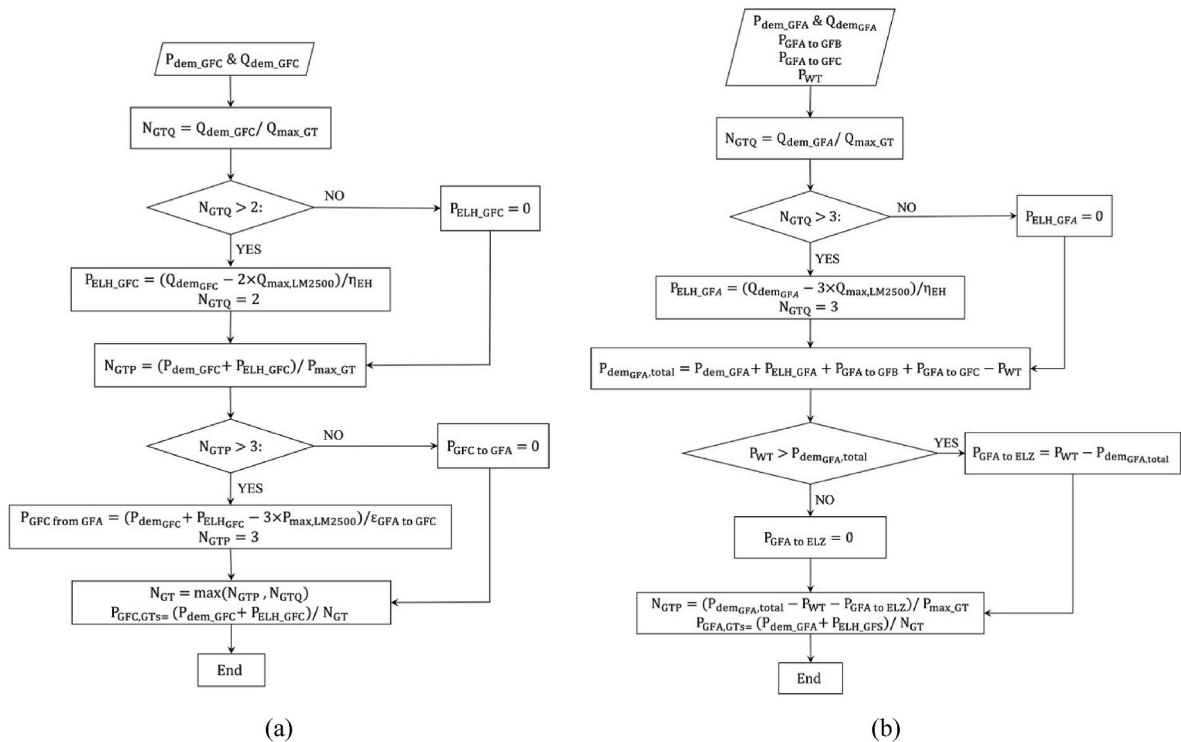


Fig. 5. Condition-based operation flowchart, (a) GFC operation, (b) GFA operation.

### 3.2. Scenario 2: optimization

While the condition-based operation excels in providing the best economically efficient decisions at each time step, leveraging optimization offers significant untapped potential in making energy management decisions over an extended time span. By incorporating an optimization code, the microgrid gains predictive capabilities, allowing it to anticipate future conditions, such as wind availability, and strategically plan its energy usage. For instance, the optimization code can intelligently choose to store excess energy during periods of high wind generation, ensuring a reserve for times when wind resources may be limited. This proactive approach optimizes energy storage and utilization, maximizing the utilization of renewable resources and minimizing reliance on conventional energy sources during adverse conditions. Consequently, the integration of predictive optimization empowers the microgrid to make well-informed, forward-looking decisions, resulting in enhanced overall performance and economic efficiency.

Another compelling advantage of the optimizer lies in its ability to manage the entire microgrid integration comprehensively. While the condition-based approach is confined to managing each platform separately according to predefined rules, the optimizer can holistically consider all assets, resources, and demands within the system. This increased freedom allows the optimizer to explore a wide range of possibilities and optimize the complex interplay of various components. However, this versatility also adds to the complexity of the optimization problem.

The optimization process involves testing numerous options and scenarios for running the microgrid over the given time span. Each scenario satisfies the energy balance requirements, but different costs and emissions are associated with each alternative. The iterative nature of the procedure enables the optimizer to continuously refine its approach, and ultimately identify the best solution that optimizes cost, efficiency, and emissions.

#### 3.2.1. Digital twin of the microgrid

The optimizer relies on both precise predictions and high-speed processing to explore different scenarios effectively. To achieve this, the implementation of Artificial Intelligence (AI) techniques is essential in creating robust forecasting modules that anticipate changes in wind availability, demand patterns, and other dynamic factors. Moreover, the optimizer requires fast-responding models or “digital twins” of microgrid subsystems, and in the case of subsystems with nonlinear behavior, such as gas turbines and wind turbines, Artificial Neural Networks (ANNs) are utilized.

The use of ANN models allows for processing data, predicting system behavior, and capturing complex patterns through hidden layers, enabling accurate representations of the subsystems’ dynamics. A Bayesian technique is utilized to tune the hyperparameters of the ANN models, employing Gaussian process models (Wu et al., 2019). The training of ANNs for gas turbines and wind turbines is conducted using the backpropagation algorithm, with 80% of the data allocated for cross-validation and the remaining 20% for testing. Detailed information on the hyperparameters and models’ inputs and outputs can be found in Table 2 and Table 3, respectively. Additionally, for the electrolyzer, a polynomial regression is applied to fit the efficiency curve shown in Fig. 3, while the hydrogen flow rate is calculated using Eq. (12).

**Table 2**  
Subsystem models inputs and output.

Subsystem	Input parameters	Output parameters
Gas turbine	$P_{MGT,dem}, FR, T_{amb}$	$\dot{m}_f$
Wind turbine	$T_{amb}, P_{amb}, S_w, D_w$	$P_{WT}$
Electrolyzer	$P_{ELZ}$	$\dot{m}_{H_2}$

$$\dot{m}_{H_2} = \eta_{ELZ} \times \frac{P_{ELZ}}{LHV_{H_2}} \quad (12)$$

The gas turbine models used in this study were developed based on real data, obtained from operating the LM2500 gas turbine with natural gas on an offshore platform. To create a model capable of predicting gas turbine operation with blends of natural gas and hydrogen, the models were fine-tuned and adjusted slightly using insights from the results presented in (Stuen, 2021), which investigated the impact of hydrogen fuel on LM2500 engines.

The accuracy of the models is evaluated by calculating maximum absolute error (MAE), mean absolute error (MAE), and mean absolute percentage error (MAPE) as defined in Eqs. (13) and (14). In the equations,  $X_{act}$  and  $X_{pred}$  are the actual values and predicted values from the model and  $n$  is the number of data in the test set. The errors are reported in Table 4.

$$MAE = \frac{1}{n} \sum_{i=1}^n |X_{pred} - X_{act}| \quad (13)$$

$$MAPE = \frac{1}{n} \sum_{i=1}^n \left| \frac{X_{pred} - X_{act}}{X_{act}} \right| \quad (14)$$

The gas turbine and wind turbine’s model prediction in comparison to real operation data is visualized in Fig. 6. The model takes into careful consideration the NOx emissions of the gas turbines.

### 3.3. Optimization parameters and objective function

In addressing the current challenge, the optimization process must accomplish multiple tasks, including identifying power set-points for all gas turbines, determining the hydrogen/natural gas blend for GFA-GT1, and deciding on the power input to the electrolyzer. To optimize the microgrid’s operation, a day of operation is considered to be the optimization window, and the smart management system must conduct the optimization ahead of this time span. The management system operates at a time step of 1 h, necessitating it to make decisions for the dispatchable units (gas turbines and electrolyzer) every hour, summing up to a total of 216 parameters ( $9 \times 24$  h). These parameters must be carefully established to optimize the microgrid’s performance. Each parameter is bound by defined upper and lower limits based on its specific physical characteristics.

The gas turbines’ power setpoint is constrained within the range of 9–22 MW, as defined in Eq. (15). Additionally, the hydrogen/natural gas blend for the GFA-GT1 engine is subject to a limitation, considering that the LM2500 gas turbine can tolerate a maximum hydrogen volume of 75%. These bounds are incorporated into the model through the fuel heating value ratio (FHR), defined in Eq. (16). With a lower heating value of 12.7 MJ/m<sup>3</sup> for hydrogen and 40.6 MJ/m<sup>3</sup> for methane, the engine’s acceptable minimum FHR is determined to be 0.516 (Eq. (17)). Furthermore, the power allocated to the electrolyzer is restricted by its capacity to ensure it does not exceed its operational limit (90 MW), as outlined in Eq. (18).

$$P_{GT} = [P_{GT,1}, P_{GT,2}, \dots, P_{GT,24}], P_{GT,min} < P_{GT,i} < P_{GT,max} \quad (15)$$

$$FHR_{GT} = (\dot{m}_{NG} \times LHV_{NG}) / (\dot{m}_{NG} \times LHV_{NG} + \dot{m}_{H_2} \times LHV_{H_2}) \quad (16)$$

$$FHR_{GT} = [FHR_{GT,1}, FHR_{GT,2}, \dots, FHR_{GT,24}], 0.516 < FHR_{GT,i} < 1 \quad (17)$$

$$P_{GFA\_to\_ELZ} = [P_{GFA_{toELZ,1}}, P_{GFA_{toELZ,2}}, \dots, P_{GFA_{toELZ,24}}], 0 < P_{GFA\_to\_ELZ,i} < P_{GFA\_to\_ELZ,max} \quad (18)$$

The primary objective of the optimization process is to minimize the total cost of operation, which encompasses various factors (Eq. (19)). These factors include the cost of purchasing natural gas ( $C_{NG}$ ), the taxes

**Table 3**

ANN models optimized configuration.

Subsystem	No. of neurons, layer 1	No. of neurons, layer 2	No. of neurons, layer 3	AF, layer 1	AF, layer 2	AF, layer 3	LR
Gas turbine	42	17	–	sigmoid	ReLU	–	0.72
Wind turbine	45	100	22	SELU	ReLU	linear	0.57

**Table 4**

Models prediction error.

Subsystem	mAE	MAE	MAPE
Gas turbine	0.017 [kg/s]	0.004 [kg/s]	0.21%
Wind turbine	0.801 [MW]	0.152 [MW]	0.61%
Electrolyzer	1.6e-5 [kg/s]	1.2e-5 [kg/s]	0.05%

associated with CO<sub>2</sub> and NO<sub>x</sub> emissions ( $C_{NG,tax}$  and  $C_{NOx,tax}$ ), as well as the maintenance costs related to the gas turbines and electrolyzation components ( $C_{MGT}$  and  $C_{ELZ}$ ).

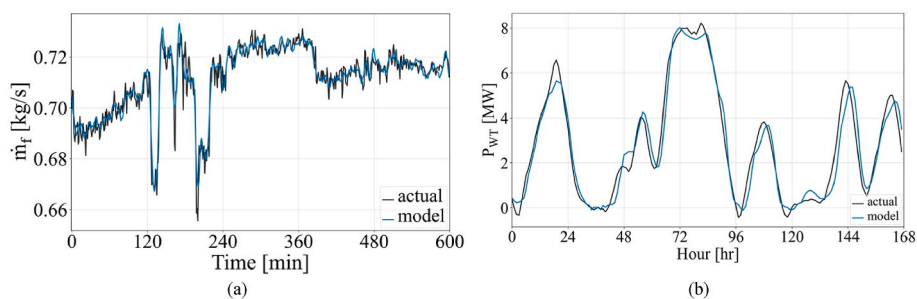
$$C_{total} = C_{NG} + C_{NG,tax} + C_{NOx,tax} + C_{MGT} + C_{ELZ} \quad (19)$$

The first two terms of the total cost equation (Eq. (19)) are determined based on the total amount of natural gas consumed by all 7 gas turbines throughout the optimization day. The cost of purchasing natural gas ( $C_{NG}$ ) is calculated using the daily fuel price. The term  $C_{NG,tax}$  represents the specific tax imposed by the Norwegian government on natural gas to regulate CO<sub>2</sub> emissions. For the petroleum industry, the tax value in 2022 amounted to 1.65 NOK (about 0.16 EUR) per standard cubic meter of natural gas consumed (“Tax rates in Norway”).

The tax for NO<sub>x</sub> emissions ( $C_{NOx,tax}$ ) is computed based on the NO<sub>x</sub> emitted from the engines, which is calculated using the power output of each engine at each time step. A correlation between NO<sub>x</sub> emissions and power output is established, fitted to real data presented in Fig. 7, derived from measurements obtained from the actual engine and reported in (Sundsbo Alne, 2007). The value of tax for NO<sub>x</sub> emissions was 23.79 NOK (about 2.36 EUR) per kilogram of emission in 2022 (“Tax rates in Norway”). Additionally, the maintenance cost of the gas turbines, electrolyzer, compressor, and water desalination system is computed using the values reported in (Tilocca et al., 2023).

The optimization process primarily aims to reduce the calculated cost, but an additional factor must be considered in the objective function and that is the preservation of hydrogen in the tank. Focusing solely on cost reduction would lead the optimization algorithm to prioritize immediate hydrogen consumption, disregarding its potential future value when wind power is limited. To address this issue, it becomes crucial to incentivize the preservation of hydrogen at the end of each day.

Optimizing for a limited time span means that the optimizer’s vision is confined to that specific window, and it cannot anticipate future needs beyond that period. Consequently, it may use the stored hydrogen at early time steps, potentially missing the opportunity to benefit from it in subsequent optimization windows. To counteract this, it is essential to encourage the preservation of hydrogen for future utilization.

**Fig. 6.** Visualization of ANN models’ accuracy, (a) gas turbine, (b) wind turbine.

This incentive is essential irrespective of the optimization window’s duration, as it accounts for an unpredictable future following any finite period of optimization. To calculate this incentive, an estimation of the saved hydrogen’s value for the next day is necessary, as it can offset natural gas costs, including both price and tax. The incentive for preserving hydrogen is determined using Eq. (20).

$$Inc_{HyT} = m_{HyT} \times \frac{LHV_{H_2}}{LHV_{NG}} \times (C_{NG} + C_{NG,tax}) \quad (20)$$

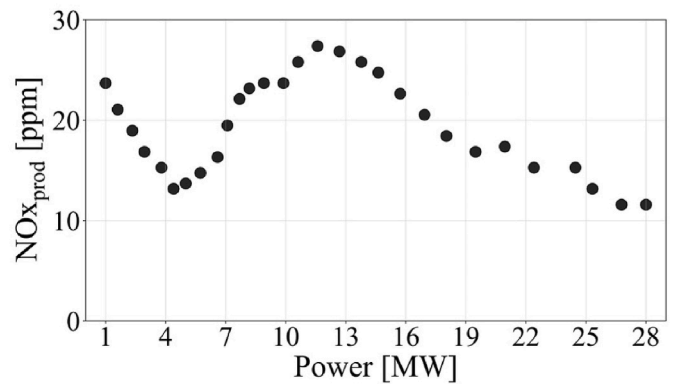
Consequently, the objective value to be reduced by the optimizer will become as stated in Eq. (21):

$$OV = C_{total} - Inc_{HyT} \quad (21)$$

### 3.3.1. Hybrid optimization approach

Optimizing the power setpoints for each gas turbine and the electrolyzer can lead to significantly long computational times due to a large number of optimization parameters ( $9 \times 24$  parameters for each day). Additionally, the consideration of constraints (Eq. (1) to Eq. (11)) further adds to the duration of optimization. Notably, the hydrogen fuel conservation constraint (Eq. (11)) introduces complexity to the problem due to its nature.

This constraint ensures that the hydrogen consumption at each time step “i” (dependent on  $P_{GFA-GT1,i}$  and  $FHR_i$ ) must not exceed the amount available in the tank. However, the tank’s content is influenced by both the hydrogen produced (dependent on  $P_{GFA-to-ELZ}$ ) up to that time step and the hydrogen consumed (dependent on  $P_{GFA-GT1}$  and  $FHR$ ) up to

**Fig. 7.** NO<sub>x</sub> production at different power outputs of LM2500 (Sundsbo Alne, 2007).



that time step. These quantities are also optimization parameters, making the constraint interrelated with the optimization parameters, resulting in intricacies within the optimization process. The constraint is shown in Eq. (22) below:

for  $1 \leq i \leq 24$ :

$$\psi(FHR_1, FHR_2, \dots, FHR_i, P_{GFA-GT1,1}, P_{GFA-GT1,2}, \dots, P_{GFA-GT1,i}, P_{GFA-10-ELZ,1}, P_{GFA-10-ELZ,2}, \dots, P_{GFA-10-ELZ,i-1}) \leq 0 \quad (22)$$

To overcome the complications of the optimization, a novel hybrid approach is proposed to enhance the optimization process while ensuring compliance with constraints. The approach involves prioritizing the optimization of power balance for each platform, rather than focusing solely on optimizing individual components such as gas turbines and the electrolyzer. The optimizer first determines the most favorable power transfer values between GFA and GFC, as well as between GFA and ELZ, to achieve an optimized power balance across the system. Subsequently, the optimal operation of gas turbines on each platform is determined in the next step. This decision for each platform is based on the power balance requirements derived from the platform's demand and the power transfers identified in the preceding step.

Therefore, the optimization algorithm is structured into two levels: the field optimization level (outer optimization loop) and the platform optimization level (inner loop). At the field optimization level, the focus is on searching for the optimum power transfer values. Once these values are set, the platform optimization level takes over to optimize the operation of the gas turbines based on the power balance requirements.

By breaking down the optimization process into two levels, the number of optimization parameters is reduced. This reduction mitigates the challenges associated with the curse of dimensionality. Additionally, the constraints of power balance are imposed between the two optimization levels, ensuring a stable and reliable system operation.

The outer loop optimization, which plays a critical role in the

process, utilizes Genetic Algorithm (GA) for efficient decision-making. For platform optimization (the inner loop), a simplified approach is employed to reduce computational costs. Prior to optimization, a comprehensive database of platform operations is prepared, encompassing all possible combinations of engine operation within the platform. The platform optimizer's task is to search through this database and identify combinations that meet the power and heat demand requirements. From these combinations, the optimizer selects the one with the lowest cost among the available choices. The optimization process flowchart is depicted in Fig. 8, providing an overview of the optimizer's operation. As it is depicted, within the GA optimization loop, the optimizer determines the power flow of transmission cables and the fuel heating value ratio of GT1 on GFA.

In the next step, the net power imposed on each platform is calculated based on the demand of the platform and the transferred values defined by the level 1 optimizer. Subsequently, the optimization of platforms A and C is carried out based on the net power and heat demand of the platform. The optimizer selects rows from the database that closely align with the boundary conditions for heat and power output. From these rows, the optimizer chooses the solution with the minimum cost.

The proposed hybrid optimization approach results in a much faster optimization process. The platform optimization (inner loop, level 2) is a table look-up and filtering process, which consumes minimal time. Most of the optimization duration is attributed to field optimization, which involves only 72 ( $3 \times 24$ ) parameters. By reducing the number of optimizing parameters, the method significantly increases the speed of optimization. Within just 1 h of running the optimization, the proposed approach provides the optimized answer. This reduction in computational time allows for more rapid decision-making and real-time adjustments to achieve optimal power balance and platform operations in the offshore microgrid.

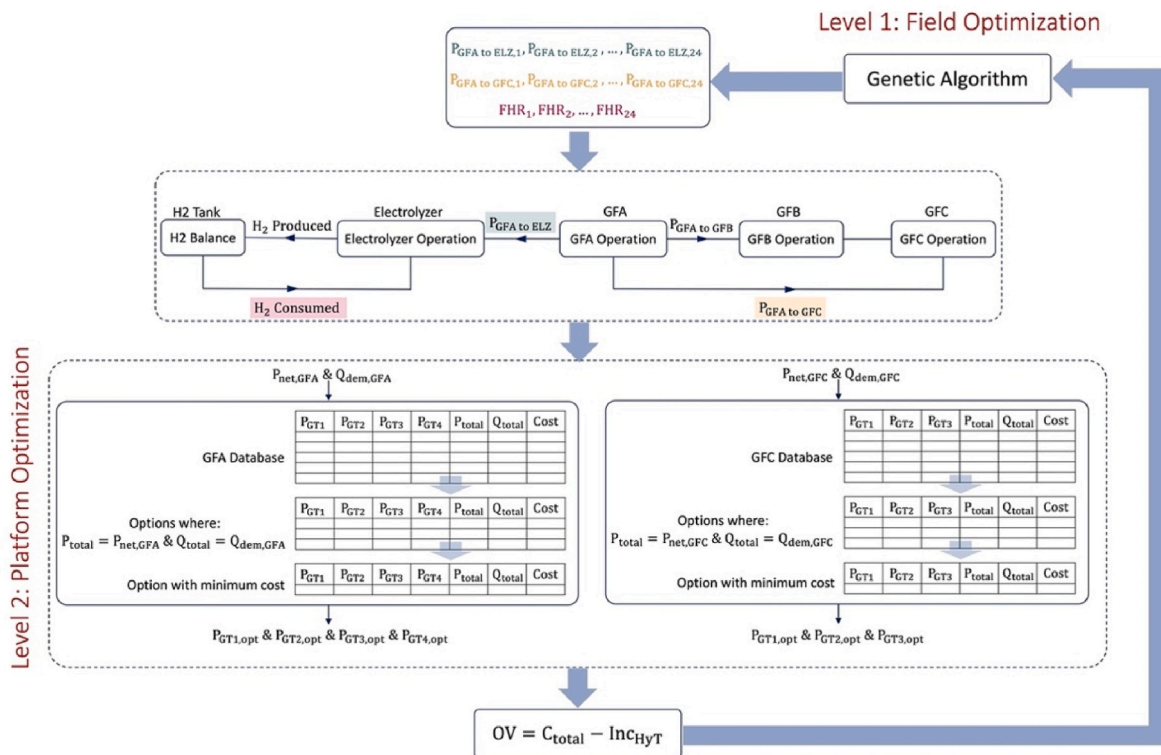


Fig. 8. The new optimization approach; the outer loop is responsible for power flow in connection cables and fuel ratio, and the inner loop optimizes the platforms' operation.



#### 4. Results and discussion

The integrated microgrid of Gullfaks field and Hywind Tampen, along with the electrolyzer, is simulated to evaluate its operation for a week-long period from 24/01/2022 to 30/01/2022. The simulation includes both condition-based and optimization approaches to assess the benefits of employing an optimizer in the process. While the condition-based approach provides immediate decisions for each time step during operation, the optimizer requires pre-planning and provides decisions in advance within a designated optimization window. In this study, the optimization window spans a day, and the time step is set at 1 h, allowing for hourly variations in operational decisions.

The utilization of the optimizer necessitates the use of forecast data instead of actual data prior to the operation. Weather data plays a critical role in estimating the power output from wind farms and serves as an input for the gas turbine model. In this study, weather forecasts were obtained from the Norwegian Meteorological Institute (Norwegian Meteorological Institute, 2022), which provides updates every 6 h. Specifically, the forecast data utilized in this research was collected from the 6 p.m. update the day before. Both the forecast data employed for optimization and the actual weather data used in the condition-based operation are depicted in Fig. 9. Fig. 10 illustrates the wind power calculated by the wind turbine model based on both the actual weather data and the forecasted data.

To optimize the microgrid, accurate knowledge of the platforms' demand patterns is crucial. However, due to the unavailability of detailed demand data and historical records for the Gullfaks platforms, only average values and common variations are accessible (Tangerås and Tveiten, 2018). As a result, constructing a demand model and providing precise forecasts based on historical data and weather information becomes infeasible. Nevertheless, previous studies in demand prediction have shown promising results, achieving a mean absolute error of less than 5% (Tan et al., 2019). In this study, the demand patterns are generated based on the available information from (Tangerås and Tveiten, 2018), utilizing random distributions. Fig. 11 presents the demand profiles for the three platforms. The power demand distribution is generated using a random distribution, incorporating specific values for the average, minimum, and maximum values collected from (Tangerås and Tveiten, 2018). A similar approach is applied for the heat distribution, but with a sequential pattern that aligns more closely with the platform's heating demands. The criteria employed for demand data generation are reported in Table 5.

The forecasted demand is adjusted using randomly distributed error values, with a maximum deviation of 7% and a mean of 5%. It is important to note that the literature suggests achieving demand predictions with a maximum error of 5% for O&G platforms (Tan et al., 2019). However, in this work, a deliberately higher error margin is considered to ensure a conservative approach.

Over the course of the week, the combined power demand from the

three platforms amounts to 59,203 GJ, while the total heat demand is 11,969 GJ. The power generated by the wind farm during this period is 55,373 GJ, resulting in a shortfall of 3830 GJ to meet the power demand or 15,799 GJ when considering both heat and power requirements. The deviation of wind power from the total power demand is visualized in Fig. 12. Notably, there are three distinct time periods with low wind power generation, indicating a need for increased participation of gas turbines in the operation during those intervals. For the remaining duration of the week, the wind power aligns relatively closely with the total power demand, although occasional surpluses and deficiencies are observed.

The simulation started with an empty hydrogen tank at the beginning of the week. In the condition-based approach, each time step (1 h) throughout the week was analyzed hence the flowcharts shown in Fig. 5 were conducted  $7 \times 24$  times. The optimization process, on the other hand, was run seven times, with each run taking approximately 1 h to complete. The condition-based operation was carried out using actual data at each hour, while the optimizer was employed one day ahead of the actual day of operation, utilizing forecasted data. A visual comparison of these two approaches is provided in Fig. 13.

It is important to highlight that although the optimizer in this study utilized forecast data to conduct the optimization process, the evaluation of its performance is conducted based on real data to mirror real-life applications. In practical use, the optimizer relies on forecasts to generate an efficient schedule, but its true value lies in how well this schedule performs on the actual day when the real wind power or demands arises. Therefore, accurate forecasts and models are crucial to achieve optimal performance from the optimizer. Otherwise, the deviation between forecasted and real data may significantly impact the optimizer's efficiency. In the current study, the optimized schedule resulted in low costs, which slightly increased when real values were employed on real data which was due to forecast errors when compared to actual data.

The total power generated by all the gas turbines is presented in Fig. 14. As depicted, the optimizer successfully managed to operate the gas turbines with considerably less power compared to the condition-based approach. However, there were three time spans where the power production of the gas turbines was nearly the same for both scenarios. These time spans coincided with periods of wind power deficiencies (Fig. 12).

Figs. 15 and 16 provide the total power produced by each platform. The analysis of Figs. 15 and 16 highlights interesting observations regarding the gas turbine performance in the optimized and condition-based scenarios. Notably, GFA demonstrates slightly higher power output from the gas turbines in the optimized scenario compared to the condition-based scenario, while the opposite trend is observed for GFC.

In both scenarios, the gas turbine production in GFA remains below the total demand, primarily because wind power contributes to fulfilling a portion of the demand. This relationship is supported by the three

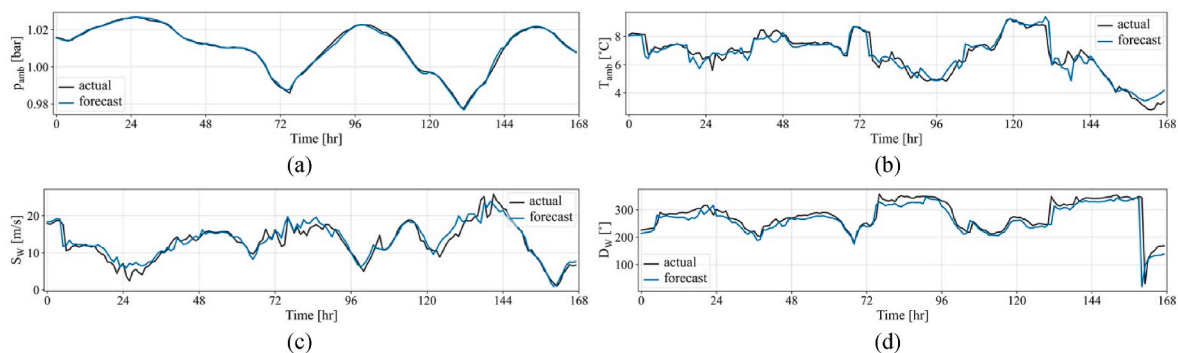


Fig. 9. Weather data and forecasts compared to real data, (a) ambient pressure, (b) ambient temperature, (c) wind speed, and (d) wind direction. The data is downloaded from (Norwegian Meteorological Institute, 2022).

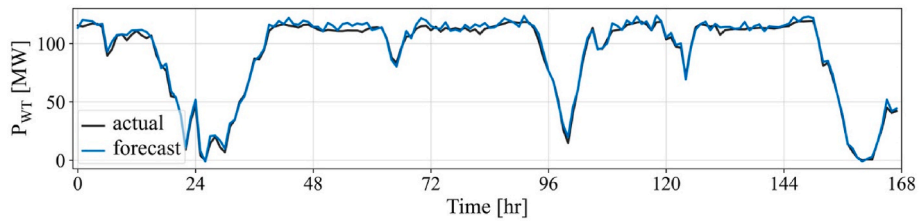


Fig. 10. Wind farm power production is calculated based on actual weather data as well as weather forecasts.

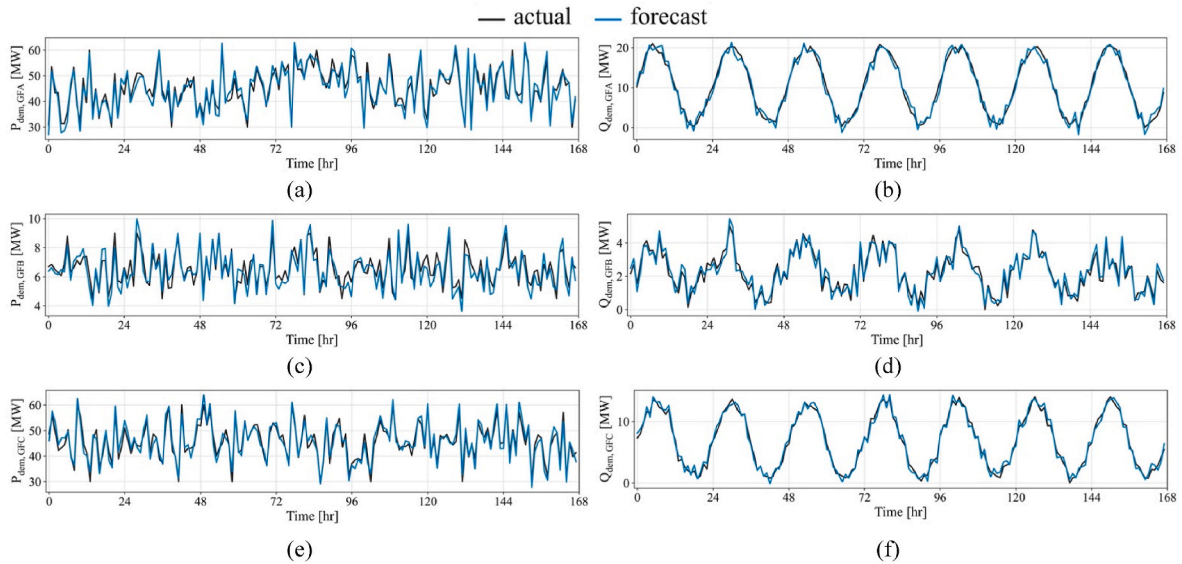


Fig. 11. Demand patterns and predictions for Gullfaks platforms, (a) demand power on GFA, (b) demand heat on GFA, (c) demand power on GFB, (d) demand heat on GFB, (e) demand power on GFC, and (f) demand heat on GFC.

Table 5  
Models prediction error.

Platform	Power			Heat		
	max [MW]	mean [MW]	min [MW]	max [MW]	mean [MW]	min [MW]
GFA	60	36	30	21	15	0
GFB	9	5.4	4	5	2	0
GFC	60	36	30	14	10	0

instances of increased gas turbine production shown in Fig. 15, where the production of gas turbines reaches the demand values during periods of low wind power.

Conversely, in GFC, the gas turbines' production closely matches the demand in the condition-based scenario, but the optimized operation falls short of meeting the demand (Fig. 16). Examining Fig. 17 reveals that the optimizer opted to direct power from GFA to GFC in order to compensate for the shortfall. In other words, the optimizer decided to compensate for the GFC demand partly from its gas turbines, and partly

by getting power from GFA. On GFA however, the power produced by gas turbines was more or less similar in the condition-based and optimization scenario. Therefore the power transmitted to GFC from GFA was not attributed to GFA gas turbines, but might be from the wind power. Fig. 17 can reveal the source of the power transmitted from GFA to GFC. This allocation pattern aligns with the variations in wind power, indicating that a portion of the wind power delivered to GFA is redirected to GFC in the optimized scenario. It could be seen that the power transmission from GFA to GFC during times of low wind power in the optimized scenario has been decreased in comparison to other times.

As mentioned earlier, power transmission between GFA and GFC is possible in both directions. The occurrences of power transfer from GFC to GFA seldom times, as indicated in Fig. 18, align with the times of deficiency in wind power production, which is expected.

Notably, for the condition-based operation, the power transmission option is used only if the gas turbines on the platform are incapable of meeting the demand (flowchart in Fig. 5), which is not the case in this study and therefore zero power transmissions for condition-based operation is shown in Figs. 17 and 18. However, the optimizer

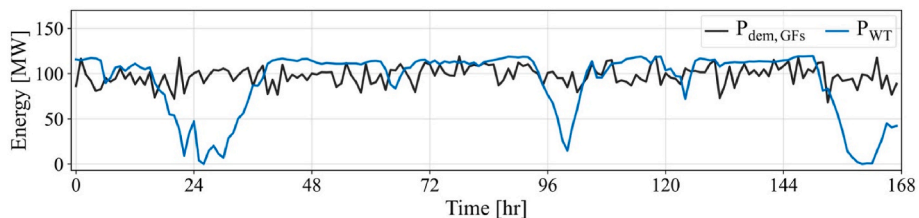


Fig. 12. Total power demand from three Gullfaks platforms vs. the power generated by the wind farm.

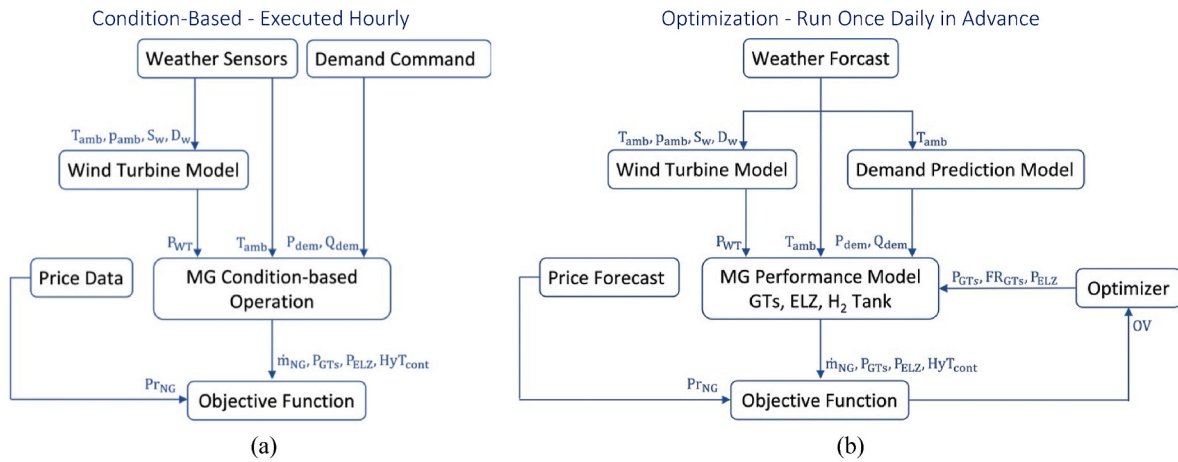


Fig. 13. The process of control and management of the microgrid and the data transfer; (a) condition-based and (b) optimization.

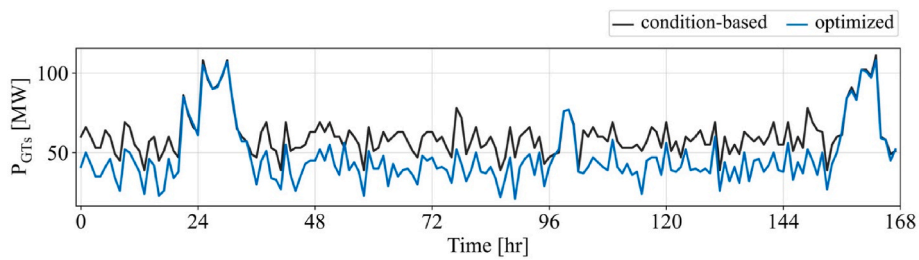


Fig. 14. The total power produced by the seven gas turbines on the three Gullfaks platforms.

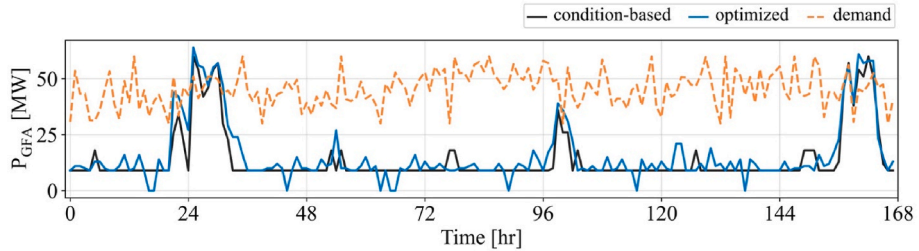


Fig. 15. The total power produced by the four gas turbines on the GFA platform.

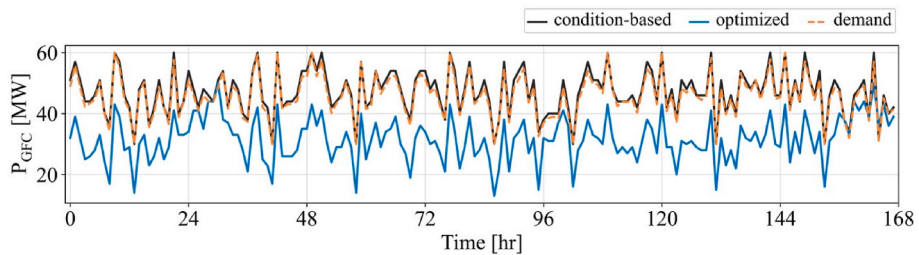


Fig. 16. The total power produced by the three gas turbines on the GFC platform.

discovers that it is more efficient to transfer power from other platforms rather than running the gas turbines on its own platform, as demonstrated in the optimized scenario in these figures.

In the optimized scenario, it was observed that the gas turbines produced less power compared to the condition-based operation. Instead, the optimized scenario utilized a greater proportion of wind power to meet the demands of the platforms. This naturally raises the question of what happens to the surplus power generated in the

condition-based operation. The only plausible explanation is that it is stored through the allocation of power to water electrolysis and hydrogen production. The rates of hydrogen production and consumption for both scenarios are illustrated in Figs. 19 and 20, respectively, and the amount of hydrogen available in the tank is shown in Fig. 21. The data clearly indicates that the condition-based operation achieves greater energy savings, whereas the optimizer primarily utilizes energy during the optimization window.

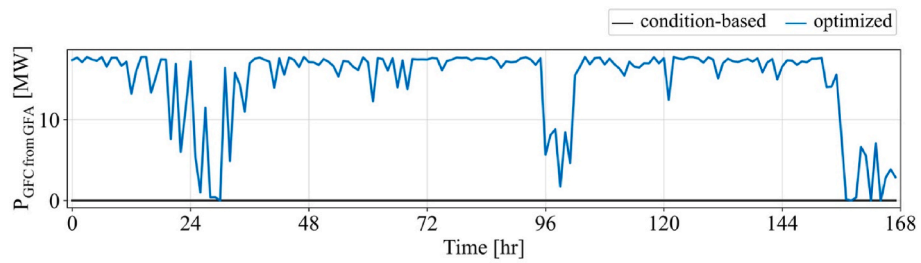


Fig. 17. The power received by GFC from GFA.

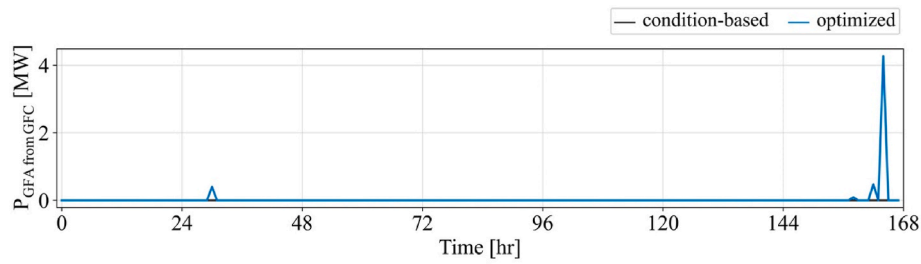


Fig. 18. The power received by GFA from GFC.

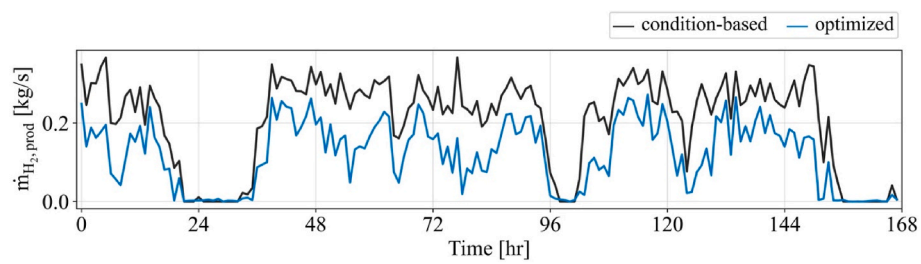


Fig. 19. The rate of hydrogen production.

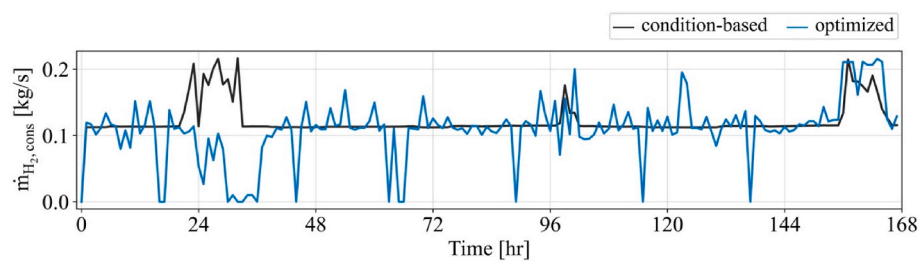


Fig. 20. The rate of hydrogen consumption.

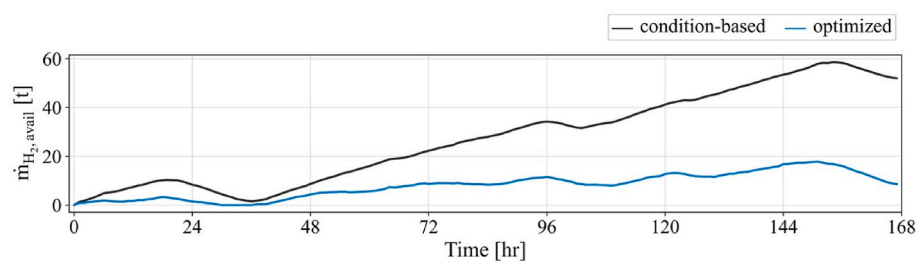


Fig. 21. Hydrogen fuel availability over the week.



Examining the consumption pattern in Fig. 20 reveals distinct differences between the condition-based and optimized operations. The condition-based scenario exhibits a consistent pattern of hydrogen consumption, with mostly constant values, but higher consumption during periods of wind deficiency. On the contrary, the optimized scenario shows more variability in hydrogen usage. Understanding the optimizer's decision-making process for hydrogen usage is challenging, as it depends not only on the tank's available quantity but also considers its impact on the cost of the current and subsequent optimization windows, as previously discussed and implemented through the hydrogen saving incentive (Eq. (20)). Never the less, it is evident from Fig. 21 that the rate of filling the hydrogen tank in condition-based operation is considerably higher than the optimization.

An overview of the total hydrogen balance for both scenarios is presented in Table 6. The relative difference reported in the tables is calculated according to Eq. (23).

$$X_{\text{rel diff}} = (X_{\text{optimized}} - X_{\text{condition-based}}) / X_{\text{condition-based}} \times 100 \quad (23)$$

Although conducting a direct hourly comparison between the condition-based operation and the optimized scenario is complex, certain observations have become evident. The condition-based approach prioritizes saving more energy and transferring less between platforms, while the optimized scenario takes the opposite approach. It should be noted, as depicted in Fig. 3, that the maximum energy-saving efficiency cannot exceed 70%. However, when power is transmitted between GFA and GFC, only 11% of the energy is wasted. Consequently, the optimizer takes advantage of this option and efficiently manages the platforms through an integrated approach. In contrast, the condition-based operation adopts a more localized approach, with power transmission between platforms occurring only when necessary. An overview of the costs, emissions, and fuel consumption for both scenarios is reported in Table 7.

The optimizer's operation throughout the week exhibits a cost reduction of 16.32% compared to the condition-based approach. However, it is important to consider the impact of the disparity in the amount of hydrogen remaining in the tank. After all, the hydrogen in the tank is a source of power that will not entail the costs associated with natural gas ( $C_{\text{NG}}$  and  $C_{\text{NG,tax}}$  in Eq. (19)). To assess this, the cost savings attributed to the hydrogen quantity are calculated by comparing the costs of using natural gas with an equivalent heat value, as detailed in Table 7 under the column "H<sub>2</sub> res. cost red.". The findings reveal that despite the condition-based scenario having a higher quantity of saved hydrogen in the tank, the optimizer still manages to achieve approximately a 12.44% cost reduction. It should be noted that the gap in hydrogen availability rates will eventually stabilize once the tank reaches full capacity. At that point, it is expected that the optimizer will consume less hydrogen, as observed during this case study. Consequently, the cost reduction prospects will continue to favor the optimized operation.

The optimized operation demonstrates a notable decrease of 16.42% in the total consumption of natural gas compared to the condition-based approach, reflecting a similar relative difference in carbon-based emissions. However, it is important to note that the optimized operation experienced a slight increase of 0.9% in NOx emissions compared to the condition-based operation. This outcome can be attributed to the gas turbine's high NOx emissions at low power outputs, as illustrated in Fig. 7. Despite the optimized operation's reduced reliance on gas

**Table 6**

Comparison of hydrogen balance after a week of operation by different scenarios.

	H2 prod.	H2 cons.	H2 res.
Condition-based	124.98 [t]	73.40 [kg]	51.58 [t]
Optimized	72.89 [t]	65.79 [kg]	7.10 [t]
Relative difference	-41.68%	-10.37%	-86.23%

**Table 7**

Overview of cost balance after a week of operation by different scenarios.

	NG cons.	NOx prod.	Total Cost	H2 res. cost red.	Total Cost - mod
Condition-based	2684.30 [t]	4.40 [t]	1136109 [€]	59657 [€]	1076452 [€]
Optimized	2243.65 [t]	4.44 [t]	950741 [€]	8213 [€]	942529 [€]
Relative difference	-16.42%	0.90%	-16.32%	-86.23%	-12.44%

turbines, the emission levels were slightly higher.

It is worth mentioning that the objective function solely focuses on operational costs (as shown in Eq. (19)). Therefore, the motivation to reduce NOx emissions primarily stems from the NOx tax. If there is a greater emphasis on minimizing NOx emissions, one can introduce an increasing coefficient (a value greater than 1) before the term  $C_{\text{NOx,tax}}$  in Eq. (19) to guide the optimizer towards more effective NOx reduction strategies.

The optimization operations discussed in this paper were primarily conducted within a 24-h window. However, the authors also explored the effects of shorter and longer optimization windows, yielding similar results. Interestingly, as the optimization window lengthened, the performance of the optimization process exhibited only marginal improvements. Nevertheless, extending the optimization window significantly increased the duration of the optimization process due to the larger number of parameters to optimize.

One advantage of utilizing a shorter optimization window is the enhanced accuracy of weather and demand data forecasts. For instance, if a 6-h window is employed, the optimizer can utilize more precise weather forecast values during the final hours of the same day. In contrast, a 24-h window necessitates relying on weather forecast values from the following day. Similar improvements in accuracy can be observed in demand forecasts when shorter prediction periods are utilized. However, it should be noted that as the optimization window decreases in duration, the performance of the optimizer diminishes. For example, in the examined 6-h version, the relative total cost reduction was -16.27% (instead of 16.32%). Thus, a trade-off between the optimizer's performance and the duration of optimization must be carefully considered.

## 5. Conclusion

This work introduced an integrated energy management system for an offshore microgrid comprising three petroleum platforms, a floating wind farm, and a setup for green hydrogen production and storage. Two of the platforms housed seven aero-derivative gas turbines, providing power and heat. A management tool was developed by integrating highly accurate, fast-response models of all components, representing a digital twin of the system. Actual component data were utilized with an AI approach to develop the digital twin. The study explored two operation approaches: "condition-based" with predefined economic rules for demand and production balance, and "optimization" which forecasted demands and renewable production to determine the efficient, low-cost, and low-emission solution.

The study presented a novel hybrid optimization approach for enhancing energy management efficiency. The algorithm involved two levels: field optimization with Genetic Algorithm, and platform optimization using a rapid database searching process. This approach achieved optimized solutions within 1 h, enabling real-time adjustments and fast decision-making in the offshore microgrid.

The research demonstrated that the intelligent management system, i.e., the optimizer operation, significantly enhances overall performance, compared to the already economical condition-based approach. Over a week of operation, the optimized scenario resulted in a 16% of cost reduction (c.a. 185,000 €) and a 16% reduction in natural gas

consumption and carbon-based emissions. The study's optimized scenario effectively determined the best operation schedule by considering the entire field and integrating units' operations. This success resulted from overcoming the limitations of the condition-based approach, which relied on a "platform approach" and predefined rules, lacking the ability to fully utilize all microgrid assets. In contrast, the optimization problem's complexity necessitated exploring different combinations of assets' operations to achieve cost efficiency; a task accomplished using demand and production forecasts.

The significance of this work can be summarized as follows:

- The study provided a real case study of an offshore petroleum field with minimal simplification, moving beyond conceptual microgrids typically studied in related literature and presenting a more realistic assessment with complex power connections between platforms.
- Unlike many microgrid studies, this work considered demand balance with respect to both power and heat. The inclusion of gas turbines equipped with waste heat recovery units enabled the management systems (condition-based and optimized) to address heat balance efficiently and also enhanced the realism of the study.
- The introduction of a hybrid optimization approach, utilizing both genetic algorithms and a database search, significantly reduced the computational time required for microgrid optimization. This allowed for the optimization of a day's operation within hourly schedules for all microgrid units.
- The use of the Python language and execution on a standard personal laptop underscored the efficiency and scalability of the proposed hybrid optimization method. This makes the approach practical and accessible for real-world offshore microgrid systems without the need for extensive computing resources.

While the advantages of the introduced method are highlighted, a few points must be considered:

- Model accuracy is crucial for the system's performance. Since all of the models are data-driven, access to operational data from the gas turbines, wind turbines, and electrolyzer is essential for developing highly accurate models.
- Data access readiness over time is also important for maintaining model accuracy as the microgrid components age. Periodic retraining of models with new data ensures the maintaining accuracy of the models.
- The accuracy of the demand forecast model is dependent on the quality and reliability of the weather forecasts, which are provided by meteorological institutions. It is essential to carefully select a trustworthy source of weather forecasts to ensure the performance of the developed structure.
- The two-level optimization approach improves efficiency but has limitations. Optimal results depend on database quality and the genetic algorithm's exploration of the outer loop. Enhancements in microgrid performance are possible with improved complexity and database accuracy.

In conclusion, this study introduced a smart integrated microgrid management system with low development costs, achieving significant cost and emission reduction in petroleum operations. These findings contribute to a more sustainable energy future in the offshore O&G industry, emphasizing the potential of advanced energy management techniques in addressing climate change and promoting environmental responsibility.

#### CRedit authorship contribution statement

**Reyhaneh Banihabib:** Conceptualization, Methodology, Data curation, Software, Development, Writing – original draft, Writing – review & editing. **Mohsen Assadi:** Funding acquisition, Supervision.

#### Declaration of competing interest

The authors declare the following financial interests/personal relationships which may be considered as potential competing interests: Reyhaneh Banihabib reports financial support was provided by European Union's Horizon 2020 research and innovation program under the Marie Skłodowska-Curie grant agreement No. 861079.

#### Data availability

The data will be uploaded alongside the article

#### Acknowledgments

This project has received funding from the European Union's Horizon 2020 research and innovation program under the Marie Skłodowska-Curie grant agreement No. 861079. The authors wish to acknowledge Dr. Arild N. Nystad for his valuable input and support during the formative stages of this research, which greatly contributed to the development of the ideas presented in this paper.

#### Nomenclature

AI	Artificial Intelligence
ANN	Artificial Neural Network
C	Cost
dem	Demand
ELZ	Electrolyzer
ETS	European Union Trading System
FHR	Fuel heating value ratio
GFA	Gullfaks A
GFB	Gullfaks B
GFC	Gullfaks C
GHG	Greenhouse gases
GT	Gas turbine
hr	Hour
HyT	Hydrogen tank
IEM	Integrated energy microgrids
Inc	Incentive
LHV	Lower heating value
LNG	Liquefied Natural Gas
M	Mass (stored)
m	Mass (consumption)
MAE	Mean absolute error
MAPE	Mean absolute percentage error
NCS	Norwegian Continental Shelf
O&G	Oil and gas
ov	Objective value
P	Power
N	Number of gas turbines
NG	Natural gas
Q	Heat
red	Reduction
res	Reserved
R&D	Research and Development
WHRU	Waste heat recovery unit

#### References

- LM2500 & LM2500XPRESS Gas Turbines | GE Gas Power." <https://www.ge.com/gas-power/products/gas-turbines/lm2500> (accessed May 25, 2023).
- Adrian, Hjellestad, 2022. Offshore Wind Power and Hydrogen for Oil and Gas Platform Electrification. Masters, University of Bergen, Bergen, Norway.
- Al-Shetwi, A.Q., 2022. Sustainable development of renewable energy integrated power sector: trends, environmental impacts, and recent challenges. *Sci. Total Environ.* 822, 153645 <https://doi.org/10.1016/j.scitotenv.2022.153645>.
- Amin, K., Fors, T., 2020. Hydrogen Power with Siemens Gas Turbines.

- Anekwe, I.M.S., Tetteh, E.K., Akpasi, S., Atuman, S.J., Armah, E.K., Isa, Y.M., 2023. Carbon dioxide capture and sequestration technologies – current perspective, challenges and prospects. In: *Green Sustainable Process for Chemical and Environmental Engineering and Science*. Elsevier, pp. 481–516. <https://doi.org/10.1016/B978-0-323-99429-3.00034-5>.
- Anglani, N., Di Salvo, S.R., Oriti, G., Julian, A.L., 2020. Renewable energy sources and storage integration in offshore microgrids. In: 2020 IEEE International Conference on Environment and Electrical Engineering and 2020 IEEE Industrial and Commercial Power Systems Europe (IEEEIC/ICPS Europe). IEEE, pp. 1–6. <https://doi.org/10.1109/IEEEIC/ICPSEurope49358.2020.9160760>.
- Brentnø, J., 2016. *Process Simulation and Evaluation of Options for Heat and Power Generation on Offshore Oil and Gas Installations*. Norwegian University of Science and Technology, Trondheim.
- Cheng, C., Hughes, L., 2023. The role for offshore wind power in renewable hydrogen production in Australia. *J. Clean. Prod.* 391, 136223 <https://doi.org/10.1016/j.jclepro.2023.136223>.
- de Souza Nascimento, M.M., Shadman, M., Silva, C., de Freitas Assad, L.P., Estefen, S.F., Landau, L., 2022. Offshore wind and solar complementarity in Brazil: a theoretical and technical potential assessment. *Energy Convers. Manag.* 270, 116194 <https://doi.org/10.1016/j.enconman.2022.116194>.
- Desmond, C., Murphy, J., Blonk, L., Haans, W., 2016. Description of an 8 MW reference wind turbine. *J Phys Conf Ser* 753, 092013. <https://doi.org/10.1088/1742-6596/753/9/092013>.
- Dokhani, S., Assadi, M., Pollet, B.G., 2023. Techno-economic assessment of hydrogen production from seawater. *Int. J. Hydrogen Energy* 48 (26), 9592–9608. <https://doi.org/10.1016/j.ijhydene.2022.11.200>.
- Durakovic, G., del Granado, P.C., Tomasgard, A., 2023. Powering Europe with North Sea offshore wind: the impact of hydrogen investments on grid infrastructure and power prices. *Energy* 263, 125654. <https://doi.org/10.1016/j.energy.2022.125654>.
- Giampieri, A., Ling-Chin, J., Roskilly, A.P., 2023. Techno-economic assessment of offshore wind-to-hydrogen scenarios: a UK case study. *Int. J. Hydrogen Energy*. <https://doi.org/10.1016/j.ijhydene.2023.01.346>.
- Goldmeier, J., 2019. *Power to Gas: Hydrogen for Power Generation Fuel Flexible Gas Turbines as Enablers for a Low or Reduced Carbon Energy Ecosystem*.
- Grainger, D., Bindingsbø, A.U., Brekke, O., De Koeijer, G., Rekaa Nilssen, O., Pettersen, J., 2021. Reducing CO2 emissions from offshore oil and gas production. *SSRN Electron. J.* <https://doi.org/10.2139/ssrn.3820726>.
- Grasso, M., 2019. Oily politics: a critical assessment of the oil and gas industry's contribution to climate change. *Energy Res. Social Sci.* 50, 106–115. <https://doi.org/10.1016/j.erss.2018.11.017>.
- GREENSTAT. Optimal utnyttelse av energi fra havvind i Sørlege Nordsjø II Offshore H2-produksjon og kabel til land. May 6, 2023. [https://api.greenstat.no/uploads/optimal\\_utnyttelse\\_av\\_energi\\_fra\\_havvind\\_i\\_sorlege\\_nordsjo\\_ii\\_hr\\_in\\_a20d9e91a9.pdf?updat\\_ed\\_at=2022-10-06T14:26:19.192Z](https://api.greenstat.no/uploads/optimal_utnyttelse_av_energi_fra_havvind_i_sorlege_nordsjo_ii_hr_in_a20d9e91a9.pdf?updat_ed_at=2022-10-06T14:26:19.192Z).
- Hachem, J., Schuhler, T., Orhon, D., Cuif-Sjostrand, M., Zoughaib, A., Molière, M., 2022. Exhaust gas recirculation applied to single-shaft gas turbines: an energy and exergy approach. *Energy* 238, 121656. <https://doi.org/10.1016/j.energy.2021.121656>.
- Haszeldine, R.S., Flude, S., Johnson, G., Scott, V., 2018. Negative emissions technologies and carbon capture and storage to achieve the Paris Agreement commitments. *Phil. Trans. Math. Phys. Eng. Sci.* 376 (2119), 20160447 <https://doi.org/10.1098/rsta.2016.0447>.
- International Energy Agency, 2020. *The Oil and Gas Industry in Energy Transitions*.
- International Energy Agency, 2022. Norway 2022 energy policy review. August. 26, 2023. <https://iea.blob.core.windows.net/assets/de28c6a6-8240-41d9-9082-a5dd65d9f3eb/NORWAY2022.pdf>.
- International Renewable Energy Agency (IRENA), 2019. Climate Change and Renewable Energy National Policies and the Role of Communities, Cities and Regions. August. 26, 2023, [Online]. <https://www.mofa.go.jp/files/000498436.pdf>.
- Jing, L., Zhao, T., Wang, Y., Zhou, J., 2022. Modeling and simulation of offshore oil and gas platform AC/DC hybrid microgrid. In: 2022 4th International Conference on Smart Power & Internet Energy Systems (SPIES). IEEE, pp. 1439–1444. <https://doi.org/10.1109/SPIES55999.2022.10082439>.
- Kopp, M., Coleman, D., Stiller, C., Scheffer, K., Aichinger, J., Scheppat, B., Mainz, Energiepark, 2017. Technical and economic analysis of the worldwide largest Power-to-Gas plant with PEM electrolysis. *Int. J. Hydrogen Energy* 42 (19), 13311–13320. <https://doi.org/10.1016/j.ijhydene.2016.12.145>.
- Korpås, M., Warland, L., He, W., Tande, J.O.G., 2012. A case-study on offshore wind power supply to oil and gas rigs. *Energy Proc.* 24, 18–26. <https://doi.org/10.1016/j.egypro.2012.06.082>.
- Kumar, S., Baalisampang, T., Arzaghi, E., Garaniya, V., Abbassi, R., Salehi, F., 2023. Synergy of green hydrogen sector with offshore industries: opportunities and challenges for a safe and sustainable hydrogen economy. *J. Clean. Prod.* 384, 135545 <https://doi.org/10.1016/j.jclepro.2022.135545>.
- Li, C., Fosso, O.B., Molinas, M., Jingpeng, Y., Raboni, P., 2020. Defining three distribution system scenarios for microgrid applications. In: 2020 IEEE 4th Conference on Energy Internet and Energy System Integration (EI2), pp. 982–987. <https://doi.org/10.1109/EI250167.2020.9347144>.
- Li, C., Othman, M., Ahamad, N.B., Molinas, M., 2022. Marine integrated energy microgrids. In: 2022 International Conference on Renewable Energies and Smart Technologies (REST), pp. 1–5. <https://doi.org/10.1109/REST54687.2022.10022621>.
- Li, Z., Sui, H., Zhang, R., Wang, G., Cai, H., 2023. Short-circuit fault detection scheme for DC microgrids on offshore platforms. *Journal of Power Electronics* 23 (5), 839–849. <https://doi.org/10.1007/s43236-023-00621-3>.
- Lim, Y.J., Goh, K., Kurihara, M., Wang, R., 2021. Seawater desalination by reverse osmosis: current development and future challenges in membrane fabrication – a review. *J. Membr. Sci.* 629, 119292 <https://doi.org/10.1016/j.memsci.2021.119292>.
- Luo, J., et al., 2023. Advances in subsea carbon dioxide utilization and storage. *Energy Rev.* 2 (1), 100016 <https://doi.org/10.1016/j.enrev.2023.100016>.
- Norwegian Meteorological Institute, 2022. Norwegian Meteorological Institute: MEPS Archive, MET Norway Thredds Service.
- Norwegian Petroleum Directorate, 2023. Emissions to Air <https://www.norskpeteroleum.no/en/environment-and-technology/emissions-to-air/#:~:text=In%202022%2C%20greenhouse%20gas%20emissions,Norway%20aggregate%20greenhouse%20gas%20emissions> July. 24, 2023.
- Norwegian Petroleum Directorate Professor Olav Hanssens vei, 2020. KraftFraLand to the Norwegian Continental Shelf. Stavanger. May 04, 2023. [Online]. <https://www.regjeringen.no/contentassets/f189f2bba3d42f8be6578371e30eac0/kraft-fra-land-til-norsk-sokkel-2020.pdf>.
- Oliveira-Pinto, S., Rosa-Santos, P., Taveira-Pinto, F., 2019. Electricity supply to offshore oil and gas platforms from renewable ocean wave energy: overview and case study analysis. *Energy Convers. Manag.* 186, 556–569. <https://doi.org/10.1016/j.enconman.2019.02.050>.
- Panda, D.K., Das, S., 2021. Smart grid architecture model for control, optimization and data analytics of future power networks with more renewable energy. *J. Clean. Prod.* 301, 126877 <https://doi.org/10.1016/j.jclepro.2021.126877>.
- Peters, R., Vaessen, J., van der Meer, R., 2020. Offshore hydrogen production in the North Sea enables far offshore wind development. In: Day 4 Thu, May 07, 2020. OTC. <https://doi.org/10.4043/30698-MS>.
- Polleux, L., Guerassimoff, G., Marmorat, J.-P., Sandoval-Moreno, J., Schuhler, T., 2022. An overview of the challenges of solar power integration in isolated industrial microgrids with reliability constraints. *Renew. Sustain. Energy Rev.* 155, 111955 <https://doi.org/10.1016/j.rser.2021.111955>.
- Riboldi, L., Alves, E.F., Pilarczyk, M., Tedeschi, E., Nord, L.O., 2020. Optimal design of a hybrid energy system for the supply of clean and stable energy to offshore installations. *Front. Energy Res.* 8 <https://doi.org/10.3389/fenrg.2020.607284>.
- Roussanal, S., et al., 2019. Offshore power generation with carbon capture and storage to decarbonise mainland electricity and offshore oil and gas installations: a techno-economic analysis. *Appl. Energy* 233 (234), 478–494. <https://doi.org/10.1016/j.apenergy.2018.10.020>.
- Shezan, Sk A., et al., 2023. Evaluation of different optimization techniques and control strategies of hybrid microgrid: a review. *Energies* 16 (4), 1792. <https://doi.org/10.3390/en16041792>.
- Stuen, T.H., 2021. *Influence of Hydrogen Use as a Fuel on Aeroderivative Gas Turbine Performance*. Norwegian University of Science and Technology.
- Sundsbo Ane, K., 2007. *Reduction of NOx Emissions from the Gas Turbines for Skarv Idun. Masters*. Norwegian University of Science and Technology, Trondheim.
- Svendsen, H.G., Høldyk, A., Vrana, T.K., Mosgren, I.R., Wiik, J., 2022. Operational planning and power management system for offshore platform with wind energy supply – impacts on CO2 reduction and power quality. In: *Petroleum Technology*, 10. American Society of Mechanical Engineers. <https://doi.org/10.1115/OMAE2022-78802>.
- Tampen - Equinor, Hywind. April. 17, 2023. <https://www.equinor.com/energy/hywind-tampen>.
- Tan, W., Zhang, A., Feng, Y., Sun, Y., Huang, H., Siyuan, W., 2019. Study on short-term load forecasting method considering meteorological factors of offshore oilfield grid microgrid. In: 2019 IEEE Innovative Smart Grid Technologies - Asia (ISGT Asia), pp. 850–853. <https://doi.org/10.1109/ISGT-Asia.2019.8881350>.
- Tangerås, B.-T., Tveiten, Å.S., 2018. *Hywind Tampen, Project NPV Calculation with and without Subsidies*.
- Tiloca, G., S'anchez, D., Torres Garc'ia, M., Escamilla Perejon, A., 2023. A methodology to quantify product competitiveness and innovation requirements for micro gas turbine systems in hydrogen backup applications. In: *ASME Turbo Expo 2023: Turbomachinery Technical Conference and Exposition*. ASME Turbo Expo, Boston.
- Ventrelli, S., 2022. Combining renewable microgrids and energy storage: decarbonizing offshore assets by means of offshore floating solar and wind. In: Day 1 Mon, October 31, 2022. SPE. <https://doi.org/10.2118/210821-MS>.
- Watson, S.M., 2020. Greenhouse gas emissions from offshore oil and gas activities – relevance of the Paris agreement, law of the sea, and regional seas programmes. *Ocean Coast Manag.* 185, 104942 <https://doi.org/10.1016/j.ocecoaman.2019.104942>.
- Wu, J., Chen, X.-Y., Zhang, H., Xiong, L.-D., Lei, H., Deng, S.-H., 2019. Hyperparameter optimization for machine learning models based on bayesian optimization. *Journal of Electronic Science and Technology* 17 (1), 26–40. <https://doi.org/10.11989/JEST.1674-862X.80904120>.
- Yu, Q., Liu, Y., Li, D., Jiang, Z., Long, G., 2020. Research of SSO and suppression method of distributed micro grid in offshore oil platform. In: 2020 39th Chinese Control Conference (CCC). IEEE, pp. 6214–6218. <https://doi.org/10.23919/CCC50068.2020.9188859>.
- Zare, P., Davoudkhani, I.F., Zare, R., Ghadimi, H., Mohajeri, R., Babaei, A., 2023. Maiden application of zebra optimization algorithm for design PIDN-TIDF controller for frequency control in offshore fixed platforms microgrid in the presence of tidal energy. In: 2023 8th International Conference on Technology and Energy Management (ICTEM), IEEE, Feb, pp. 1–7. <https://doi.org/10.1109/ICTEM56862.2023.10083612>.
- Zhang, Q., Ogren, R.M., Kong, S.-C., 2018. Thermo-economic analysis and multi-objective optimization of a novel waste heat recovery system with a transcritical CO2 cycle for offshore gas turbine application. *Energy Convers. Manag.* 172, 212–227. <https://doi.org/10.1016/j.enconman.2018.07.019>.

Zhang, Q., et al., 2021. Sustainable and clean oilfield development: how access to wind power can make offshore platforms more sustainable with production stability. *J. Clean. Prod.* 294, 126225 <https://doi.org/10.1016/j.jclepro.2021.126225>.  
Carbon Capture and Storage - Norwegianpetroleum.No, 2023. August. 20, 2023. [Online]. <https://www.norskpetroleum.no/en/environment-and-technology/carbon-capture-and-storage/>.  
Hydrogen - TechnipFMC plc. <https://www.technipfmc.com/en/what-we-do/new-energy/hydrogen/>. May 6, 2023.

Hywind Tampen approved by Norwegian authorities - equinor.com." <https://www.equinor.com/news/archive/2020-04-08-hywind-tampen-approved> (accessed June. 11, 2023).  
Tax rates in Norway." <https://www.regjeringen.no/no/tema/okonomi-og-budsjett/skatter-og-avgifter/avgiftssatser-2023/id2929584/> (accessed May 3, 2023).  
Views from the industry: equinor. June. 16, 2023. <https://www.dnv.com/cases/views-from-the-industry-equinor-183622>.